This project has received funding from the European Union's Horizon 2020 research and innovation programme under grant agreement No. 700748

LIQUEFACT

Assessment and mitigation of Liquefaction potential across Europe: a holistic approach to protect structures/infrastructure for improved resilience to earthquake-induced Liquefaction disasters.

H2020-DRA-2015

GA no. 700748

DELIVERABLE D7.3

Full and detailed case study report of the application of the risk/resilience assessment toolbox for the selected past EILD cases

Authors:	Giuseppe Modoni, Rose Line Spacagna, Luca Paolella, Alessandro Rasulo, Mauro D'Apuzzo (UNICAS) Keith Jones, Maria Antonietta Morga (ARU) Carlo Lai, Francesca Bozzoni, Cludia Meisina (UNIPV) Mirko Kosič, Matjaž Dolšek, Janko Logar (ULJ) António Viana da Fonseca, Maxim Millen, Sara Rios, Cristiana Ferreira (UPORTO) Sadik Oztoprak, Ilknur Bozbey, Cihan Oser, Sinan Sargin, Namik Aysal, Ferhat Ozcep, M. Kubilay Kelesoglu (IUC) Alessandro Flora, Emilio Bilotta (UNINA) Vincenzo Fioravante (ISMGEO) Abdelghani Meslem (NORSAR)
Responsible Partner:	Università degli Studi di Cassino e del Lazio Meridionale
Version:	1.0
Date:	31.10.2019
Distribution Level (CO, PU)	PU

This project has received funding from the European Union's Horizon 2020 research and innovation programme under grant agreement No. 700748

DOCUMENT REVISION HISTORY

Date	Version	Editor	Comments	Status
31/10/2019	1	Giuseppe Modoni	First Draft	Final

LIST OF PARTNERS

Partecipant	Name	Country
UNICAS	Università degli Studi di Cassino e del Lazio Meridionale	Italy
ARU	Anglia Ruskin University	UK
UNIPV	University of Pavia	Italy
UPORTO	University of Porto	Portugal
NORSAR	Stiftelsen Norsar	Norway
Istan-Uni	Istanbul Universitesi	Turkey
UNINA	Universita degli Studi di Napoli Federico II	Italy
ULJ	Univerza V Ljubljani	Slovenia
ISMGEO	Istituto Sperimentale Modelli Geotecnici	Italy
TREVI	Trevi, Società per Azioni	Italy

This project has received funding from the European Union's Horizon 2020 research and innovation programme under grant agreement No. 700748

GLOSSARY

Acronym	Description
AC	Asbestos Cement
AGI	Associazione Geotecnica Italiana
AHEAD	Archive of Historical Earthquake Data
AHR	Average Head Ratio
ALARP	As Low As Reasonably Practicable
AEL	Annualized Earthquake Loss
AFE	Annual Frequency of Exceedance
ASTM	American Society for Testing and Materials International
BRT_i	Building Recovery Time (for the generic activity)
BTM	Building Typology Matrix
CAD	Computer-Aided Drafting
CALTRANS	California Department of Transportation
CAV	Cumulative Absolute Velocity
CCS	Consorcio de Compensación de Seguros
CEN	European Committee for Standardization
CEA	California Earthquake Authority
CES	Christchurch Earthquake Sequence
CGD	Canterbury Geotechnical Database
CLE	Limit Condition Emergency
CPT	Cone Penetration Test
CPTe	Electrical Cone Penetration Test

CPTm	Mechanical Cone Penetration Test
CPTu	Cone Penetration Test with Piezocone
CRR	Cyclic Resistance Ratio
CRS	Coordinate Reference System
CSR	Cyclic Stress Ratio
CT	Crust Thickness
CTL	Cumulative Thickness of Liquefiable Layers
Csv	Comma Separated Values
CTMS	Commissione Tecnica per la Microzonazione Sismica
DCI	Damage Consequence Index
DEM	Gigital Elevation Model
DPC	Department of Civil Protection
DTM	Digitail Terrein Model
EDP	Engineering Demand Parameter
EERI	Earthquake Engineering Research Institute
EILD	Earthquake Induced Liquefaction Disaster
EMEC	European-Mediterranean Earthquake Catalogue
EPV	Effective Peak Velocity
EQC	Earthquake Commission
ESHMs	European Seismic Hazard Maps
ESP	Equivalent Soil Profile
ESRI	Environmental Systems Research Institute
ETRS	European Terrestrial Reference System

EU	European Union
EWS	Early Warning Systems
FEMA	Federal Emergency Management Agency
FGDC	Federal Geographic Data Commettee
F_L, FS_L	Factor of safety against Liquefaction
FLT	Functionality Loss Time
FORM	First Order Reliability Method
FOSM	First Order Second Moment
GDAL	Geospatial Data Abstraction Library
GEM	Global Earthquake Model
GeoTIFF	Georeferenced Tagged Image File Format
GIS	Geographical Information System
GMPE	Ground Motion Prediction Equation
GNU	General Public License
GRS	Geodetic Reference System
GSM	Guidelines for Seismic Microzonation
H_{crust}	Non-liquefiable crust thickness
HDPE	High Density Polyethylene
H_{liq}	Thickness of Liquefiable Layer
HR	Head Ratio
ICC	International Building Code
ICMS	Indirizzi e criteri per la microzonazione sismica
IM	Earthquake Intensity Measure

INGV	Istituto Nazionale Geofisica e Vulcanologia
INV_DAM$_i$	inventory losses for the business activity i
IR	Implementing Rules
ITRS	Internation Terrestrial Reference System
JER	Japanese Earthquake Reinsurance
JGS	Japan Geotechnical Society
KML	Keyhole Markup Language
LDI	Lateral Displacement Index
LDP	Liquefaction Demand Parameter
Li	Loss of Income
LPI	Liquefaction Potential Index
LPI$_{ISH}$	Ishihara-inspired Liquefaction Potential Index
LRFD	Load and Resistance Factors Design
LRG	Liquefaction Reference Guide
LSs	Limit State
LSN	Liquefaction Severity Number
MASW	Multichannel Analysis of Surface Waves
MBIE	Ministry of Business, Innovation and Employment (N. Z.)
MCEs	Maximum Credible Earthquakes
MCS	Macro Seismic Scale
MMI	Modified Mercalli Intensity
MPVC	Modified polyvinyl chloride
Mw	Moment Magnitude

NAICS	North American Industry Classification System
NCEER	National Center for Earthquake Engineering Research
NERA	Network of European Research Infrastructures for Earthquake Risk Assessment and Mitigation
NERIES	Network of Research Infrastructures for European Seismology
NEHRP	National Earthquake Hazard Reduction Program
NTC	Italian National Building Code
NZGS	New Zealand Geotechnical Society
OASIS	Organization for the Advancement of Structured Information Standards
OGC	Open Geospatial Consortium
OMG	Object Management Group
PBD	Performance Based Design
PEBA	Performance Based Earthquake Assessment
PEER	Pacific Earthquake Engineering Research
PESH	Potential Earth Science Hazards
PGA	Peak Ground Acceleration
PGD	Peak Ground Displacement
PGDf	Permanent Ground Deformation
PGV	Peak Ground Velocity
PL	Probability of Liquefaction
P_{LS}	probability of exceedance of designated limit states
PRR	Plans for Prevention of Risk
PSHA	Probabilistic Seismic Hazard Analysis
RAIF	Resilience Assessment and Improvement Framework

RC	Reinforced Concrete
Rc	Repair cost
RDBMS	Relational Data Base Management System
RER	Regione Emilia Romagna
RR	Repair Rate
RRI	Rapid Risk Identification
S	one-dimensional volumetric reconsolidation settlement
Sa	Spectral Acceleration
SBT	Soil Behavior Type
SCPT	Seismic Cone Penetration Test
SHEEC	SHARE European Earthquake Catalogue
SHM Map	Map of Seismically Homogenous Microzones
SLM_i	Service Interruption Multiplier (for the generic activity)
SLS	Serviceability Limit State
SM	Seismic Microzonation
SORM	Second Order Reliability Method
SPT	Standard Penetration Test
SQL	Structured Query Language
SSI	System Serviceability Index
TC4-ISSMGE 1999	Technical Committee for Earthquake Geotechnical Engineering of the International Society for Soil Mechanics and Geotechnical Engineering
TWG	Thematic Working Group
UBI	Uninhabitable Building Index
UBIi	Upgrade Benefit Index

UL	Utility Loss
ULS	Ultimate Limit State
US	United States
UTM	Universal Transverse Mercator
Vs	Shear Wave Velocity
W3C	World Wide Web Consortium
WGS	World Geographic System
WCS	Web Coverage Service
WFS	Web Feature Service
WMS	Web Map Service
ZA_{LQ}	Attention Zone
ZR_{LQ}	Respect zone
ZS_{LQ}	Susceptibility zone
a_{max}	maximum horizontal acceleration
a_{rms}	Root Mean Square Acceleration
CN	Overburden correction factor
Dw	Groundwater depth
Dr	Soil Relative Density
Ds	Shear-induced building settlement
Fc	Fine content
Fs	Sleeve friction
G	Shear modulus

Ic	Soil Behaviour Type Index
Kα	Corrected term for influence of static shear stress
Kσ	Corrected term for overburden pressure
MSF	Magnitude Scaling Factor
$N1_{60}$	SPT number of blows.
$(N1_{60})_{cs}$	Equivalent clean sand normalized number of blows
Pa	Atmospheric pressure
Qc	Tip resistance in cone penetration test
$(qc_{1N})_{cs}$	Equivalent clean sand normalized cone tip resistance
Rd	depth-dependent shear stress reduction coefficient
Ru	Pore Pressure Ratio
S	Soil Factor
Sa(T)	Acceleration response spectrum
SSI	Soil Structure Interaction
T	Fundamental Period
U	Pore pressure
Uc	coefficient of uniformity
Vs	Shear wave velocity
Vs1	Normalized shear wave velocity
Z	Depth
β*k*	Damage standard deviation value

This project has received funding from the European Union's Horizon 2020 research and innovation programme under grant agreement No. 700748

Δu	Excess pore pressure
εv	Volumetric consolidation strains
εh	Horizontal strain
εlim	Limiting tensile strain
η	Damping correction factor
ξsys	Equivalent viscous damping
λ	Excitation wave length
σv	Total vertical stress
σv'	Effective vertical stress
σ	Normal stress
τsoil	Shear stress of soil column mass
ϕdeg	Equivalent degraded friction angle of the liquefiable layer
ψ	State parameter
γ	Shear strain
P	Mass density of the soil
ρ_{dyn}	Shaking-induced the settlement

This project has received funding from the European Union's Horizon 2020 research and innovation programme under grant agreement No. 700748

CONTENTS

This project has received funding from the European Union's Horizon 2020 research and innovation programme under grant agreement No. 700748

This project has received funding from the European Union's Horizon 2020 research and innovation programme under grant agreement No. 700748

This project has received funding from the European Union's Horizon 2020 research and innovation programme under grant agreement No. 700748

LIST OF FIGURES AND TABLE

FIGURES

This project has received funding from the European Union's Horizon 2020 research and innovation programme under grant agreement No. 700748

This project has received funding from the European Union's Horizon 2020 research and innovation programme under grant agreement No. 700748

This project has received funding from the European Union's Horizon 2020 research and innovation programme under grant agreement No. 700748

TABLES

This project has received funding from the European Union's Horizon 2020 research and innovation programme under grant agreement No. 700748

This project has received funding from the European Union's Horizon 2020 research and innovation programme under grant agreement No. 700748

SUMMARY

The holistic assessment of liquefaction risk at different scales, from single structures to aggregates, and the improvement of community resilience is the subject of the present deliverable. In particular, the performed analyses regard a number of worldwide case studies where earthquake have produced extensive damage and are carried with the aim of testing the risk assessment procedures implemented in the project to identify critical steps and validate the underlying assumption. Bearing this goal in mind, spatial databases have been created collecting data on base seismicity and subsoil properties, subsoil investigation, boreholes, CPT and SPT profiles, data on the characteristics of buildings, roads or pipelines, earthquake induced liquefaction damages observed after severe earthquakes. In the different cases empirical relations, mechanical based schemes have been implemented to connect information and map the results of the analyses. As a result, liquefaction hazard, risk and cost-effectiveness analyses for mitigation have been assembled into Geographical Information Systems.

After a chapter introducing the adopted methodology, the risk assessment procedure implemented in all technical work packages of the project, namely WP2 (European Liquefaction Hazard Map - Macrozonation - and Methodology for Localized Assessment of Liquefaction Potential - Microzonation), WP3 (Structural Liquefaction Resilience & Vulnerability Assessment Methodologies), WP4 (Comparative Analysis of State of the Art Liquefaction Mitigation Measures), WP5 (Community Resilience and Built Asset Management Planning Framework) and framed in WP6 (Liquefaction Mitigation Planning Software) is applied on six different case studies:

- A single building
- A large city - Christchurch (New Zealand)
- A medium city - Adapazari (Turkey)
- A small town and industrial district - Terre del Reno (Emilia-Romagna – Italy)
- A pipeline network - Urayasu (Japan)
- A transportation infrastructure – (Emilia-Romagna – Italy)

The databases and the outcomes Geographical Information Systems are presented in the deliverable D7.2 of the present project (*Risk analysis on the selected past EILD cases, respectively for a large to medium city, a small industrial district and a lifeline*), while the description of database creation, the analyses carried out to filter information, the procedures adopted for validation and the detailed overview of results is described herein. The present deliverable illustrates how the Risk assessment can be pursued on different systems highlighting difficulties and uncertainties that affect the assessment, looking at case studies where liquefaction has pervasively affected territory and community.

This project has received funding from the European Union's Horizon 2020 research and innovation programme under grant agreement No. 700748

LIQUEFACT

Deliverable 7.3

Full and detailed case study report of the application of the risk/resilience assessment toolbox for the selected past EILD cases

This project has received funding from the European Union's Horizon 2020 research and innovation programme under grant agreement No. 700748

1 INTRODUCTION

The general scope of the project, aimed at defining an operative strategy to quantify and mitigate the liquefaction risk on critical infrastructures, the Work Package WP7 has the role of validating the defined procedures with the retrospective analysis of past events and of summarizing the outcomes into guidelines that enable operators to implement methodologies for risk assessment and the EU Commissions to produce technical standards. Bearing this goal in mind, the action has been focused on two complementary targets, i.e. evaluate the liquefaction risk of a generic system and standardize the use of ground improvement technologies for mitigating the liquefaction risk.

As widely shown in the literature, liquefaction rarely produces the dramatic and shocking number of casualties typical of other earthquake effects like building collapse, landslides, and tsunamis. Only in a few cases liquefaction affects massively the territory, like in the flow failure examples occurred in 1964 in Alaska, that caused 32 casualties, or in the more recent 2018 earthquake occurred in Palu (Indonesia). This mechanism occurs when the static shear stresses on sloping ground exceed the frictional shear strength of the soil deteriorated by the pore pressure build-up. Displacements, in this case, can be very large, in the order of tens of meters or even more, and may disrupt buildings and infrastructure over wide areas. Apart from this extreme case, the impact more frequently regards the foundation of buildings and infrastructures affecting their performance. Briefly, damage occurs in the form of horizontal ground displacements caused by liquefaction of loose granular soils (e.g. 0'Rourke and Hamada, 1992; Hamada and O'Rourke, 1992) or as transient loss of bearing capacity that result in large vertical displacements or overall instabilities. However, earthquakes all over the world (Turkey, Greece, Taiwan, India, Japan, New Zealand, Italy) have highlighted the complex behavior of the structure-foundation system subjected to earthquake vibrations. For example, the Adapazari area (Turkey) suffered extensive liquefaction with buildings that rotated significantly and others that underwent quite uniform settlements of several dozen centimeters. In other cases, ununiform settlement caused the deformation of the superstructures up to intolerable levels. Other effects can be seen on horizontal infrastructures like breakage or disconnection of pipelines or uplift of sewer manholes. These examples highlight the importance of understanding the mechanism triggering liquefaction, predicting the response of soil subjected to ground shaking and the interaction with the overlying or embedded structures and transfer this knowledge into robust operative procedures for risk assessment. The applicability of individual tools and the complete procedures needs to be examined with real situations facing the complexity of using data of different nature, origin and quality standards and merging them into a unified framework. It is thus fundamental to observe the performance of real structures and infrastructures, reconstructing in the best possible way the subsoil and structural characteristics to interpret the occurred phenomena.

"To acquire a scientific and engineering knowledge of Engineering Seismology it is necessary to develop an intimate knowledge of all aspects of the subject; much of this can be achieved by studying the effects of earthquakes in the field. Through the field study of earthquake effects on engineering structures and on the ground itself, a unique opportunity exists to develop an understanding of the behavior of full-scale structures,

when tested by nature. It is only through properly run field studies that ground and structural failures, liquefaction and slope stability can be properly back analyzed. Existing building codes and regulations, as well as the efficacy of their enforcement and implementation, can be tested only after an earthquake. Furthermore, field study allows the interaction of ideas and the testing of theories in situ between members of a mission who are drawn from different disciplines and helps the young engineer to choose his line of research on realistic grounds and with enthusiasm. "

(NICHOLAS NEOCLES AMBRASEYS (1929-2012)

This requirement is particularly valid for the risk assessment procedures where the uncertainty of each factors should be quantified with appropriate investigation. Scope of the present deliverable is to report the application of the risk/resilience assessment toolbox for a number of selected past EILD cases with the aim of validating the implemented solution against real examples (Figure 1-1).

General layout of LIQUEFACT and role of WP7.

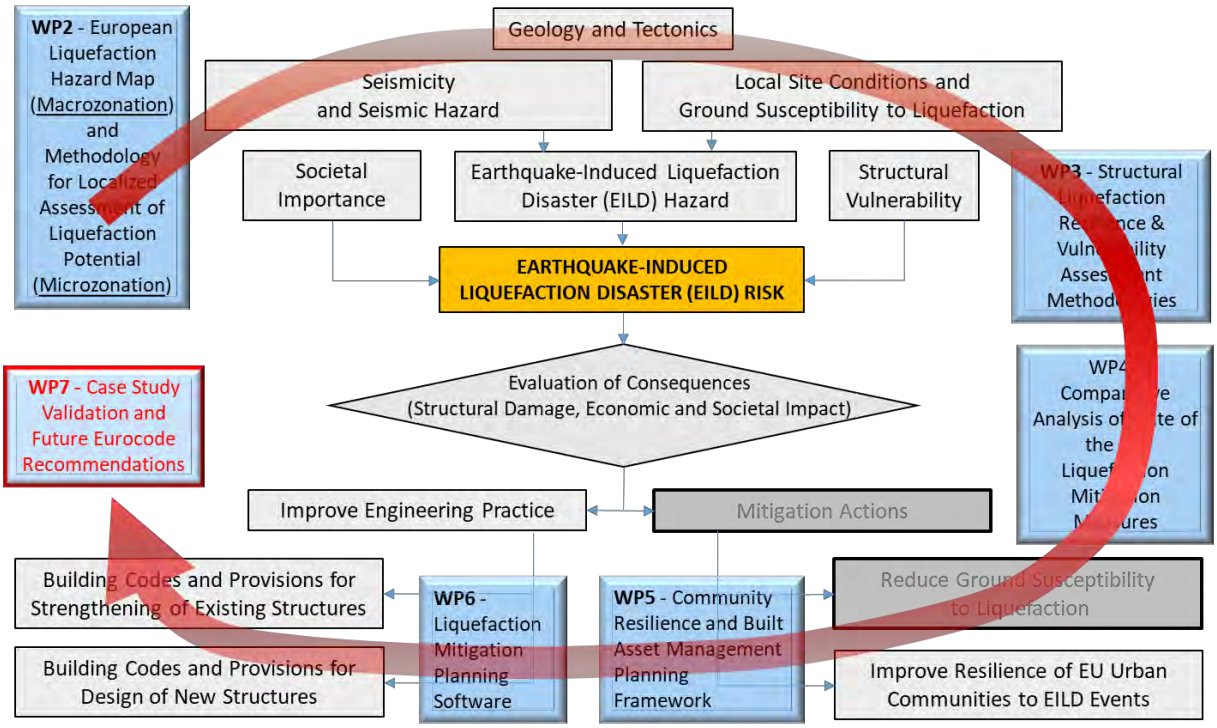

Figure 1-1 General layout of LIQUEFACT and role of WP7.

Bearing this idea in mind, the methodology implemented in the previous work packages, namely WP2 (European Liquefaction Hazard Map - Macrozonation - and Methodology for Localized Assessment of Liquefaction Potential - Microzonation), WP3 (Structural Liquefaction Resilience & Vulnerability Assessment Methodologies), WP4 (Comparative Analysis of State of the Art Liquefaction Mitigation Measures), WP5 (Community Resilience and Built Asset Management Planning Framework) and framed in WP6 (Liquefaction Mitigation Planning Software) is applied on six different case studies:

This project has received funding from the European Union's Horizon 2020 research and innovation programme under grant agreement No. 700748

- 1A single building
- A medium/large city #1- Christchurch (New Zealand)
- A medium/large city #2 - Adapazari (Turkey)
- A small town and industrial district - Terre del Reno (Emilia-Romagna – Italy)
- A pipeline network - Urayasu (Japan)
- A transportation infrastructure – (Emilia Romagna – Italy)

1.1 Liquefaction risk assessment

The assessment of liquefaction implies a sequential analysis like to one shown in Figure 1-2, where each element of the chain acts in a way that the output of the lower level forms the input of the considered element and the output of the element forms the input for the upper level.

The phenomenon regards geographical areas affected by significant seismic risk, and thus the preliminary step for risk assessment consists of the determination of the base seismic excitation. As widely described in the Deliverable 7.1, this calculation implies that a number of base seismic scenarios are derived for the studied object (a single structure, a building asset of different dimension, an infrastructure) corresponding to different annual occurrence probabilities or, equivalently, different return periods. Depending on the calculation, the characteristic parameters of the seismic motion must be assigned (see Del. 7.1 – par 4.3.1) considering with the most possible accuracy the influence of local conditions (e.g. site amplification). This step is the basis to determine the soil response with regard to liquefaction. In a preliminary analysis (Hazard assessment), this calculation that can be run with refined numerical models or with a simpler semi-empirical formulation leads to a categorisation of the ground damage.

This assessment forms the judgement criterion to decide whether further analyses need to be performed on the superstructure. Depending on the required accuracy, the analysis of the latter can be performed with more or less defined tools. However, since the subsoil response depends on the initial stress state, the load given by the overlying structure cannot be neglected. Additionally, coupled soil-structure interaction should not be overlooked in case of tall buildings whose dynamic response may be modified by liquefaction.

In general, the analysis may regard each element singularly, considering its vulnerability with regard the lower level input and provide the corresponding damage (e.g. the building affected by the excited/liquefied soil can be analysed with its structural characteristics to derive a damage level) or in a group considering its interaction with the closer elements (e.g. the building can be coupled with the lower soil in a complete soil-structure interaction assessment or with its specific role to derive the loss of functionality).

The assessment carried out over large areas implies to identify on a local basis the different factors forming risk (hazard, vulnerability and exposure) and, for each type of analysis, characterise the mechanisms defining and quantify the most suitable representative parameters (Figure 1-3). Liquefaction risk assessment is not an exception and thus demand functions must be defined for each level of Figure 1.2.

This project has received funding from the European Union's Horizon 2020 research and innovation programme under grant agreement No. 700748

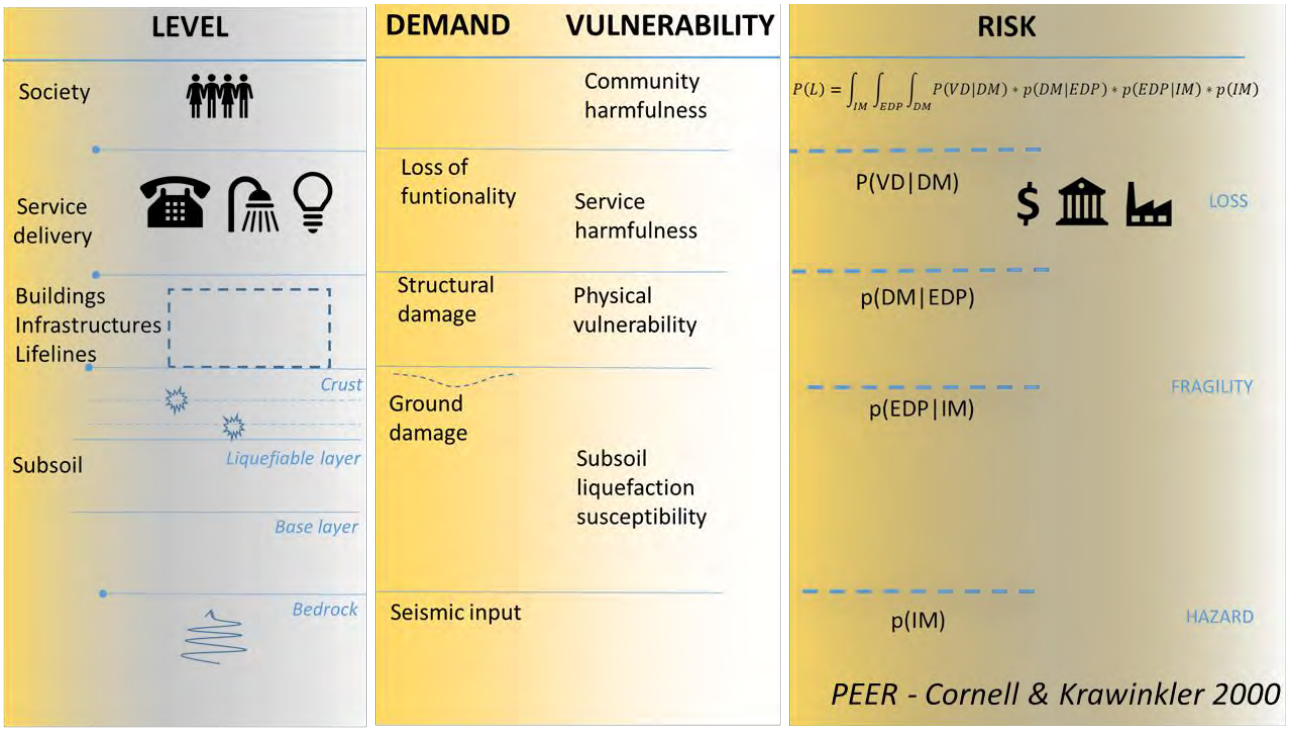

Figure 1-2 Scheme of liquefaction risk assessment.

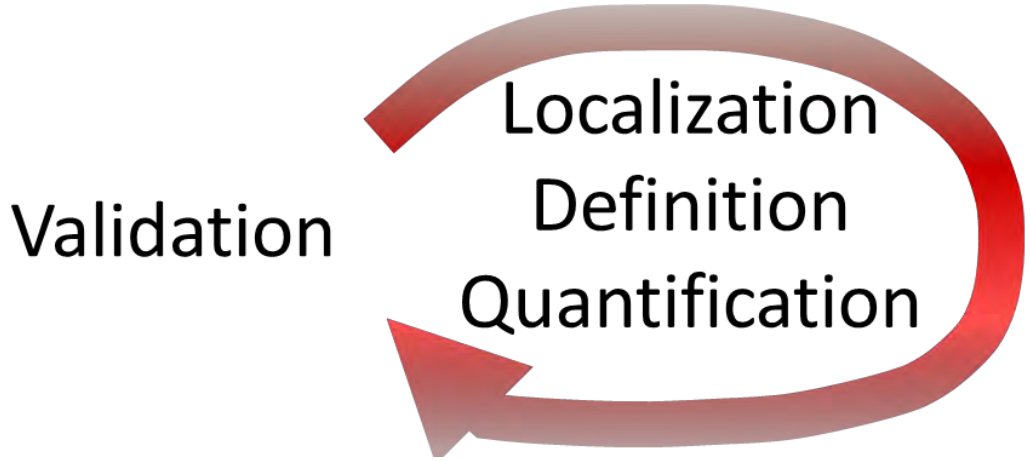

Figure 1-3 Validation scheme.

1.2 Geostatistical analysis of data

One purpose of this deliverable is to derive on an empirical basis the rules that govern the response of the different involved elements or to validate formulation developed at a theoretical level. In both cases the causality logic relating factors and effects is of paramount importance (see Figure 1-4). This process implies to recoil into a unique framework information of different nature, each derived with a specific purpose and accuracy level, and to govern the uncertainty inherently connected with each dataset and that arising when information is combined, quantifying and limiting it as much as possible. Particularly advantageous from this

This project has received funding from the European Union's Horizon 2020 research and innovation programme under grant agreement No. 700748

viewpoint is the adoption of simplified methods coupled with statistical interpretative tools, that sacrifice the accuracy of the analysis for the sake of completeness.

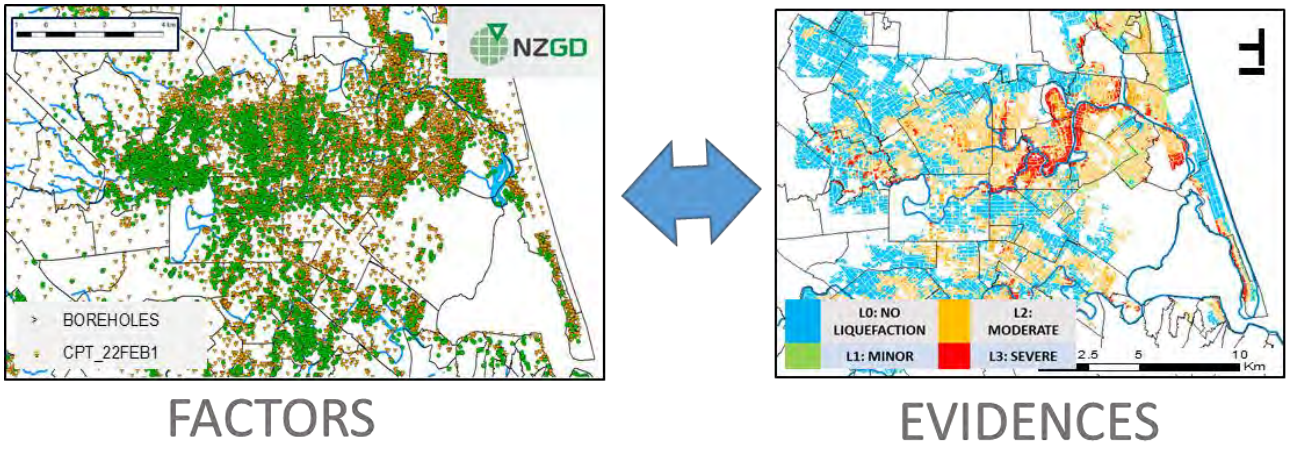

Figure 1-4 Causality link between factors and evidences (a. subsoil investigation in Christchurch area; b. damage surveyed after the February 2011 earthquake).

An example on the use of geostatistical tools is given in Figure 1-5, that reports the thickness of crust (i.e. the soil portion above the liquefiable layer) over the area of Terre del Reno (Emilia Romagna – Italy). In geostatistics (Matheron, 1965), the value of a variable in a generic point of the map is computed as a linear interpolation of the values obtained on the investigated profiles. The difference with a straight interpolation with mathematical functions (e.g. polynomial) consists in the fact that estimates are considered as statistical variables and thus a standard deviation is associated to them. This main advantage of this information is that the reliability associated to the estimate is known (a large standard deviation implies a greater uncertainty and a lower reliability). In this way, the quality of the analysis can be improved confining it to the zones where estimates are more robust. Looking at Figure 1-5.b it is immediate to see that standard deviation drops where more investigations are close to each other, while it assumes intolerable values where investigation is limited or totally missing. Hence the standard deviation map can be viewed as a tool to increase completeness of the analysis, filling the gap of information with additional investigation.

Sometimes, the original information is affected by inconsistencies, like for example largely different values of a variable even for boreholes close to each other. Possible reasons for such a discrepancy can be sought in different directions, like for instance different standards adopted in the execution of tests, to a wrong location of the borehole. In any case, removing data without a strategy supported by logical consideration sounds an arbitrary choice that renders the results of the analysis questionable. A possible alternative is thus to compare measured values with the estimates made in the same point based on the surrounding data, like in the cross-validation procedure described in Figure 1-6. The application to the case study of Terre del Reno (Emilia Romagna, Italy) reveals that while many of the available data show limited error (in the range of few percent of the estimated value), there is a relatively small portion of data for which the difference between measurement and estimate is significant. In the herein adopted procedure, it has been preferred to remove those investigation from the set of available data. A deeper assessment, necessary in case of risk sensitive

This project has received funding from the European Union's Horizon 2020 research and innovation programme under grant agreement No. 700748

areas, could provide other possible explanation to the observed scattering, saving information and interpreting them into a more complete logical framework.

The application of the two above procedures, filtering of uncertain data and removal of areas affected by low reliability, leads to transform Figure 1-5 into Figure 1-7.

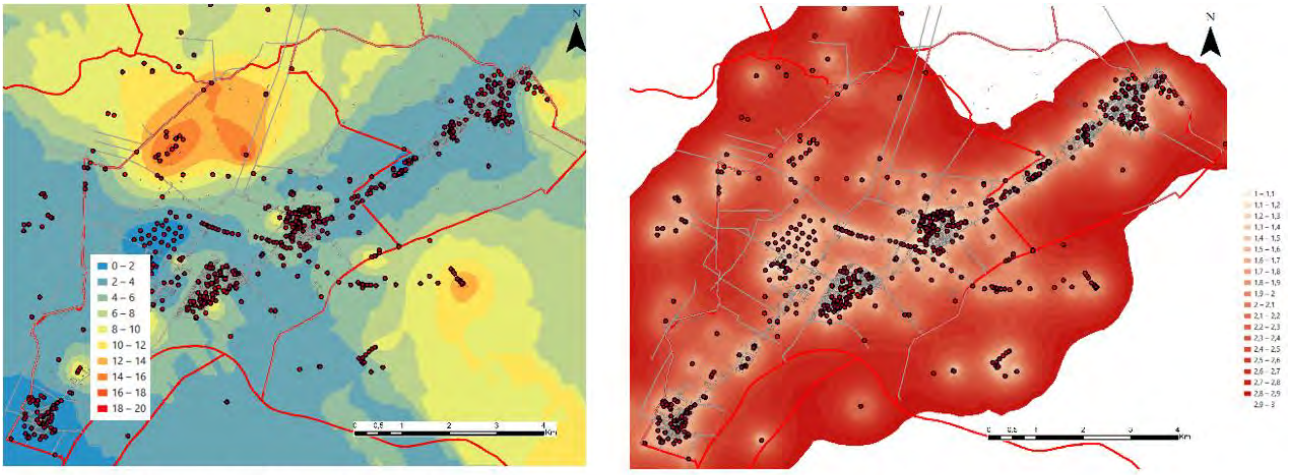

a. Estimated crust thickness from CPT tests (m)

b. Standard deviation of the estimate

Figure 1-5 Geostatistical mapping of the crust thickness (a. mean estimate; b. standard deviation).

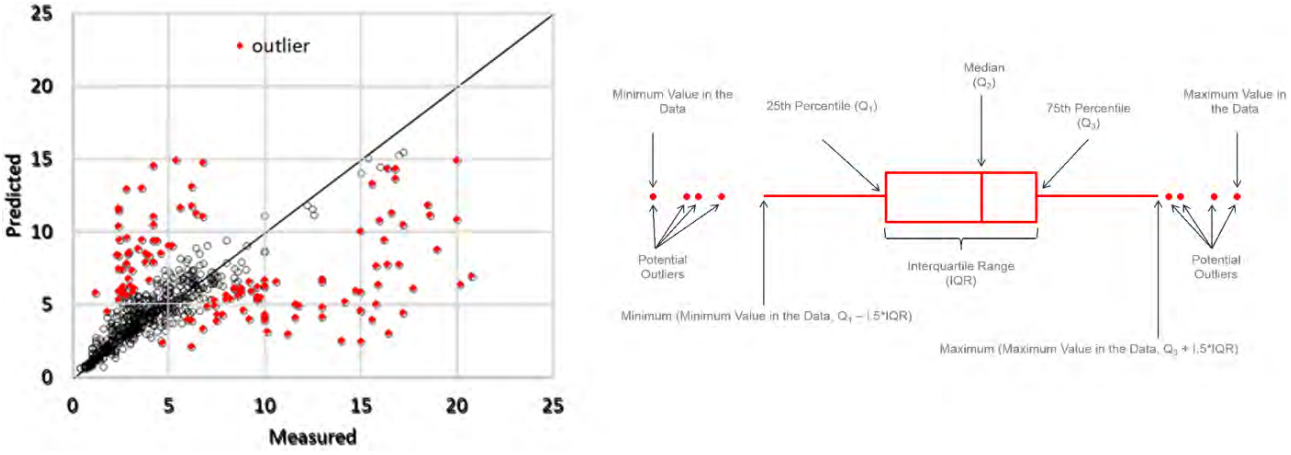

Figure 1-6 Cross validation of data to remove inconsistent information applied to the crust thickness in Terre del Reno (Emilia Romagna – Italy).

This project has received funding from the European Union's Horizon 2020 research and innovation programme under grant agreement No. 700748

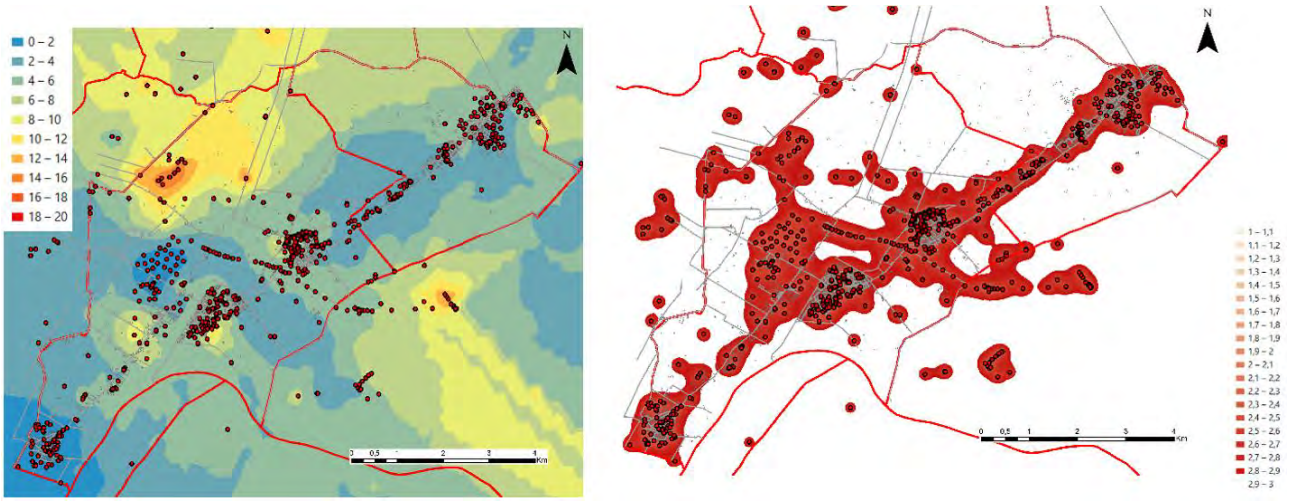

Figure 1-7 Geostatistical mapping of the crust thickness (a. mean estimate; b. standard deviation) after applying cross-validation and removal of low reliability areas.

1.3 Validation criterion

One of the main concerns of validation is to find a suitable criterion that quantifies the predictive capability of the models. In the present work, the method based on the Receiver Operating Curve (ROC) (Kongar et al., 2015) is adopted. It establishes a binary classification of predictions and observations in a way that, for a specific event and an adopted predictive model, data can be summarized into 2 x 2 contingency tables that identifies true positives (PP), true negatives (NN), false positives (FP), and false negatives (FN) (Figure 1-8). Considering on the vertical axis the outcome of an event with a clear threshold defining damage (positive event) and on the horizontal axis a candidate predictive variable, a favourable situation is the one depicted in case A of Figure 1-9 with positive and negative events/predictions defined with clear thresholds. The ROC curve reports the true positive ratio, i.e. the ratio of positive prediction over the number of positive events, on the vertical axis and the false positive ratio, i.e. the number of positive predictions over the number of negative events, on the horizontal axis. For a zero threshold of the prediction variable, the true positive and false positive ratios are both equal to 1. When the predictive threshold is increased the false positive becomes progressively true negative values (the false positive ratio reduces to zero), while the true positive values persist (the true positive ratio remains constantly equal to 1). Therefore, the ROC curve heads leftward to the vertical axis. Thereafter, when the predictive threshold is further increased, the true positive values become progressively false negative (the true positive ratio reduces to zero) and the curve moves to the origin of the axes. In this optimal condition, the size of the Area below the Receiver Operating Curve (Area Under Curve – AUC) is equal to 1.

In case of poorly performing predictive models, the dots in the binary plot are randomly distributed in the binary classification plot (case B in Figure 1-9). As a consequence, there is simultaneous reduction of True Positive and False Positive occurrences with increasing of the prediction threshold. The Receiver Operating Curve describes a 1:1 line in the false positive -true positive ratio plot and the size of AUC is equal to 0.5. The value of AUC is thus used to estimate the quality of prediction.

This project has received funding from the European Union's Horizon 2020 research and innovation programme under grant agreement No. 700748

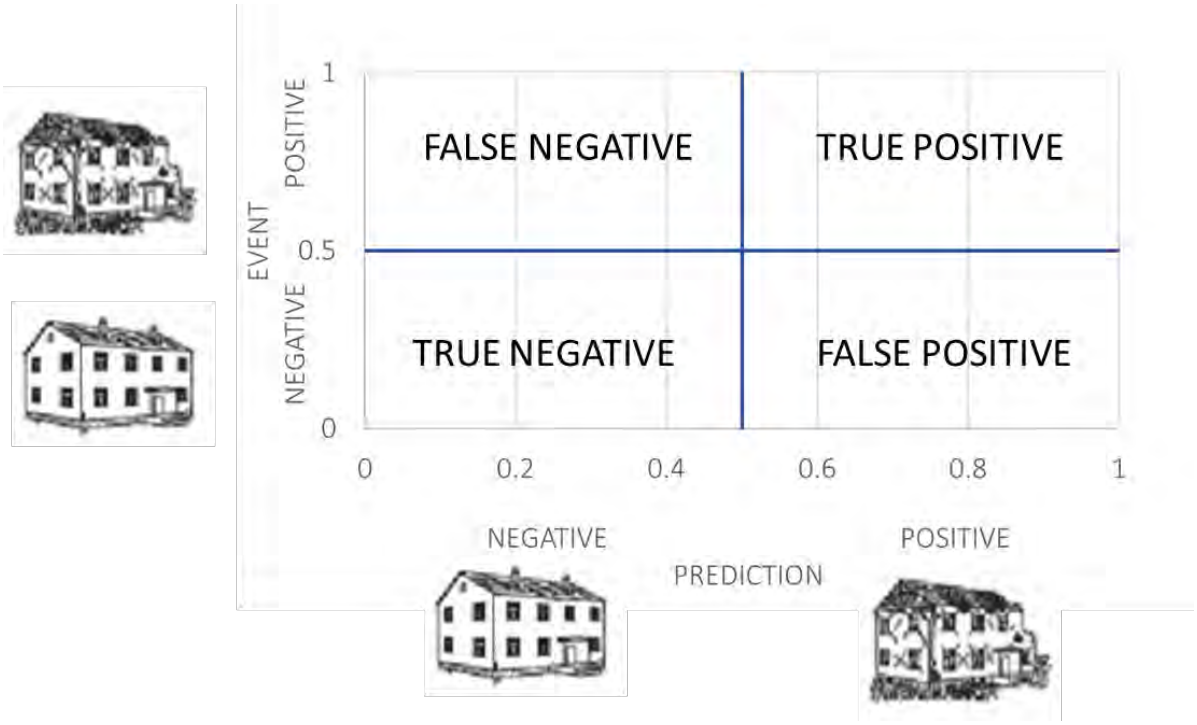

Figure 1-8 Contingency table for binary test.

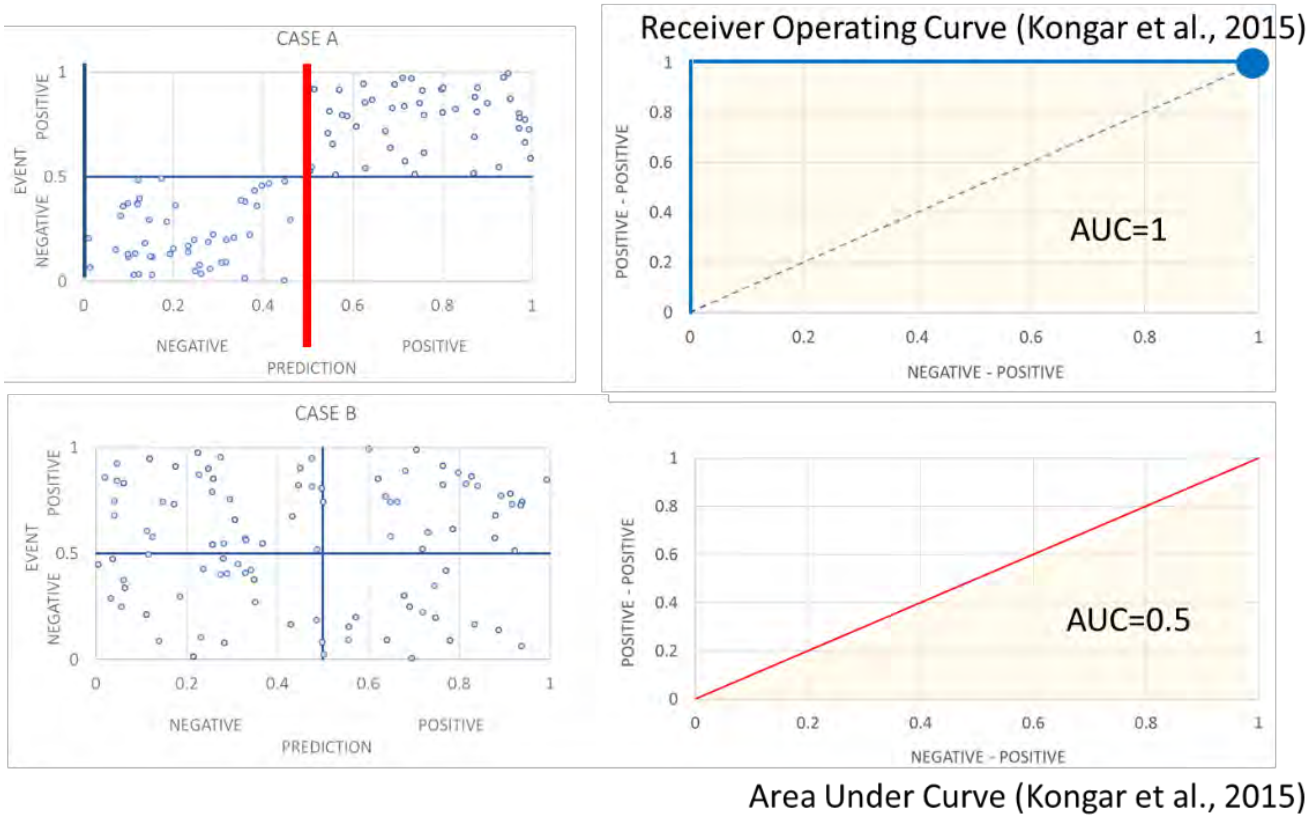

Figure 1-9 Validation criterion (Kongar et al., 2015).

Once validity of the predictive method is ensured, the last step consists in defining the optimal threshold of the predicted variable able to classify negative and positive events. To this aim, increasing values of the threshold are considered and the Mathews Correlation Coefficient defined in Eq.1.1. (Powers, 2011) has been computed for each of them. The maximum value of this function provides the best estimate of the threshold characterising the event.

$$MCC = \frac{PP\ X\ NN - NP\ X\ PN}{\sqrt{(PP+NP)(PP+PN)(NN+NP)(NN+PN)}} \quad (1.1)$$

1.4 Liquefaction hazard

The methodology for the assessment of liquefaction hazard is described in detail in chapter 4 of the deliverable 7.1 and briefly summarised in the flow chart of Figure 1-10. The procedure implies calculation of the safety factor along the investigated profile and the calculation of the integral of Eq.1.2. Depending on the functions f1(FSL) and w(z) (see Figure 1-11) different indicators may be computed.

$$INDEX = \int_{Z_{min}}^{Z_{max}} f_1(FSL)\, w(z) dz \quad (1.2)$$

As can be easily seen, each indicator differs from the other and thus a different performance is expected when applying them to estimate liquefaction hazard over the investigated area. The classical LPI (Iwasaki, 1978) index adopts a linear weight function of the complement of FSL to 1, reaching zero at a depth equal to 20 m. According to this formulation there is no contribution where FSL>1. The modification introduced to this indicator by Ishihara (e.g. Maurer, 2015) considers the presence of a crust and adopts a hyperbolic weight function, giving in this way larger importance to the shallower liquefiable strata. The settlement w (Zhang et al., 2002) puts the function f_1(FSL) equal to the vertical deformation, expressed as a function of the safety factor and of the normalized CPT resistance. Differently from the previous two, this method computes a contribution even when FSL>1. The Liquefaction Severity Index (LSN) (van Ballegooy, 2012) adopts the same function f_1(FSL) of Zhang et al., (2002) but introduces a hyperbolic weight function.

The objective of validation is to evaluate the predictive capability of the adopted indicator comparing the value assumed in an investigated profile with the effects observed in the surrounding area after an assigned earthquake. In the following, the above described procedure is applied on three different examples, respectively the case studies of May 20th 2012 in Terre del Reno (Italy) M_W=6.14, the event of February 22nd in Christchurch (New Zealand) M_W=6.2 and March 11th in Urayasu (Japan), M_W=9.

In the first case, the map with liquefaction evidence (sand boils, ground fissures) surveyed after the earthquake has been overlapped to the map of investigated profiles (Figure 1-12.a). The validation has been thus associated to the set of CPTs, identifying a circular area with radius equal to 15 m around the log and marking the event as positive if liquefaction evidences was noticed within this area, negative in the opposite case. The width of the area has been selected considering the strong heterogeneity of the subsoil and the detail of investigation performed after the test.

The Receiver Operating Curves for the indicators defined in Figure 1-11 are reported in Figure 1-13. All curves show a more and less satisfactory performance, with some relative difference possibly dictated by the

mathematical definition. It is very difficult to draw a conclusion from this plot, making a classification and identifying the best indicator, although the traditional LPI and its modified version LPIish seem to perform slightly better than the others.

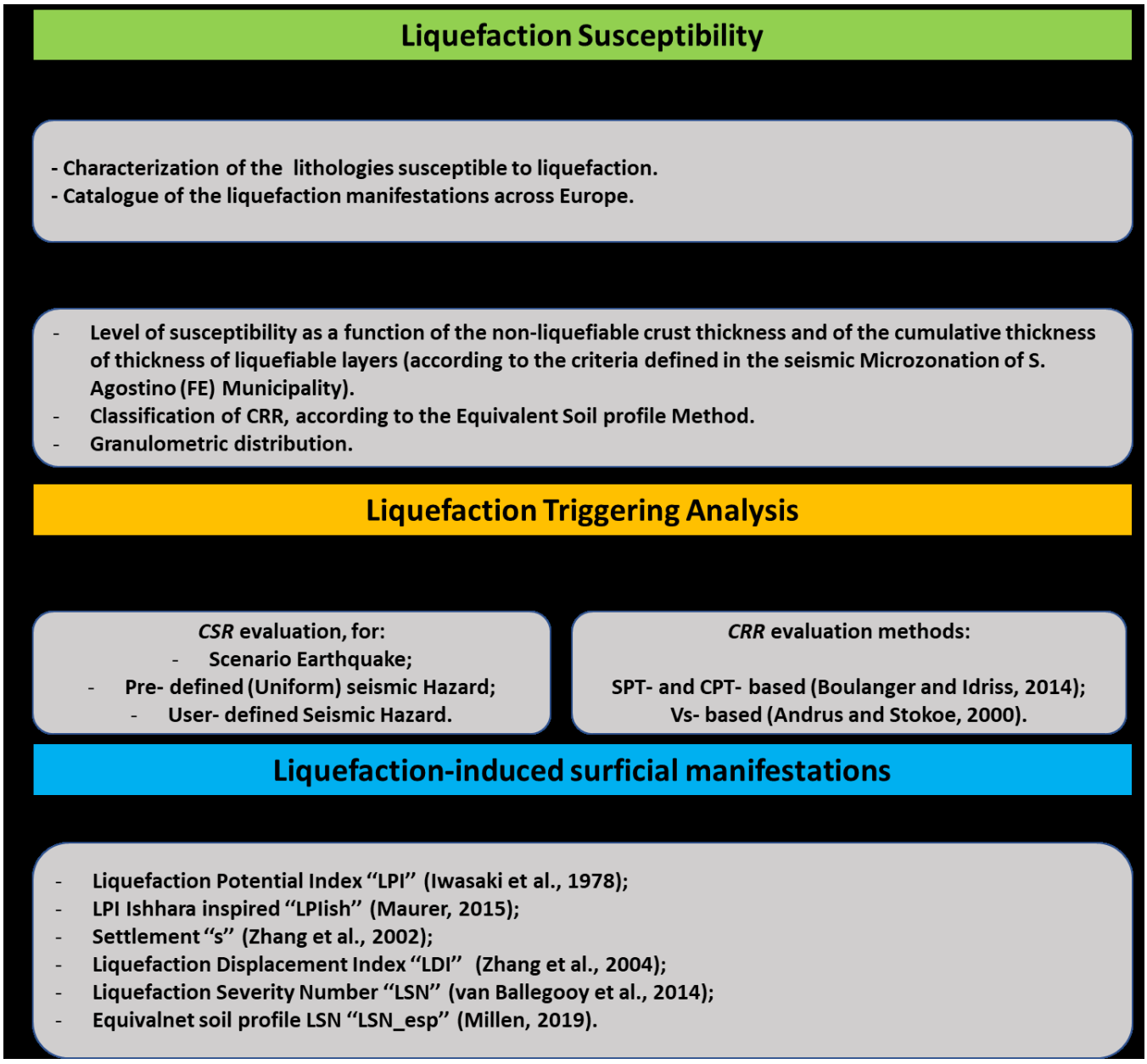

Figure 1-10 Hazard assessment procedure and indicators (Deliverable 7.1).

This project has received funding from the European Union's Horizon 2020 research and innovation programme under grant agreement No. 700748

INDEX	REFERENCE	f_1(FSL)	w(z)	Z	
LPI	Iwasaki, 1978	$1 - FSL$ if $FSL < 1$; 0 if $FSL \geq 1$	$10 - 0.5z$	$Z_{min} = 0$; $Z_{max} = 20m$	Liquefaction for FSL < 1 Linear weight with depth
LPIish	Maurer, 2015	$1 - FSL$ if $FSL \leq 1 \cap H1 \cdot m(FSL) \leq 3$; 0 otherwise Where: $m(FSL) = exp\left(\frac{5}{25.56(1-FSL)}\right) - 1$	$\frac{25.56}{z}$	$Z_{min} = H1$; $Z_{max} = 20m$	Crust thickness (H_1) Power-law depth weight
W	Zhang et al., 2002	$\varepsilon_v = \varepsilon_v(FSL, qc1N_{cs})$	-	$Z_{min} = 0$; $Z_{max} = max\,depth$	ε_v (Dr, FSL) also for FSL>1
LSN	van Ballegooy, 2014	$\varepsilon_v = \varepsilon_v(FSL, qc1N_{cs})$	$\frac{1000}{z}$	$Z_{min} = 0$; $Z_{max} = 20m$	Hyperbolic depth weight

Figure 1-11 Definition of hazard indicators.

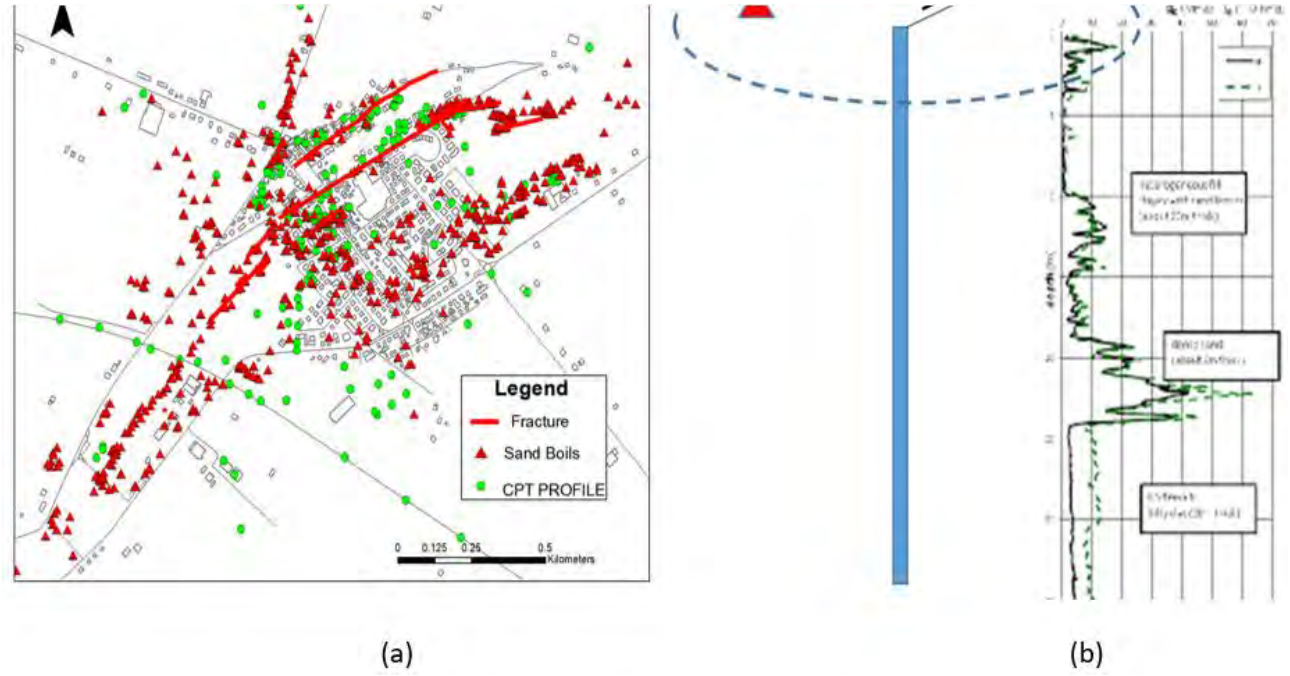

Figure 1-12 Map of San Carlo Emilia with the position of CPT tests and observed land damage (a) and criterion adopted for validation (b).

This project has received funding from the European Union's Horizon 2020 research and innovation programme under grant agreement No. 700748

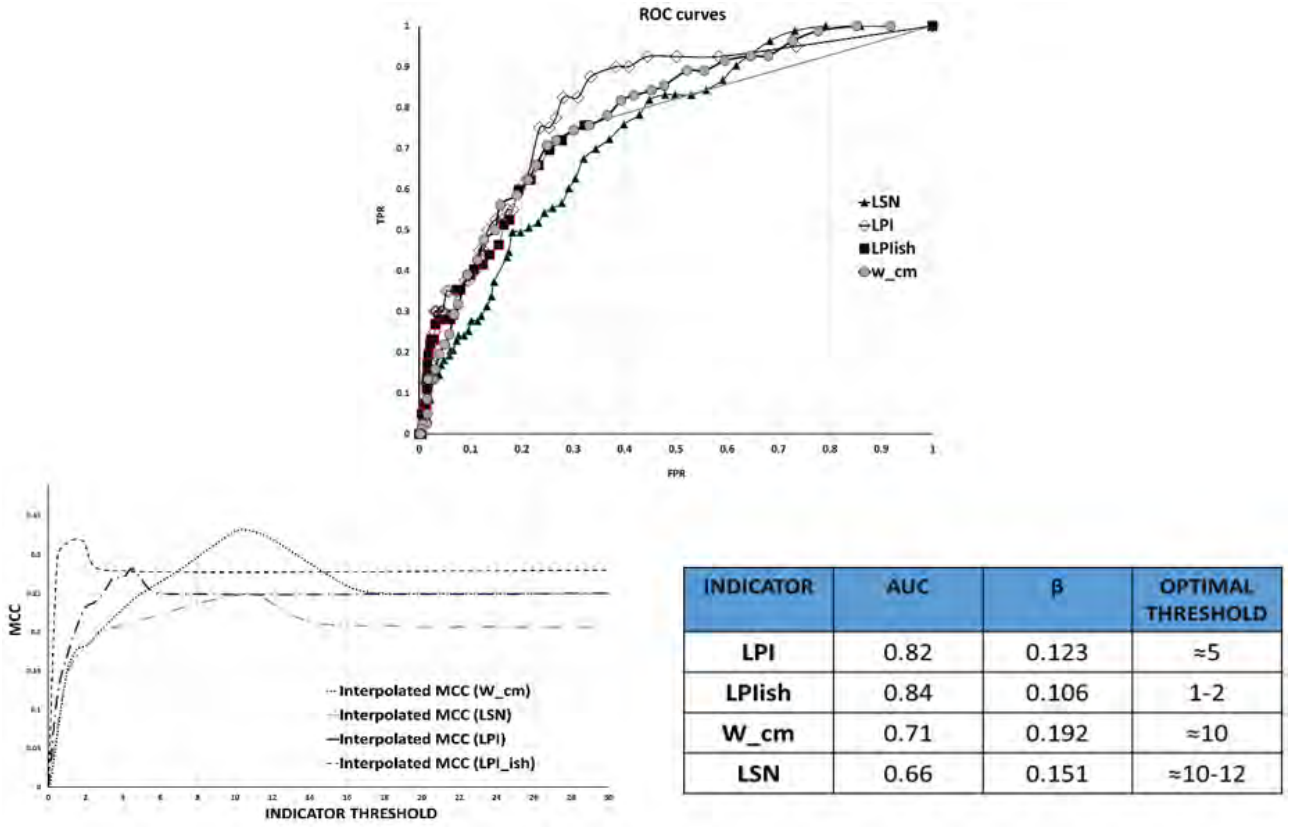

INDICATOR	AUC	β	OPTIMAL THRESHOLD
LPI	0.82	0.123	≈5
LPIish	0.84	0.106	1-2
W_cm	0.71	0.192	≈10
LSN	0.66	0.151	≈10-12

Figure 1-13 Receiver operating curve and Mathews Correlation Coefficients for the hazard indicators defined in Figure 1-11 evaluated on the May 20th earthquake in Terre del Reno.

The trend of Mathews Correlation Coefficient shows the optimal threshold for all indicators in accordance with the values proposed by the authors. The utility of such a results can be seen from Figure 1-14, reporting the maps over the three villages forming the municipality of Terre del Reno (Sant'Agostino, San Carlo and Mirabello).

This project has received funding from the European Union's Horizon 2020 research and innovation programme under grant agreement No. 700748

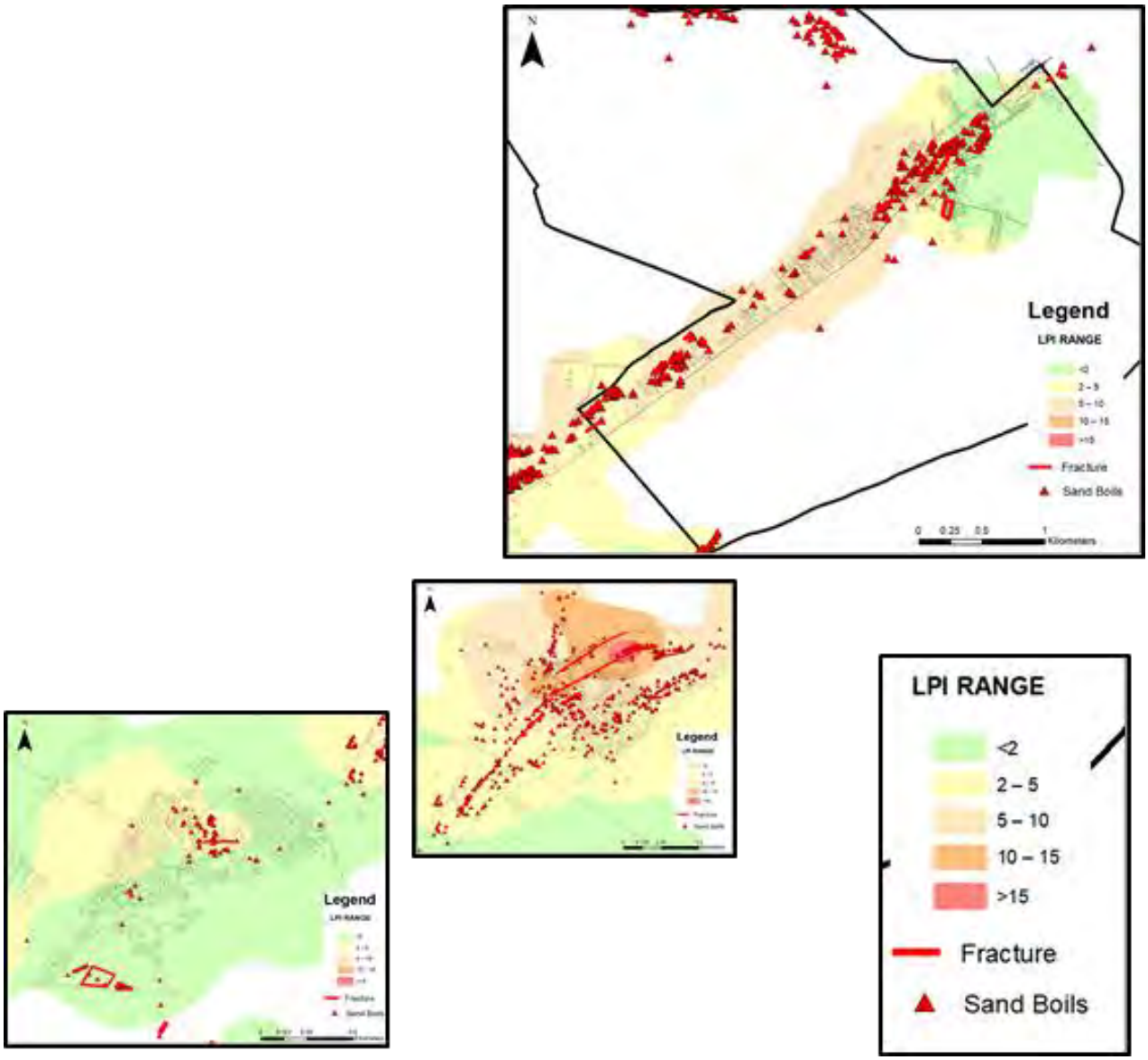

Figure 1-14 Distribution of the Liquefaction Potential Index over the villages of Sant'Agostino, San Carlo and Mirabello evaluated on the May 20th earthquake in Terre del Reno and map of observed land damage.

The second examined example is the February 22nd 2011 earthquake in Christchurch. As before, the criterion for validation is centred on the CPT profiles, but this time the information of land damage has been taken from the map given by the Earthquake Commission (Figure 1-15), that classifies with different colours the different areas of the city depending on the noticed evidences of liquefaction. Therefore, the event for each CPT profile is positive if the log falls in an area with liquefaction evidences, negative in the opposite case.

This time the result is less satisfactory than before with maximum AUC coefficient equal to 0.75, again for LPI_{ish}. A possible explanation has been sought in the more heterogeneous stratigraphy for the city of Christchurch compared with the case study of Terre del Reno. As pointed out by Cubrinovski and Van Ballegooy (2017), the dense alternation of liquefiable and non-liquefiable layers creates the conditions for a

more complex dynamic response (called system response by the authors) of the deposit, where liquefaction does not affect all layers, as postulated by the indicators, but affects selectively some of them and propagates with time to closer layers. Based on the above consideration, the analysis was repeated on selected subsoil profiles, i.e. those more closely referable to a simple three layers model (only one liquefiable layer surrounded by two non-liquefiable layers). To this aim, the Equivalent Soil Profile criterion has been applied, as defined in the Deliverables 3.1 and 3.2 of the present project (see also Millen et al., 2019), excluding from the present analysis those CPT profiles giving errors larger than 5% (Figure 1-17).

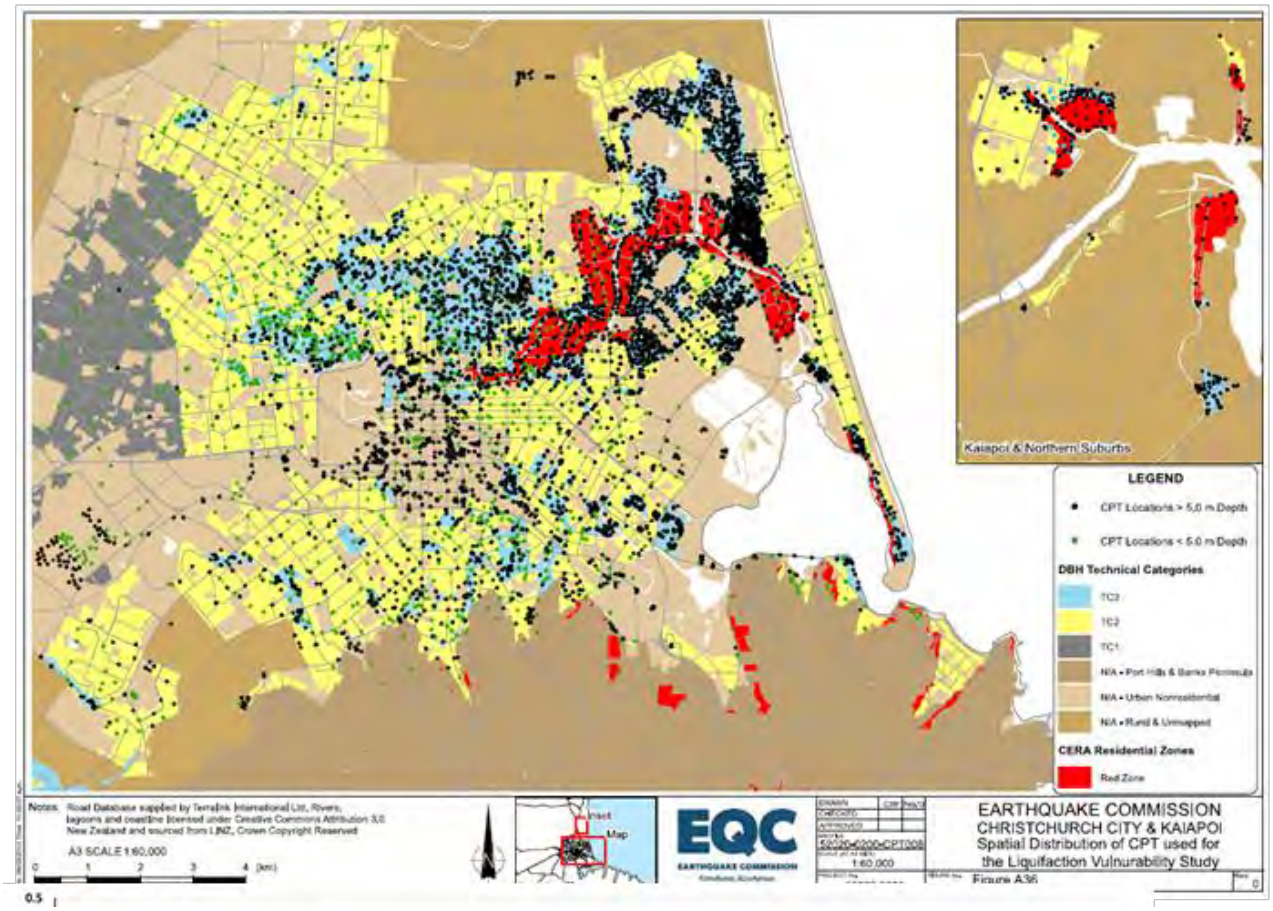

Figure 1-15 Map of Christchurch with the position of CPT tests and observed land damage.

This project has received funding from the European Union's Horizon 2020 research and innovation programme under grant agreement No. 700748

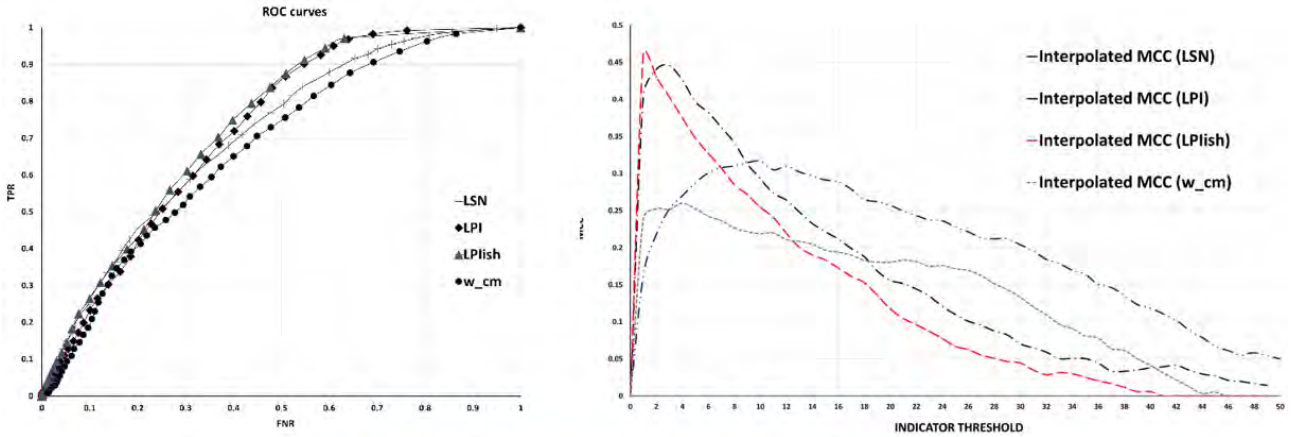

INDICATOR	AUC	β	OPTIMAL THRESHOLD
LPI	0.74	0.491	≈3
LPIish	0.75	0.655	≈1-2
W_cm	0.69	0.801	≈5
LSN	0.72	0.431	≈10

Figure 1-16 Receiver operating curve and Mathews Correlation Coefficients for the hazard indicators defined in Figure 1.11 evaluated on the Feb 22nd earthquake in Christchurch.

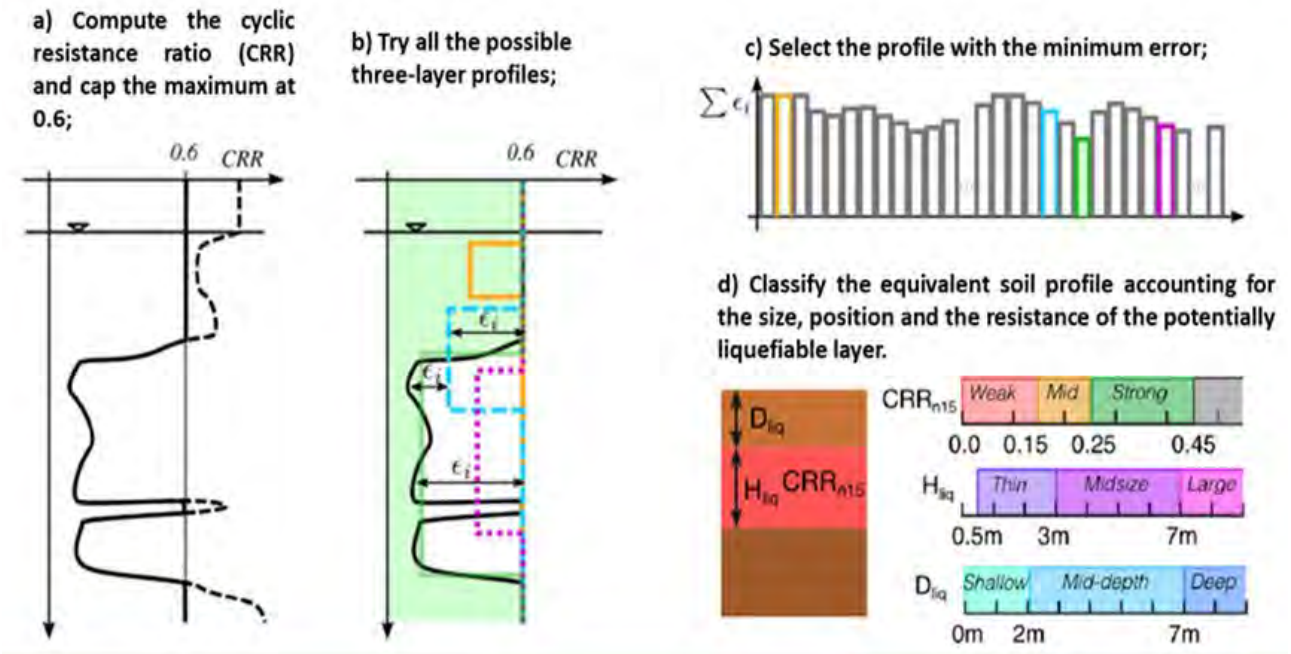

Figure 1-17 Equivalent Soil Profile criterion (Millen et al., 2019).

The test defined in Figure 1-9 has thus been repeated on selected CPT profile respecting with a certain accuracy the approximation to a three layers model and the results are plotted in Figure 1-18. This time, the performance improves significantly for all prediction indicators, with AUC coefficients reaching values as high

as 0.87. It is also interesting to see that the optimal threshold values for the indicators, corresponding to the maximum of the Mathews Correlation Coefficients are similar for all the performed analyses.

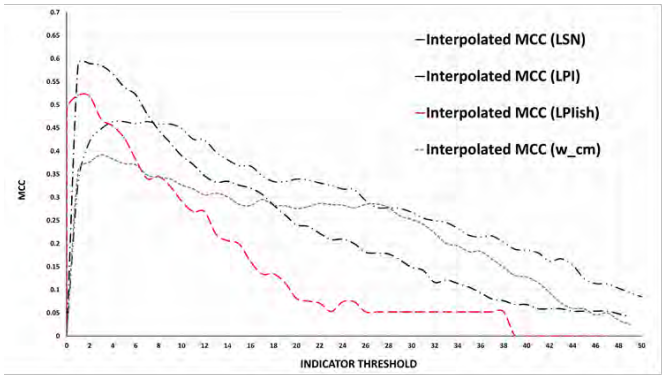

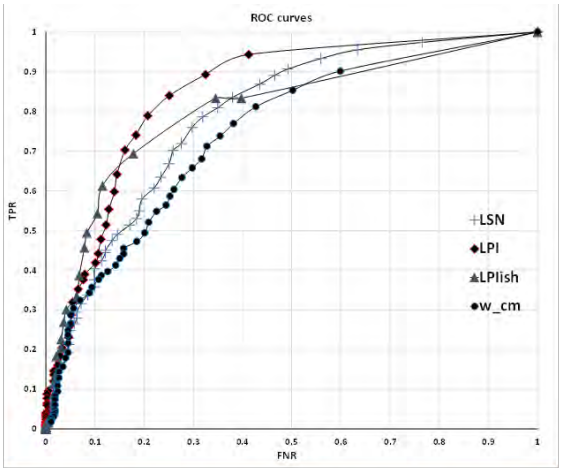

INDICATOR	AUC	β	OPTIMAL THRESHOLD
LPI	0.87	0.396	≈3-5
LPIish	0.80	0.633	≈2
W_cm	0.77	0.357	≈3-4
LSN	0.80	0.301	≈8-10

Figure 1-18 Performance of hazard indicators for the Feb 22nd 2011 earthquake of Christchurch applied on CPT profiles referable to a three layers model.

1.5 Vulnerability of buildings

The functions defining fragility of buildings requires the following three categories to be defined:

- a taxonomy defining homogenous typologies of buildings for which vulnerability functions can be defined; each category should include structures if similar geometrical and mechanical properties to minimize uncertainty; in fact, if the typology includes different structure (materials, dimensions and construction procedures etc.), the demand parameter (the variable related to damage) will be more uncertain and its distribution affected by a larger variability;
- the engineering damage parameter (EDP), i.e. one or more variables defining the behaviour of the structure with regard to pre-defined limit conditions;
- a damage scale for buildings (FEMA, 1992 and 1998) relating the loss of functionality and the economic cost for restoring the original conditions to values of the EDP.

Traditionally, in the design standards, the performance assessment of the buildings is focused on the distortion of the structure, as can be seen from Figure 1-19 where the Appendix H of the Eurocode 7 (ENV 1997-1.2004) is reported. Among the different possible variable to quantify this effect, the relative rotation (or angular distortion) is taken into account, that quantifies the deformation of the structure scaled from the

rigid movements (average settlement and tilting). Values of β ranging between 1/2000 and 1/300, respectively for open framed and masonry infilled structures, are suggested as limits for the serviceability limit state assessment in the case of sagging deformation mode (half for hogging mode); a value of 1/150 is considered as indicative for the attainment of an ultimate limit state.

This concept is exploited and further developed in the popular plot from Boscardin and Cording (1989), that relates the damage of a structure to the attainemnt of a relative rotation and a horizontal strain (Figure 1-20).

prEN 1997-1:2004(E)

Annex H
(informative)
Limiting values of structural deformation and foundation movement

(1) The components of foundation movement, which should be considered include settlement, relative (or differential) settlement, rotation, tilt, relative deflection, relative rotation, horizontal displacement and vibration amplitude. Definitions of some terms for foundation movement and deformation are given in figure H.1.

(2) The maximum acceptable relative rotations for open framed structures, infilled frames and load bearing or continuous brick walls are unlikely to be the same but are likely to range from about 1/2000 to about 1/300, to prevent the occurrence of a serviceability limit state in the structure. A maximum relative rotation of 1/500 is acceptable for many structures. The relative rotation likely to cause an ultimate limit state is about 1/150.

(3) The ratios given in (2) apply to a sagging mode, as illustrated in figure H.1. For a hogging mode (edge settling more than part between), the value should be halved.

(4) For normal structures with isolated foundations, total settlements up to 50 mm are often acceptable. Larger settlements may be acceptable provided the relative rotations remain within acceptable limits and provided the total settlements do not cause problems with the services entering the structure, or cause tilting etc.

(5) These guidelines concerning limiting settlements apply to normal, routine structures. They should not be applied to buildings or structures, which are out of the ordinary or for which the loading intensity is markedly non-uniform.

This project has received funding from the European Union's Horizon 2020 research and innovation programme under grant agreement No. 700748

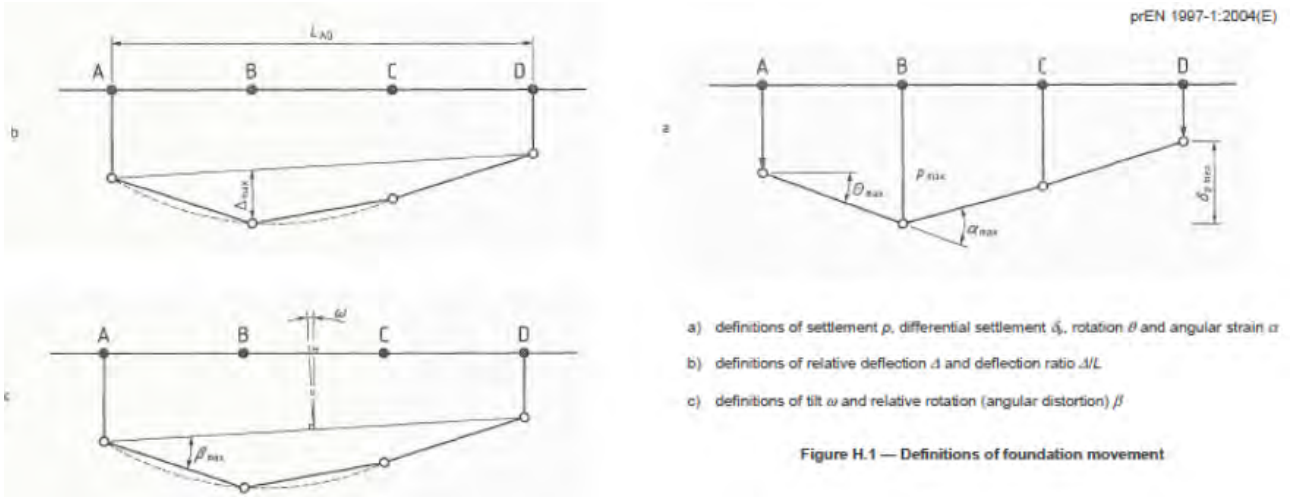

Figure 1-19 Appendix H from Eurocode 7 (ENV, 1997, 2004).

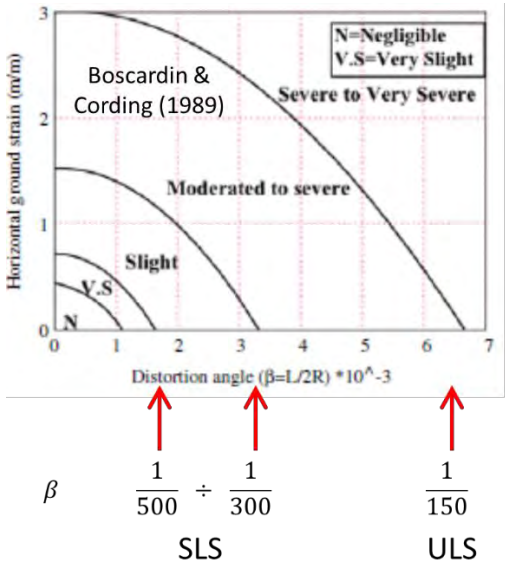

Figure 1-20 Relationship of Damage to Angular Distortion and Horizontal Extension Strain Boscardin & Cording (1989).

The same concept is borrowed by Bird et al. (2006) to quantify the damage induced by liquefaction coupling it with the drift induced by shaking (Figure 1-21). Ishihara and Yoshimine (1992) state that 'because of nonhomogeneous conditions in the soil deposits, the settlements seldom occur uniformly even in small localized areas and differential settlements become the major cause of the damage to lifelines or other facilities. "Differential ground settlements will occur due to heterogeneity in soil stiffness and stratigraphy both laterally and with depth. Estimating differential ground movements on a regional scale has an even greater uncertainty than the estimation of uniform or average movements. This is principally because of the lack of sufficient geotechnical data; a borehole at each corner of a building would allow a reasonable estimation of the variability in the settlements, even though retaining the other uncertainties listed in the previous sub-section. In the absence of this degree of detailed geotechnical data, for convenience, the

variability may be modelled as random (i.e. aleatory), assuming a statistical distribution such as normal or lognormal, with a mean and variance. Hence the distribution of differential settlements over the footprint of a building, in terms of a percentage of the absolute settlements, can be obtained.

Deterministic limit values for the settlement associated to each damage level of buildings, like those reported in Table 1.1 for rigid body settlements and rotation (Bird, 2005), are not very reliable due to the large variety of situations. In fact, these limits ignore the variability in building dimensions associated with the grouping of many buildings into a single classification. Fragility curves like those reported in Figure 1-22 are more able to consider the variability in the geometric and material properties within a building class.

These functions report the limit values of the Engineering Demand Parameter in terms of cumulated distribution, instead of a single value. Log normal probabilistic models characterised by median values and dispersion are frequently adopted.

Fragility curves for RC buildings are computed by Fotopoulou et al. (2018) using the maximum differential settlement as EDP. The authors performed several numerical analyses on framed RC buildings of different heights (two storeys structure representative of low rise, four storeys representative of medium rise, nine storeys representative of high rise buildings), flexible foundation (isolated footings) and mechanical characteristics typical of low code design buildings (see Figure 1-23). The analysis has been performed assigning variable profiles of foundation settlements and assuming the maximum differential settlement as the Engineering Demand Parameter. Two different damage mechanisms have been considered, namely a flexural damage of the building members and a shear failure of the columns. The calculation results (Figure 1.24) show dispersion coefficients not very different from one case to the other (0.50÷0.54) and median values decreasing with the building height.

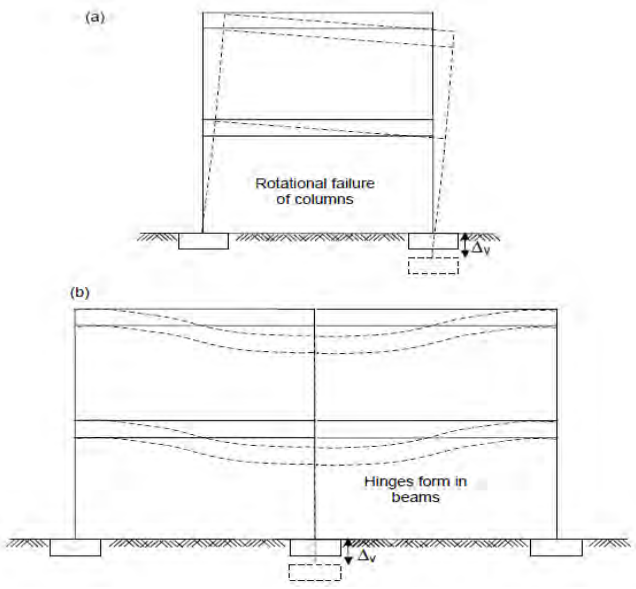

Figure 1-21 Definition of engineering damage parameter for buildings (Bird et al., 2006).

This project has received funding from the European Union's Horizon 2020 research and innovation programme under grant agreement No. 700748

Table 1-1 Suggested limit states for rigid body settlement and rotation due to earthquake ground deformation beneath RC frame buildings (Bird, 2005).

Damage state	Structural damage (see Table 2 for full description)	Additional description (rigid body deformation)	Settlement (Δ) only	Rotation (θ) only
Slight	Hairline cracks only	Repairs may be necessary for aesthetic reasons	$\Delta \leq 0.1$ m	$\theta \leq 0.6°$ 1/100
Moderate	Some cracks in load-bearing elements	Repairable damage, serviceability and/or functionality affected	0.1 m $< \Delta \leq$ 0.3 m	$0.6° < \theta \leq 2.3°$ 1/100–1/25
Extensive	Wide cracks and buckling of longitudinal reinforcement	Uninhabitable, but repairable	0.3 m $< \Delta \leq$ 1.0 m	$2.3° < \theta \leq 4.6°$ 1/25–1/12.5
Complete	Repair not feasible, shear failures or excessive displacement	Demolition cheaper than repair. Structural integrity affected, possible instability	≥ 1.0 m	$\theta \geq 4.6° \geq$ 1/12.5

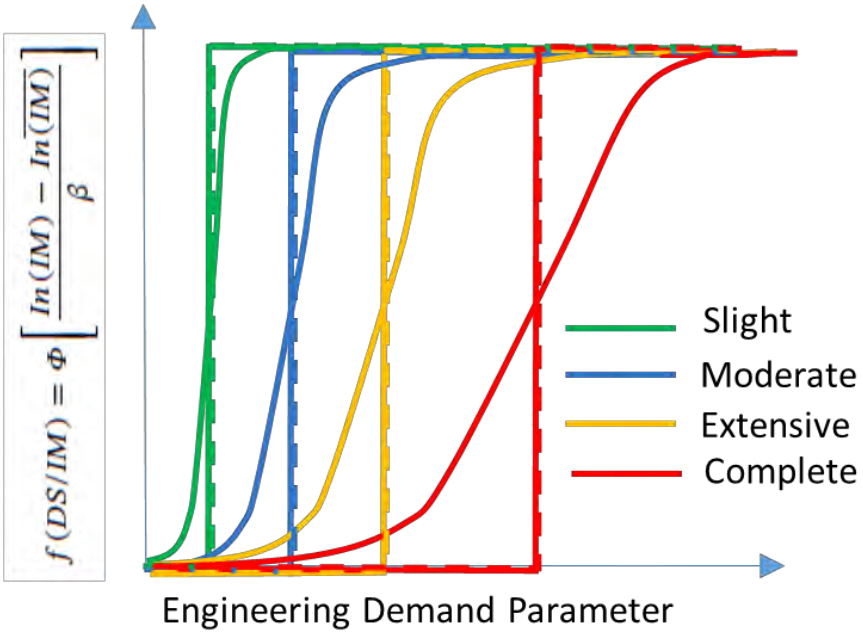

Figure 1-22 Definition of fragility functions.

This project has received funding from the European Union's Horizon 2020 research and innovation programme under grant agreement No. 700748

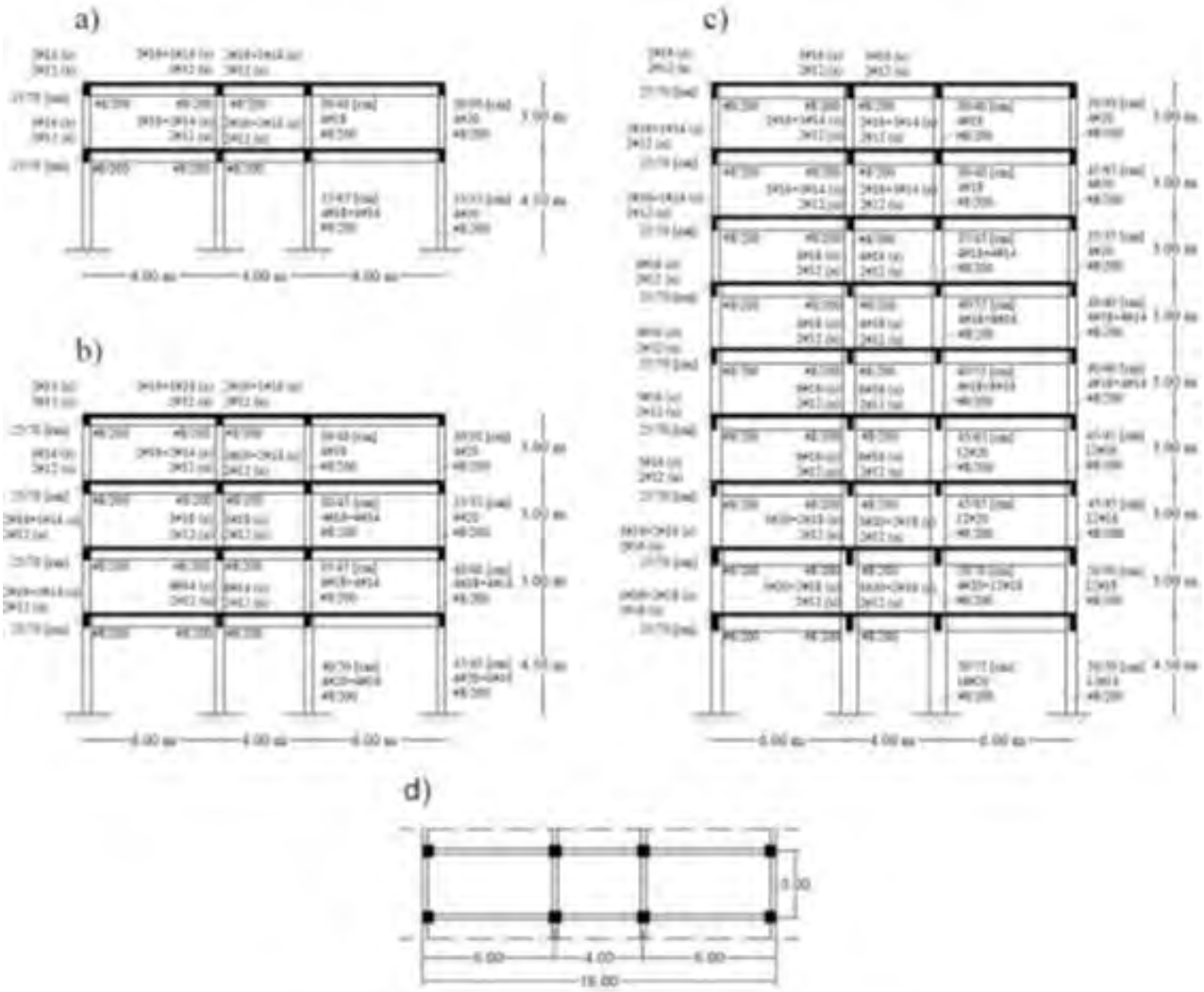

Structural damage band	Description
None to slight	Linear elastic response, flexural or shear type hairline cracks (< 1.0 mm) in some members, no yielding in any critical section
Moderate	Limit State 1 (LS_1): steel bar yielding Member flexural strengths achieved, limited ductility developed, crack widths reach 1.0 mm, initiation of concrete spalling Limit State 2 (LS_2): ε_c = 0.0125, ε_s = 0.0045
Extensive	Significant repair required to building, wide flexural or shear cracks, buckling of longitudinal reinforcement may occur Limit State 3 (LS_3): High-code frames: ε_c = 0.04, ε_s = 0.010 Low-code frames: ε_c = 0.025, ε_s = 0.006
Complete	Repair of building not feasible either physically or economically, demolition required, could be due to shear failure of vertical elements or excessive displacement Limit State 4 (LS_4): High-code frames: ε_c = 0.06 Low-code frames: ε_c = 0.045

Figure 1-23 Analysed structures and damage conditions assumed by Fotopoulou et al. (2018).

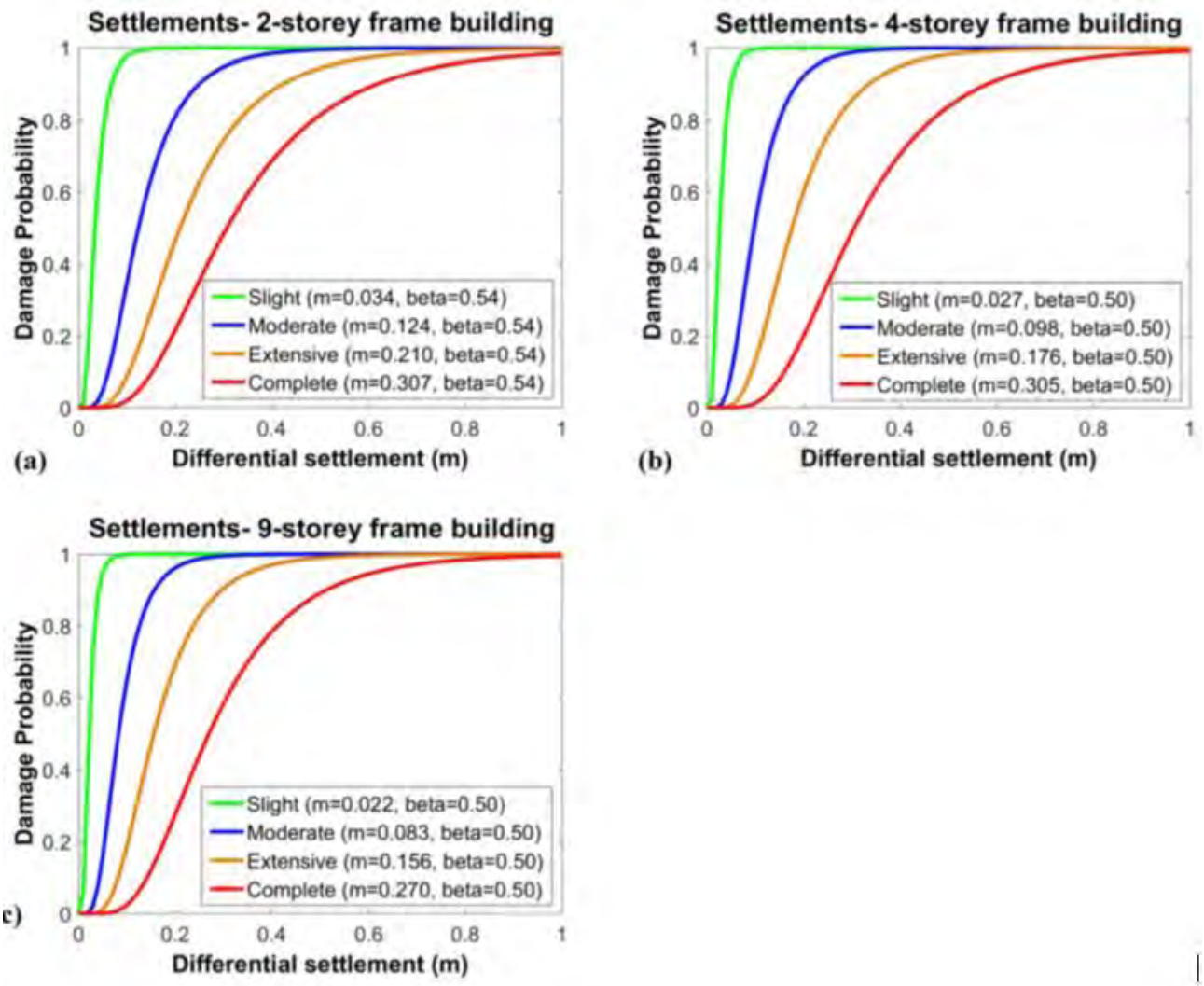

Parameters of fragility functions for the studied RC buildings subjected to settlements.

Building	Differential displacement profile	Median Differential settlement (m)				Dispersion β
		LS_1	LS_2	LS_3	LS_4	
2- storey	Settlements- middle column	0.034	0.124	0.210	0.307	0.54
4- storey	Settlements- middle column	0.027	0.098	0.176	0.305	0.50
9- storey	Settlements- middle column	0.022	0.083	0.156	0.270	0.50

Figure 1-24 Fragility curves for reinforced concrete buildings (Fotopoulou et al., 2018).

1.5.1 Differential vs absolute settlements

The prediction of differential settlements below building is generally not an easy task, moreover in case of shaken liquefiable soils. Apart from the difficulties connected with the mechanical characterisation of the phenomenon, itself object of continuous development, the factors governing the phenomenon are not fully known. The list of factors influent on the differential settlements, extracted from the Eurocode 7 (PREN 1997, 2008) and reported in Figure 1-25, include random and systematic variations of the ground properties,

ununiform loading distributions, stiffness of the structure, loading history and rate of ground movements before and after the seismic event.

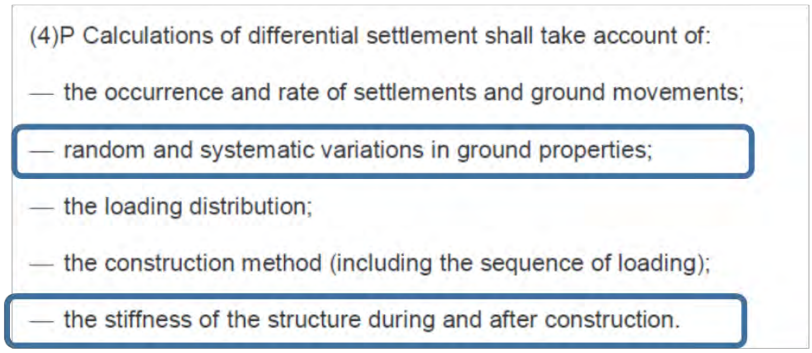

Figure 1-25 Factors governing differential settlements of buildings (extracted from PREN 1997, 2008).

To explore the role of some of these factors, various calculation has been performed in this project with a specifically adopted numerical code (FLAC by ITASCA; 2016, vers. 2D and 3D). In all analyses, a three-layer subsoil has been studied, adopting for the non-liquefiable layers simple hysteretic models coupled with Mohr Coulomb failure criterion, for the liquefiable layer a recently developed elasto-plastic Critical State model (PM4 sand, Ziotopoulou & Boulanger, 2013). The model parameters have been set considering the available tests performed on the different soils and the validity of the model has been proved comparing prediction and observation on a case study in Terre del Reno (Emilia Romagna) after the earthquake occurred in May 2012. The model is able to predict the differential settlement of a small house that suffered maximum settlements of few centimetres on one side and about 40 centimetres on the other side basically due to inclined layering of the subsoil.

The model has then been firstly adopted to evaluate with a parametric analysis the role of the flexural stiffness of the foundation. To this aim, the response of a 10 m wide plate carrying a uniform load equal to 50 kPa and subjected to variable seismic excitation. The latter has been taken from the recorded May 20th earthquake in Emilia Romagna and scaled with different factors (respectively 0.7, 1.0 and 1.6) to estimate the influence of seismic input. For this analysis, the subsoil stratigraphy has been fixed considering a 4m thickness of a crust overlying a 6m thick liquefiable layer.

The analyses repeated for different flexural stiffness on the foundation plate (from 0 to 260 MN*m) are summarily shown in Figure 1-27 where the relative rotation □ is reported as a function of the maximum settlements w_{max}; for a given stiffness, there is a clear relation between relative rotation and settlement, both increasing with the seismic input; for a given earthquake, the maximum settlement shows a limited dependency on the stiffness of the foundation, but the relative rotation decreases significantly. It is particularly worth noting that the relation between relative rotation and settlement for the case of zero stiffness is similar to the one found experimentally under static conditions by Grant et al. (1974).

This project has received funding from the European Union's Horizon 2020 research and innovation programme under grant agreement No. 700748

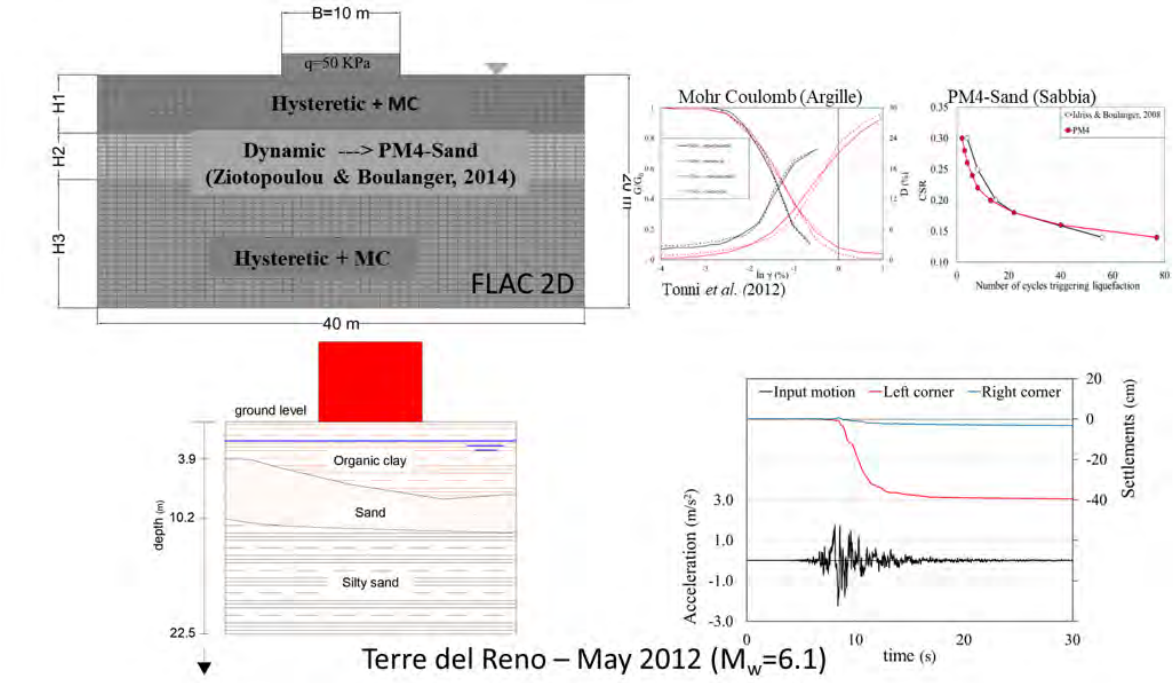

	General							Damping		PM4sand					
Layer	ρ (kg/m³)	K (Mpa)	G (Mpa)	n	k (m/s)	ϕ (°)	c (kPa)	L1	L2	Dr	G_0 (MPa)	h_{po}	n^d	n^b	A_{d0}
Clayey crust	1250	65.8	14.1	0.48	8.15E-12	0	50	-3	0.5						
Deeper clayey layers	1330	388	83	0.55	1.02E-13	0	50	-2.2	0.3						
Sandy layers	1449	13.79	29.88	0.44	2.00E-06	33	0			variable	500	0.4	2.2	0.1	0.1

Figure 1-26 Validation of the numerical model versus a case study in Terre del Reno.

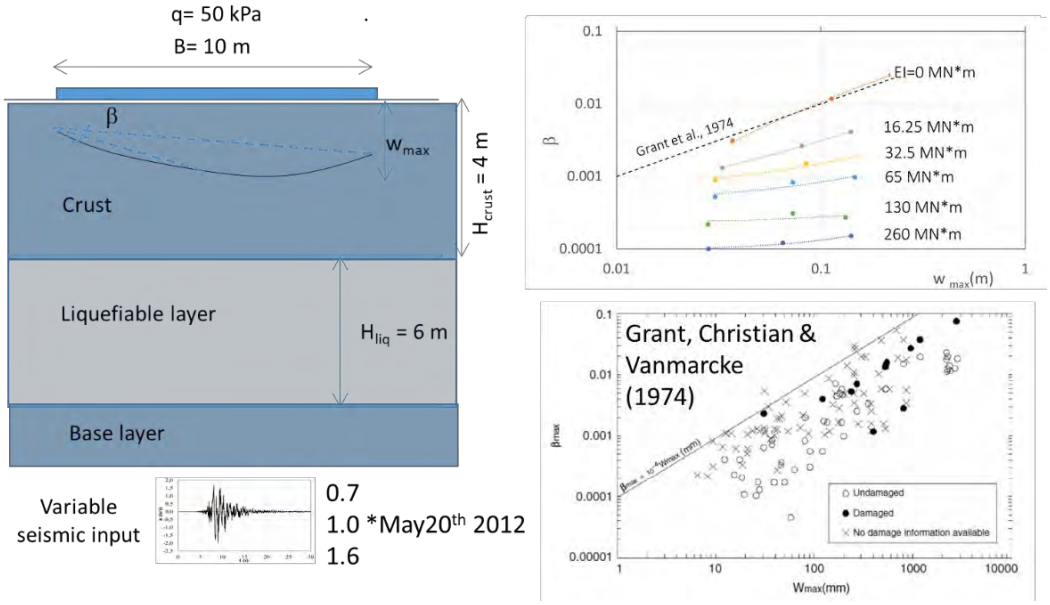

Figure 1-27 Influence of building stiffness on the relation between relative rotation and maximum settlement.

This plot suggests that the deformation mechanisms of the foundation and so the relation between angular distortion and absolute settlement, is not much dependent on the cause of the settlement and that an

increase of the foundation stiffness may protect the structure against deformation but not against absolute settlements.

The other factor considered in this study is the variability of soil properties that is often indicated as one of the main reasons for differential settlements of buildings. To investigate this issue, a spatial variability model has been built on the mechanical properties of the liquefiable layer and random field analyses have been run considering several seismic scenarios and foundation types. Considering the geometrical layout of Figure 1-27, the relative density of the liquefiable layer has been studied from the results of CPT tests performed in the area. Data of tip resistance have been converted into values of relative density (Idriss & Boulanger (2008) whose random distribution and autocorrelation function has been analysed. The random distribution has been modelled with a log-normal function; the autocorrelation has been modelled with an exponential function. The autocorrelation distance in the vertical direction has been found equal to 0.77 m with a maximum likelihood criterion defined by Honjo & Kazumba (2002), the autocorrelatin distance in the horizontal direction has been seen from the literature to vary between 2 and 5 m depending on the depositional history of the deposit (Studlein et al., 2012). In the present case the lower value (2 m) has been assumed for this distance to maximize subsoil heterogeneity and the distortional effects on the foundation.

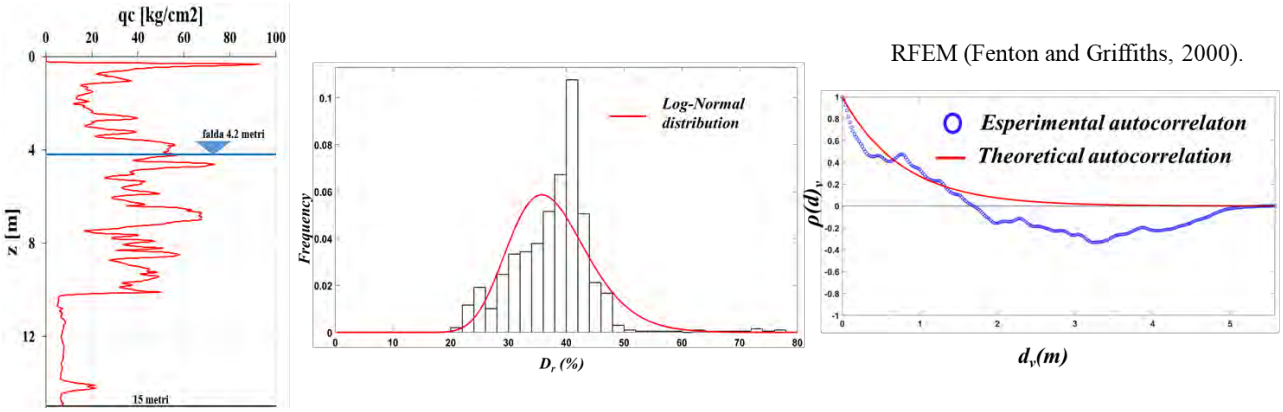

Figure 1-28 Spatial variability model.

A large numbers of random field scenarios of the relative density then been generated on the liquefiable layer of Figure 1-27 with the RFEM code (Fenton, G. A., & Griffiths, D. V. 2000). Figure 1-29 reports some examples of random field scenarios utilised for the calculation of settlements. Two types of foundation have been examined considering them representative of typical situations: an isolated footing of 0.8 m width carrying a unit load of 100 kPa; a flexible plate of 10 m width carrying a uniformly distributed load of 50 kPa. In order to generalize as much as possible the range of examined situations, crust thicknesses variable between 1 and 4 m have been given and each simulation has been repeated for three seismic inputs, obtained by scaling the acceleration time history of the May 20th earthquake of Emilia Romagna times 0.7, 1 and 1.6.

For each combination of parameters, twenty different scenarios have been generated and studied with the finite difference code FLAC (Itasca, 2016).

This project has received funding from the European Union's Horizon 2020 research and innovation programme under grant agreement No. 700748

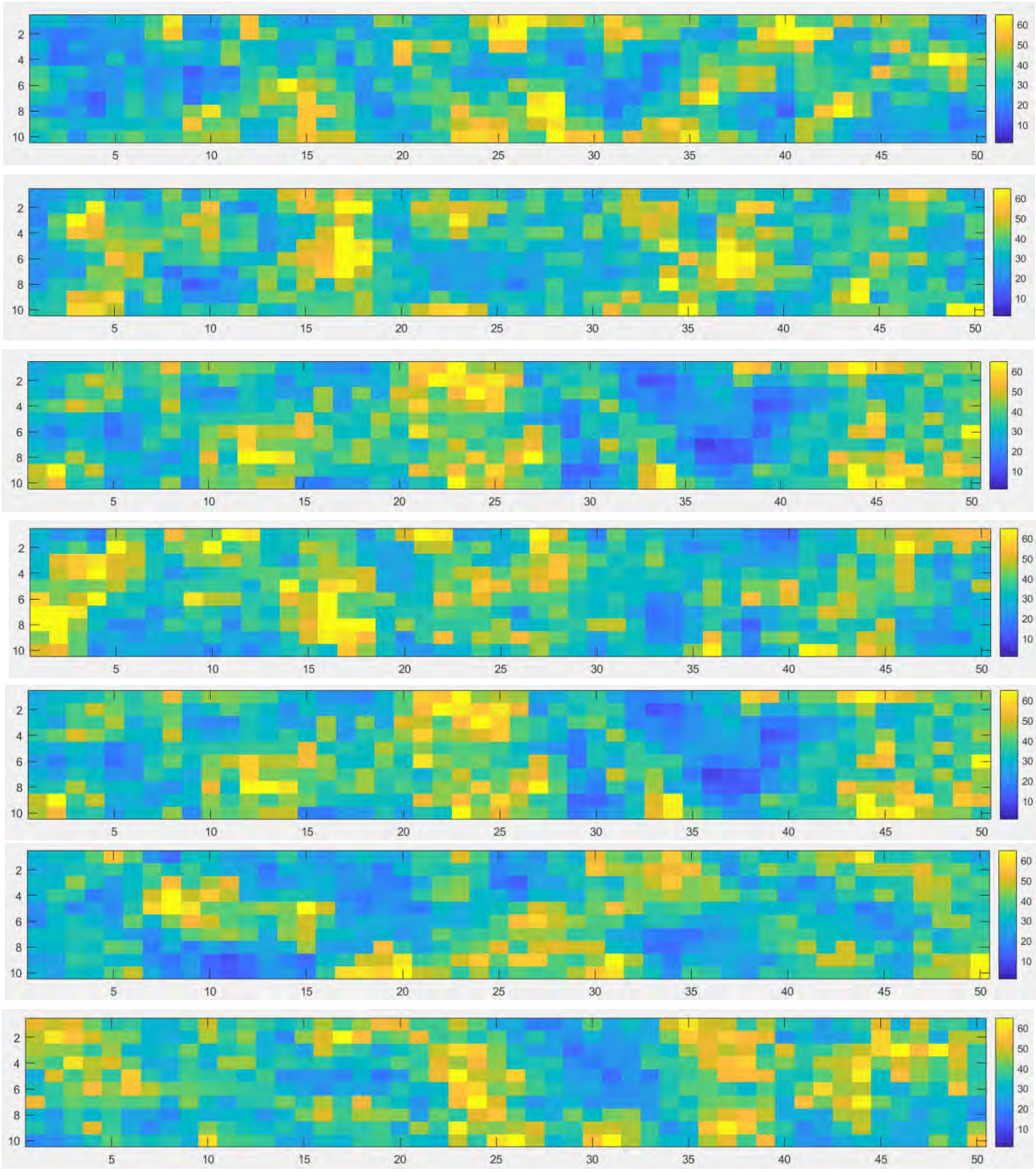

Figure 1-29 Random field scenarios generated in the present study.

The results are reported in terms of differential vs absolute settlements (Figure 1-30.a and b): in the case of isolated footings (Figure 1-30.a), the absolute settlement is the maximum vertical displacement of the foundation among the twenty values calculated for each combination of parameters (seismic input and crust

thickness), while the differential settlement is the maximum difference among the twenty values; in the case of plate foundation the differential settlement is the maximum difference among two generic points of the plate, which is plotted versus the maximum observed settlement of the entire foundation. The results show a large variability among the different considered cases, with settlements ranging from few centimetres to the order of one meter depending on the assigned crust thickness and seismic input. However, it is interesting to note the proportionality between the differential and absolute settlements, with the former in the range between the half and total absolute settlement w_{max}. This result suggests assuming the absolute settlement as the indicator of damage for the building, instead of the differential settlement, the latter more difficult to compute for the abovementioned considerations. Looking at the results of Figure 1-30, the differential settlement can be quantified as a portion (0.5÷1) of the absolute settlement (w_{max}).

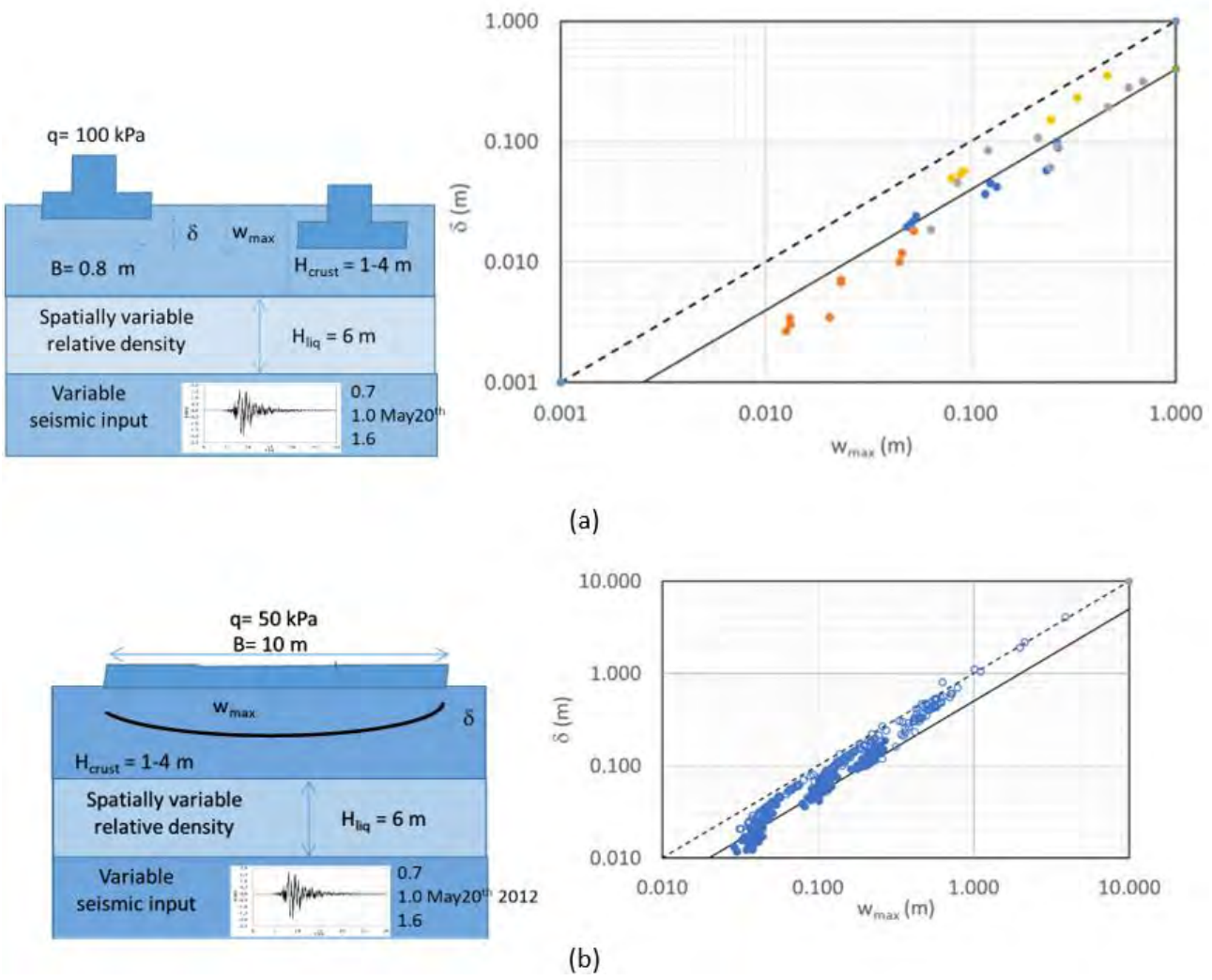

Figure 1-30 Differential vs absolute settlement from the parametric analysis of isolated footings (a) and plate foundations (b).

This project has received funding from the European Union's Horizon 2020 research and innovation programme under grant agreement No. 700748

1.5.2 Absolute settlements calculation

The above relation highlights the importance of quantifying the absolute settlement to estimate the performance of the foundation. In the following, three up to date methods have been reported that provide simplified equations aimed at computing the settlements of foundation induced by liquefaction. In all cases, the proposed formulas fit the results of a large number of numerical simulations.

1.5.3 Karamitros et al. formula (2013)

Karamitros et al. (2013) gives a simplified analytical formula for the computation of the seismic settlements of strip and rectangle footings resting on a clay crust overlying a liquefiable layer. Such settlement is associated to a ''sliding-block'' type of punching failure through the clay crust and within the liquefied sand layer. In particular, liquefaction-induced settlements are correlated to the seismic excitation characteristics and the post-shaking degraded static factor of safety, while the effect of shear-induced dilation of the liquefied subsoil is also taken into account.

The proposed expression for the dynamic settlement ρ_{dyn} (i.e. the settlement during shaking) is shown in eq. 1.2, being *c* a foundation aspect ratio correction (1.3, where *c'*=0.003), a_{max} the peak bedrock acceleration, T the representative period of the motion, N the number of cycles of the excitation, Z_{liq} the thick liquefiable sand layer, B the structure width and FS_{deg} the degraded static factor of safety of the foundation.

$$\rho_{dyn} = c a_{max} T^2 N \left(\frac{Z_{liq}}{B}\right)^{1,5} \cdot \left(\frac{1}{FS_{deg}}\right)^3 \quad (1.2)$$

$$c = c' \left(1 + 1{,}65 \cdot \frac{L}{B}\right) \leq 11{,}65c' \quad (1.3)$$

$$a_{max} T^2 N = \int_{t=0}^{t} |v(t)| dt \quad (1.4)$$

FS_{deg} in eq. 1.2 can be calculated as the degraded bearing capacity ($q_{ult,deg}$) divided by the bearing pressure (q) (1.5). The foundation bearing capacity failure mechanism is simulated by the Meyerhof and Hanna (1978) model for a crust on a weak layer using the degraded friction angle in (1.5.a). where r_u is the average excess pore pressure ratio of the liquefied sand and ϕ_0 is the initial friction angle. Superficial crust is beneficial and there is an upper bound beyond where failure occurs entirely within the crust and does not get affected by the liquefiable layer.

$$\varphi_{deg} = tan^{-1}(1 - r_u) tan(\varphi_0) \quad (1.5.a)$$

$$FS_{deg} = \frac{q_{ultdeg}}{q} \quad (1.5.b)$$

Such methodology was evaluated against results from a large number of relevant centrifuge and large-scale experiments, as well as against observations of the performance of shallow foundations in the City of Adapazari, during the 1999 Kocaeli Earthquake. Even if good agreement was found among analytical

predictions and liquefaction-induced settlements, in future applications the parameters of the numerical analyses should be respected.

1.5.4 Bray & Macedo (2017)

Combining in-situ observation, experimental test and numerical analyses, Bray and Macedo (2017) propose a method to evaluate the shear-induced building settlement (Ds) due to liquefaction below the building. The simplified procedure for estimating liquefaction-induced building settlement involves these steps:

- Perform a liquefaction triggering assessment and calculate the safety factor against liquefaction (FSL) for each potentially liquefiable soil layer preferably using a CPT-based method (e.g., Boulanger and Idriss 2016).
- Calculate the post-liquefaction bearing capacity factor of safety (FS) using the simplified two-layer solution of Meyerhof and Hanna (1978), where the average shear strength of the non-liquefied crust layer represents the top layer and the post-liquefaction residual shear strength of the liquefied soil layer represents the bottom layer. If the post-liquefaction bearing capacity FS is less 1.0 for light or low buildings or less than 1.5 for heavy or tall buildings, large movements are possible, and the potential seismic building performance can generally be judged to be unsatisfactory.
- Estimate the likelihood of sediment ejecta developing at the site by using ground failure indices such as LSN, LPI, or the Ishihara (1985) ground failure design chart. If the amount of sediment ejecta is significant, estimate the amount of building settlement as a direct result of loss of ground due to the formation of sediment ejecta (De). This can best be done using relevant case histories to estimate the amount of ejecta and then assuming that the ejecta has been removed below the building foundation.
- Estimate the amount of volumetric-induced building settlement (Dv) preferably using a CPT-based method (e.g., Zhang et al. 2002).
- Estimate the shear-induced building settlement (Ds) due to liquefaction below the building using Eq. 1.6:

$$ln(Ds) = c1 + 4.59 \cdot ln(Q) - 0.42 \cdot ln(Q)^2 + c2 \cdot LBS + 0.58 \cdot ln(tanh(HL)) - 0.02 \cdot B + 0.84 \cdot ln(CAVdp) + 0.41 \cdot ln(Sa) + \varepsilon \quad (1.6)$$

$$LBS = \int W * \frac{\varepsilon_{shear}}{z} dz \quad (1.7)$$

where Ds is in mm, LBS is calculated with 3.29, c1=-8.35 and c2= 0.072 for LBS ≤ 16, and c1= -7.48 and c2=0.014 otherwise. Q is in units of kPa, HL is in m, B is in m, CAV_{dp} is in g-s, and Sa1 is in g; ε is a normal random variable with zero mean and 0.50 standard deviation in Ln units. CAV_{dp} is the standardised Cumulate Absolute Velocity as defined in Campbell and Bozorgnia (2012) where N is the number of discrete 1 second time intervals, x is PGAi-0.025 (PGAi is the value of the peak ground acceleration(g) in time interval i, inclusive of the first and last values) and H(x) is 0 if x<0 or 1 otherwise. LBS is an index of equivalent liquefaction-induced shear strain on the free-field (ε_{shear}), defined as the integration along the soil column of the strain estimated by means of the CPT-based procedure proposed in Zhang et al. (2004), weighted by the depth in order to provide more importance to the soil close to the foundation). εshear is calculated based on the estimated Dr of the liquefied soil layer and the calculated safety factor against liquefaction triggering (FSL). z(m) is the depth measured from the ground surface > 0 and W is a foundation-weighting factor wherein W = 0.0 for z less than Df, which is the embedment depth of the

foundation, and W= 1.0 otherwise. Finally, the total liquefaction-induced building settlement (Dt) can be estimated from Eq. 1.8, as:

$$Dt = De + Dv + Ds \quad (1.8)$$

1.5.5 Bullock et al. formulation (2018)

The authors present a comprehensive predictive relation for the settlement of shallow-founded structures on liquefiable ground during earthquakes. The relation is derived interpolating with a non-linear regression and latent variable analysis the results of an extensive fully coupled three-dimensional numerical parametric study of soil–structure systems, validated with centrifuge experiments and adjusted with case history observations to capture all mechanisms of settlement below the foundation, including volumetric and deviatoric strains as well as ejecta. The resulting probabilistic building settlement model incorporates the influence of the soil profile, the presence and properties of the structure and the characteristics of the ground motion, thus providing engineers with a comprehensive procedure for predicting liquefaction-induced settlement of a mat-founded building. The formula is written as:

$$\ln(\bar{S})_{num} = f_{so} + f_{fnd} + f_{st} + s_o \ln(CAV) \quad (1.9)$$

where $\ln(\bar{S})_{num}$ is the natural logarithm of the median predicted numerical foundation settlement (mm) and f_{so}, f_{fnd} and f_{st} are functions that capture effects due to the characteristics of the soil profile, foundation and the structure, respectively.

The first term is computed as:

$$f_{so} = \left[\sum_i H\left(H_{S,i} - 1 + \varepsilon\right) f_{S,i} f_{H,i}\right] + [c_0 + c_1 ln(CAV)] F_{LPC} \quad (1.10)$$

$$S, i_{(SPT)} = \begin{cases} a_0 & N_{1,60,i} < 12.6 \\ a_0 + a_{1,SPT}\left(N_{1,60,i} - 12.6\right) & 12.6 \le N_{1,60,i} < 17.2 \\ a_0 + 4\, a_{1,SPT} & 17.2 \le N_{1,60,i} \end{cases}$$

$$S, i_{(CPT)} = \begin{cases} a_0 & q_{c1N,i} < 112.4 \\ a_0 + a_{1,CPT}\left(q_{c1N,i} - 112.4\right) & 112.4 \le q_{c1N,i} < 140.2 \\ a_0 + 27.8\, a_{1,CPT} & 140.2 \le q_{c1N,i} \end{cases} \quad (1.11)$$

$$f_{H,i} = b_0 H_{S,i} \exp\left[b_1 (max(DSI)^2 - 4)\right] \quad (1.12)$$

H(-) is the Heaviside step function; ε is an infinitesimal positive quantity to make H(-) equal to 1 for an argument of zero; FLPC is a flag that is equal to 1 if a low-permeability layer is present above the uppermost susceptible layer; $N_{1;60}$ is the corrected standard penetration test (SPT) blow count in the i^{th} layer; $q_{c1N;i}$ is the corrected normalized cone penetration test (CPT) tip resistance in the ith layer; $H_{S;i}$ is the thickness of the i^{th} susceptible layer; and $D_{S;i}$ is the depth from the bottom of the foundation to the centre of the i_{th} susceptible layer. The term related to the presence of a low-permeability cap indicates that its influence is dependent on motion intensity.

This project has received funding from the European Union's Horizon 2020 research and innovation programme under grant agreement No. 700748

The second term is computed as:

$$f_{fnd} = f_q + f_{B,L}$$

$$f_q = \{d_0 + d_1\, ln[min(CAV, 1000)]\} \ln(q)\ exp\{d_2\, min[0,\ B - max(D_{S,1}, 2)]\}$$

$$f_{B,L} = \{e_0 + e_1\, ln[max(CAV, 1500)]\}\, [\ln(B)]^2 + e_2(L/B) + e_3 D_f \qquad (1.13)$$

where q is the bearing pressure of the foundation (in kPa), B is the width of a rectangular foundation (m); L=B is its unitless length-to-width ratio; and D_f is the depth from the surface to the bottom of the foundation (m). $D_{S;1}$ is the depth to the centre of the uppermost susceptible layer with $N_{1;60}$ less than 17.2 blows (q_{c1N} less than 140.2). The exponential decay term included in f_q reduces the influence of q for profiles where there are no loose susceptible layers within the foundation's depth of influence. This decay term, determined to maximise model performance with respect to the numerical database, engages for layer depths greater than B (taken here as the depth of influence), rather than 1.2 B (per Tokimatsu et al., 2017) or 1.5B (per Boussinesq's solution), which were based on the size of stress bulbs beneath a square footing. Using a threshold of B rather than either of these values offered improved model R2 and reduced bias for models with deep layers and multiple layers. This slight difference may be the result of a highly non-linear and elasto-plastic soil response considered in this numerical study, which contradicts simplifying assumptions used by previous researchers in their formulation of the foundation's zone of influence.

The form and intensity threshold captured the effects of the foundation dimensions well (as demonstrated later in this paper). The orders of scaling (natural logarithm squared for B and linear for L=B and D_f) were determined by inspection to minimize residuals.

The third term is:

$$f_{st} = \{f_0 + f_1\, ln[min(CAV, 1000)]\} h_{eff}^2 + f_2\, min[(M_{st}/10^6, 1)] \qquad (1.14)$$

where h_{eff} is the effective height of the structure (m) and M_{st} is the inertial mass of the structure (kg). The orders of the terms in this equation reflect the expectation that the building's effective moment of inertia should affect its ratcheting behaviour, which in turn influences settlement. An upper and a lower bound are given to CAV are included to allow the functional form to capture the trends discussed in points (e), (f), and (i) in the previous section describing trends in the numerical model.

This project has received funding from the European Union's Horizon 2020 research and innovation programme under grant agreement No. 700748

Table 1-2provides the coefficients for this relation as determined by a non-linear regression analysis.

This project has received funding from the European Union's Horizon 2020 research and innovation programme under grant agreement No. 700748

Table 1-2 Coefficients and uncertainty parameters for the model in eqs.3.32 to 3.36.

Model parameter	Value	Model parameter	Value
a_0	1·000	e_0	−0·8727
$a_{1,SPT}$	−0·2174	e_1	0·1137
$a_{1,CPT}$	−0·0360	e_2	−0·0947
b_0	0·3026	e_3	−0·2148
b_1	−0·0205	f_0	−0·0137
c_0	1·3558	f_1	0·0021
c_1	−0·1340	f_2	0·1703
d_0	−1·3446	s_0	0·4973
d_1	0·2303	σ_{num}	0·3314
d_2	0·4189		

The numerical prediction (lnS_{num}) is used as a floor because this is expected to be an accurate estimate of settlement due to shear-type (deviatoric)deformations. A correction is the applied to fit with observation:

$$ln(\bar{S})_{adj} = ln(\bar{S})_{num} + k_0 + k_1 min\left(H_{S,1}, 12\right)^2 + k_2 min(q, q_c) + k_3\, max(q - q_c, 0) \geq ln(\bar{S})_{num} \quad (1.15)$$

with its coefficients provided in Table 1-3. The model coefficient of the term for large q (k3) is negative and counteracts the effects of increased $H_{S;1}$ for large values of q.

Table 1-4 Coefficients for the adjustment of the predictive formula as in 3.37.

Model parameter	Value	Model parameter	Value
k_0	−1·5440	k_3	−0·0218
k_1	0·0250	q_c (assumed in kPa)	61
k_2	0·0295	σ_{adj}	0·6746

A summary of the above defined calculation method is reported in Figure 1.31.

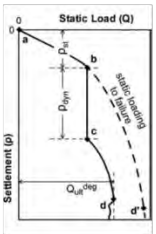

Karamitros et al. (2013)

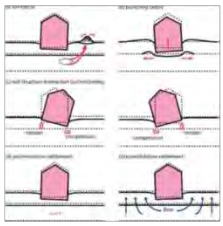

Bray & Macedo (2017)

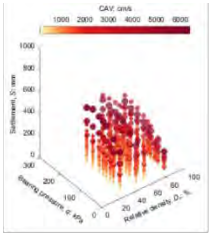

Bullock et al. (2018)

INDEX	REFERENCE	IM	SUBSOIL	BUILDING
ρ	Karamitros et al., 2013	$a_{max}\, T^2 N = \pi^2 \int_{t=0}^{N \cdot T} \lvert v(t) \rvert dt$	Three-layer	Foundation bearing pressure
Ds	Bray and Macedo, 2017	CAVdp, Sa1	Three-layer	Building geometry, depth and contact pressure of foundation
Sadj	Bullock et al.,2018	CAV	Multi-layer Low/high permeability cap	Building geometry, Inertial mass, foundation embedment depth, foundation contact pressure

Figure 1-31 Calculation schemes of liquefaction induced settlements.

This project has received funding from the European Union's Horizon 2020 research and innovation programme under grant agreement No. 700748

1.6 Damage assessment of buildings

The capability of the above computed settlements to quantify damage of buildings and the possibility to adopt them as Engineering Damage Parameters to simulate fragility is assessed in the present paragraph with refernce to the case studies of Terre del Reno (Emilia Romagna) and Christchurch (New Zealand). Databases have thus been created collecting the characteristics of buildings (base dimensions, height, number of floors, structural characteristics), subsoil properties (thickness of liquefiable layer and crust, relative density, etc.), seismic inputs (considering the M_w6.14 event of May 20th 2012 for Terre del Reno and the M_w6.2 event of February 22nd for Christchurch). The damage provoked on each building by liquefaction has been quantified looking at the reports produced after the earthquake. It has been classified as minor, moderate or major considering the severity of the different types of injuries according to the criterion defined by Van Ballegooy et al. (2014). Figure 1-32 reports the adopted classification scale together with examples of damaged buildings from the two cases.

The validation criterion depicted in Figure 1-9 (Kongar et al., 2015) has thus been adopted for the two cases. The Receiver Operator Curves are firstly drawn for the different methods on the database of Terre del Reno (Figure 1.33), where the major part of the buildings is made of masonry. The results show a relatively good performance for the method proposed by Bullock et al. (2018), slightly lower for the Bray and Macedo (2017), significantly lower for the method of Karamitros et al. (2019). The estimate based on the Liquefaction Severity Number is also reported for comparison. It shows a poor relation with damage, but it must be considered that this parameter is computed for free field conditions, i.e. without considering the presence of buildings. The optimal threshold for the Bullock et al. (2018) method is equal to about 10 mm for the damage level 1 (Minor), 44 mm for damage level 3 (Major).

The same test performed for the case of Christchurch is shown in Figure 1-34. A first extensive application of the test over the entire area of the city shows a relatively poor performance for all indicators that give similar AUC coefficients (0.63). Seeking an explanation for such a result, a distinction has then been made among the buildings considering that many of them are low rise and rest on relatively complex subsoil.

This project has received funding from the European Union's Horizon 2020 research and innovation programme under grant agreement No. 700748

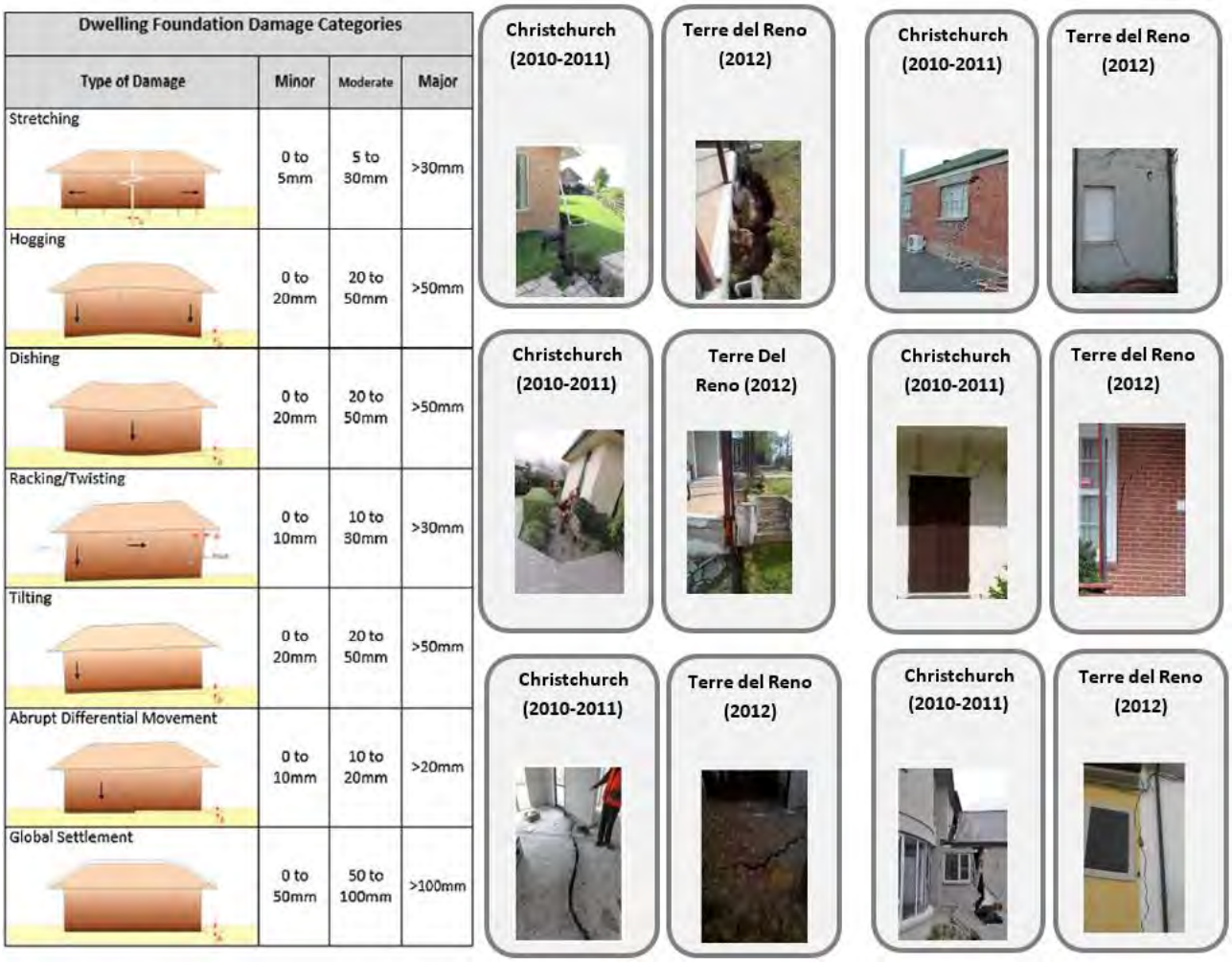

Dwelling Foundation Damage Categories			
Type of Damage	Minor	Moderate	Major
Stretching	0 to 5mm	5 to 30mm	>30mm
Hogging	0 to 20mm	20 to 50mm	>50mm
Dishing	0 to 20mm	20 to 50mm	>50mm
Racking/Twisting	0 to 10mm	10 to 30mm	>30mm
Tilting	0 to 20mm	20 to 50mm	>50mm
Abrupt Differential Movement	0 to 10mm	10 to 20mm	>20mm
Global Settlement	0 to 50mm	50 to 100mm	>100mm

Figure 1-32 Damage survey criterion and example from Christchurch and Terre del Reno (Van Ballegooy et al., 2014).

This project has received funding from the European Union's Horizon 2020 research and innovation programme under grant agreement No. 700748

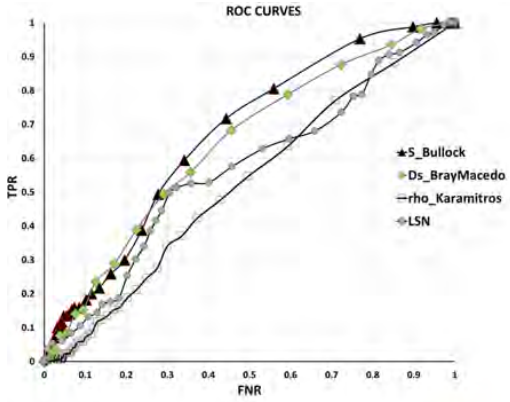

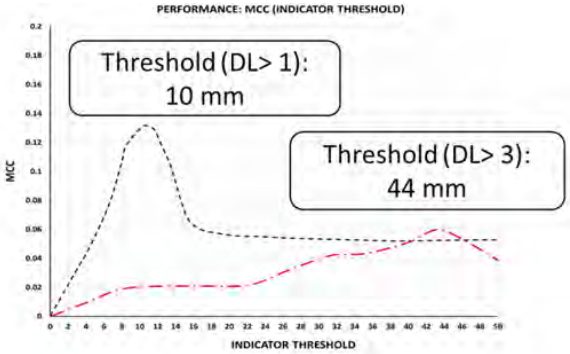

INDICATOR	AUC
Sadj	0.71
Ds	0.68
ρ	0.56
LSN	0.58

Figure 1-33 Validation of settlements as EDP for building vulnerability in in Terre del Reno.

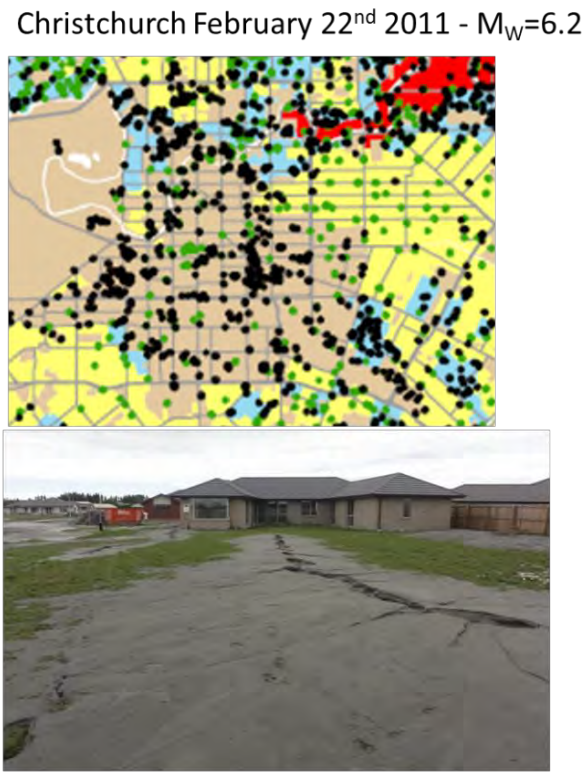

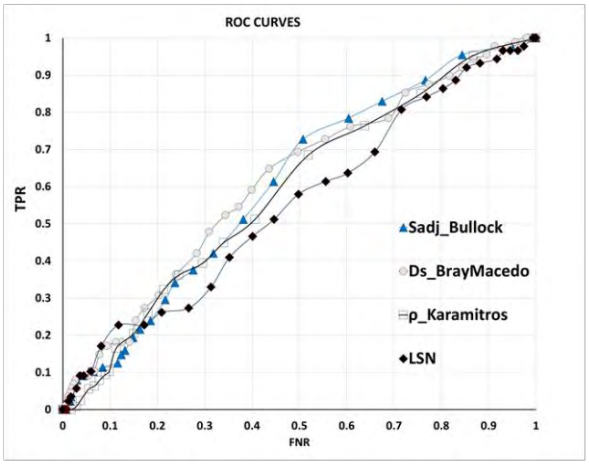

INDICATOR	AUC
Sadj (Bullock et al., 2018)	0.63
Dt (Bray Macedo, 2017)	0.63
P (Karamitros et al., 2013)	0.63
LSN (van Ballegooy et al., 2014)	0.57

Figure 1-34 Validation of settlements as EDP for building vulnerability in Christchurch.

This project has received funding from the European Union's Horizon 2020 research and innovation programme under grant agreement No. 700748

Therefore, the analysis has been restricted to the buildings having at least two floors, for which the load transferred onto the foundation is significant. Additionally, the test described in Figure 1-17 has been performed recovering the Equivalent Soil Profile and excluding from the database of buildings those resting on subsoil not respecting this test (with an error >10%). In this way, the test has been applied only to those situations that respecting the basic assumptions of the calculation methods. Finally, a different threshold has been considered for the test, assuming as positive event the buildings affected by moderate damage. The results shown in Figure 1-35 show a significant increase on the performance of the indicators with AUC in the range of 0.72-0.74.

Christchurch February 22nd 2011 - M_W=6.2

- Number of building levels >2
- Three layer subsoil (ESP_{err}<10%)
- Moderate damage

Taylor et al. (2015)

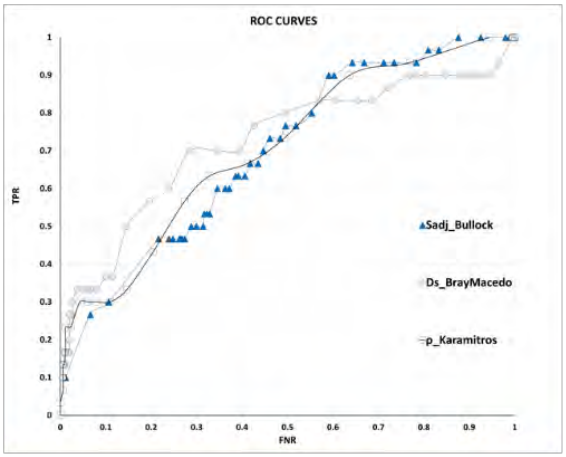

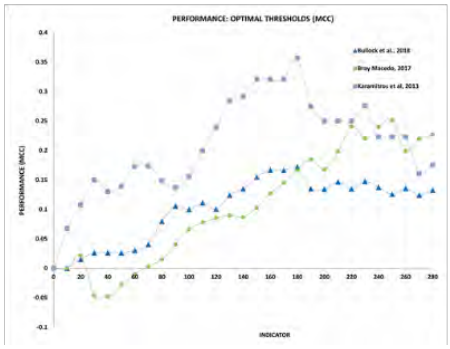

INDICATOR	AUC	OPTIMAL THRESOLD (MCC)
Sadj_mm (Bullock et al., 2018)	0.72	≈180 mm
Pdyn_mm (Karamitros et al., 2013)	0.74	≈180 mm
Dt_mm (Bray & Macedo 2017)	0.74	≈250 - 260 mm

Figure 1-35 Validation of EDP for building vulnerability for high rise buildings, three layer subsoil model and moderate damage level in Christchurch.

The test has then been repeated considering the buildings affected by major damage (Figure 1-36), and despite the number of buildings become lower, the performance of all methods, in particular Bray and Macedo (2017). increases further. It can be thus concluded that the absolute settlement of buildings is a good candidate to predict damage, more suitable than the free field indicators defined in Figure 1-11. The quality of prediction increases when they are applied to situations complying with their basic assumptions.

This project has received funding from the European Union's Horizon 2020 research and innovation programme under grant agreement No. 700748

Christchurch February 22nd 2011 - M_W=6.2

- Number of building levels >2
- Three layer subsoil (err<10%)
- Major damage

Taylor et al. (2015)

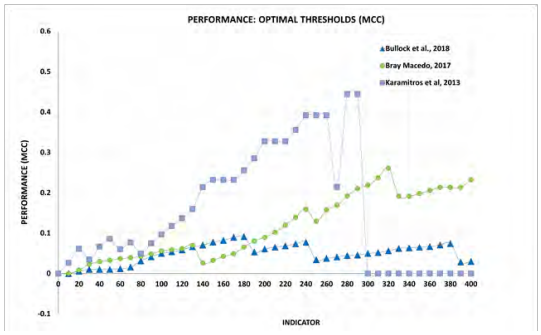

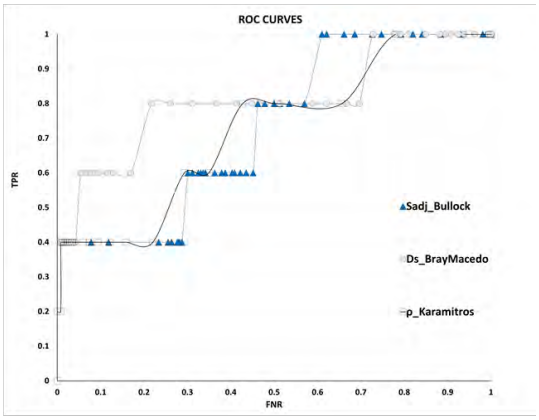

INDICATOR	AUC	OPTIMAL THRESOLD (MCC)
Sadj_mm (Bullock et al., 2018)	0.74	≈180 mm
Pdyn_mm (Karamitros et al., 2013)	0.75	≈280-290 mm
Dt_mm (Bray & Macedo 2017)	0.89	≈320 mm

Figure 1-36 Validation of EDP for building vulnerability for high rise buildings, three layer subsoil model and major damage level in Christchurch.

1.1. Bibliography

Bird, J., Bommer, J., Crowley, H., Pinho, R. 2006. "Modelling liquefaction-induced building damage in earthquake loss estimation". Soil Dynamics and Earthquake Engineering 26 (2006) 15–30.

Bird JF, 2005, Earthquake loss estimations: modelling losses due to ground failure. PhD Thesis. Imperial College London, University of London.

Boscardin M.D., Cording E. J., 1989, Building response to excavation-induced settlement, Journal of Geotechnical Engineering, Vol. 115, No. 1, January, 1989. ©ASCE, ISSN 0733-9410/89/0001-0001. Paper No. 23066.

Bray, J.D. and Macedo, J. (2017). 6th Ishihara lecture: Simplified procedure for estimating liquefaction induced building settlement. Soil Dynamics and Earthquake Engineering, 102: 215–231. http://dx.doi.org/10.1016/j.soildyn.2017.08.026.

Bullock, Z., Karimi, Z., Dashti, S., Porter, K., Liel, A. B., Franke, K. W. 2018. "A physics-informed semi-empirical probabilistic model for the settlement of shallow-founded structures on liquefiable ground". Géotechnique [https://doi.org/10.1680/jgeot.17.P.174]

Cubrinovski, M., van Ballegooy, S. 2017. "System response of liquefiable deposits". 3rd Int. Conf. on Performance Based Design in Earthquake Geotechnical Engineering.

FEMA, Federal Emergency Management Agency, 1992. "FEMA 178 - NEHRP Handbook for the Seismic Evaluation of Existing Buildings", Washington, D. C., Developed by the Building Seismic Safety Council (BSSC) for the Federal Emergency Management Agency (FEMA).

FEMA/NIBS, 1998. "HAZUS - Earthquake Loss Estimation Methodology". Vol. 1, 1998.

Fenton, G. A., & Griffiths, D. V. (2000). Rberar2d. RFEM.

Fotopoulou S., Karafagka S., Pitilakis K., 2018, Vulnerability assessment of low-code reinforced concrete frame buildings subjected to liquefaction-induced differential displacements, Soil Dynamics and Earthquake Engineering 110 (2018) 173–184.

Honjo, Y., Kazumba, S. (2002). Estimation of autocorrelation distance for modeling spatial variabilityof soil properties by Random Field theory. The 47th Geotechnical Engineering Symposium, JGS, (p. 279-286).

Idriss, I. M., and Boulanger, R. W. 2008. "Soil liquefaction during earthquakes". Monograph MNO-12, Earthquake Engineering Research Institute, Oakland, CA, 261 pp.

Ishihara K, Yoshimine M. Evaluation of settlements in sand deposits following liquefaction during earthquakes. Soils Found 1992;32(1):173–188.

Itasca Consulting Group, Inc. (2016) FLAC — Fast Lagrangian Analysis of Continua, Ver. 8.0. Minneapolis: Itasca.

Karamitros, D.K., Bouckovalas, G. D., Chaloulos, Y.K. 2013. "Seismic settlements of shallow foundations on liquefiable soil with a clay crust". Soil Dynamics and Earthquake Engineering. 46. 64-76.

Kongar I., Rossetto T., Giovinazzi S., 2015, Evaluating Desktop Methods for Assessing Liquefaction-Induced Damage to Infrastructure for the Insurance Sector, 12th International Conference on Applications of Statistics and Probability in Civil Engineering, ICASP12 Vancouver, Canada, July 12-15, 2015

Matheron, G. 1965. "Les variables régionalisées et leur estimation: une application de la théorie des fonctions aléatoires aux sciences de la nature". Masson, Paris, France.

Millen, M., Ferreira, C., Quintero, J., Gerace, A. and Viana da Fonseca, A. (2019). Simplified equivalent soil profiles based on liquefaction performance. 7th International Conference on Earthquake Geotechnical Engineering. Rome, Italy.

Powers, D. M. W., (2011), Evaluation: from precision, recall and F-measure to ROC, informedness, markedness and correlation, J. of Mach. Lear. Tech, 2(1), 37-63.

Stuedlein, A., Kramer, S., Arduino, P., & Holtz, R. (2012). Geotechnical characterization and random field modeling of desiccated Clay. J. Geotech. Geoenviron. Eng., 138 (11), pp. 1301-1313.

Tokimatsu, K., Kojimaa, H., Kuwayama, S., Abe, A., and Midorikawa, S. (1994). "Liquefaction-induced damage to buildings in 1990 Luzon earthquake." J. Geotech. Eng., 120(2), 290–307.

van Ballegooy, S., Malan, P., Lacrosse, V., Jacka, M.E., Cubrinovski, M., Bray, J.D., O'Rourke, T.D., Crawford, S.A., Cowan, H. 2014. "Assessment of Liquefaction-Induced Land Damage for Residential Christchurch". Earthquake Spectra (30) No. 1: pages 31–55, February 2014.

Ziotopoulou, K., and Boulanger, R. W. 2013. "Numerical modeling issues in predicting post-liquefaction reconsolidation strains and settlements". In Proceedings of the 10th International Conference on Urban Earthquake Engineering.

This project has received funding from the European Union's Horizon 2020 research and innovation programme under grant agreement No. 700748

2 EFFECTIVE STRESS LIQUEFACTION ANALYSIS OF A RESIDENTIAL BUILDING IN TERRE DEL RENO (EMILIA ROMAGNA – ITALY)

2.1 Introduction

The occurrence in recent times of impactant liquefaction phenomena, *e.g.* Adazapari in Turkey 1999, Emilia Romagna in Italy 2012, has raised in the European community the need for identifying in the regions susceptible to liquefaction strategies to mitigate effects. Generally, liquefaction risk analysis covers wide areas and are thus carried out with simple tools that process rich geotechnical databases in reasonably short time. With this aim, simplified methods exist to automatically process results of in-situ tests (*e.g.* CPT, SPT, sonic measurements) and provide areal distributions of indicators describing the soil's liquefaction vulnerability (Iwasaki, 1978; Zhang *et al.*, 2002; Zhang *et al.*, 2004; Maurer, 2014; van Ballegooy, 2014). These results are then combined with fragility models that describe the response of buildings to quantify damage. In these analyses the structures are classified on a probabilistic basis and represented as categories, i.e. not looking at their specific properties (geometrical and mechanical). Aim of this assessment is to derive a cumulative indication of the risk affecting the area and form the bases for further, more detailed analyses focused on the single structures (buildings or infrastructure).

In fact, the outcomes of areal risk analyses are not enough accurate to directly undertake specific mitigation actions on structures and any further judgment must be based on specific analyses predicting the effects of liquefaction on more accurate models. In particular, this is the case when strategic structures (*e.g.* hospitals, emergency management headquarters etc.) are of concern. Here more sophisticated analyses must be performed considering in detail the seismic motion, geotechnical properties of the subsoil, mechanical behaviour of materials and load distributions.

This option is investigated in this chapter by means of numerical analyses. A well-documented case study subjected to liquefaction has been taken as reference to calibrate a numerical model that has been subsequently used to analyse various effects. The analysis is particularly focused on the influence of subsoil variability on the settlements induced by liquefaction.

2.2 The case study

The case study has been identified in the municipality of Terre del Reno, Emilia Romagna (Italy) (Figure 2-1). The building, made of a masonry three storeys structure built at the end of the sixties with a rectangular layout 13.10 m long and 11.10 m wide, is located in San Carlo (Figure 2-2). From the report prepared for its reconstruction after the earthquake, it is seen that the building is founded on a shallow slab of unknown (likely poor) structural characteristics. In Figure 2-3, the plan of the building at the ground level and the two side views are reported.

This project has received funding from the European Union's Horizon 2020 research and innovation programme under grant agreement No. 700748

Figure 2-1. Satellite image of the Emilia Romagna Region (Italy) with indication of the Terre del Reno municipality (modified from Google Earth).

Figure 2-2. Satellite image of via Rossini, in the Terre del Reno municipality, with indication of the selected case study (modified from Google Earth).

This project has received funding from the European Union's Horizon 2020 research and innovation programme under grant agreement No. 700748

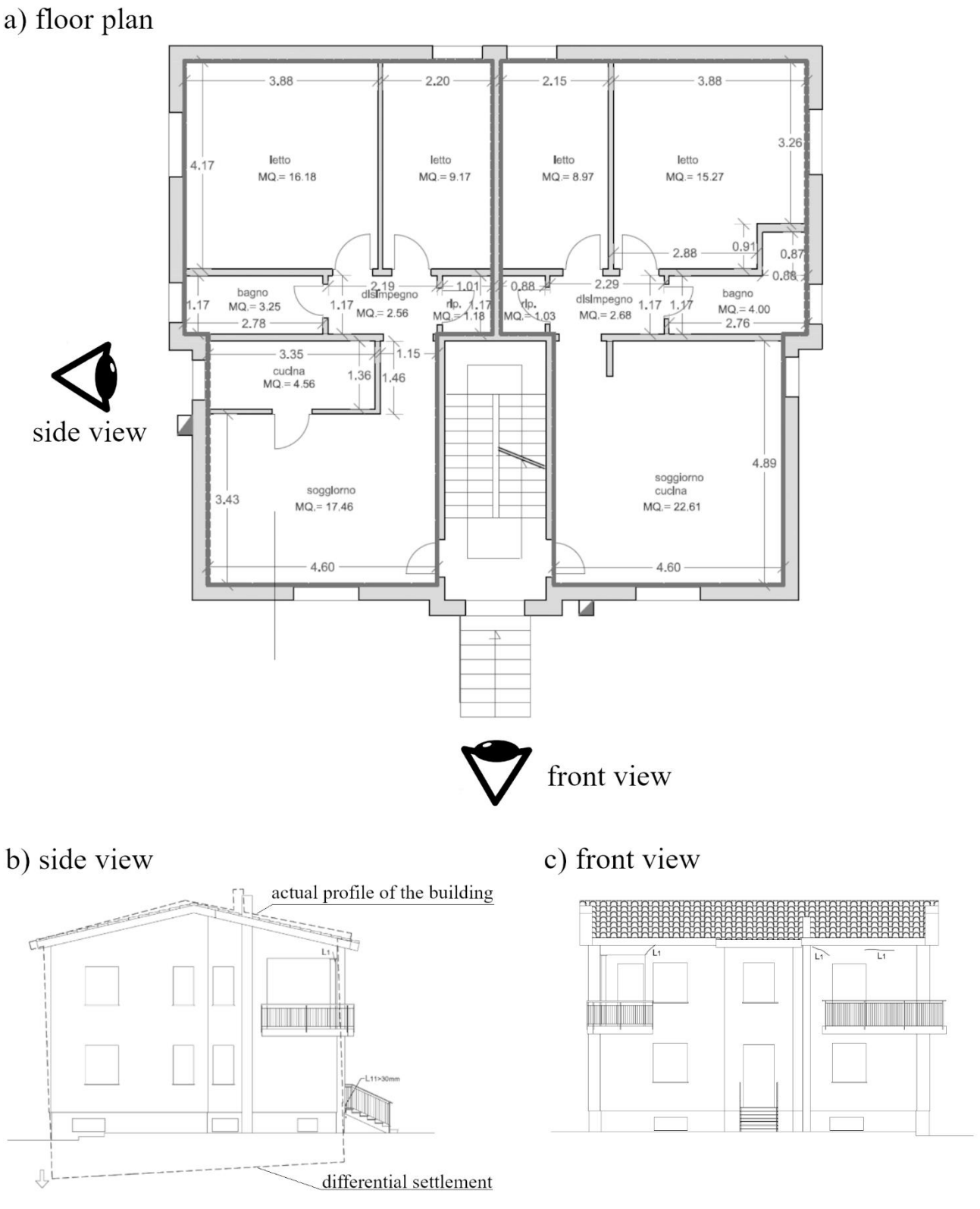

Figure 2-3. Layout of the selected case study. Floor plan and side views with indication of the movement undergone by the structure and observed cracks (modified from Emilia Romagna database).

This project has received funding from the European Union's Horizon 2020 research and innovation programme under grant agreement No. 700748

After the May 20th 2012 Mw.6.1 earthquake the building underwent significant differential settlements of in the East-West direction (Figure 2-4.b) with an absolute settlement of 35 cm on the west side (Figure 2-4.c) and 5 cm of the East side (Figure 2-4.d). On the other direction North-South settlements were practically uniform, so the building can be considered as rigidly rotated, possibly due to the rigidity given by the coupled masonry walls and slab foundation.

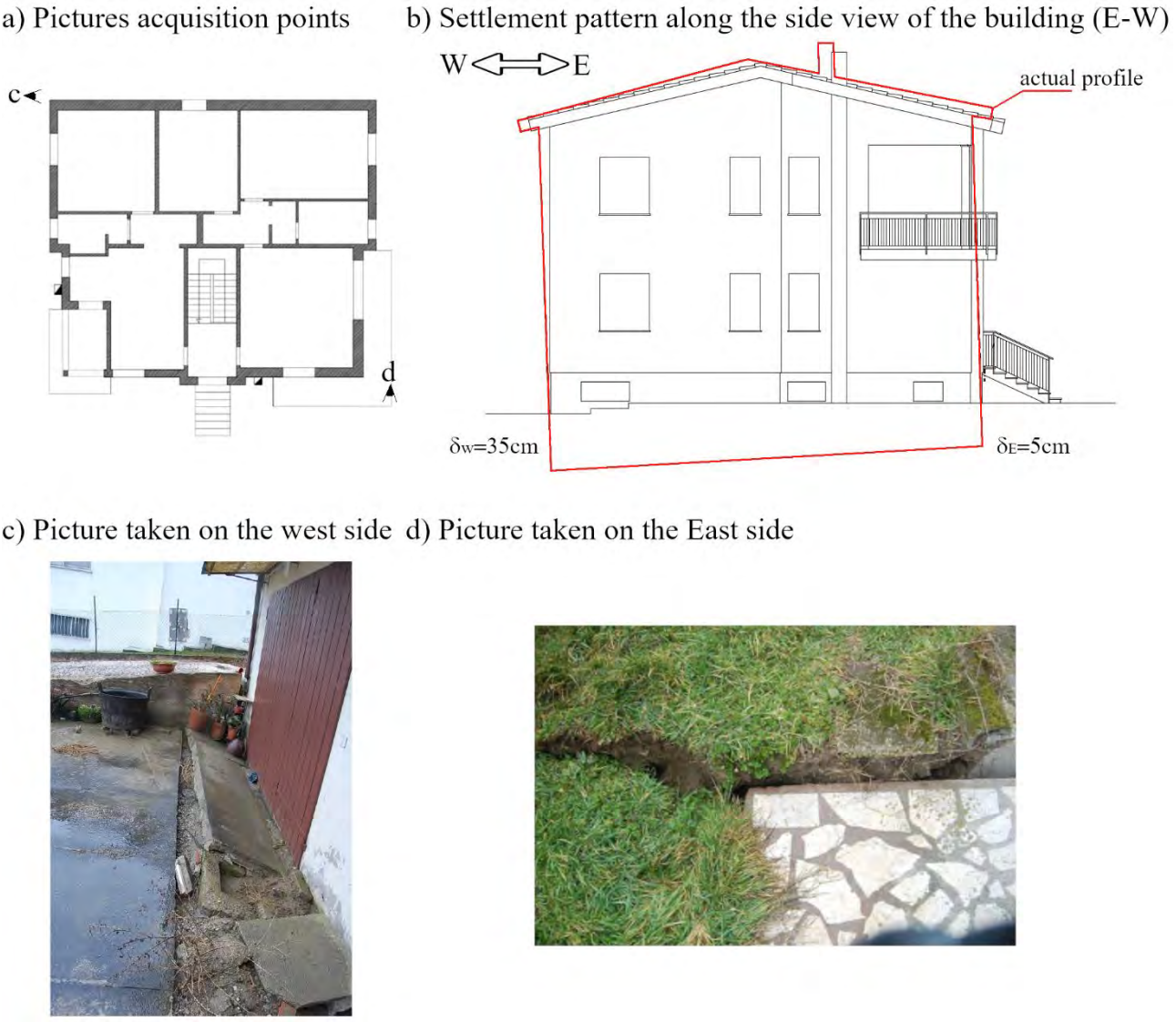

Figure 2-4. After earthquake settlement scenario of the west and east side of the building.

2.3 Input motion

The municipality of Terre del Reno has been heavily struck by the Emilia Romagna 2012 earthquake sequence (Figure 2-5) and particularly by the main events occurred in May 20th 2012.

This project has received funding from the European Union's Horizon 2020 research and innovation programme under grant agreement No. 700748

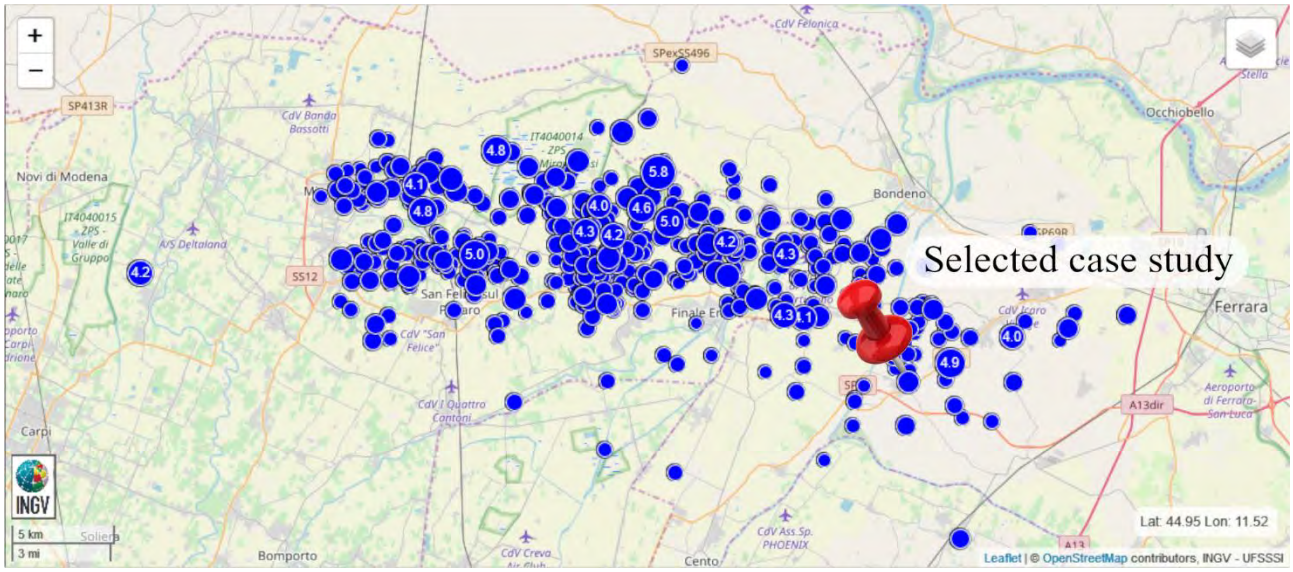

Figure 2-5. Map reporting the epicentres of the Emilia Romagna 2012 seismic sequence (INGV database).

The herein performed analysis refers to this main shock. The event hit the area of interest at 02:03:50 (UTC) with a moment magnitude M_w=6.1 and epicentre located about 15km far from the selected case study at geographic coordinates latitude=44.9, longitude=11.26. The epicentral depth is estimated at 10 km from the ground level.

In Figure 2-6 the recorded acceleration time histories signals for the two cardinal directions are reported, taken from the ITACA seismic database http://itaca.mi.ingv.it (Luzi *et al.*, 2019). The plots show similar values of peak ground acceleration in the North and East directions with values respectively equal to 0.264 and 0.261g (Figure 2-6.a). The Fourier transform performed on the two signals (Figure 2-6.c) reveals that the most significant energy content ranges between 0.4 and 6.0Hz for both directions. However, the Arias intensity profiles proposed in Figure 2-6.d show that the larger amount of energy is released in the North direction. Therefore, considering the last observation the North component of the seismic motion is taken into account for the next calculation.

Being the closest seismic station recording the above signals located in the municipality of Mirandola, the motion considered in the present application has been obtained by applying an attenuation law applying a procedure described in the next paragraphs. The position of the epicentre, recording station and studied building are reported in Figure 2-7.

This project has received funding from the European Union's Horizon 2020 research and innovation programme under grant agreement No. 700748

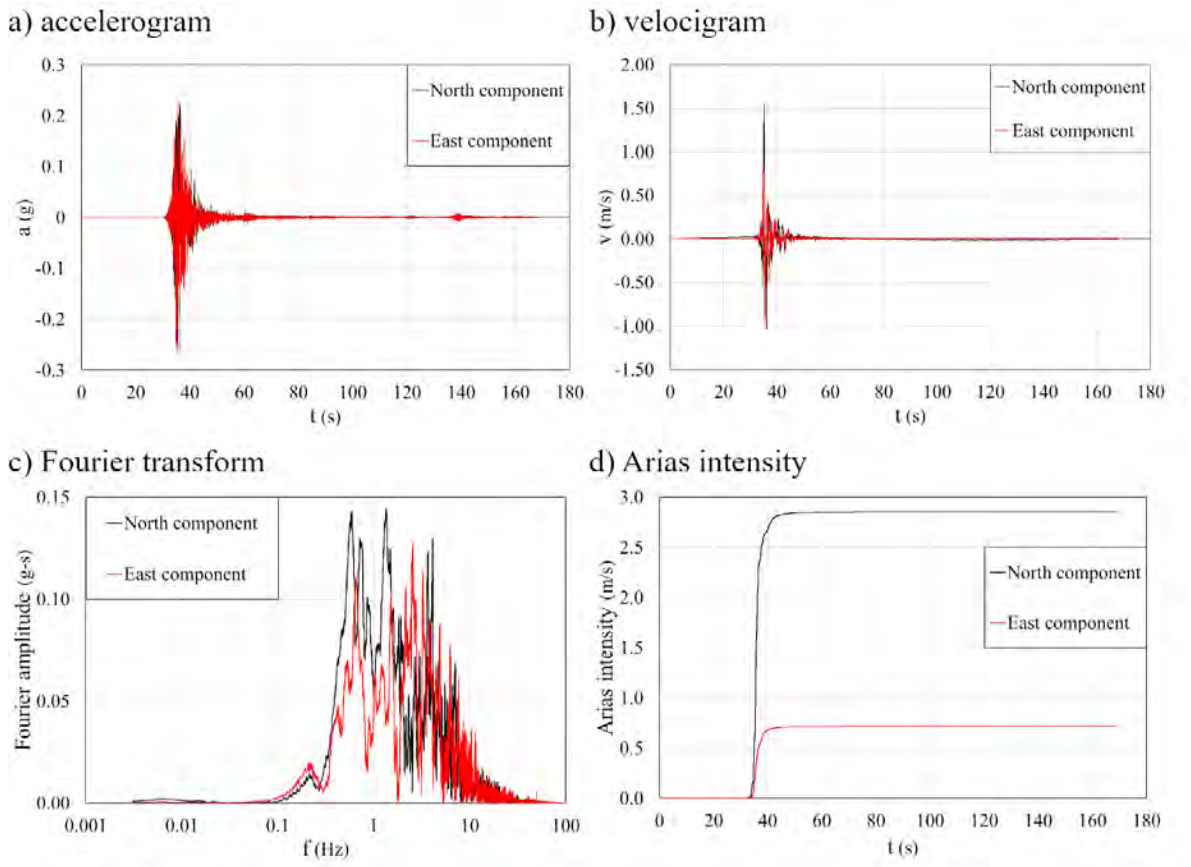

Figure 2-6. Seismic signals recorded in the North and East direction for the main shock on 20th May 2012. a) accelerograms; b) velocigram; c) Fourier transform, d) computed Arias intensity.

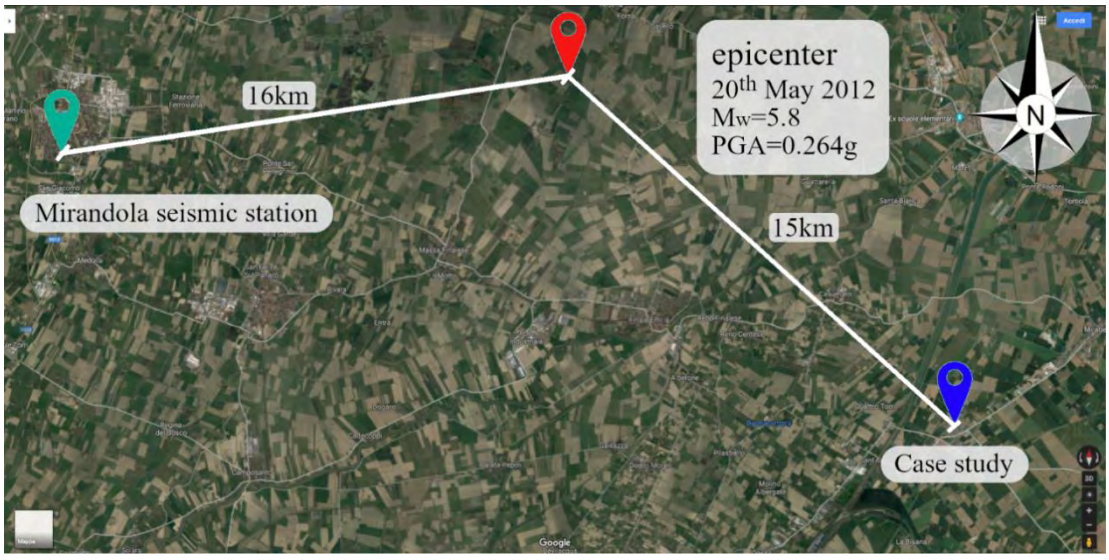

Figure 2-7. Satellite map reporting the location of the case study, the epicentre and the seismic recording station.

2.3.1 Signal deconvolution at the bedrock in Mirandola

The attenuation law (Bindi *et al.* (2011) is applied firstly to compute the seismic signal at the epicentre, then in San Carlo where the studied building is located. In both case, convolution and deconvolution analyses had to be performed to obtain the input signal for the present analysis. The acceleration time history recorded at the ground level in Mirandola has been firstly deconvoluted at the seismic bedrock by means of an equivalent-linear analysis performed with the open source software Strata (Kottke and Rathje, 2009). The subsoil profile (Figure 2-8), its physical and mechanical characteristics (Table 2-1) and the stiffness degradation and damping curves (Figure 2-9) are extracted from the works of Fioravante *et al.* (2013) and Sinatra and Foti (2015).

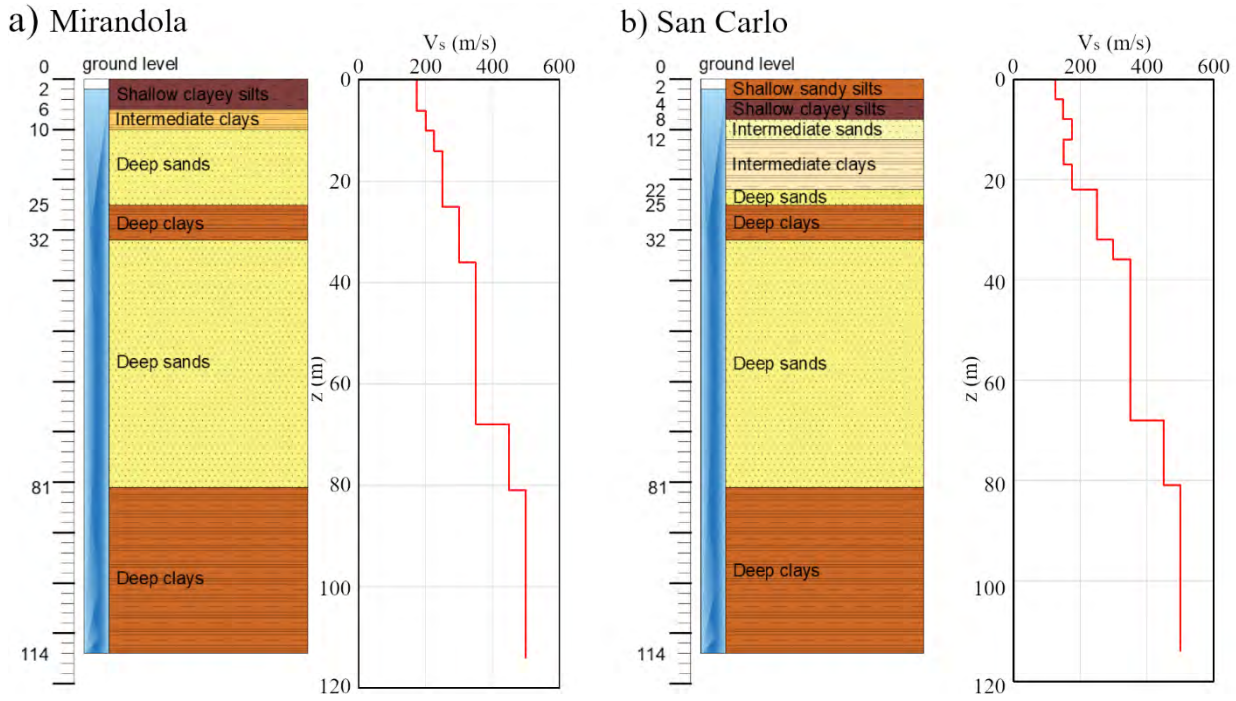

Figure 2-8. Subsoil profiles for the villages of Mirandola (where the motion is recorded) and San Carlo (case study).

Table 2-1 Physical characteristics of Mirandola and San Carlo subsoils.

Mirandola				San Carlo			
Unit	Depth (m)	γ (kN/m^3)	Vs (m/s)	Unit	Depth (m)	γ (kN/m^3)	Vs (m/s)
Shallow clayey silts	0÷6	18	175	Shallow sandy silts	0÷4	16.5	125
Intermediate clays	6÷10	18.5	200	Shallow clayey silts	4÷8	17	150
Deep sands	10÷14	19.5	225	Intermediate sands	8÷12	18.5	175
	14÷25	20	250	Intermediate clays	12÷17	18	150
Deep clays	25÷32	20	300		17÷22	18.5	175
Deep sands	32÷36	20	300	Deep sands	22÷25	19	250
	36÷68		350	Deep clays	25÷32	19.5	250
	68÷81		450	Deep sands	32÷36	20	300
Deep clays	81÷114	21	500		36÷68		350
					68÷81		450
				Deep clays	81÷114	21	500

This project has received funding from the European Union's Horizon 2020 research and innovation programme under grant agreement No. 700748

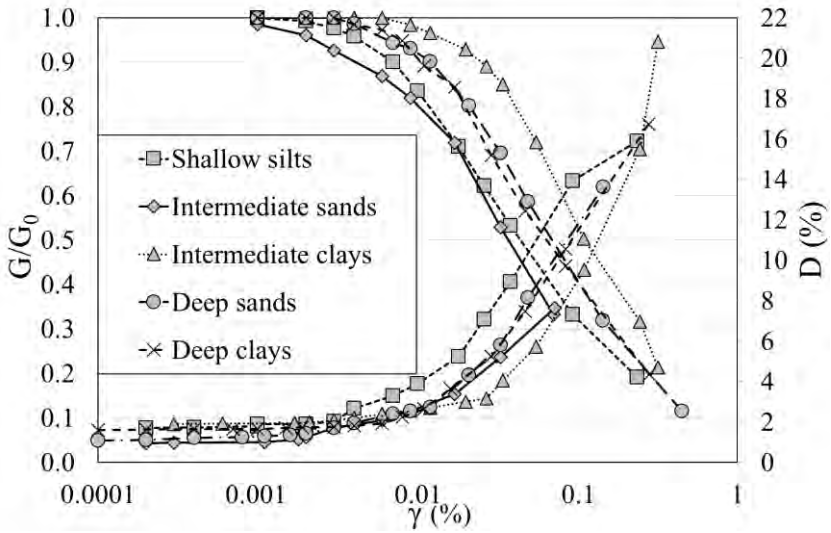

Figure 2-9. Stiffness modulus degradation and damping curves of Mirandola and San Carlo subsoils.

The comparison between recorded and deconvoluted signals at Mirandola is shown in Figure 2-10.a and Figure 2-10.b the latter showing a magnification of the most significant portion. The Figures reveal a signal amplification while it propagates upwards passing from a maximum acceleration of 0.175g to the recorded 0.264 g.

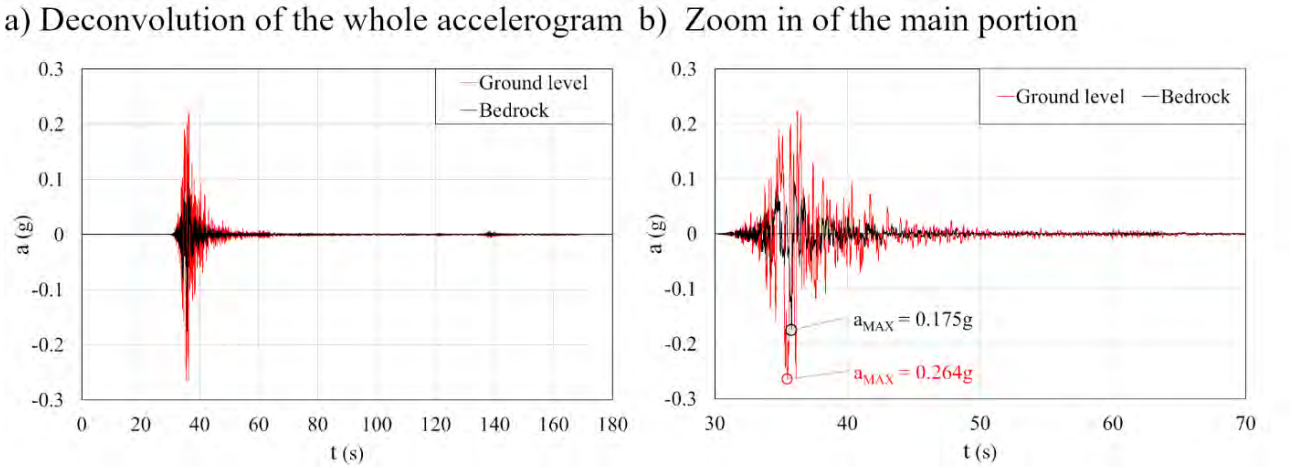

Figure 2-10. Comparison between the recorded accelerogram and its deconvolution to the bedrock (114m depth).

The comparison between the two signals, recorded at the ground level and deconvoluted at the bedrock, in terms of Fourier transform (Figure 2-11.a) and in particular the amplification function (Figure 2-11.b) reveals significant amplification for frequencies ranging between 1 and 7 Hz.

This project has received funding from the European Union's Horizon 2020 research and innovation programme under grant agreement No. 700748

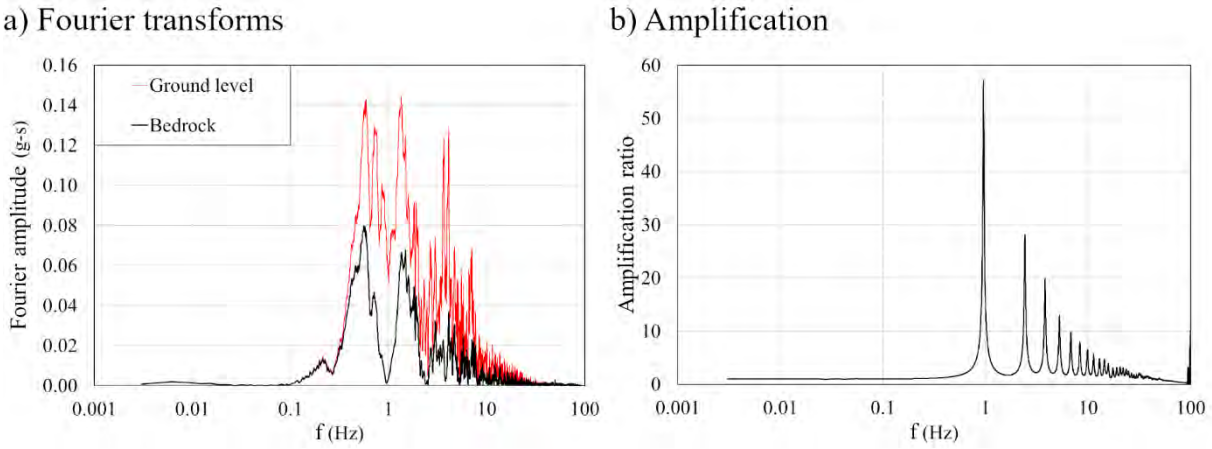

Figure 2-11. a) frequency content of recorded and deconvoluted signal; b) amplification function.

2.3.2 Signal modification from Mirandola station to San Carlo

Aiming to compute the motion acting on the selected case study, the seismic signal, firstly deconvoluted to the bedrock in Mirandola, is transposed to the epicentre and subsequently to San Carlo.

The attenuation law adopted herein is proposed by Bindi *et al.* (2011). The authors present a ground motion prediction equation (GMPE) derived from the latest release of the strong motion database for Italy. The regression is performed over the magnitude range 4.0÷6.9 and considering distances up to 200 km.

The functional form is the following:

$$log_{10}Y = e_1 + F_D(R,M) + F_M(M) + F_S + F_{sof} \quad (2.1)$$

Where:

Y	: Peak Ground Acceleration (cm/s2)
e_1	: constant
F_D(R, M)	: distance function (Equation 2)
F(M)	: magnitude scaling function (Equation 3)
F_S	: site amplification function
F_{sof}	: style of faulting correction function
M	: moment magnitude
R_{jb}	: Joyner-Boore distance or epicentral distance (in km) when the fault geometry is unknown

The proposed equation for the distance is:

$$F_D(R,M) = \left[c_1 + c_2\left(M - M_{ref}\right)\right] log_{10}\left(\frac{\sqrt{R_{JB}^2+h^2}}{R_{ref}}\right) - c_3\left(\sqrt{R_{JB}^2+h^2} - R_{ref}\right) \quad (2.2)$$

This project has received funding from the European Union's Horizon 2020 research and innovation programme under grant agreement No. 700748

While the magnitude function is:

$$F_M(M) = \begin{cases} b_1(M - M_h) + b_2(M - M_h)^2 & for\ M \le M_h \\ b_3(M - M_h) & otherwise \end{cases} \quad (2.3)$$

Where M_{ref}, M_h, R_{ref} are coefficients should be determined through the analysis. In particular, after some trial regressions and after Boore and Atkinson (2008), the following variables have been fixed: R_{ref} = 1km; M_{ref} = 5; M_h = 6.75; b_3 = 0.

The functional form F_S in Equation 1 represents the site amplification and it is given by $F_S = s_j C_j$, for j=1,…,5, where s_j are the coefficients to be determined through the regression analysis, while C_j are dummy variables used to denote the five different EC8 site classes (AEC8 through EEC8). In the present study F_S is equal to 1 being the input signal deconvoluted to the bedrock. The functional form F_{sof} represents the style of faulting correction and it is given by $F_{sof} = f_j E_j$, for j=1,…,4, where f_j are the coefficients to be determined during the analysis and E_j are dummy variables used to denote the different fault classes. We considered 4 types of style of faulting: normal (N), reverse (R), strike slip (SS) and unknown (U).

The coefficients computed for the present case are given in Table 2-2.

Table 2-2 Adopted coefficient for the Bindi et al. (2011) attenuation law.

e_1	c_1	c_2	h	c_3	b_1	b_2	s_A	s_B
3.672	-1.940	0.413	10.322	1.340E-04	-0.262	-0.0707	0.000	0.162

s_C	s_D	s_E	f_1	f_2	f_3	f_4	σ_B	σ_W	σ
0.240	0.105	0.570	-0.050	0.105	-0.054	0.000	1.720E-01	2.900E-01	3.370E-01

Equations 2 and 3 give F_M=0.1404 and F_{sof}=0.105. Thus, the median PGA prediction for the specific case study is reported in Figure 2-12 together with its standard deviation. The attenuation law for the specific case study (red line in Figure 2-12) is obtained by imposing the PGA value recorded in Mirandola (0.175g) for its specific epicentral distance (R_{jb}=16km) (cyan dot in Figure 2-12). Therefore, the PGA in San Carlo (R_{jb}=15km) is equal to 0.187g (blue dot in Figure 2-12).

This project has received funding from the European Union's Horizon 2020 research and innovation programme under grant agreement No. 700748

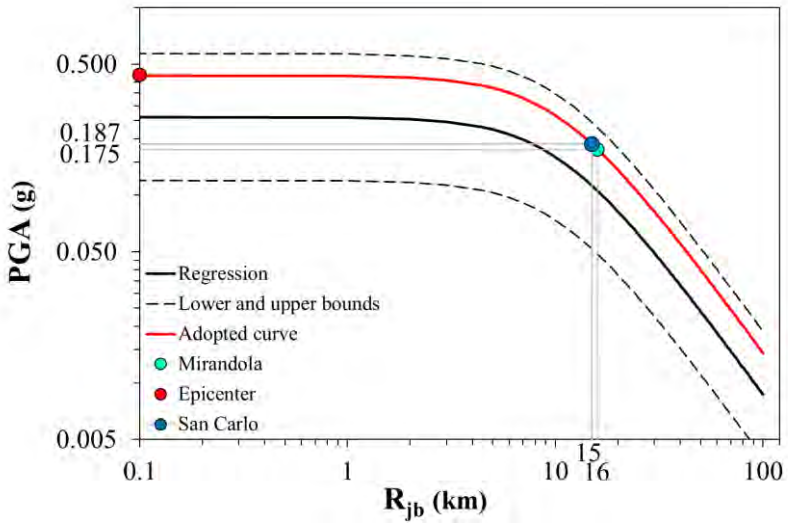

Figure 2-12. Bindi et al. (2011) attenuation law for the specific case study. The median prediction is represented by the continuous black line, the standard deviation is represented by the black dotted lines, the attenuation law calibrated on the specific case study represented by the red line. The PGA at the bedrock in correspondence of Mirandola, the epicentre and San Carlo are respectively indicated by the cyan, red and blue dots.

The motion at the seismic bedrock in San Carlo is computed transferring the deconvoluted signal in Mirandola to the epicentre and then to San Carlo with the previously recalled attenuation law (Figure 2-13). Being the two sites located a similar epicentral distance, the resulting accelerograms (at the bedrock) are similar each other.

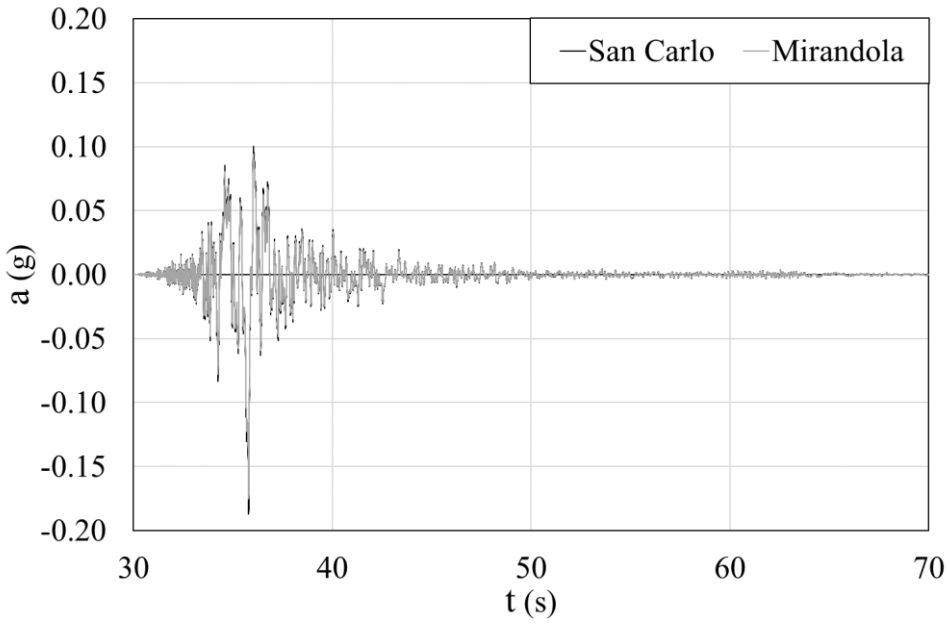

Figure 2-13. Accelerogram computed in correspondence of the San Carlo bedrock.

This project has received funding from the European Union's Horizon 2020 research and innovation programme under grant agreement No. 700748

2.3.3 Signal convolution at the ground level in San Carlo

Once the motion has been computed in correspondence of the bedrock in San Carlo, a linear equivalent analysis has been accomplished to compute the outcropping seismic motion (parameters reported in Paragraph 2.3.1). Figure 2-14 shows the comparison between the seismic acceleration time history computed at the bedrock of San Carlo and its convolution at the ground level. In particular, Figure 2-14.b shows an increase of the maximum acceleration from 0.19g to 0.28g.

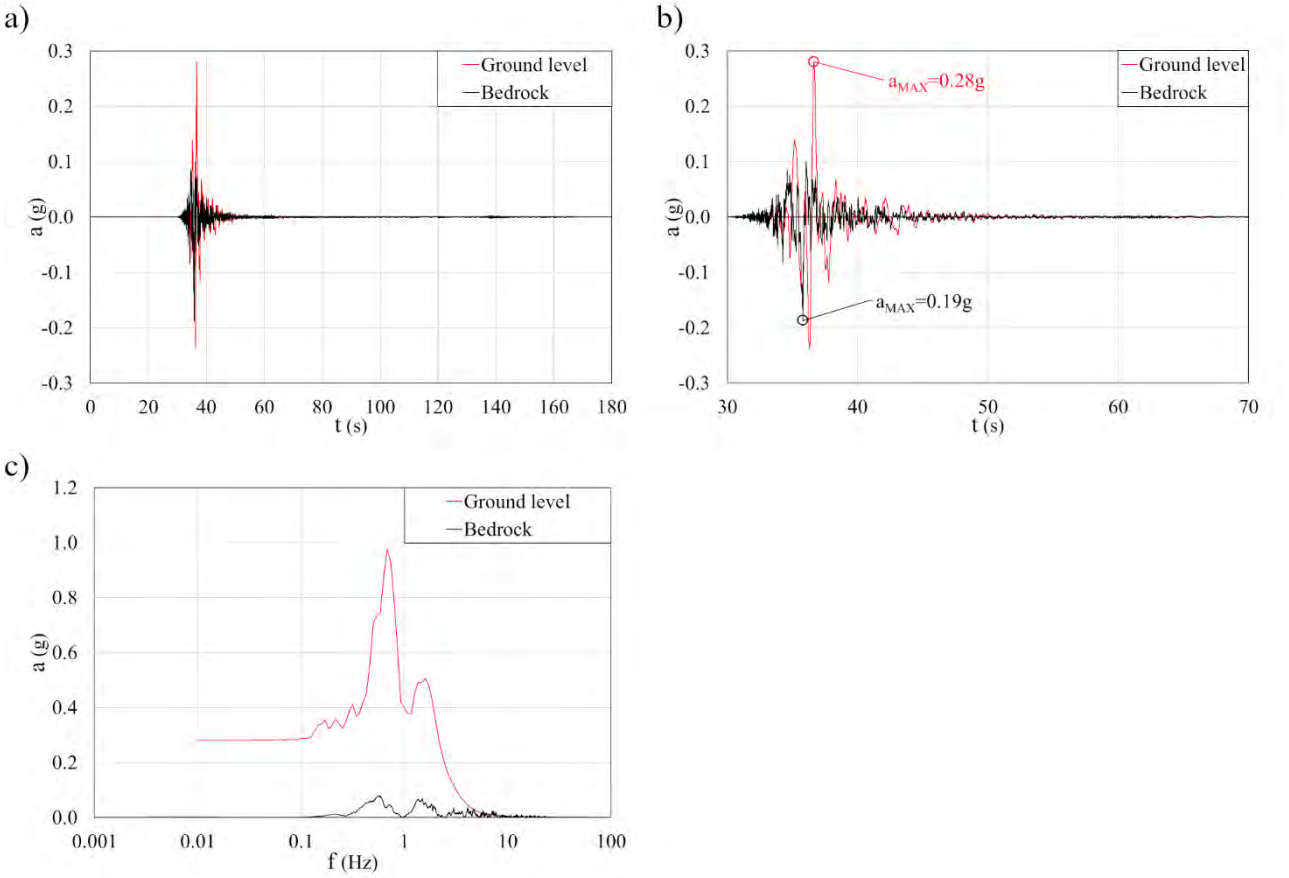

Figure 2-14. Comparison between the accelerogram computed at the bedrock in San Caro and its convolution at the ground level for the May 20th, 2019 seismic event. a) whole recorded event; b) zoom in on the most significant portion; c) comparison in terms of frequency contents.

2.3.4 Validation of the signal processing

The above presented procedure is validated by applying it to the seismic event occurred on May 29th 2019. In this case a temporary station was mounted in San Carlo by the Italian Institute of Geophysics and Volcanology to study the ongoing seismic sequence (Figure 2-15). Therefore, the signal of the May 29th earthquake was recorded both by the seismic station of Mirandola and by this station installed in San Carlo.

This project has received funding from the European Union's Horizon 2020 research and innovation programme under grant agreement No. 700748

Figure 2-15. Satellite map reporting the location of the case study, the epicentre and the seismic recording station for the May 29th, 2012 seismic event (modified from Google Earth).

Figure 2-16 reports the recorded accelerograms in the two cardinal directions, respectively the N-S signal with a black line, the E-W with a red line. Figure 2-17 shows, for both the cardinal components: a) the recorded signal in Mirandola deconvoluted at the bedrock; b) the Bindi et al. (2011) attenuation law are calibrated respecting epicentral distance and PGA of the recorded motion; c) the deconvoluted seismic signal is scaled according with the expected PGA value; d) the predicted and recorded accelerograms. The comparison between computed and recorded accelerograms (Figure 2-17.d) shows the effectiveness of the proposed procedure being able to realistically estimate the actual values of PGA. In particular, a value of 0.059g has been estimated against 0.059g recorded for the North component and a value of 0.061g has been estimated against 0.084g recorded for the East component.

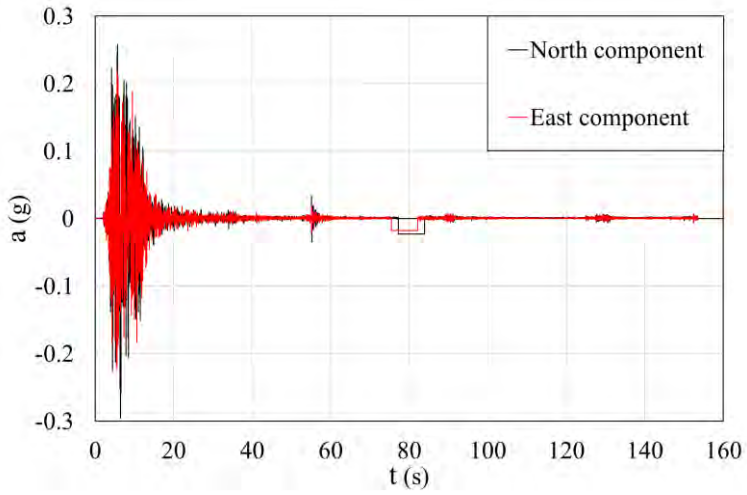

Figure 2-16. May 29th, 2019 recorded accelerograms.

This project has received funding from the European Union's Horizon 2020 research and innovation programme under grant agreement No. 700748

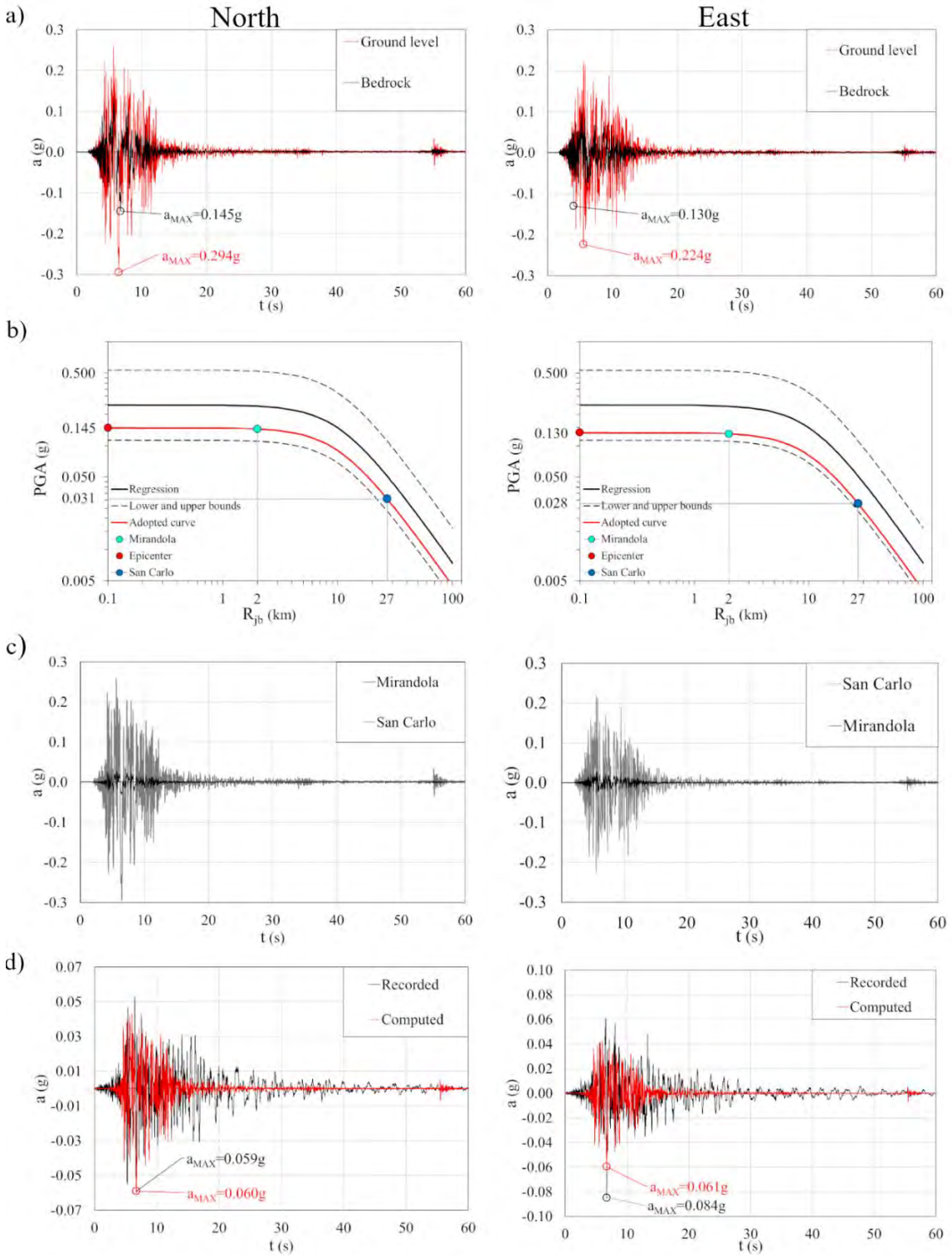

Figure 2-17. Proposed procedure for both the cardinal components: a) the recorded signal in Mirandola are deconvoluted to the bedrock; b) the Bindi et al. (2011) attenuation law are calibrated respecting epicentral distance and PGA of the recorded motion; c) the deconvoluted seismic signal is scaled according with the expected PGA value; d) the predicted and recorded accelerograms are compared.

This project has received funding from the European Union's Horizon 2020 research and innovation programme under grant agreement No. 700748

2.4 Numerical calculation

The numerical analysis has been performed with the Finite Difference code Flac v8 (Itasca Consulting Group, Inc., 2016). This software was chosen considering its flexibility, the possibility of performing two and three-dimensional analyses and of using advanced constitutive models.

2.4.1 Subsoil profile

The subsoil profile was built looking at different CPTU tests performed in the area surrounding the studied building. In particular, the results of four CPT tests performed closer to the building (less than 9 m distance from the building Figure 2-18.a) are considered.

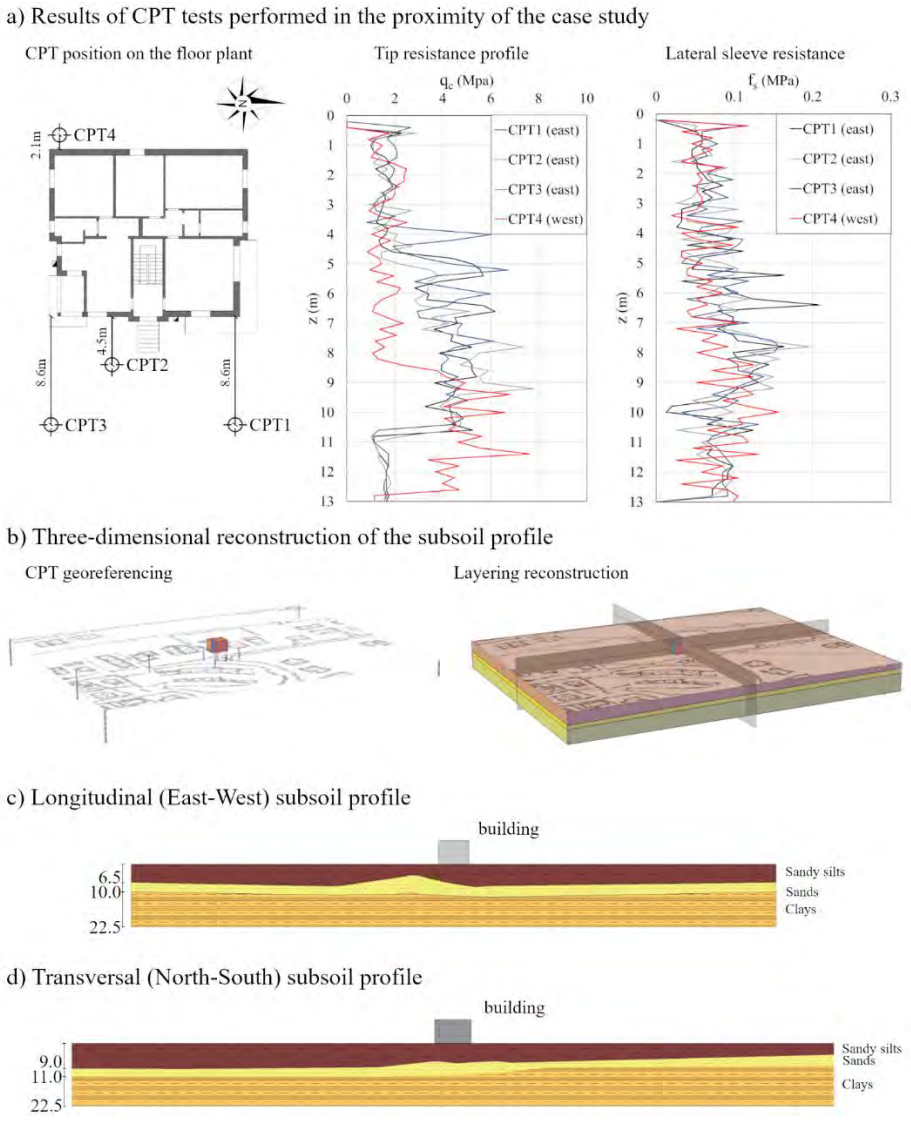

Figure 2-18. Case study three-dimensional subsoil profile. a) closest CPT tests, b) 3D reconstruction procedure, c) longitudinal subsoil profile, d) transversal subsoil profile.

This project has received funding from the European Union's Horizon 2020 research and innovation programme under grant agreement No. 700748

Figure 2-18.b shows the results of CPT tests in terms of tip and sleeve resistance. While the lateral sleeve resistance remains almost constant with depth, the tip resistance sharply changes highlighting the presence of different subsoil layers. The combined analysis reveals that thickness of strata changes in the east-west direction while it constant uniform in north-south direction. Including in the analysis further CPT tests, the three-dimensional subsoil profile of the area of interest has been built (Figure 2-18.b) for the first 23m of depth. In Figure 2-18.c and Figure 2-18.d two orthogonal cross sections intersecting the case study are presented.

2.4.2 Geometrical discretization

In order to solve the differential equations describing the wave motion, the geometrical domain was discretized. According to literature indications (Kuhleimeyer & Lysmer, 1973) the propagation of seismic waves in continum media can be simulated with sufficient accuracy if the element's dimension is smaller than one tenth the minimum propagating wavelength:

$$\Delta x \leq \frac{V_S}{10\, f} \tag{2.4}$$

Where:

V_s : lower shear wave propagation velocity

f : maximum correctly simulated frequency

For the above discussed reason, the input motion has been estimated at the model's base following the procedure shown in Paragraph 2.3.3. The acceleration history computed at the bedrock in San Carlo is thus convoluted up to the bottom of the clay deposit at 22.5 m depth. The results of this procedure are proposed in Figure 2-19 in terms of acceleration time history, frequency contents, velocity history and Arias intensity.

In Figure 2-20 the shear wave propagation velocity profile derived by a CPTU test performed in proximity of the case study is proposed. Based on this measures, the minimum Vs values for the three layers: sandy silts, sands and clays (respectively 60, 150 and 50m/s) are derived.

By assuming a maximum frequency of 10Hz the minimum elements' dimension are 0.5 m for the crust (sandy silts) and 1.5 m for the sandy and clayey layers for a total amount of elements equal to 13980. Finally, the implemented mesh is reported in Figure 2-21.

This project has received funding from the European Union's Horizon 2020 research and innovation programme under grant agreement No. 700748

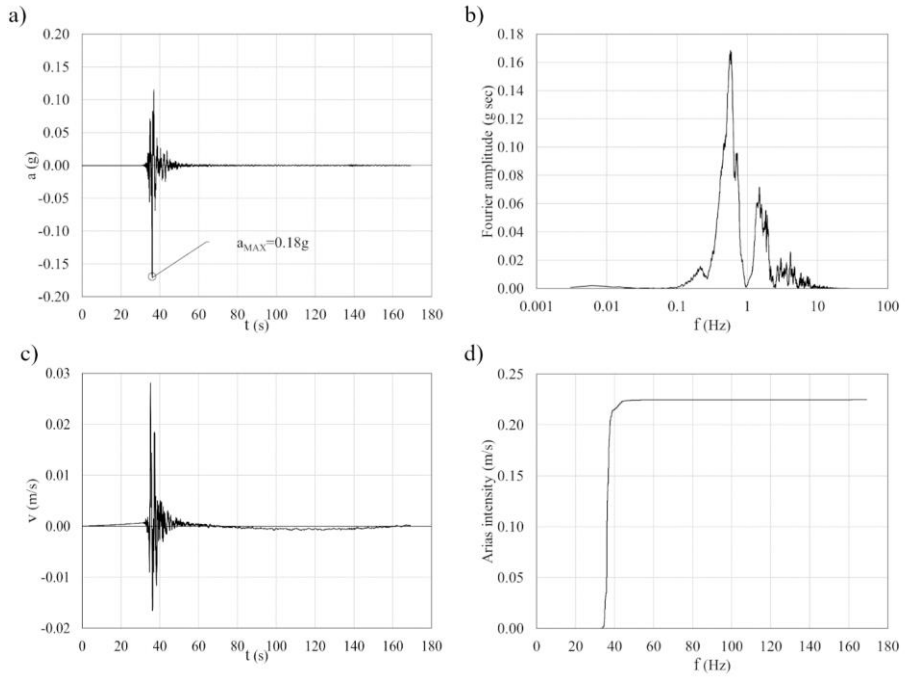

Figure 2-19. Input motion at the model's base: a) acceleration history, b) Fourier transform, c) velocity history, d) Arias intensity.

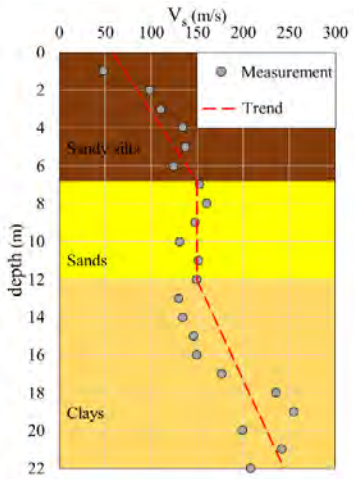

Figure 2-20. Shear wave propagation velocity profile from CPTU tests performed close to the case study.

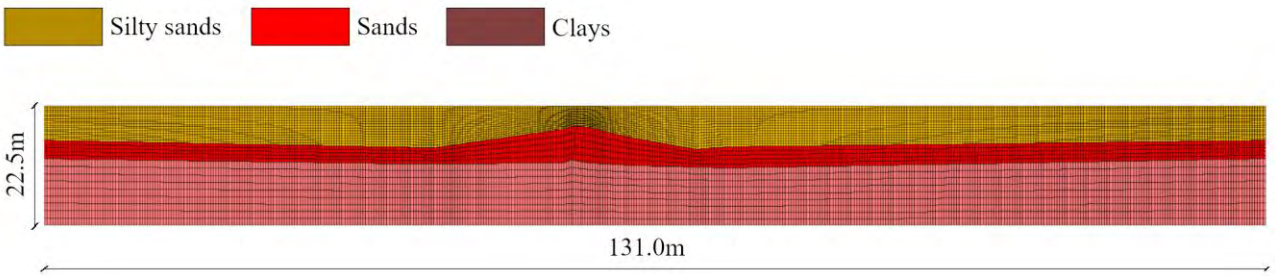

Figure 2-21. Conceived geometry discretization for the case study subsoil.

2.4.3 Constitutive models

Three different constitutive models are created and applied to the different phases of the calculation: a linear elastic model for the stress initialization, the Mohr Coulomb to take into account the stress-strain condition into the subsoil induced by building construction and the PM4 Sand to realistically simulate the behaviour of the liquefiable soil upon shaking.

Linear elastic

The linear elastic model is used herein for the stress initialization. Being a simple model, it does not take faithfully into account the complex mechanical behaviour of soils (non-linearity, occurrence of plastic strain, stress history dependence, etc.) but rather adopts a linear correspondence between stress and strain increments.

$$\begin{pmatrix} \delta\varepsilon_p \\ \delta\varepsilon_q \end{pmatrix} = \begin{pmatrix} 1/K & 0 \\ 0 & 1/3G \end{pmatrix} \begin{pmatrix} \delta p' \\ \delta q \end{pmatrix} \tag{2.5}$$

The model presents two calibration parameters: the shear stiffness (G) linking deviatoric stress with deviatoric strains and the bulk modulus (K) relating main stress with volumetric strains. The model's response can be summarized in the stress-strain relation proposed in Figure 2-22.

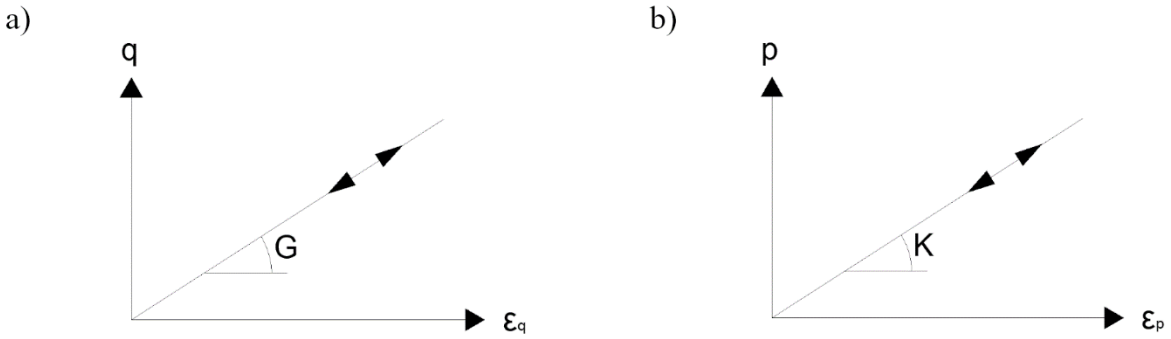

Figure 2-22. Graphical representation of the linear elastic constitutive model in the deviatoric stress – deviatoric strain plane (a) and main stress – volumetric strain plane (b).

Mohr Coulomb

The Mohr Coulomb model adopts an elasto-perfectly plastic constitutive law. Within this framework the mechanical behaviour of the material remains elastic until the failure surface is reached, subsequently indefinite plastic deformation occurs (Figure 2-23.a). The adopted failure surface can be schematically represented in the shear stress (τ) - normal stress (σ) plane (Mohr's plane) as a straight line characterized by slope φ (friction angle) and intercept c (effective cohesion) (Figure 2-23.b).

This project has received funding from the European Union's Horizon 2020 research and innovation programme under grant agreement No. 700748

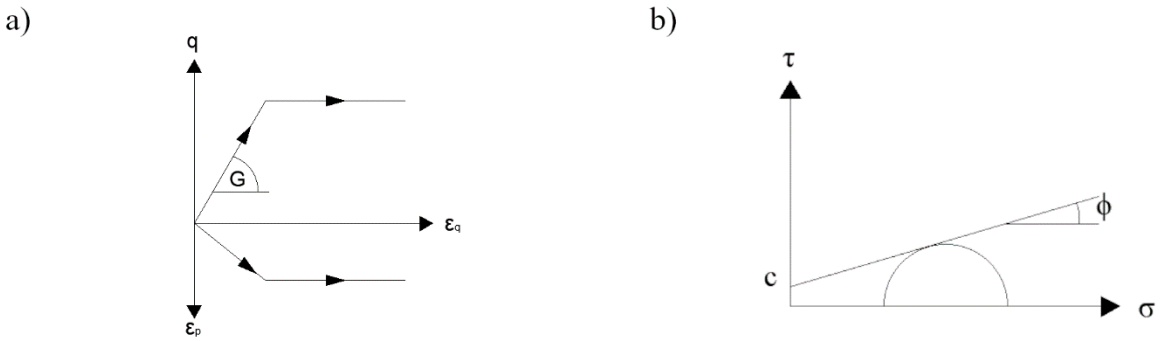

Figure 2-23. Graphical representation of the Mohr Coulomb constitutive model in the deviatoric stress – deviatoric strain plane – volumetric strain planes (a) and in the Mohr's plane.

PM4 sand

PM4 sand (Boulanger and Ziotopoulou, 2013) is a critical state (Schofield et al., 1968) based constitutive model conceptually consisting in an evolution of the Dafalias and Manzari (2004) model where the Jefferies state parameter is replaced by that proposed in Boulanger (2003) (Equation):

$$\psi = e - e_{cs} \tag{2.6}$$

$$\xi_R = D_{R,cs} - D_R \tag{2.7}$$

$$D_{R,cs} = \frac{R}{Q - ln\left(100\frac{p}{p_a}\right)} \tag{2.8}$$

It is controlled in terms of stress-ratio and conceived with multiple bounding surfaces. In particular, the model incorporates bounding, dilation, and critical surfaces of Dafalias and Manzari (2004) by removing the Lode angle dependency (e.g., friction angles are the same for compression or extension loading) such that the bounding (M^b) and dilation (M^d) ratios can be related to the critical stress (M) ratio by the following simpler expressions:

$$M^b = M \exp\left(-n^b \xi_R\right)$$

$$M^d = M \exp\left(n^d \xi_R\right) \tag{2.9}$$

Where n^b and n^d are calibration parameters and M is computed with the following equation (with φ_{cv} the constant volume or critical state effective friction angle):

$$M = 2 \sin\left(\phi_{CV}\right)$$

2.4.4 Calibration

Starting from the natural unit weights and the void ratios reported for the different strata by Fioravante *et al*. (2013) (see Table 2-3), the solid phase unit weights and dry unit weights are computed by means the sequent equations:

This project has received funding from the European Union's Horizon 2020 research and innovation programme under grant agreement No. 700748

$$n = \frac{e}{1+e} \quad (2.10)$$

$$\gamma_{nat} = \gamma_s(1-n) + \gamma_w Sn \quad (2.11)$$

$$\gamma_s = \frac{\gamma_{nat} - \gamma_w Sn}{(1-n)} \quad (2.12)$$

Table 2-3 Specific weights and porosity of strata.

Stratum	e	n	γ_{nat} (kN/m^3)	S	γ_s (kN/m^3)	γ_{dry} (kN/m^3)
Silty sands (crust)	0.9	0.5	16.5	1	22.5	11.9
Sands	1.0	0.5	18.5	1	27.2	13.6
Clays	0.8	0.4	18.0	1	24.6	13.6

For each stratum permeability is taken from the work of Sinatra and Foti (2015) based on the analysis of CPTU tests. The values are reported in Table 2-4.

Table 2-4 Values of permeability for each stratum.

Stratum	Permeability
Silty sands (crust)	1.E-7
Sands	7.E-6
Clays	6.E-8

The small strain elastic stiffness parameters are inferred from the shear wave propagation velocity computing the small strain shear modulus before (Equation 8) and computing the bulk modulus by imposing a Poisson's ratio equal to 0.3.

$$G_0 = \rho V_s^2 \quad (2.13)$$

$$E = 2G(1+\upsilon) \quad (2.14)$$

$$K = \frac{E}{3(1-2\upsilon)} \quad (2.15)$$

Being Vs variable with depth, the stiffness dependence on stress level is automatically taken into account. In Figure 2-24 the V_s, G_0 and K_0 profiles are reported for the vertical alignment passing for the middle of the building.

This project has received funding from the European Union's Horizon 2020 research and innovation programme under grant agreement No. 700748

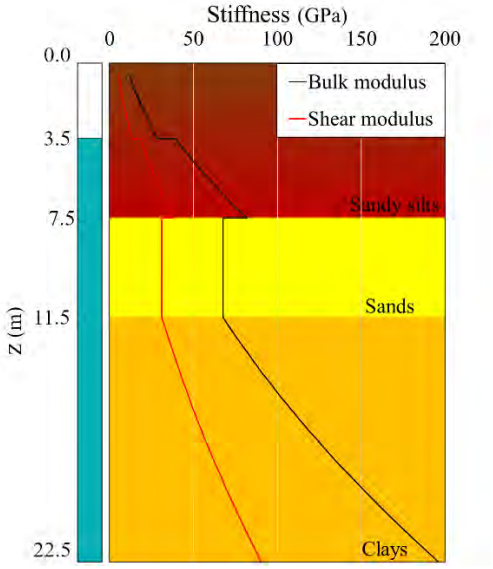

Figure 2-24. Bulk and shear stiffness moduli profiles along the vertical axis passing through the middle of the building.

In order to account for the stiffness degradation with strain of the cohesive soils (sany sands and clays layers) during cyclic shearing, the modulus degradation curves reported in Figure 2-9 are considered. Numerically, the stiffness modulus degradation is introduced in FLAC by means a cubic equation with two parameters c_0 and c_1 calibrated to fit the G/G_0 vs γ curve. These two parameters are calibrated for the two cohesive materials by numerically implementing the cyclic simple shear test and looking for the best match between numerical and experimental results. The obtain results, reported in Figure 2-25 show a good agreement in terms of shear stiffness degradation and a slight underestimation in terms of damping.

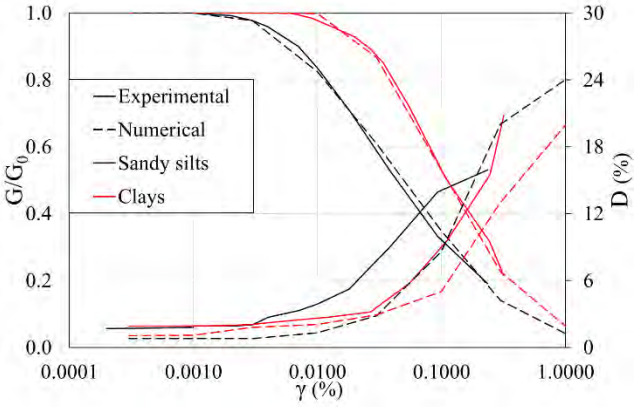

Figure 2-25. Comparison between the shear modulus degradation and damping curves numerically and experimentally obtained.

The Mohr Coulomb strength parameters: friction angle (φ), cohesion (C) and undrained cohesion (C_u) are extracted from the work of Sinatra and Foti (2015) that provides them from the analysis of CPT tests. The effective strength values and the large strain stiffness parameters for the cohesive soils are taken from the literature (Itasca Consulting Group, Inc.,2016). The collection of adopted parameters is summarized in Table 2-5.

This project has received funding from the European Union's Horizon 2020 research and innovation programme under grant agreement No. 700748

Table 2-5. Mohr Coulomb strength and stiffness parameters adopted in the simulation.

Stratum	ϕ' (°)	C' (kPa)	C_u (kPa)	K (Mpa)	G (Mpa)	c_0	c_1
Sandy silts	28	2	34	2.67	1.6	-2.8	0.2
Sands	33	0	/	16.7	10	/	/
Clays	20	8	45	0.67	0.40	-2.1	0.2

The PM4 Sand constitutive model is calibrated capturing the cyclic undrained behaviour of the liquefiable sandy layer. With this aim four triaxial undrained cyclic tests are numerically simulated looking at the best match between the obtained numerical liquefaction curve (CSR vs N_{liq}) and the experimental curve reported in Facciorusso *et al.* (2016). The collection of calibrated parameters is reported in Table 2-6 while the results of the numerical simulations and their comparison with the numerical result are shown in Figure 2-26.

Table 2-6. PM4 calibration parameters.

D_r	G_0	h_{p0}	n_b	n_d	φ_{cv} (°)
0.33	507	20	0.5	0.1	33

This project has received funding from the European Union's Horizon 2020 research and innovation programme under grant agreement No. 700748

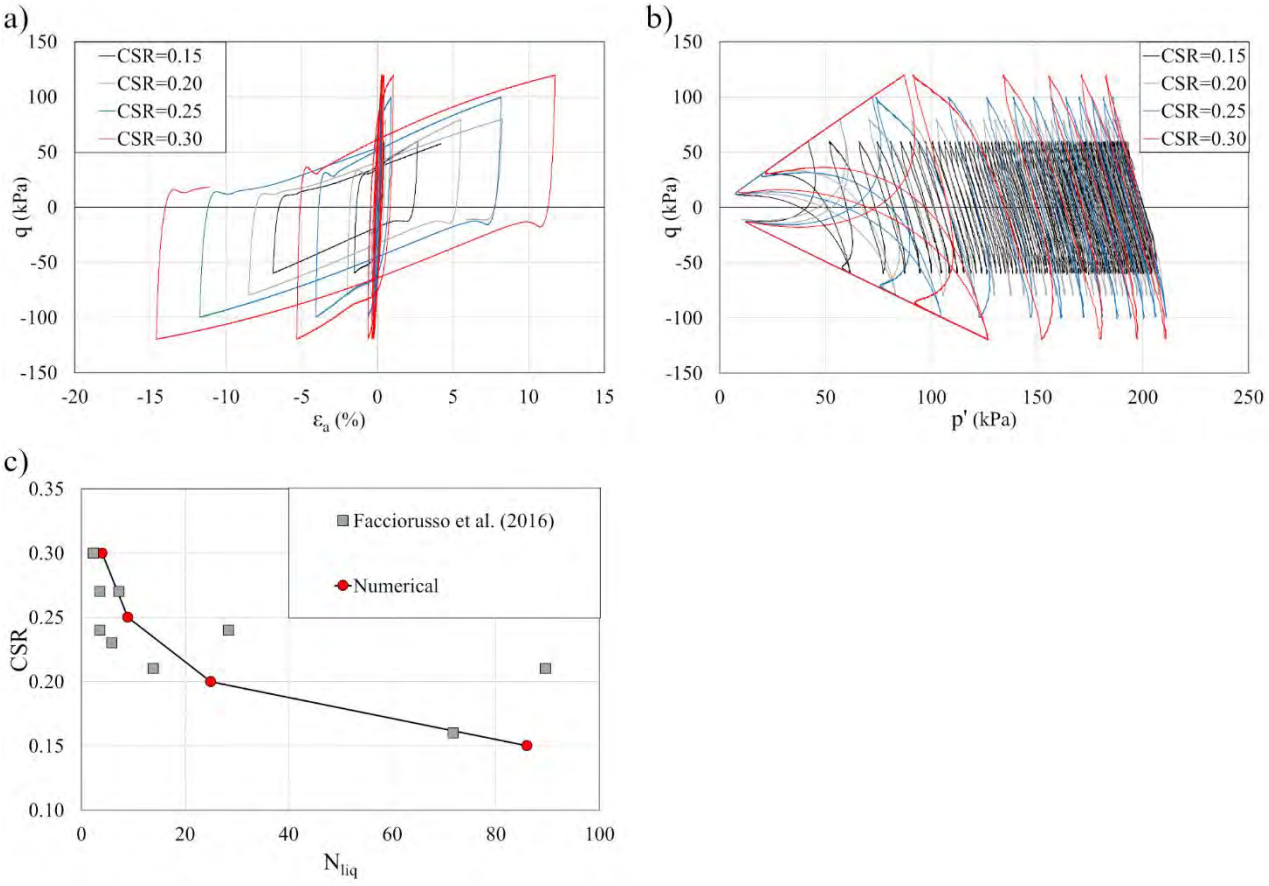

Figure 2-26. Results of the numerical liquefaction tests in terms of a) deviatoric stress against axial strain curves; b) deviatoric stress against main effective stress curves; c) liquefaction curves.

2.4.5 Calculation phases

The numerical calculation of the selected case study has been carried out with the following steps:

- *Stress initialization*

In this first phase the subsoil is modelled as a linear elastic material. Initially the model is considered completely dry assigning to each zone its dry density (Table 2-3), subsequently the pore water pressure is initialized assigning a water table located at 3.4m in depth and changing the density of submerged zones to the saturate density (Table 2-3). The vertical effective stress fields in the two initialization phases are reported in Figure 2-27.

This project has received funding from the European Union's Horizon 2020 research and innovation programme under grant agreement No. 700748

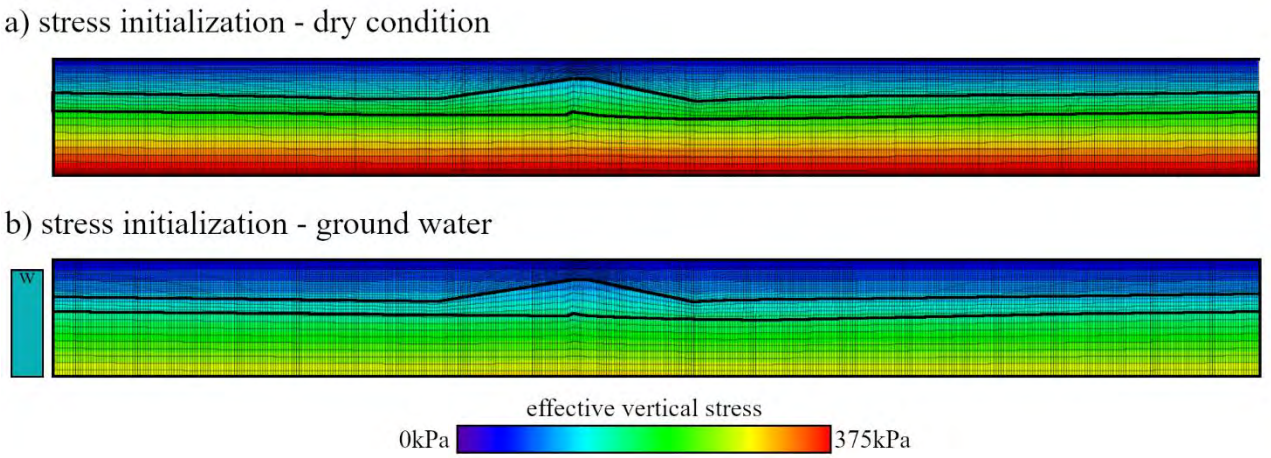

Figure 2-27. Vertical effective stress field in the stress initialization phase.

Once the model is led in the initial equilibrium state, the Mohr Coulomb hysteretic and PM4 sand models are introduced respectively for the cohesive materials (shallow sandy silts and deeper clays) and the liquefiable sandy layer. The adopted constitutive parameters are reported in Table 2-5 and Table 2-6. At the end of this phase displacements are reset to zero.

- *Application of load from the building*

The presence of the building is introduced simulating the soil excavation phase up to a depth of 0.5m and subsequently introducing a braced frame made of six beams rigidly linked each other (Figure 2-28.c). This schematization aims to reproduce the stiffness given to the building by the different walls. The poorly reinforced concrete foundation slab has been simulated with a beams (ID 1 and 2 in Figure 2-28.c) characterized by a Young's modulus equal to 30GPa and thickness equal to 20cm. The other beams, introduced to take into account the building's stiffness, have higher width and thickness. The complete list of parameters is reported in Table 2-7.

Table 2-7. Mechanical characteristics of the structural elements.

Beam ID	Density (kg/m^3)	Young's modulus (GPa)	Width (cm)	Thickness (cm)
1 - 2	2500	30	100	20
3 – 4 – 5 – 6 – 7 -8	/	30	100	100

Corresponding to the three main walls, concentrated forces are applied to take into account the building's weight. The values of the three forces are reported in Table 2-8.

Table 2-8. Concentrated loads applied to the structural model of the building.

F_1 (kN)	F_2 (kN)	F_3 (kN)
130	195	107

Figure 2-28.a and Figure 2-28.b report the field of vertical effective stresses computed after the foundation is applied. The figure shows the weak ability of the foundation to diffuse the loads coming from the upper structure, with the most significative stress increments located just beneath the points where loads are applied.

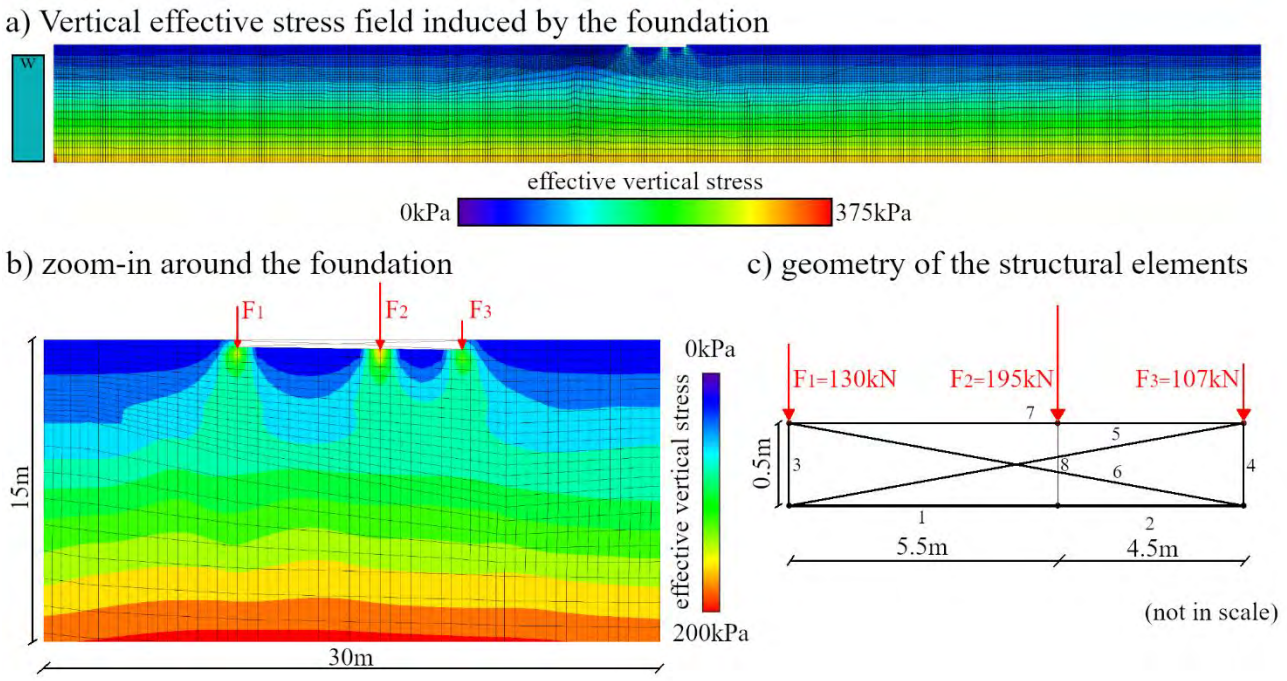

Figure 2-28. Foundation modelling. a) vertical effective stress field; b) vertical effective stress field beneath the foundation; c) geometry of the structural elements.

- *Shaking*

After introducing the foundation, the boundary conditions are changed to better simulate wave propagation within the model. In fact, the boundary conditions at the sides of the model must account for the free-field motion that would exist in the absence of the structure. Thus, to reproduce the free-field motion in a way that boundaries retain their non-reflecting properties *(i.e.* outward waves originating from the structure are properly absorbed) the so-called free-field boundary condition (Cundall et al. 1980) are imposed (Figure 2-29). In addition, aiming to absorb reflected waves, still conditions (in the normal and shear directions) are imposed to the bottom side of the model.

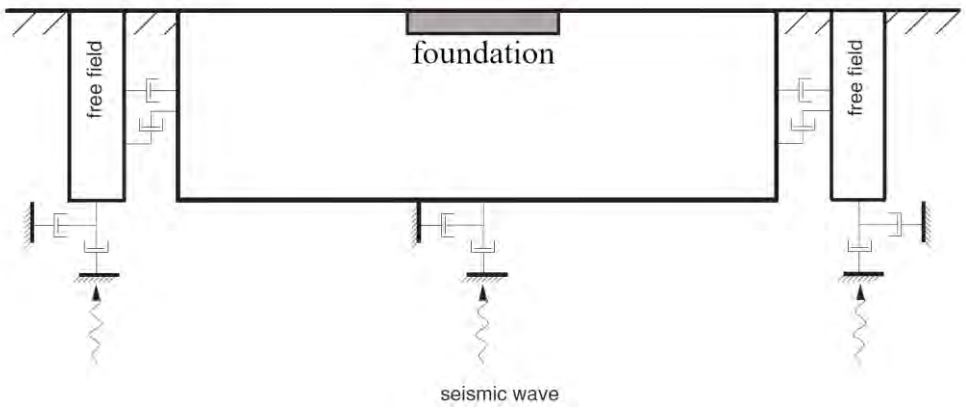

Figure 2-29. Schematic of the free-field boundary conditions.

The computed input motion proposed in Figure 2-19 is introduced by imposing a shear stress history at the model's base. In particular, the following equation is adopted to compute shear stress from the input velocigram.

$$\sigma_s = \alpha\,(\rho\,V_s)\,v_s \qquad (2.16)$$

Where σ_s is a coefficient to be calibrated to replicate at the base of the model the actual input motion, ρ is the soil density, V_s is the shear wave propagation velocity and v_s is the input velocity.

In Figure 2-30 the desired velocity time history, coming from the local seismic analysis shown in Paragraph 2.4.2, and the velocigram resulting from the applied shear stress history are compared. The figure shows the good agreement between imposed (in red) and target (in black) velocity time histories obtained with a calibration factor α=1.65.

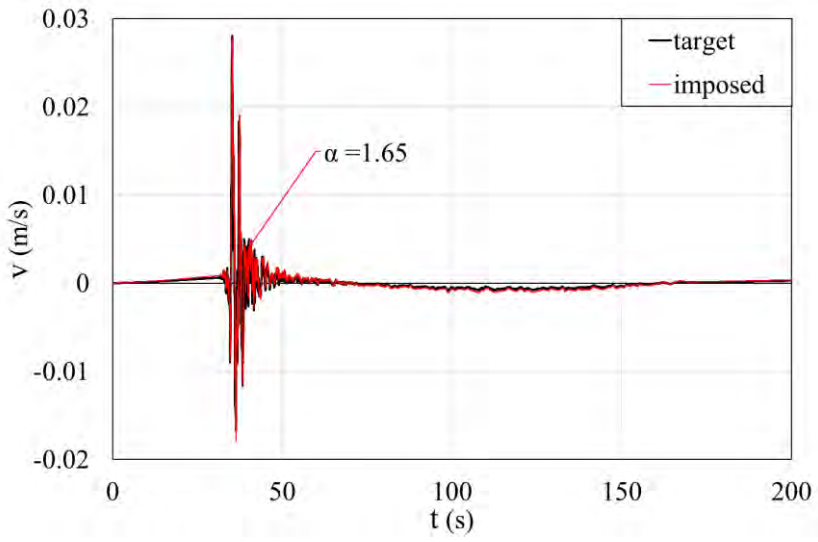

Figure 2-30. Comparison between the target velocity time history (in black) and the velocigram resulting from the imposed shear stress history (in red).

2.4.6 Calculation results

The results of simulation are presented in Figure 2-31. In particular, in Figure 2-31.c the acceleration time histories are show for the points A (the foundation level), B (in the middle point of the liquefiable sandy layer) and C (the model's bottom). During the first 36 seconds, the wave motion is slightly amplified while propagating upward from the clayey to the sandy layer and up to the foundation. At this time, the pore pressures in the sandy layer start to increase, as shown by the plot of $r_u = \Delta u/\sigma'_{zo}$ (Figure 2-31.e) and this effect progressively reduces the amplification from the sandy layer to the upper foundation, while acceleration is still amplified by the clayey stratum. When r_u approaches higher values (say larger than 0.8), which occurs around after 38 seconds, the sandy soil becomes very soft and is unable to upward propagate motion. This effect prolong until liquefaction fully develops (r_u approaching 1). Therefore, it can be said that the increase of pore pressures, and finally the liquefaction, together with the consequent decay of stiffness in the sandy soil, reduces the wave propagation with the results that the sandy layer performs as a seismic isolator for the building. From the viewpoint of building shake this effect is positive as it should reduce structural damage. On the other hand, the increase or pore pressure in the sandy soil determines (Figure 2-31.d) significant settlements that start to increase when r_u reaches values of 0.6 and continues with the progress of liquefaction. A careful analysis of Figure 2-31.a, that reports the pore pressure ratio filed at the end of the shaking, reveals that liquefaction does not occurs uniformly in the sandy layer, but it is rather localized beneath the foundation in the corner portions where the initial shear stress is more significant. The reduction of effective stress induced by the pore pressure build-up produces a decrease of strength and stiffness that induces a shear strain concentration at the boundary between the sandy and silty strata where the effect of liquefaction is more important.

The settlements time histories of the foundation reported in Figure 2-31.c show a significant differential settlement between the left and right corners of the building. In particular, the final vertical displacement at the left corner is equal to 38 cm while the one at the right corner is about 3 cm. This effect can be explained by the irregular thickness of the liquefiable layer that results to be more important on the left side of the building.

In conclusion, the above results show the ability of the adopted numerical model to reproduce the phenomena taking place at buildings foundation upon seismic shaking and liquefaction. Despite calculation has been simplified (a two-dimensional model has been implemented) the results are fully consistent with the observed response of the building and in particular with the differential settlements experienced at the two opposite corners. It is necessary to observe that advanced constitutive models are necessary to correctly reproduce phenomena taking place in the soil. In this case PM4 sand has been adopted to reproduce the non-linear, stress and density dependent response of the soil.

The above model can thus be used to predict the effects of ground improvement and design a good technical solution that fulfils requirements in terms of seismic performance (safety and serviceability). In the next paragraphs of this chapter, space is on the contrary given to analyse the effects of soil heterogeneity, retaining them responsible of differential settlements, and thus of damage, also in the case where horizontal subsoil layers are present.

This project has received funding from the European Union's Horizon 2020 research and innovation programme under grant agreement No. 700748

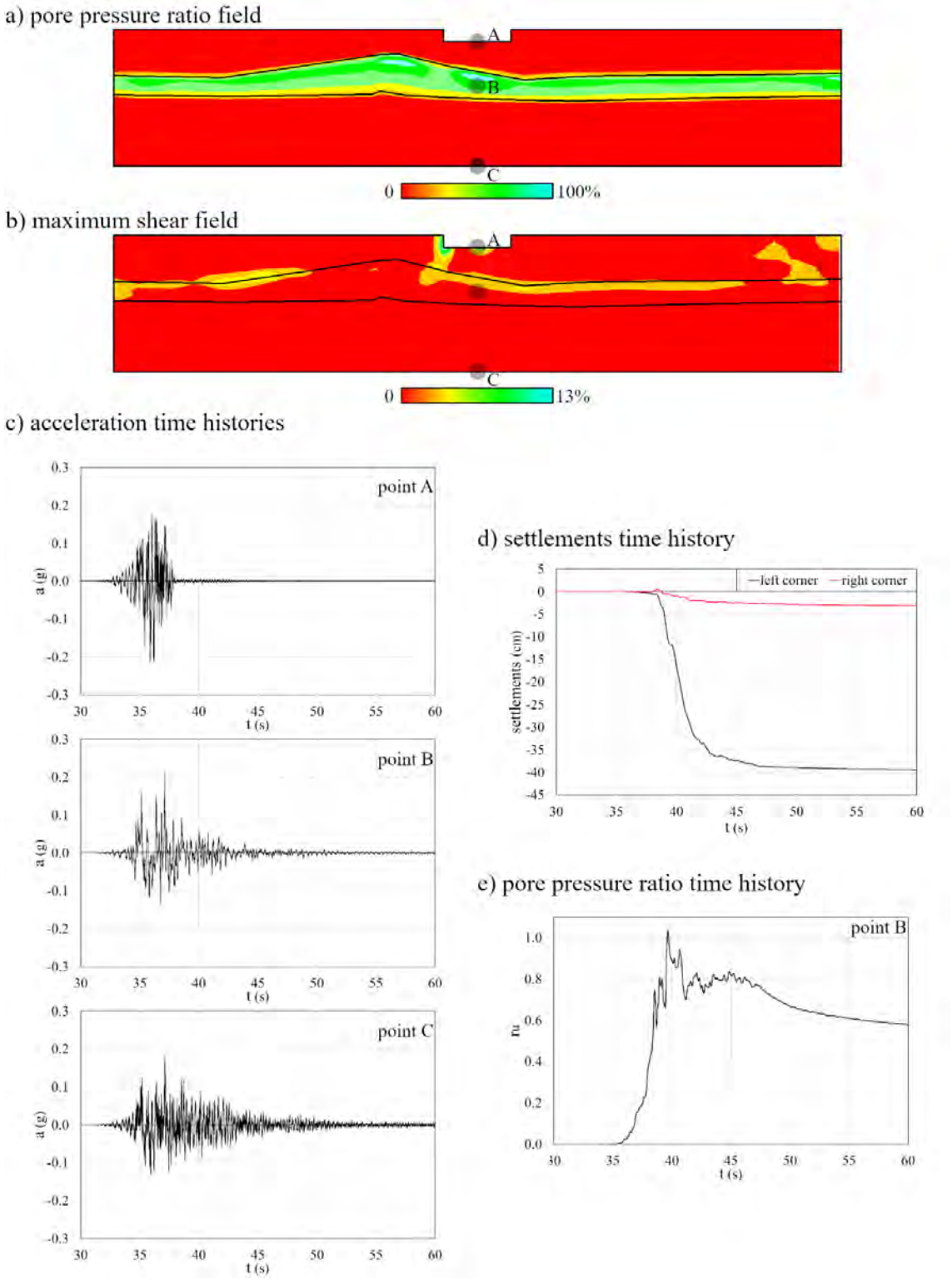

Figure 2-31. Results of the simulation in terms of a) pore-pressure ratio field; b) maximum shear field; c) acceleration time histories at the bottom of the model (point C), in the middle of the liquefiable layer (point B) and at the foundation's level (point A); d)

settlements time histories at the left corner of the foundation (in black) and at the right corner of the foundation (in red); e) pore-pressure ratio time history at the middle of the liquefiable layer.

2.5 Influence of subsoil variability on the post-liquefaction settlements

In geotechnical modelling engineers habitually schematize the soil's heterogeneity with models where strata grouping soil portions having more and less similar mechanical and physical properties and adopting characteristic parameters for design. This *modus operandi* is mostly justified by the difficulty in measuring variability in the simplified approaches typically used in the geotechnical practice and, not less important, by the difficulty in quantitatively characterize the properties' variability with sufficient accuracy. The results is that analyses are affected by some uncertainty which is not quantifiable. In the next paragraphs, the above hypothesis is called into question focusing on the effect of subsoil variability on the liquefaction induced settlements of buildings. With this aim in mind, referring to the case study proposed in Chapter 2, the spatial variability of relative density for liquefiable sandy layer has been studied statistically analysing the results of in situ tests and quantitatively characterized with the random field theory. Thereafter, following the procedure described in the previous paragraphs, simulations are run introducing different compatible randomly generated relative density scenarios and applying increasing seismic inputs. The results of the study are interpreted focusing on the differential and absolute foundation settlements, on their mutual relation and on their relevance to the building's damage.

2.5.1 Characterisation and quantification of subsoil variability

The effects of subsoil variability are studied with reference to six CPT tests performed relatively close to each other in the centre of San Carlo village – Emilia Romagna (Figure 2-32).

Figure 2-32 San Carlo municipality map reporting the CPT location.

For each CPT profile, the "soil behaviour type index (I_c)" (Robertson, 1990) is firstly computed with depth by means of the following equation (17):

$$I_c = ((3.47 - logQ_t)^2 + (\log F_r + 1.22)^2)^{0.5} \quad (2.17)$$

Where:

Q_t = normalized cone penetration resistance = $(q_t - \sigma_{v0})/\sigma'_{v0}$ (2.18)

F_r = normalized friction ratio (in %) = $(f_s/(q_t - \sigma_{v0})) \cdot 100$ (2.19)

By comparing, the obtained values with the soil classification proposed by Robertson (1990) and Robertson (2010) (Table 2-9), the subsoil profile is defined.

Table 2-9. Soil classification based on the soil behaviour type index (Robertson, 2010)

Zone	Soil Behaviour Type	Ic
1	Sensitive, fine grained	N/A
2	Organic soils – clay	> 3.6
3	Clays – silty clay to clay	2.95 – 3.6
4	Silt mixtures – clayey silt to silty clay	2.60 – 2.95
5	Sand mixtures – silty sand to sandy silt	2.05 – 2.6
6	Sands – clean sand to silty sand	1.31 – 2.05
7	Gravelly sand to dense sand	< 1.31
8	Very stiff sand to clayey sand	N/A
9	Very stiff, fine grained	N/A

Once the sandy layers along the CPT profile are recognized, the relative density Dr is computed by adopting the following equation proposed by Salgado et al. (1997.a, 1997.b)

$$D_r = 0.465 \left(\frac{q_{c1N}}{C_{dq}}\right)^{0.264} - 1.063 \quad (2.20)$$

Where C_{dq} is a coefficient depending on the physical characteristics of sand ranging from 1.64÷1.55 (a value equal to 0.9 is considered herein).

q_{c1N} is obtained firstly computing the equivalent value that would have obtained in the identical material if the vertical effective stress had been 1atm (q_{c1}) by means the following equation:

$$q_{c1} = C_N \, q_c \quad (2.21)$$

then the tip resistance is furtherly normalized with respect to the atmospheric pressure (P_a):

$$q_{c1n} = \frac{q_{c1}}{P_a} \quad (2.22)$$

The factor C_N comes from experimental evinces obtained in calibration chambers and it is also a function of q_{c1N}, that has to be estimated by means of an iterative procedure.

$$C_N = \left(\frac{P_a}{\sigma'_{vc}}\right)^{1.338-0.249(q_{c1N})^{0.264}} \quad (2.23)$$

In the following image (Figure 2-33) the results of the above presented procedure are shown in terms of tip and sleeve resistance profiles (Figure 2-33.a and Figure 2-33.b), soil behaviour type profiles (Figure 2-33.c) and relative density profiles (Figure 2-33.d).

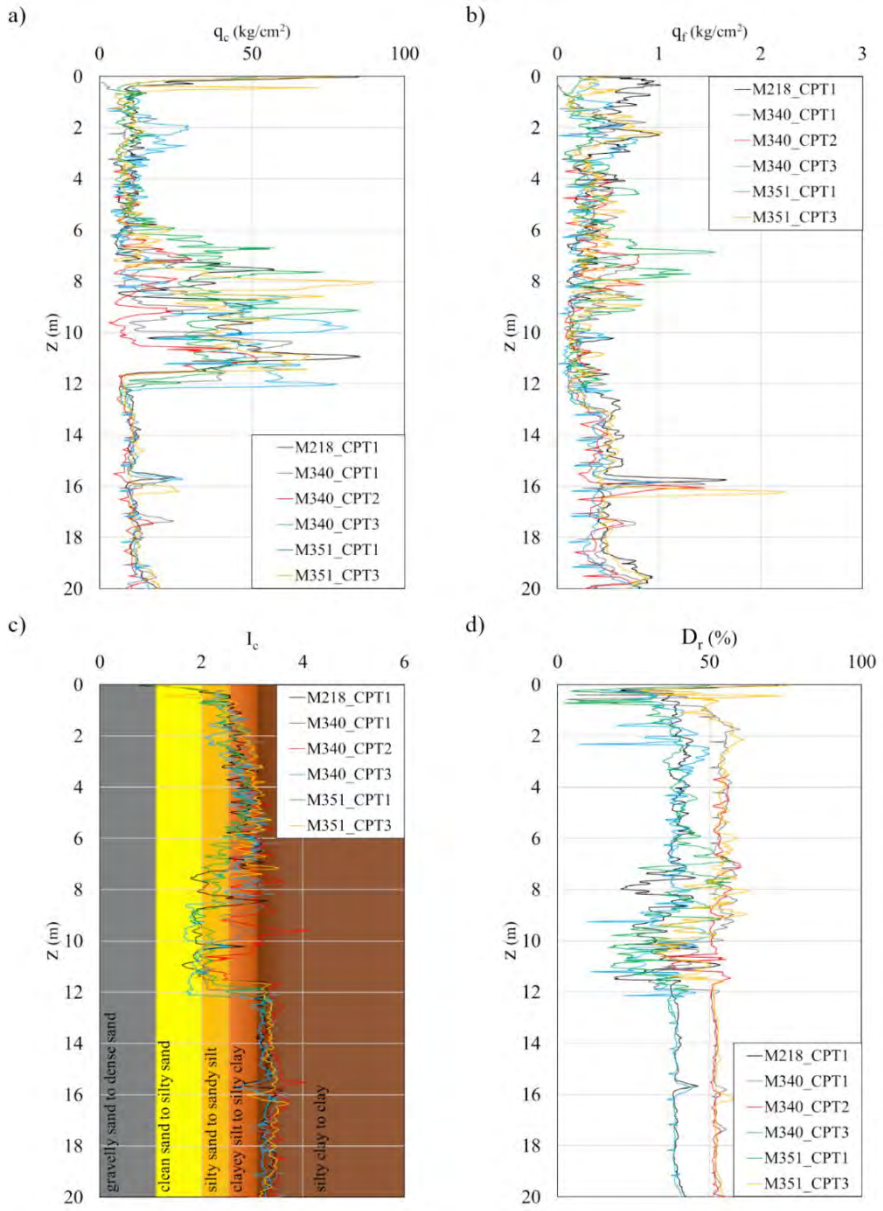

Figure 2-33 Results of the selected CPT tests performed in San Carlo.

This project has received funding from the European Union's Horizon 2020 research and innovation programme under grant agreement No. 700748

Looking at the profiles, in particular at the SBT profile of Figure 2-33.c, the sandy potentially liquefiable layer is identified from 7.0 to 12m in depth with values of relative density quite heterogeneous ranging from 19 to 62%. The experimental values of Dr for each CPT are then statistically analysed and proposed in Figure 2-34 and Figure 2-35 in terms of histograms.

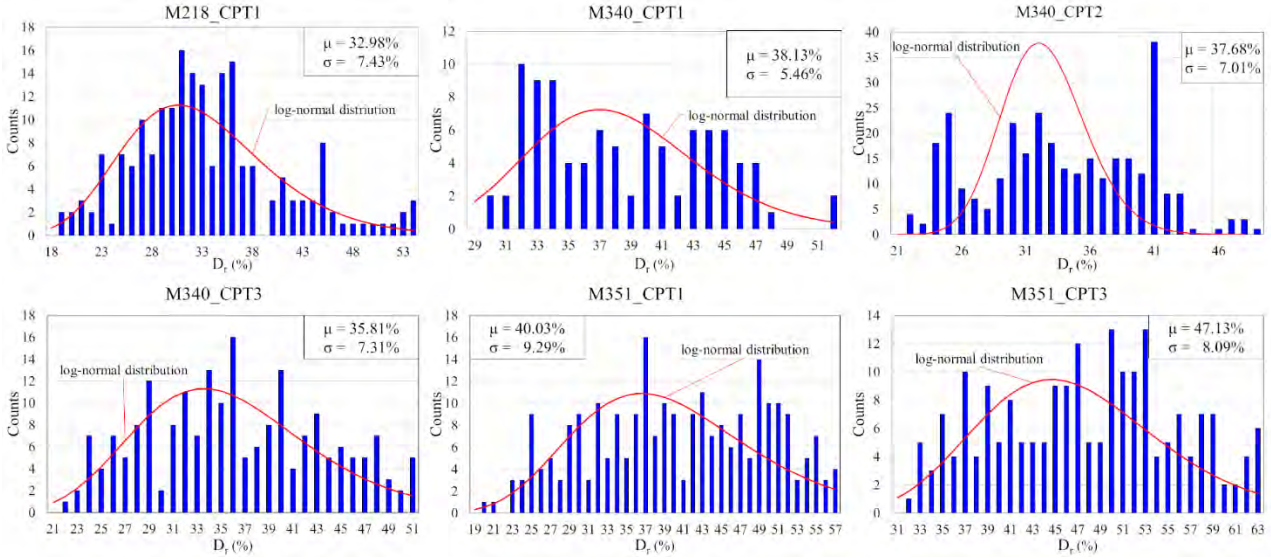

Figure 2-34 Relative density statistical distributions obtained for each CPT test.

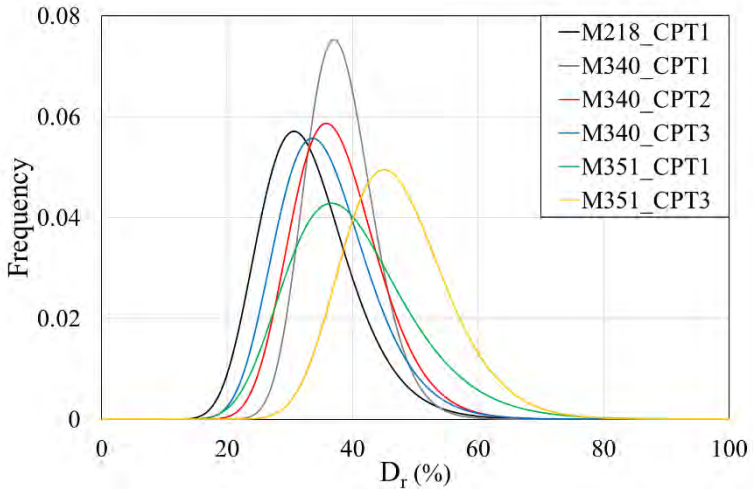

Figure 2-35 Experimental relative density frequency distributions for the six CPT tests.

For the profiles of relative density computed from each CPT tests, the autocorrelation function defined by Vanmarcke (1977) is also computed. The function is generally defined as:

$$\rho(d) = \frac{C(d)}{C(0)} = \frac{C(d)}{\sigma_x^2} = \frac{1}{\sigma_x^2(n-d)} \sum_{i=1}^{n} \left[\left(X(t) - \mu_x(t) \right) \left(X(t+d) - \mu_x(t+d) \right) \right] \quad (2.24)$$

This project has received funding from the European Union's Horizon 2020 research and innovation programme under grant agreement No. 700748

Where *d* is the considered distance between pairs of points, *n* is the number of pairs at distance equal to *d*, *X(t)* is the expected value of the first point of the pair, *X(t+d)* is the expected value of the second point of the pair and $\mu_x(t)$ is the distribution's mean value.

The experimental values of correlation are thus modelled with the Markov correlation, a negative exponential function characterised by the unique parameter θ.

$$\rho(d) = exp\left(\frac{-2|d|}{\theta}\right) \tag{2.25}$$

where θ is the correlation distance: the distance beyond which the values of the considered variable are spatially no more correlated. Loosely speaking, θ is the distance within which points are significantly correlated (*i.e.* by more than about 10%). Conversely, two points separated by a distance more than θ will be largely uncorrelated. Mathematically, θ is defined in Equation 2.26 as the area under the correlation function (Vanmarcke, 1984):

$$\theta = \int_{-\infty}^{\infty} \rho(\tau)\ d\tau = 2\int_{0}^{\infty} \rho(\tau)\ d\tau \tag{2.26}$$

The values of the correlation distance θ are inferred by means the maximum likelihood method conceived by Honjo and Kazumba (2002). The method consists in the maximization of a maximum likelihood function defined as follows:

$$L_z(\theta) = -\frac{n}{2}\ln(2\pi) - \frac{1}{2}\ln|V_{ij}| - \frac{1}{2}\left(D_r - \mu_{D_r}\right)^T V_{ij}^{-1}\left(D_r - \mu_{D_r}\right) \tag{2.27}$$

$$D_r = \begin{bmatrix} D_r(r_1) \\ \vdots \\ D_r(r_n) \end{bmatrix} \qquad \mu_{D_r} = \begin{bmatrix} \mu_{D_r} \\ \vdots \\ \mu_{D_r} \end{bmatrix} \qquad V_{ij} = \sigma_{D_r}^2 \exp\left(-\frac{|r_i - r_j|}{\theta}\right) \tag{2.28}$$

Where n is the number of D_r values, μ_{Dr} is the mean of D_r, σ_{Dr} is the standard deviation of D_r, V_{ij} is the matrix of the covariance and r_i is the space vector at the point i. Figure 2-36 shows the maximum likelihood functions computed for each relative density field and reported together with the maximum values indicated with hollow dots. Once the correlation length is estimated, the whole correlation functions is given (Figure 2-37).

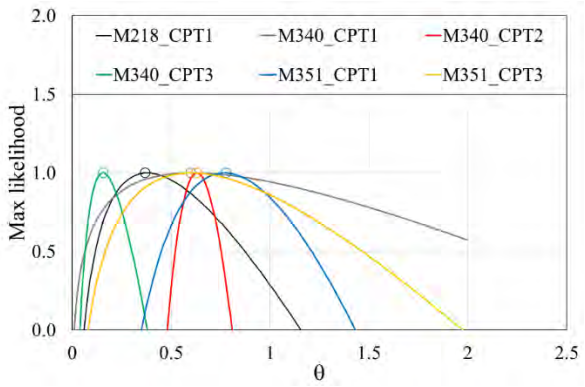

Figure 2-36 Maximum likelihood functions estimated for each relative density field.

This project has received funding from the European Union's Horizon 2020 research and innovation programme under grant agreement No. 700748

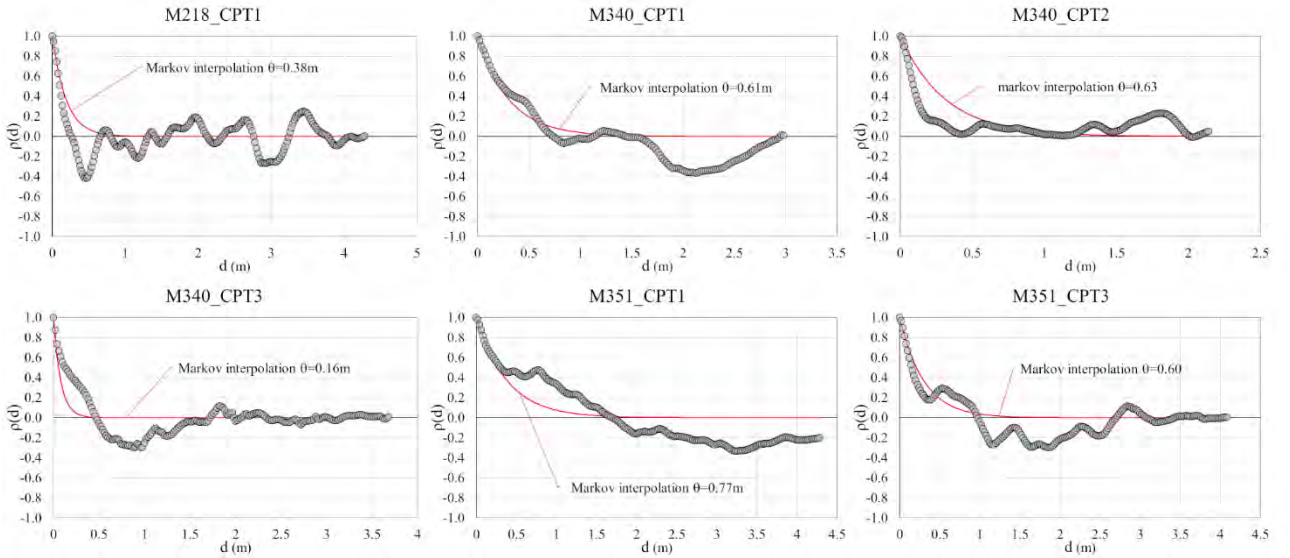

Figure 2-37 Experimental correlation function and its numerical interpolation for each performed CPT.

The mean value (μ), standard deviation (σ), covariance (COV), minimum and maximum recorded values of relative density and correlation length (θ) are reported in Table 2-10 for each performed test.

Table 2-10 Statistics parameters characterizing the relative density distribution in the sandy layer.

CPT ID	μ (%)	σ (%)	COV (%)	$D_{r,min}$ (%)	$D_{r,MAX}$ (%)	θ
M218_CPT1	32.98	7.43	0.22	18.81	53.51	0.38
M340_CPT1	38.13	5.46	0.26	29.77	51.99	0.61
M340_CPT2	37.68	7.01	0.20	21.33	48.21	0.63
M340_CPT3	35.81	7.31	0.23	21.75	50.72	0.16
M351_CPT1	40.03	9.29	0.28	19.61	57.48	0.77
M351_CPT3	47.13	8.09	0.25	31.51	61.92	0.60

The above results define the spatial variability of relative density in the vertical direction. The same study should be repeated in the horizontal direction, but for this a CPT tests located a close distance should be available. Being the number and location of tests performed in the present study not sufficient for such analysis, the statistical and geostatistical parameters regarding the horizontal direction are taken as typical values reported in the literature. Among various authors Ching *et al.* (2018) gave values of correlation length ranging from 2 and 6m for sandy deposits. Therefore, willing to emphasize the effects of variability in the present calculation, a value of θ=2m has been considered in the next calculation.

2.5.2 The reference geometry

Once the spatial variation of relative density is characterized, its effects on the mechanical response of a potentially liquefiable subsoil is analysed generating random fields consistent with the adopted model and running numerical simulations. Following the conceptual scheme of the case studied in the previous paragraphs, a system composed by a building founded on a three-layered subsoil: a sandy liquefiable stratum confined by two cohesive strata is considered (Figure 2-38). This time the subsoil layering is taken as horizontal to isolate the effects of spatial variability not contaminating differential settlements with ununiform thickness of liquefiable layer seen in Figure 2-18.

Figure 2-38 Adopted reference subsoil profile adopted.

The constitutive models are again the hysteretic Mohr Coulomb and the PM4 Sand respectively for the cohesive and sandy potentially liquefiable materials. The materials' physical and mechanical properties are those already proposed in Table 2-3, Table 2-4, Table 2-5 and Table 2-6. A standard 10m width strip foundation subjected to a uniformly distributed load of 50kPa.

2.5.3 Generated scenarios of relative density

In this study sixty different relative density distributions are generated keeping constant the value of correlation length (θ_x=2.00m θ_y=1.26m) and increasing values of covariance (COV=0.2 – 0.3 – 0.4). To this aim the free software RFEM (Fenton and Griffiths, 2000) has been used adopting the input parameters shown in Table 2-11.

Table 2-11 Parameters adopted for the relative density fields generation in RFEM.

Parameter	COV_{Dr}=0.2	COV_{Dr}=0.3	COV_{Dr}=0.4
μ_{Dr} (%)	37.68	37.68	37.68
σ_{Dr} (%)	7.01	11.3	15.07
θ_x	1.26	1.26	1.26
θ_y	2.00	2.00	2.00
N_x	50	50	50
N_y	10	10	10

Δ_x (m)	0.8	0.8	0.8
Δ_y (m)	0.4	0.4	0.4
Number of scenarios	20	20	20

μ_{Dr}: mean, σ_{Dr}: standard deviation, θ_x: correlation length in the horizontal direction, θ_y: correlation length in the vertical direction, N_x: number of clusters in the horizontal direction, N_y: number of clusters in the vertical direction, Δ_x: cluster's length, Δ_x: cluster's height.

Three examples of randomly generated relative density fields are presented in Figure 2-39, while Figure 2-40 shows the same field shown in Figure 2-39.c generated into the FLAC mesh.

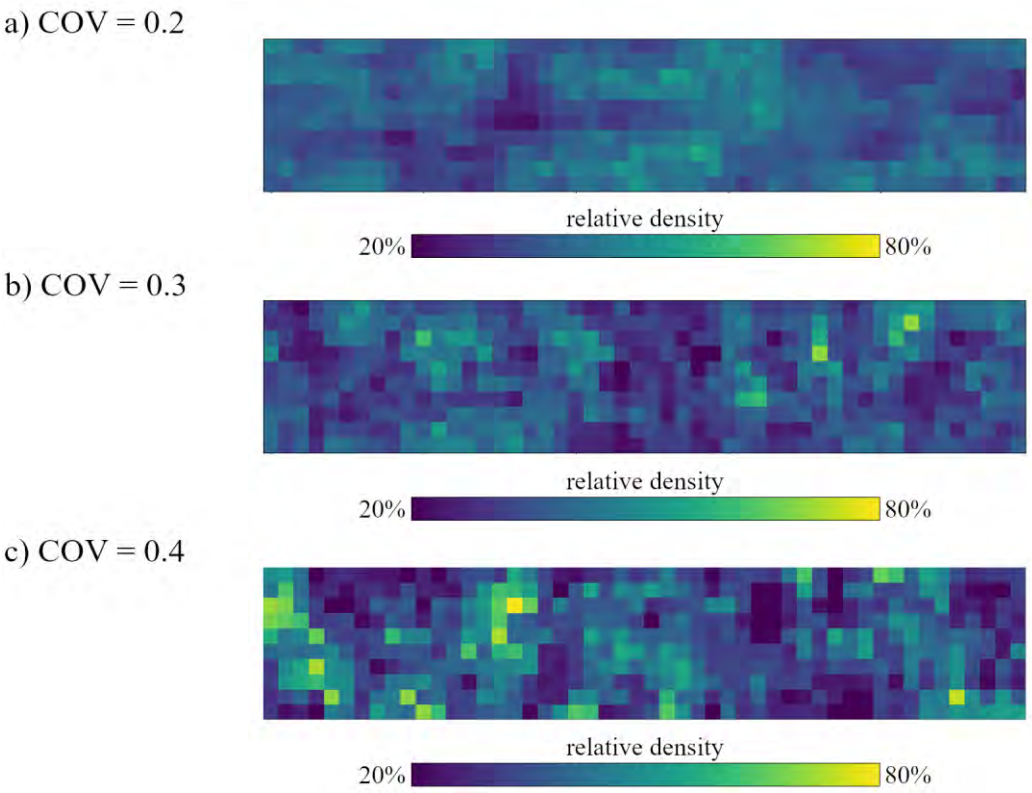

Figure 2-39 Examples of randomly generated relative density field.

This project has received funding from the European Union's Horizon 2020 research and innovation programme under grant agreement No. 700748

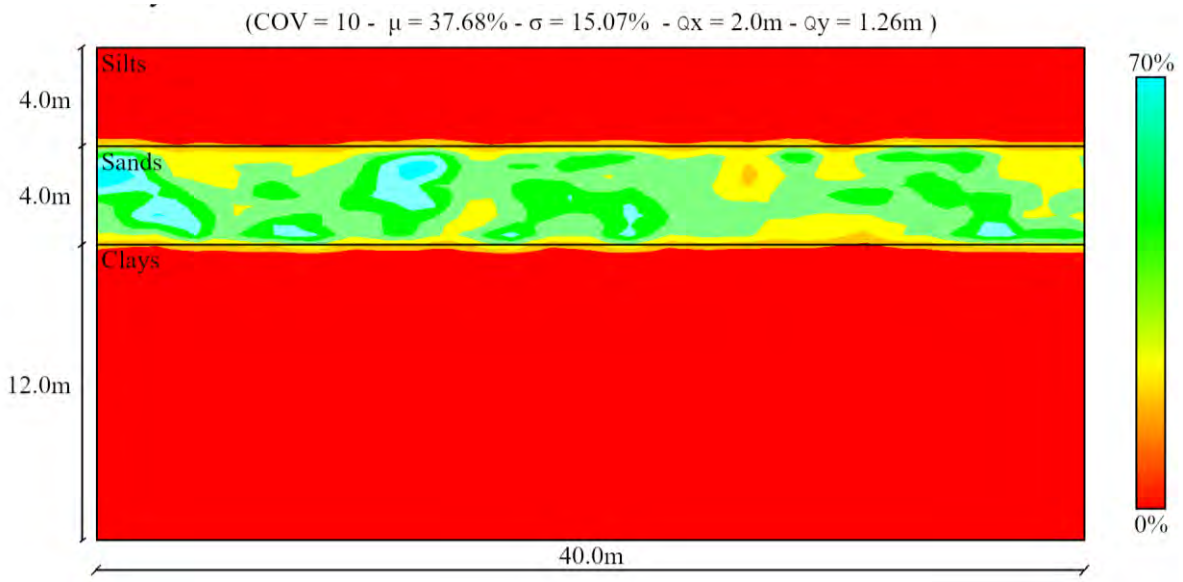

Figure 2-40 Relative density field randomly generated with a covariance equal to 10 ed imported into the FLAC grid.

2.5.4 Seismic input

The effect of variability is studied herein in combination with three levels of seismic input obtained scaling the accelerogram computed in Paragraph 2.4.2 for factors equal to 70% (a_{max}=0.12g), 100% (a_{max}=0.17g) and 160% (a_{max}=0.27g). The three adopted accelerograms are reported in Figure 2-41.

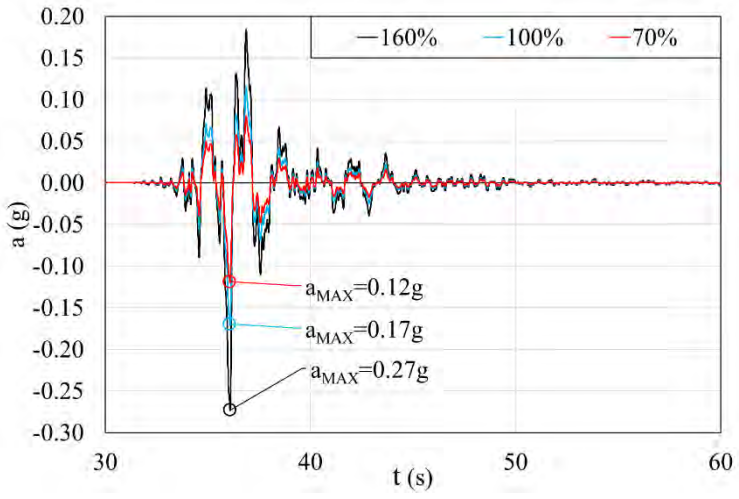

Figure 2-41 Scaled accelerograms adopted for the parametric study.

2.5.5 Results of calculation

In this paragraph, the results coming the performed simulations are proposed in terms of foundation settlement profiles. In order to highlight the roles played by the subsoil variability Figure 2-42, Figure 2-43 and Figure 2-44 show for each seismic level (α = 70%-100%-160%) the settlement profiles for the three

analysed levels of variability (COV = 02–0.3–0.4). In each graph, the settlement profile obtained by considering the mean relative density is plotted for reference (with a red curve). There is an evident connection between the subsoil homogeneity and uniformity of settlements. In particular, the higher subsoil variability produces more heterogeneous settlement profiles.

As a summary, Figure 2-45 reports for each investigated value of covariance the settlements profiles corresponding to the three levels of seismic intensity. This analysis reveals that higher earthquake intensities tend to produce to less homogeneous settlement profiles and thus the effects of subsoil heterogeneity are more relevant for lower intensity earthquakes, as the increase of intensity produce a levelling of results.

The discrepancy between the settlement profile given by the uniform porosity distribution and the average value of settlement given by the variable porosity fields are reported in Figure 2-46 in terms of skewness (Equation 2.24) that practically measure along the foundation how much the mean value of the settlements coming from the different porosity scenarios differs from the value computed with the uniform porosity distribution.

$$sk = \frac{\sum_{i=1}^{nos}(w_i - w_{n=cost})}{(nos-1)\,\sigma^3} \qquad (2.29)$$

where *nos* is the number of analysed scenarios, w_i is the settlement given by the scenario *i*, $w_{n=cost}$ is the settlement given by the constant distribution of porosity and σ is the standard deviation.

The figure shows that for low seismic excitations (α=70% - black lines) the spatial variability of porosity generally introduces a settlement overestimation respect to the case of constant porosity. This effect become less and less evident with increasing seismic input.

In Figure 2-47 the relation between the absolute and differential settlement are shown for the whole collection of performed analysis. The results clearly show a direct proportionality between the parameters according with other studies reported in the literature (*e.g.* Viggiani, 1993).

The last outcome has a practical application in the liquefaction risk analysis of buildings on wide areas when soil damage is typically inferred by automatically processing results of in-situ test collected in big dataset. Typically, such simplified analyses consider the soil damage in terms of an index that often correspond to the liquefaction induced absolute settlement (*e.g*. Zhang *et al.,* 2002; Karamitros *et al.*, 2013; Bray and Macedo 2017; Bullock *et al.*, 2018). On the other hand, it is well known that, limiting the attention to the liquefaction phenomenon, damage in superstructures is essentially due to its experienced differential settlements. The obtained relation, showing a linear correspondence between absolute and differential liquefaction induced settlements, supports the idea that simplified indexes based on absolute settlements can be conveniently adopted to perform the risk assessment of buildings over large areas. This result is exploited as a base for some of the analyses performed in the next chapters.

This project has received funding from the European Union's Horizon 2020 research and innovation programme under grant agreement No. 700748

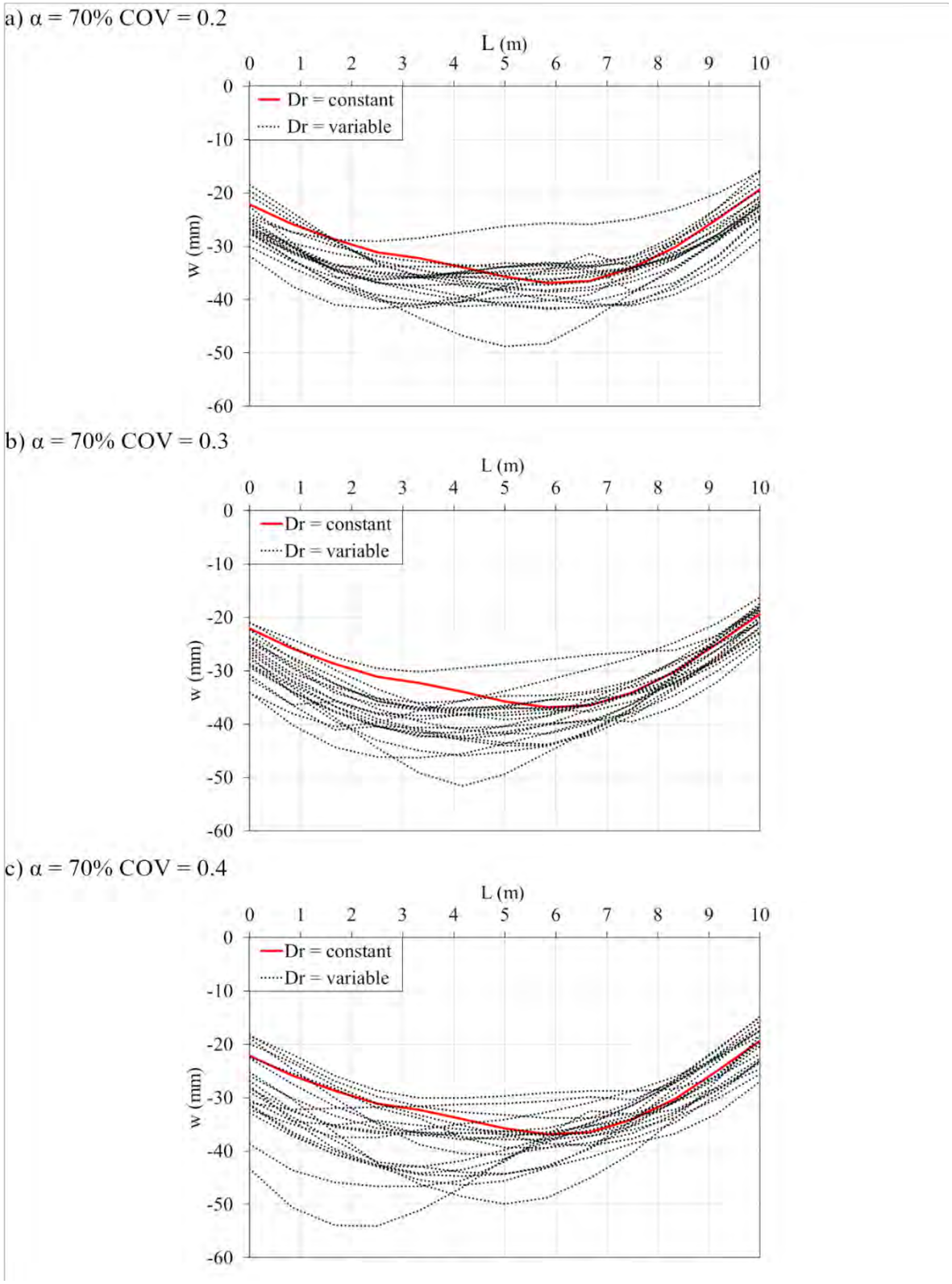

Figure 2-42 Settlement profiles beneath the foundation for the 70% scaled accelerogram and different values of covariance of the relative density field.

This project has received funding from the European Union's Horizon 2020 research and innovation programme under grant agreement No. 700748

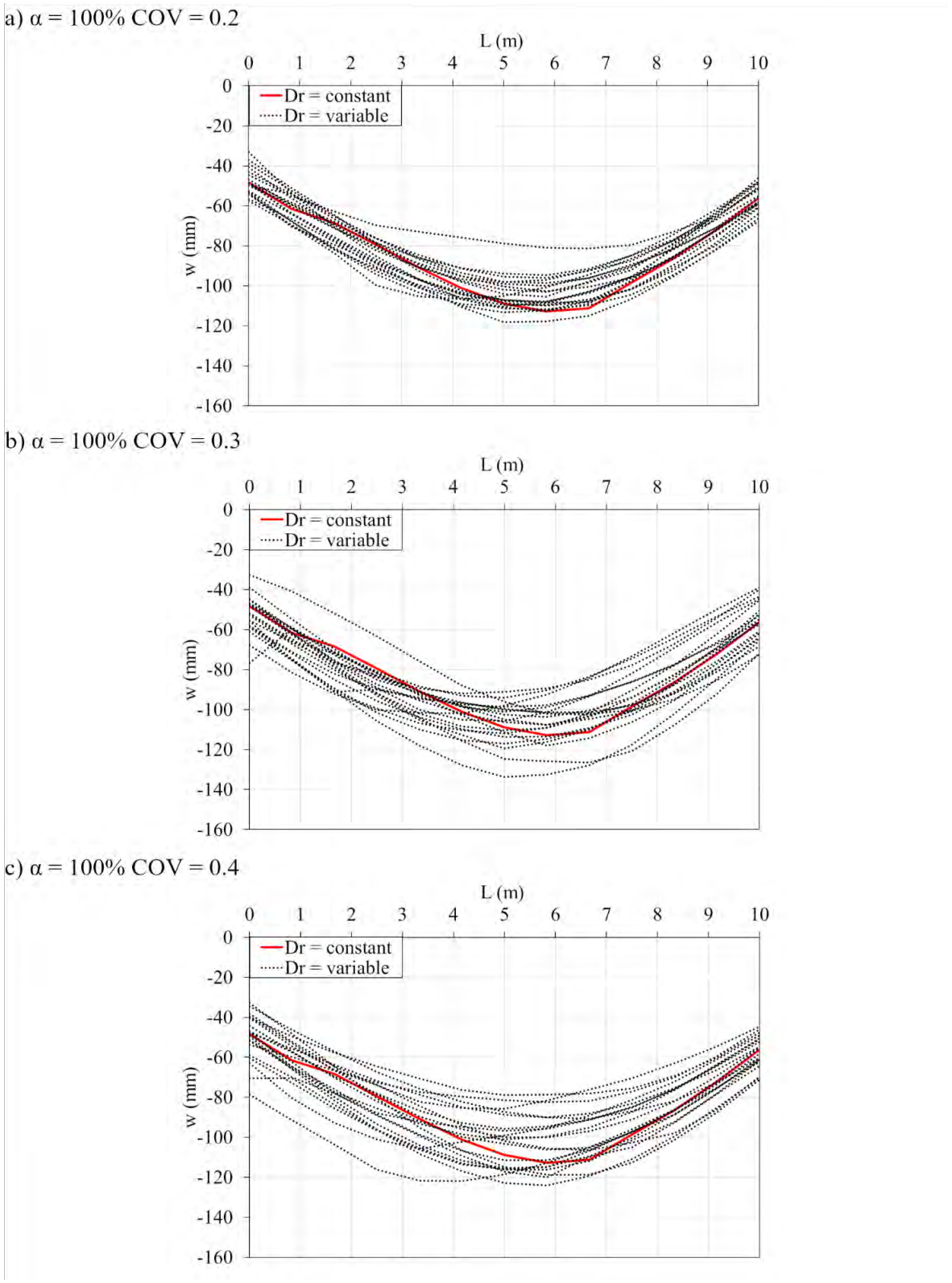

Figure 2-43 Settlement profiles beneath the foundation for the reference accelerogram and different values of covariance of the relative density field.

This project has received funding from the European Union's Horizon 2020 research and innovation programme under grant agreement No. 700748

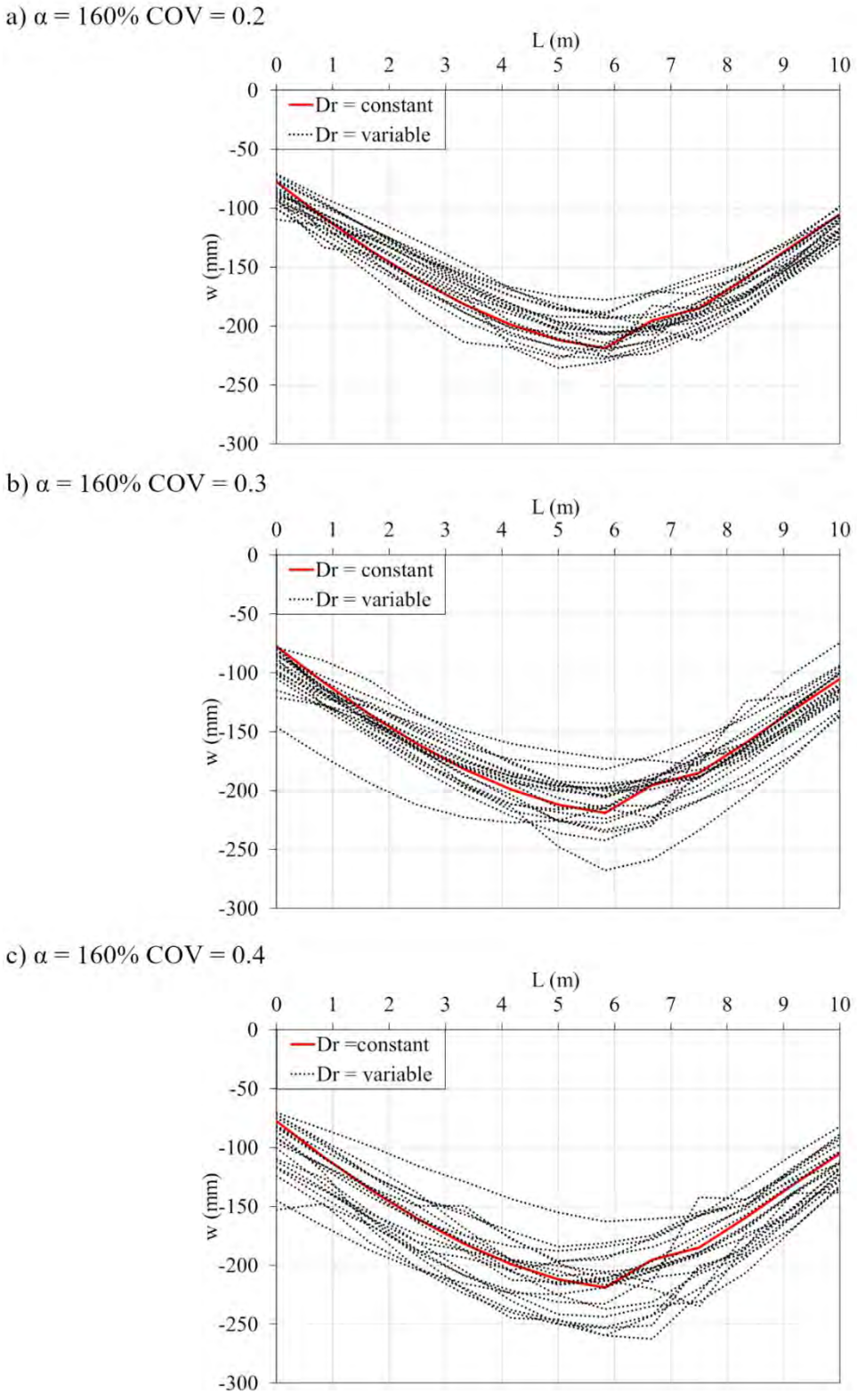

Figure 2-44 Settlement profiles beneath the foundation for the 160% scaled accelerogram and different values of covariance of the relative density field.

This project has received funding from the European Union's Horizon 2020 research and innovation programme under grant agreement No. 700748

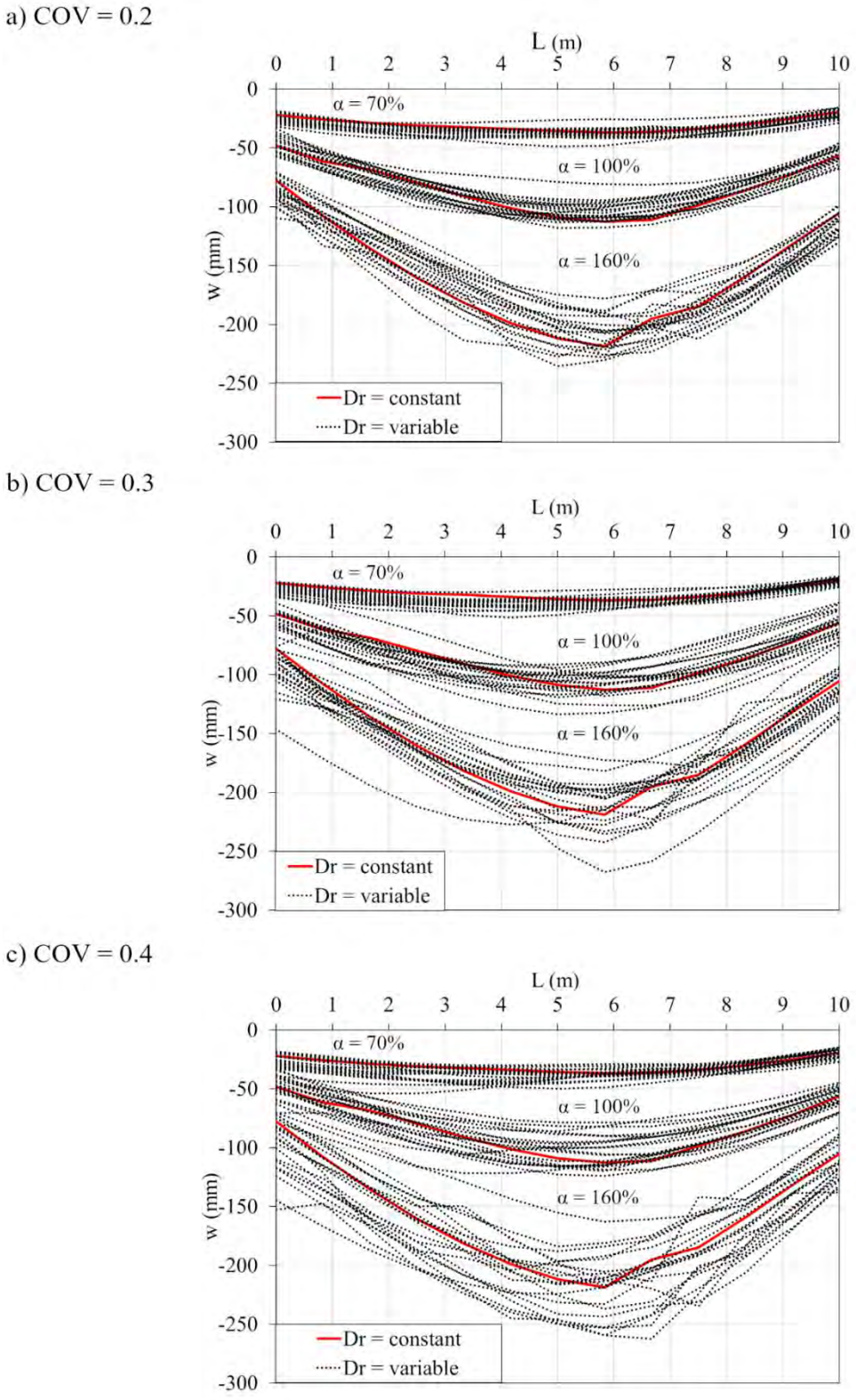

Figure 2-45 Settlement profiles beneath the foundation for different values of covariance of the generated relative density field and increasing input motion.

This project has received funding from the European Union's Horizon 2020 research and innovation programme under grant agreement No. 700748

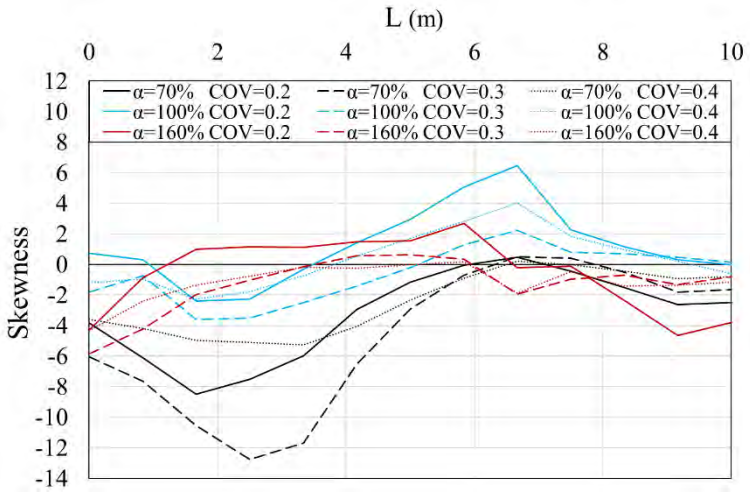

Figure 2-46 Skewness profiles for the analysed scenarios.

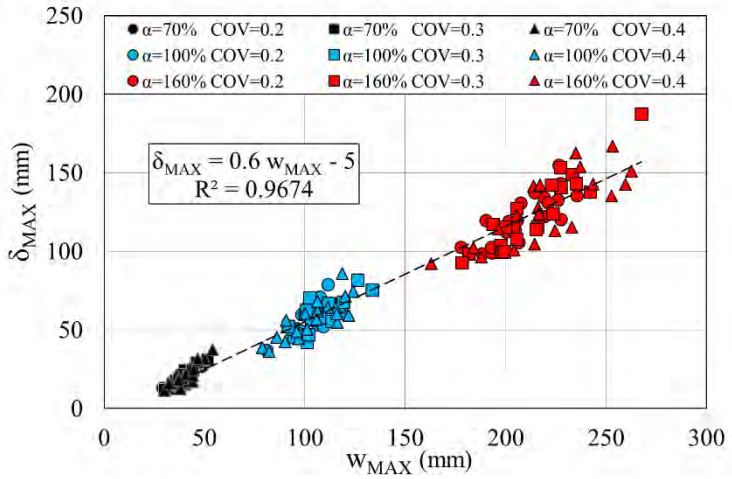

Figure 2-47 Absolute and differential settlements computed for each analysed porosity scenario.

2.6 Bibliography

Bindi, D., Pacor, F., Luzi, L., Puglia, R., Massa, M., Ameri, G., and Paolucci, R. (2011). Ground motion prediction equations derived from the Italian strong motion database. Bulletin of Earthquake Engineering, 9(6), 1899-1920.

Boore DM, Atkinson GM (2008) Ground-Motion prediction equations for the average horizontal component of PGA, PGV, and 5%-damped PSA at spectral periods between 0.01 s and 100 s. Earthquake Spectra 24:99–138.

Boulanger, R. W. (2003). High overburden stress effects in liquefaction analyses. Journal of geotechnical and geoenvironmental engineering, 129(12), 1071-1082.

Boulanger, R. W., and Ziotopoulou, K. (2013). "Formulation of a sand plasticity plane-strain model for earthquake engineering applications." Journal of Soil Dynamics and Earthquake Engineering, Elsevier, 53, 254-267, 10.1016/j.soildyn.2013.07.006.

Burland, J. B., and Burbridge, M. C. (1985, December). Settlement of foundations on sand and gravel. In Institution of Civil Engineers, Proceedings, Pt 1 (Vol. 76).

Dafalias, Y.F., Manzari, M.T.: Simple plasticity sand model accounting for fabric change effects. J. Eng. Mech. 130(6), 622–634 (2004).

Facciorusso, J., Madiai, C., and Vannucchi, G. (2016). The 2012 Emilia earthquake (Italy): geotechnical characterization and ground response analyses of the paleo-Reno river levees. Soil Dynamics and Earthquake Engineering, 86, 71-88.

Fenton, G. A., and Griffiths, D. V. (2000). Bearing capacity of spatially random soils. In Proc., PMC2000 Conf., CD-Rom Proceedings. Paper PMCZ000-097.

Fioravante, V., Giretti, D., Abate, G., Aversa, S., Boldini, D., Capilleri, P. P., ... and Facciorusso, J. (2013). Earthquake geotechnical engineering aspects of the 2012 Emilia-Romagna earthquake (Italy).

Itasca Consulting Group, Inc. (2016). FLAC - Fast Lagrangian Analysis of Continua, Ver. 8.0. Minneapolis: Itasca.

Iwasaki, T.; Tatsuoka, F.; Tokida, K.; Yasuda, S. 1978. A Practical method for assessing soil liquefaction potential based on case studies at various sites in Japan. [conference]: 2nd International conference on Microzonation. - 1978: 885-896.

Kottke, A. R., and Rathje, E. M. (2009). Technical manual for Strata.

Kuhleimeyer , R., & Lysmer, J. (1973). Finite element method accuracy for wave propagation problems. Journal of the soil mechanics and foundations division, ASCE, 99(SM5), 421-427.

Luzi L, Pacor F, Puglia R (2019). Italian Accelerometric Archive v3.0. Istituto Nazionale di Geofisica e Vulcanologia, Dipartimento della Protezione Civile Nazionale. doi: 10.13127/itaca.3.0

Maurer, B. W., Green, R. A., Oliver, S. and Taylor, O. S. 2014. Moving Towards an Improved Index for Assessing Liquefaction Hazard: Lessons from Historical Data. Soils and Foundations, 55(4): 778-787.

Robertson, P.K., 1990. Soil classification using the cone penetration test. Canadian Geotechnical Journal, 27(1): 151-158.

Robertson, P.K., 2010. Soil behaviour type from the CPT: an update. 2nd International Symposium on Cone Penetration Testing, CPT'10, Huntington Beach, CA, USA. www.cpt10.com

Schofield, A., Wroth, P.: Critical State Soil Mechanics. McGraw-Hill, London (1968)

Sinatra, L., and Foti, S. (2015). The role of aftershocks in the liquefaction phenomena caused by the Emilia 2012 seismic sequence. Soil Dynamics and Earthquake Engineering, 75, 234-245.

van Ballegooy, S.; Malan, P.; Lacrosse, V.; Jacka, M.E.; Cubrinovski, M.; Bray, J.D.; O'Rourke, T.D.; Crawford, S.A.; Cowan, H. 2014. Assessment of Liquefaction-Induced Land Damage for Residential Christchurch. Earthquake Spectra (30) No. 1: pages 31–55, February 2014.

Vanmarcke, E. H. (1984). Random Fields: Analysis and Synthesis. Cambridge, Massachusetts: MIT Press.

Viggiani, C. (1993). Fondazioni. Cooperativa Universitaria Editrice Napoletana.

Zhang, G.; Robertson, P.K.; Brachman R.W.I. 2002. Estimating liquefaction-induced ground settlements from CPT for level ground. Canadian Geotechnical Journal 39: 1168–80.

Zhang, G.; Robertson, P.K., Brachman, R.W.I. 2004. Estimating liquefaction-induced Lateral Displacements from CPT for level ground. Journal of Geotechnical and Geoenvironmental Engineering. AUGUST 2004.

This project has received funding from the European Union's Horizon 2020 research and innovation programme under grant agreement No. 700748

3 LIQUEFACTION RISK ASSESSMENT OF A MEDIUM/LARGE CITY: CASE STUDY #1 CHRISTCHURCH (NEW ZEALAND)

3.1 Introduction

The city of Christchurch (pop. 366.100, 2013) is an important industrial and agricultural centre in the South Island of New Zealand and is the second largest city of the country. It is located on the eastern (Pacific) coast of the South Island, in the Canterbury Region. From the geological viewpoint, the City is situated over recent deposits of alluvial gravels laid down by the Waimakariri River, and fine marine sediments deposited on the coastal margin of the floodplain and in estuaries and lagoons. The sediments are about 700 metres deep: principally coarse-grained fluvial greywacke sands, gravels and silts, but with extensive sands in the eastern, seaward part of the city and with intermingled estuarine deposits especially in the central, south, and south eastern areas. The sediments lie on 200-300 meters of volcanic rock overlying greywacke basement at about 1000 m depth. To the south of the city, the sediments become shallower against the weathered volcanic cone of Banks Peninsula. The Port Hills are mantled with loess soils over the basalt rock.

In 2010-2011, the Canterbury region suffered a severe earthquake sequence known as Christchurch Earthquake Sequence (CES) that produced huge damage to buildings and infrastructural assets mostly caused by liquefaction (Figure 3-1 and Figure 3-2). The 2010 – 2011 Canterbury earthquake sequence includes several thousands of events, four of them with Mw ≥ 6. The event occurred on September 4th 2010 (Mw7.1), named Darfield earthquake due to the location of the epicentre, and the subsequent earthquake of February 22nd 2011 (Mw 6.2) named Christchurch earthquake as its epicentre was located just below the city, resulted in 185 fatalities.

The damage caused by liquefaction on buildings and infrastructures was very impactant also for the life of the community that had to face a long and exhausting recovery process to regain normality. Although not being the only case of such a size, the 2010-2011 earthquake sequence in Christchurch (New Zealand) is probably the most impressive example of liquefaction induced damage over an urban environment. About 15.000 families lost their homes and 8.000 were permanently displaced, 70% of the buildings in Central Business District had to be demolished, 900.000 tons of liquefied soil were removed from the ground surface after the events (Tonkin & Taylor, 2016).

This project has received funding from the European Union's Horizon 2020 research and innovation programme under grant agreement No. 700748

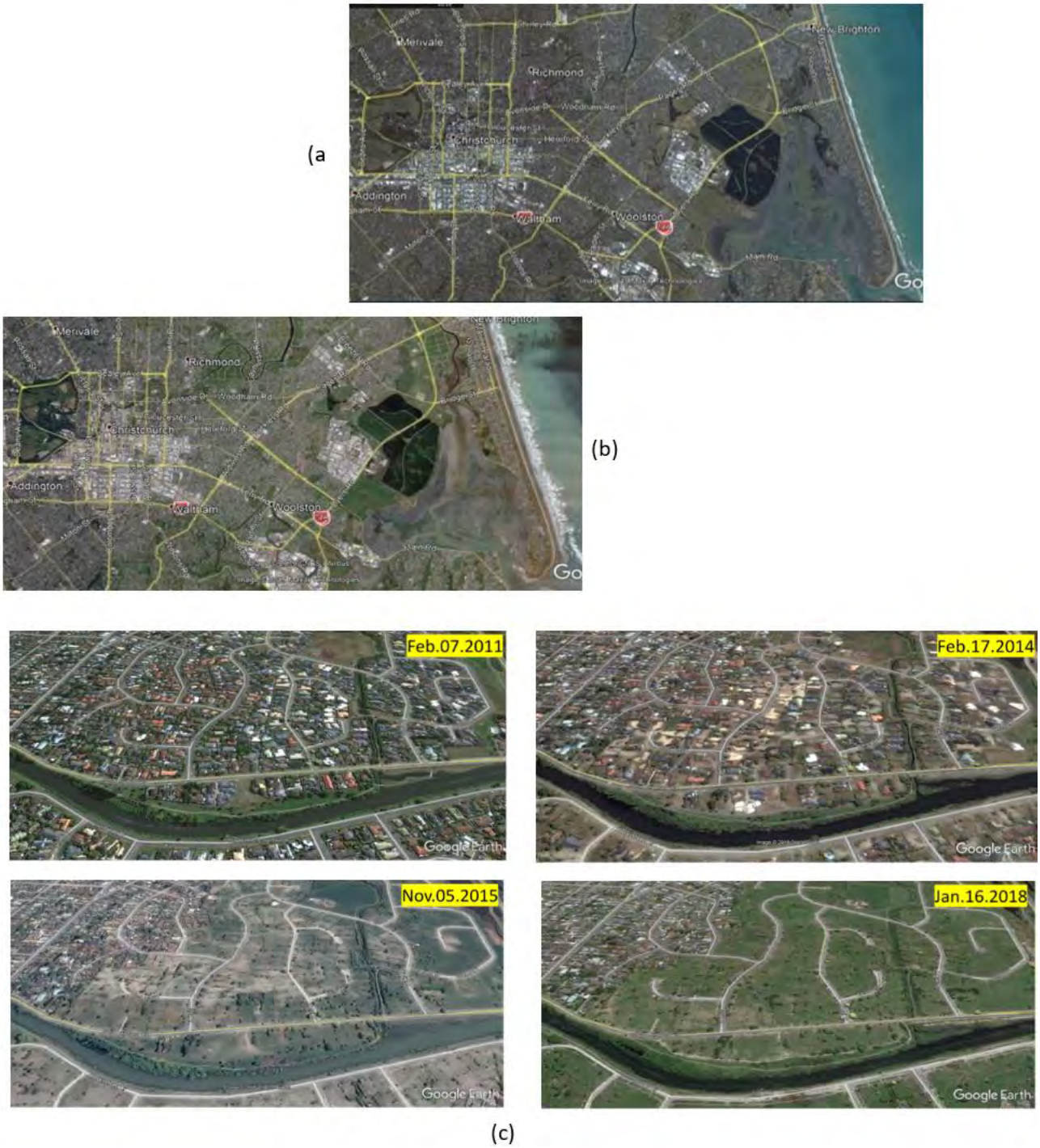

Figure 3-1 Overview of Christchurch before the earthquake sequence in 2010 (a) and after in 2019 (b) and evolution of landscape in the red zone of Christchurch across the February 2011 earthquake (c).

This project has received funding from the European Union's Horizon 2020 research and innovation programme under grant agreement No. 700748

Figure 3-2 a) differential settlement resulting in tilt and damage to residential house (Cubrinovski et al., 2012); b) Building on pile foundations in area of severe liquefaction showing large settlement of the surrounding soils relative to the foundation beams (Cubrinovski et al., 2011a); c) Effect of lateral spreading on the roadway (Goldsworthy, 2012); d) Flotation of pipe below causes the manhole to rise (Goldsworthy, 2012); e) Rotation of bridge abutments.

The geological and hydrogeological setting, (NZL Geologic Units Map **http://maps.gns.cri.nz**; http://data.gns.cri.nz/geology/; Brown & Weber, 1992) and the historical seismicity of the Region (http://www.geonet.org.nz) show that the probability of liquefaction triggering exist and it is not negligible.

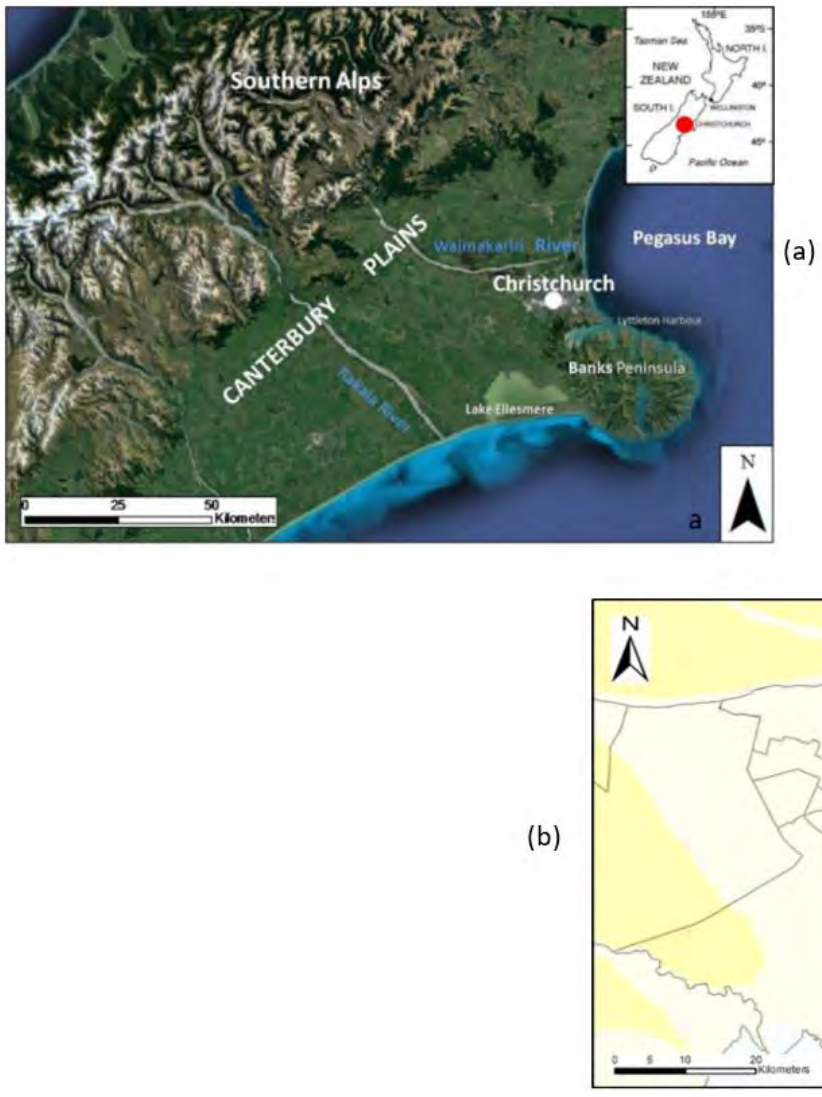

Figure 3-3 Overview of Christchurch the Canterbury Region (a); Geology of Christchurch City (b).

After the major earthquakes, several studies were promoted and a huge number of in-situ tests were carried out by several teams of geotechnical engineers in order to evaluate liquefaction vulnerability and to quantify the liquefaction-induced land damage and make estimate of damage to residential properties, public buildings, lifelines and more generally infrastructures. Such activity promoted the creation of the Canterbury Geotechnical Database (CGD), that Tonkin and Taylor company developed initially for the Canterbury Earthquake Recovery Authority (CERA) to manage the rebuild of Christchurch following the 2010/2011 Canterbury Earthquake Sequence "C.E.S.". Following the success of the Canterbury Geotechnical Database (CGD), the Ministry of Business, Innovation and Employment (MBIE) encouraged the development of the

New Zealand Geotechnical Database "NZGD" https://www.nzgd.org.nz, which also incorporates data previously held on the Auckland Geotechnical Database, which was initially set up by Watercare.

The NZGD is primarily aimed at providing more efficient access to geotechnical information and facilitating the data sharing between the private and public sectors. It can also be used for more strategic purposes such as assisting with natural disaster recovery, increasing resilience around New Zealand, catastrophe loss modelling, and informing land planning and regulatory processes.

At the date of May 2019, the NZGD database contained over 35 800 cone penetration test records, 18 700 boreholes, 1 000 piezometers with accompanying groundwater monitoring records, 6 000 laboratory test records (plus other data and maps) and it is constantly updated (Figure 3-4).

Figure 3-4 a) In May 2019, the NZGD database contained over 35 800 cone penetration test records, 18 700 boreholes, 1 000 piezometers with accompanying groundwater monitoring records, 6 000 laboratory test records (plus other data and maps) and it is constantly updated.

The information stored in the database is mostly a collection of raw data including scientific and engineering properties of the ground conditions rather than a comprehensive interpretation of the data, because the data is normally gathered, interpreted and conveyed to the client by individual geotechnical engineers. In addition to data sharing, the following benefits are provided:

- easy access to geotechnical information (provided by other stakeholders) and with minor costs;
- high-level assessments can be carried out for specific projects using information from the surrounding area to better inform the geotechnical profile prior to committing to more detailed studies;
- seismic ground performance data in Christchurch can be accessed for use as a benchmark for expected ground performance in similar geological settings, particularly areas with complex subsurface geological models;
- infrastructure providers can be more informed in their asset management: they can better target more vulnerable areas for strengthening, and, following an event, optimise the repair/replacement effort;

- sub-surface data can be provided to regulatory authorities and decision makers to enable them to make well-informed land planning decisions and determine the appropriateness of investment strategies and solutions;
- regulatory guidance can be prepared to assess the likely impact of new, or changes to existing, design guidelines and building codes;
- specialist contractors can assess opportunities for investing in specialist equipment and ground improvement construction techniques; quantity surveyors and estimators can be assisted in estimating appropriate foundation rebuilding costs so property owners can specify appropriate sum insured values for their insurance policies;
- improved catastrophe loss modelling for insurance and hazard management is enabled, while emergency response specialists are able to carry out appropriate scenario response activities.

Among the above outlined advantages, access to a such an extensive geotechnical dataset allows the scientific community to perform research studies that would not be normally possible due to time and budget constraints.

The CEBA Database

The Canterbury Earthquake Sequence also resulted in significant damage to the building structures, particularly in the central Christchurch. Therefore, the Christchurch City Council undertook a rapid damage survey of all types of buildings, defining two assessment levels, namely 1 and 2. In particular, immediately after the September 2010 and the February 2011 earthquakes, the Christchurch City Council (CCC) undertook post-earthquake building safety evaluation task as per the guidelines developed by New Zealand Society of Earthquake Engineering (NZSEE) and endorsed by the Department of Building and Housing (DBH, current Ministry of Business, Innovation and Employment, MBIE) [2]. The "Christchurch Eq RAPID Assessment Form" was designed and used to evaluate building damage and to place colour tags. Depending on the accessibility and results of Level 1 assessment, a colour tag was given to each building that advised on their occupational safety. The purpose of the rapid inspection was to quickly assess a building in order to identify its danger to the public safety. Subsequently, another survey form, the Detailed Engineering Evaluation (DEE) form, was used specifically for commercial and multi-storey residential buildings to collect details including structural, site and damage information. The "DEE" was issued to commercial and large buildings by the Canterbury Earthquake Recovery Authority (CERA) to ensure public safety, but particularly focused on the non-residential (commercial) and large (multi-unit/multistorey residential) buildings. A "Detailed Engineering Evaluation Summary Data" form, designed by DBH Engineering Advisory Group (EAG) was used to collect information about structures which may have been affected by the earthquakes.

3.2 Hazard assessment

The assessment of hazard for the city of Christchurch has been performed following the analyses described in the flow chart of Figure 3-5. According to this scheme, liquefaction hazard is given by the combination of seismic hazard and liquefaction susceptibility, that are the two subjects shown in the next paragraphs.

This project has received funding from the European Union's Horizon 2020 research and innovation programme under grant agreement No. 700748

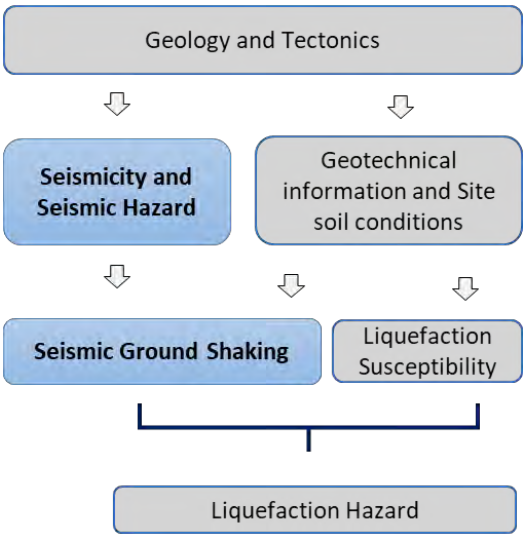

Figure 3-5 Flowchart describing the hazard assessment for the city of Christchurch.

3.2.1 Seismicity

The M_w6.2 February 2011 Christchurch Earthquake is one of the selected scenarios among the Liquefact Project case studies. Since its hypocentre was 10km SE to the Christchurch City Centre, it was the most destructive event of the Canterbury Earthquake Sequence which initiated with the M_w7.1 (September 2010) Darfield earthquake. Although this earthquake developed a larger magnitude, its epicentre was located approximately 44 km west of the Christchurch CBD and thus effects were less dramatic. Considering all the events, between September 2010 and September 2012, the Canterbury Seismic Sequence had 45 ML $\geq$ 5.0 and 3 ML $\geq$ 6.0 aftershocks (Figure 3-6 and Table 3-1). The characteristics of the main events are summarised in Table 3-2. Before the 2010 Darfield earthquake, the city of Christchurch was instrumented with a large network of strong motion stations. Within Christchurch there were seven SMSs as part of the National Strong Motion Network and nine as part of Canterbury regional strong motion network. Additionally, there were SMSs located in both Lyttleton (LPCC) and Kaiapoi (KPOC), all combined as part of the GeoNet project (GNS Science 2013). This network of SMSs recorded a vast database of strong ground motions during the Canterbury earthquake sequence. Within a year following the 22 February 2011 Christchurch earthquake, nine additional SMSs were installed in the Christchurch area as part of the National Strong Motion Network.

Table 3-1 Numbers of Canterbury region earthquakes from 4 September 2010 to 3 September 2012.

Magnitude (ML) Range	Number of events
7.0 and above	1
6.0-6.9	2
5.0-5.9	42
4.0-4.9	383
3.0-3.9	3921
Tot.	4341

Table 3-2 Canterbury Earthquake Sequence seismologic data (Quigley et al., 2016).

This project has received funding from the European Union's Horizon 2020 research and innovation programme under grant agreement No. 700748

Earthquake name and date (year month day hour) (UTC)	Latitude[a]	Longitude[a]	M_L[b]	M_w[b]	PGA horizontal (g)[c]	PGV horizontal (cm s^{-1})[c]	PGA vertical (g)[c]	Terrestrial area (km^2) with PGA ≥0.1[d]	Terrestrial area (km^2) with PGA ≥0.2[d]	Terrestrial area (km^2) with PGA ≥0.3[d]
M_w 7.1 Darfield earthquake (2010.09.03.1635)	−43.538	172.164	7.1	7.1	0.76	115	1.3	9230	3600	1300
October aftershock (2010.10.18.2232)	−43.626	172.564	5.1	4.8	0.28	16	0.21	221	36	0
Boxing Day aftershock (2010.12.25.2130)	−43.554	172.662	4.9	4.7	0.27	18	0.52	174	24	0
M_w 6.2 Christchurch earthquake (2011.02.21.2351)	−43.566	172.691	6.3	6.2	1.41	81	2.21	1700	630	260
February aftershock I (2011.02.22.0004)	−43.589	172.661	5.8	5.5	0.56	44	0.93	550	380	120
February aftershock II (2011.02.22.0150)	−43.590	172.634	5.9	5.6	0.75	29	0.69	700	380	180
April aftershock (2011.04.16.0549)	−43.613	172.760	5.3	5	0.68	32	0.48	280	127	25
June aftershock (2011.06.13.0101)	−43.568	172.753	5.6	5.3	0.45	28	0.69	860	240	100
M_w 6.0 Christchurch earthquake (2011.06.13.0220)	−43.564	172.743	6.4	6	1.54	102	1.14	1120	310	170
June 21 aftershock (2011.06.21.1034)	−43.599	172.525	5.4	5.2	0.26	11	0.62	494	112	25
December M_w 5.8 earthquake (2011.12.23.0058)	−43.486	172.796	5.9	5.8	0.31	30	0.98	550	95	0
December M_w 5.9 earthquake (2011.12.23.0218)	−43.530	172.743	6	5.9	0.44	44	0.39	740	200	80

[a] Epicentral latitude and longitude in decimal degrees.
[b] Earthquake Richter magnitude (M_L) and moment magnitude (M_w) from Geonet (www.geonet.org.nz).
[c] Processed vertical and geometric mean horizontal peak ground accelerations and velocities from Geonet time series and Bradley et al. (2014).
[d] Areas estimated using interpolation of recorded strong ground motions; method outlined in Bradley (2014); areal extents refer to terrestrial (includes onshore and estuary) environments only.

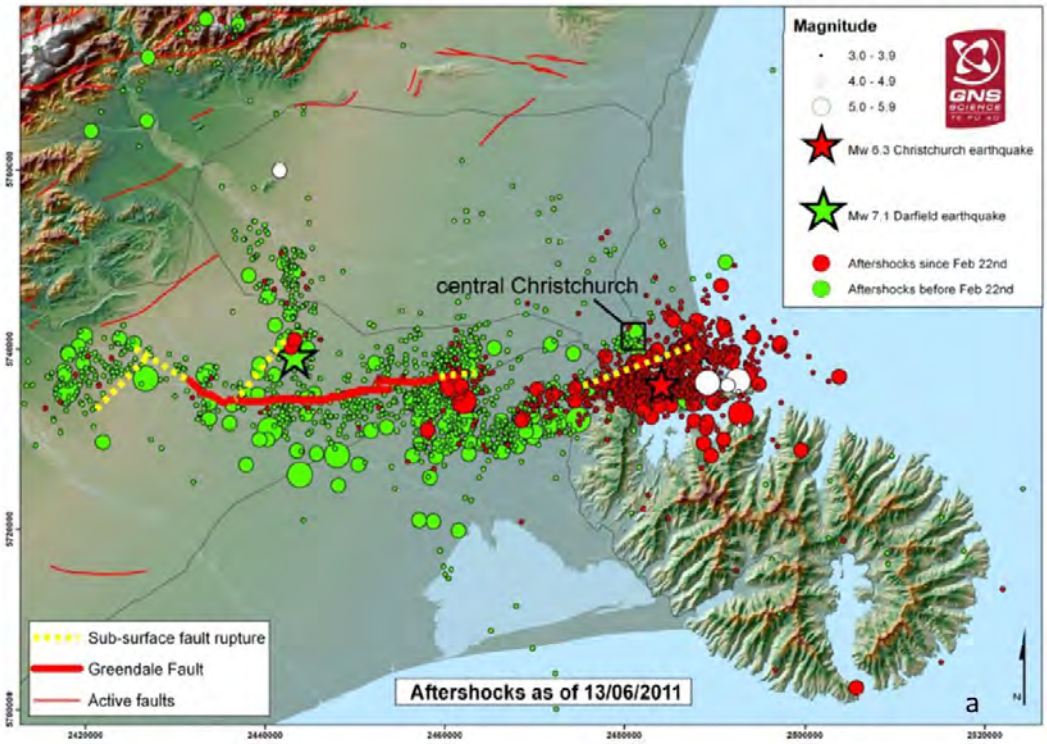

Figure 3-6 Epicenters and faults of the seismic events characterizing the 2010-2011 Christchurch Earthquake Sequence (as at June 2011). Projected surface locations of major blind faults in yellow and location of mapped surface ruptures in red.

For each of the main events of the 2010-2011 Earthquake Sequence, the spatial distributions of Peak Ground Acceleration estimated from ground motion records available in the New Zealand Geotechnical Database (e.g. contours of PGA were produced by O'Rourke et al. (Canterbury Geotechnical Database (2015) "Ground Motion", Map Layer CGD5170 - 30 June 2015, retrieved [date] from https://canterburygeotechnicaldatabase.projectorbit.com/.) for the main earthquakes, computing mean acceleration the two horizontal PGAs components at each recording station) are reported in Figure 3-7.

In the present study, the attention is focused on the event of February 22nd 2011 earthquake, for which the main seismic characteristics have been computed. Figure 3-8 reports the Peak Ground Acceleration (PGA) in the whole Canterbury plain.

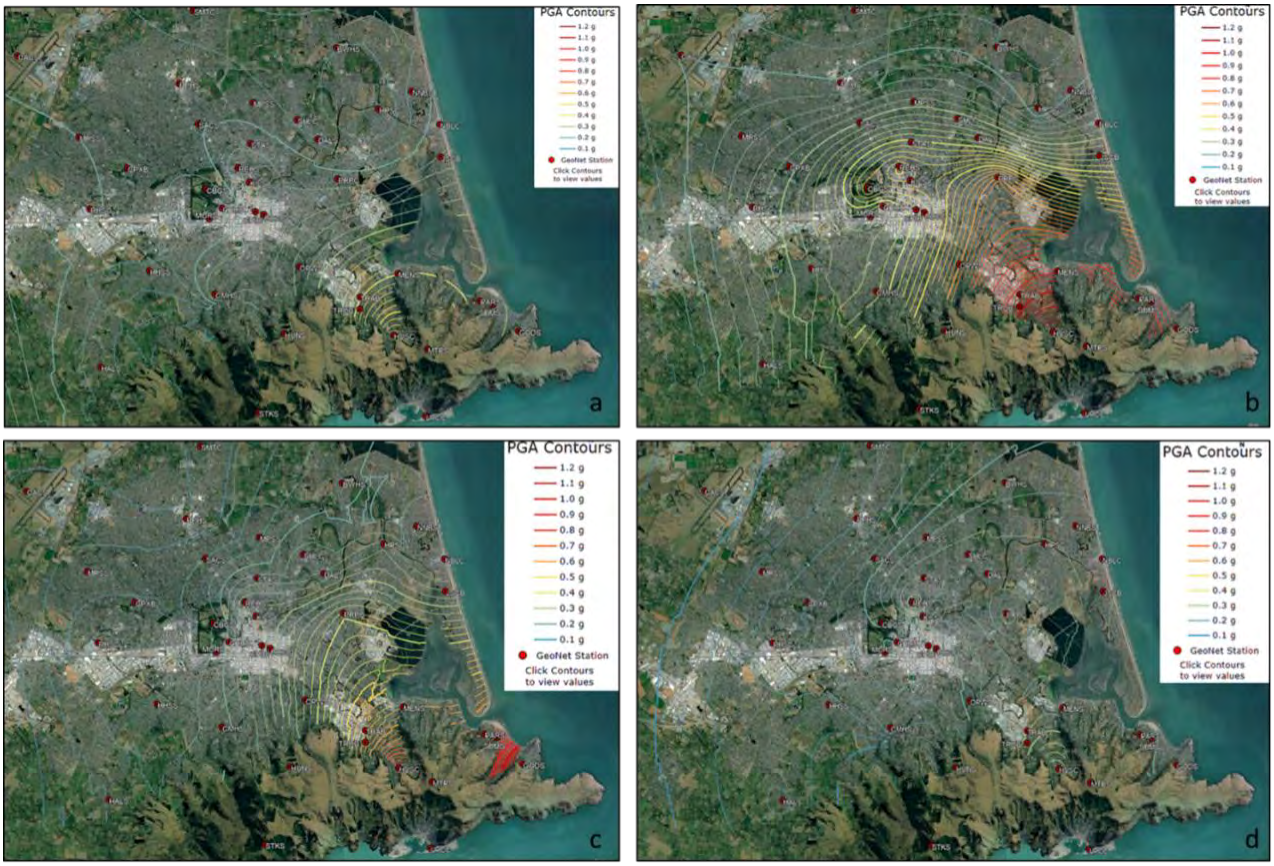

Figure 3-7 Spatial distributions of Peak Ground Acceleration estimated from recorded ground motion records a) September 2010 event; b) February 2011 event; c) June 2011 (Max event A and B); December 2011 (Max event A and B), Canterbury Geotechnical Database (2015) "Ground Motion", Map Layer CGD5170 - 30 June 2015, retrieved [date] from https://canterburygeotechnicaldatabase.projectorbit.com/.

To characterize the seismicity of Christchurch for probabilistic analyses, a generic site in Central Christchurch, which can be used for all the sites of interest in the city, was considered.

Four seismic scenarios (Fig. 3.8b), which return period ranges in 25 to 2500 years were selected and through interpolation (plus knowledge of the 'shape' of the hazard curve from the PGA and SA(2.0s)) the seismic IMs were calculated for each scenario.

This project has received funding from the European Union's Horizon 2020 research and innovation programme under grant agreement No. 700748

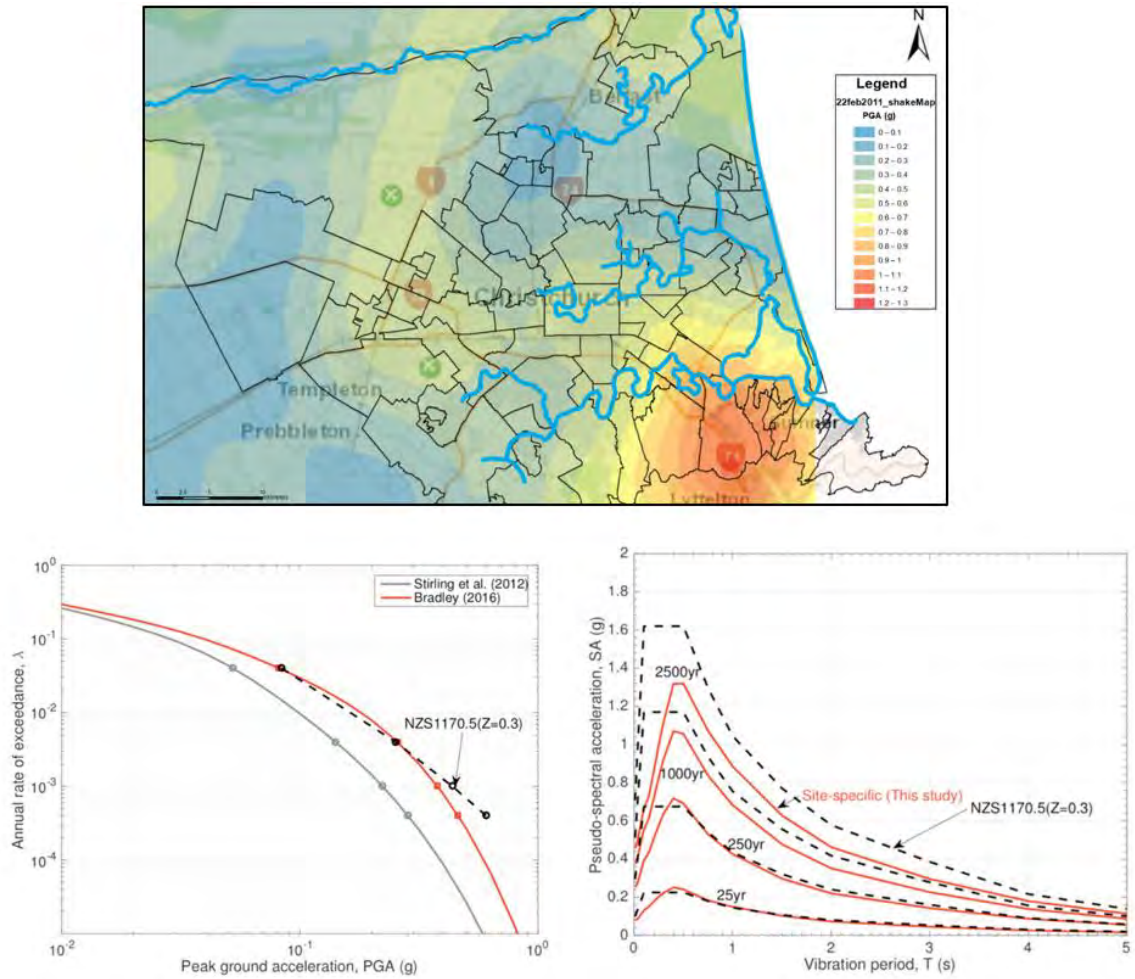

Figure 3-8 a) Spatial modelling of 22 February 2011 earthquake Peak Ground Acceleration, in GIS platform. (Data from O'Rourke et al. were used); b) PGA hazard curve and uniform hazard spectra (UHS) defined for sites in Central Christchurch (Bradley, 2016).

3.2.2 Liquefaction Susceptibility

The susceptibility analysis has been performed applying the criteria defined in the Work Package 3 of the Liquefact project (see Deliverable 3.3) to a total number of 8818 CPTs. The original data were taken from the NZGD, individually scrutinized, homogenised in their format to allow automatic processing. Thereafter data were filtered removing the profiles shallower than 10m and those not in accordance with the criterion defined in chapter 1 of this deliverable. The susceptibility criterion schematizes each subsoil profile to an equivalent three-layers model (the Equivalent Soil Profile ESP) identified by a thickness of crust and liquefiable layer and a mean Cyclic Resistance Ratio. The assimilation criterion, described in Figure 3-9, defines 22 equivalent soil classes, finding the best combination of H_crust, H_liq and CRR that give the lowest normed error. Such parameter will be used in future analyses to discriminate the profiles that can or cannot schematised with three-layers models.

This project has received funding from the European Union's Horizon 2020 research and innovation programme under grant agreement No. 700748

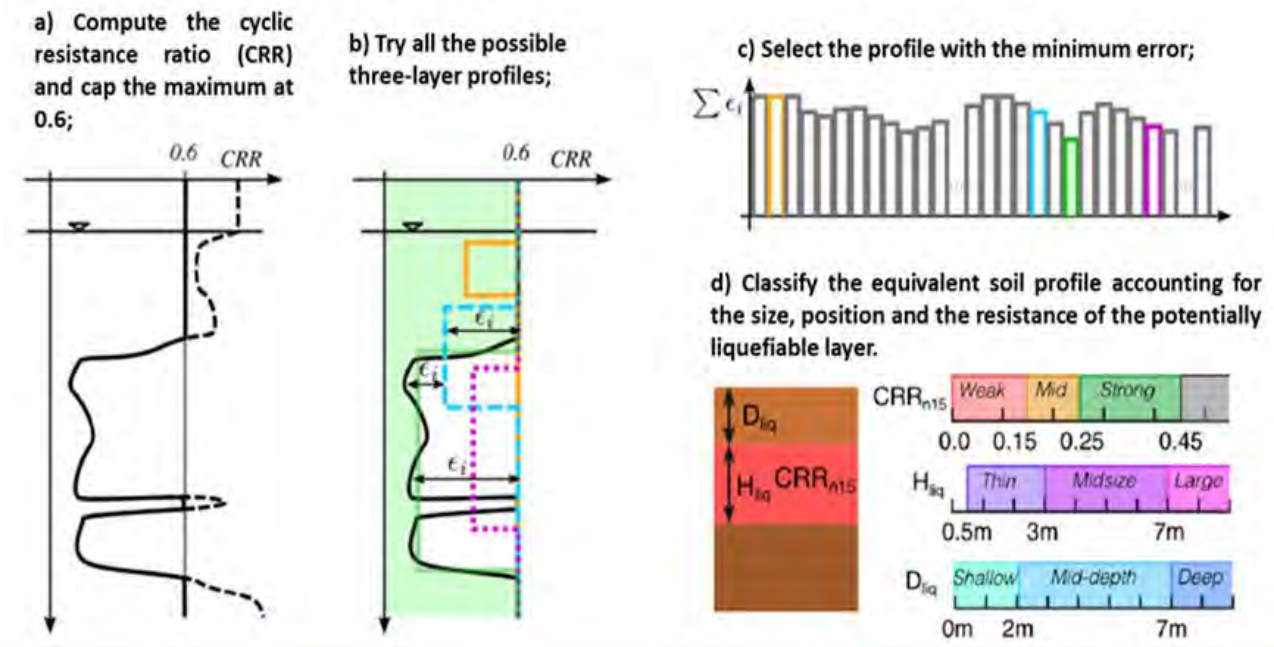

Figure 3-9 Assimilation criterion of CPT profile to an Equivalent Soil Profile.

Figure 3-10 shows the frequency distribution of the normed errors for the CPTs profiles examined in Christchurch. The fitting of soil profiles with a three layers ESP model that gives errors lower than 0.05 is considered as optimal; if the error is contained in the range 0.05-0.15 the fitting is considered acceptable; if the error is larger than 0.15 the fitting with the three layers model is not applicable. This last occurrence indicates the presence of multiple liquefiable layers separated by large non-liquefiable layers. Figure 3-10.a shows that over the total number of 8818 processed CPT profiles, only 106 (1.2%) gave errors larger than 0.15. However, the scattered position of these tests over the map (Figure 3-10.b) shows that the equivalence is rather affected by uncertainties linked to the execution and interpretation of the tests more than by local systematic variations of the stratigraphy. In all cases, engineering judgement is needed to focus on these tests and make a decision on the acceptance/rejection of the equivalence.

This project has received funding from the European Union's Horizon 2020 research and innovation programme under grant agreement No. 700748

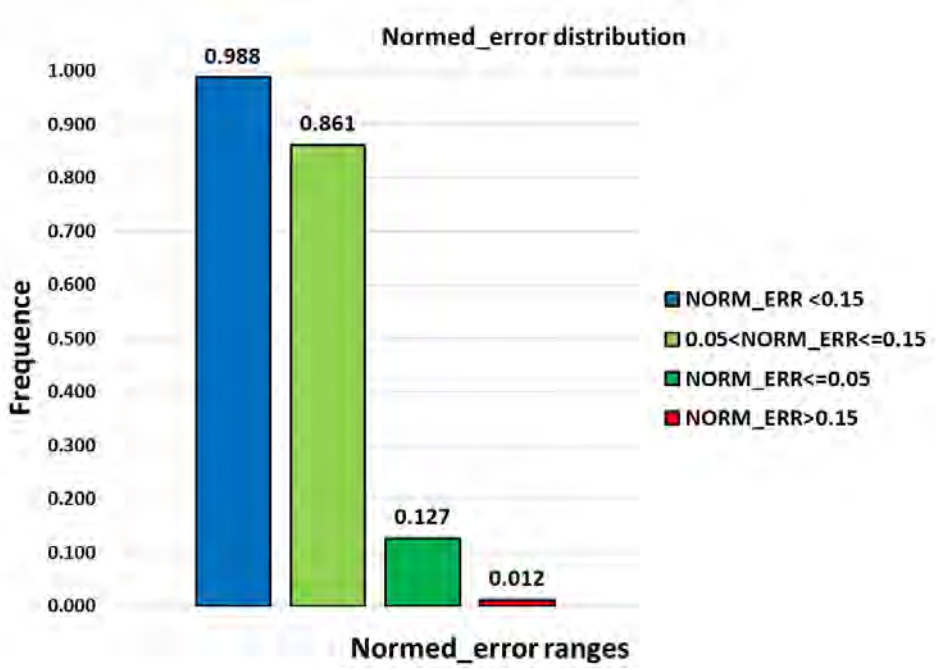

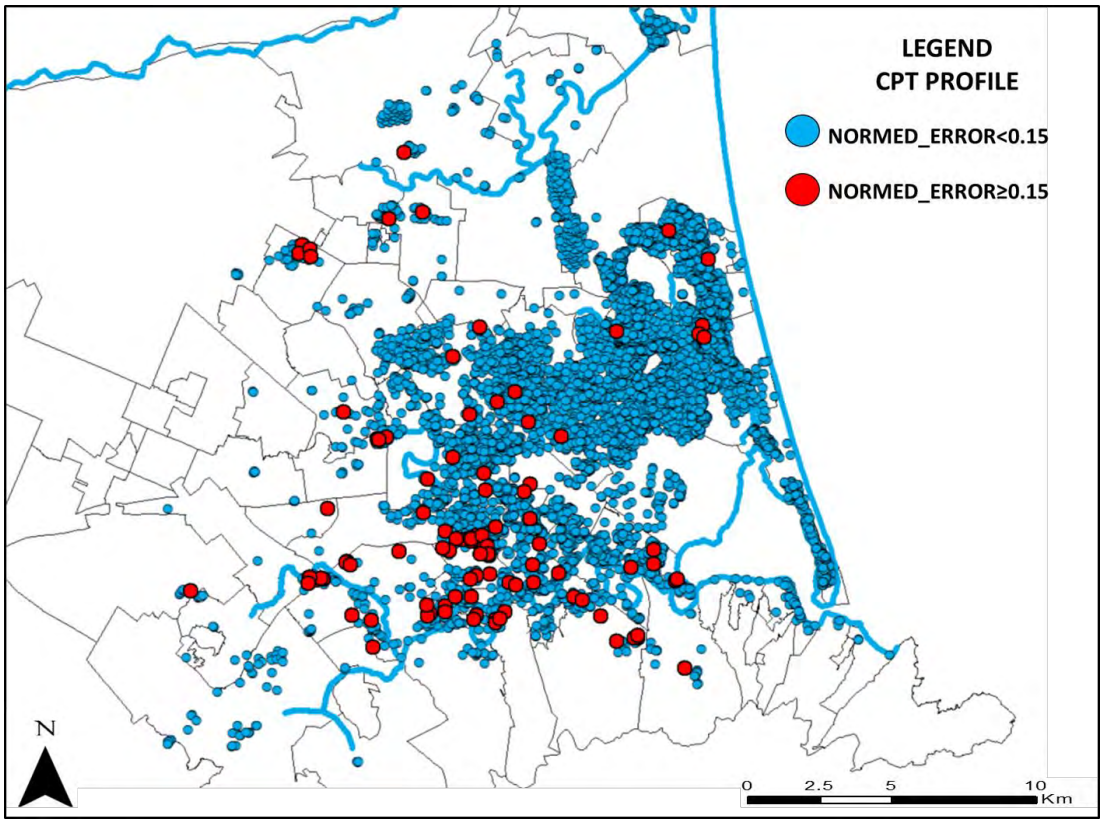

Figure 3-10 Histograms of the normed errors showing the equivalence of soil profile to the ESP model (a) and position on the map of Christchurch of the profiles with error>0.15.

This project has received funding from the European Union's Horizon 2020 research and innovation programme under grant agreement No. 700748

In addition to the above defined normed error that applies to all CPT tests independently on their depth, a Standardized Normed Error is introduced to homogenise this indicator referring to a standard depth of 20 m. In details, the error computed for CPT tests that reach depths lower than 20 metres has been amplified with the following relation to consider the influence of depth assuming statistically that the soil profile below the investigated depth is similar to the above portion.

$$Std\ Normed\ Err = Normed\ error * 20/Max\ depth$$

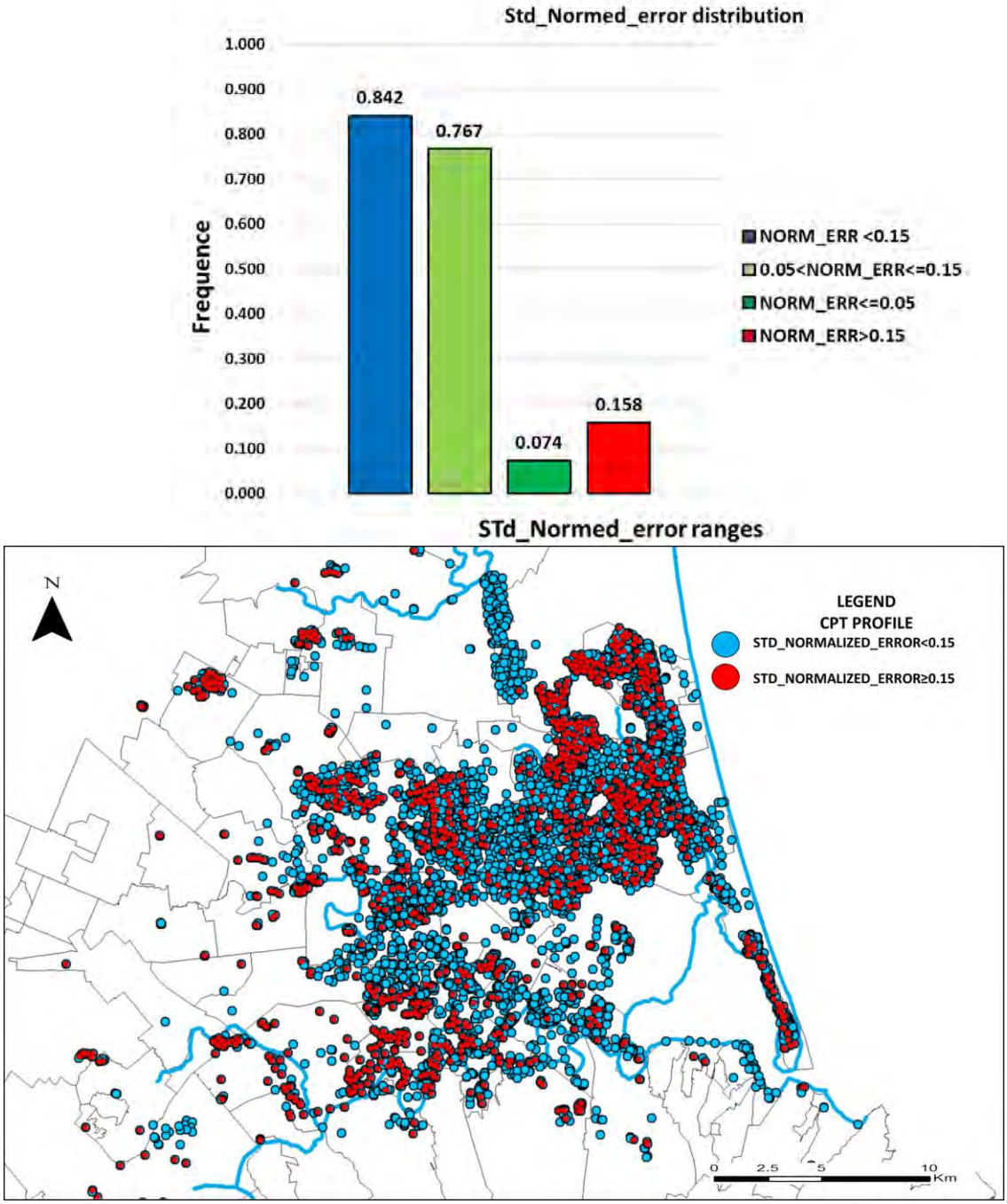

Figure 3-11 Histograms of the standardized normed error showing the equivalence of soil profile to the ESP model (a) and position on the map of Christchurch of the profiles with standardized normed error>0.15.

This project has received funding from the European Union's Horizon 2020 research and innovation programme under grant agreement No. 700748

The detailed analysis of three typical profiles is shown in the next table and figures to understand the importance of normed errors. Table 3-3 shows that the three selected profiles are representative of the above defined classes (with normed errors respectively N.E<0.05, 0.05<N.E.<0.15, 0.15<N.E.). In the table the LSN indicator (computed for the earthquake scenario of Feb 22nd 2011) has been added. As can be seen, the values computed on the real and equivalent soil profiles are similar when the standard error is lower than 0.05, while their difference is intolerable for larger standard normed errors.

Table 3-3 Example of analysis for three typical subsoil profiles with different normed errors.

LogID	Max_depth_m	GWT[m]	PGA[g]	H_crust[m]	H_liq[m]	CRR	Class	LSN_direct	LSN_esp	normed_error
912	38.1	1.71	0.50	1.71	8.20	0.161	MLS	33.6	36.6	0.016
2	40.5	2.51	0.54	7.51	4.80	0.371	SMX	11.2	1.1	0.111
220	24.3	1.06	0.45	9.26	10.60	0.131	WLD	55.2	18.6	0.175

Figure 3-12 shows the analysis of CPT test for the profile with the low error (0.016) catalogued in the present study as #912. Here the ESP equivalence is largely acceptable and the characterization of the soil profile with three layers is appropriate as there is only one and easily recognizable liquefiable layer. The profile of the Factor of Safety against Liquefaction (FSL) highlights the presence of a continuous shallow sandy layer with FSL<1, extended up to a depth of 10 m. Strata having FSL<1 can be also recognised at different depths, but they are rather scattered and do not represent continuous layers. Therefore, this profile is adequately described with a crust thickness (H_crust) equal to 1.71 m, a thickness of the liquefiable layer (H_liq) equal to 8.2 m and an average CRR of 0.16. According to the ESP method, the CPT 912 is classified as MLS, since it is characterized by a large (thickness >7m), shallow (depth <2m) liquefiable layer with an intermediate liquefaction (CRR=0.161 i.e. in the range 0.15-0.25).

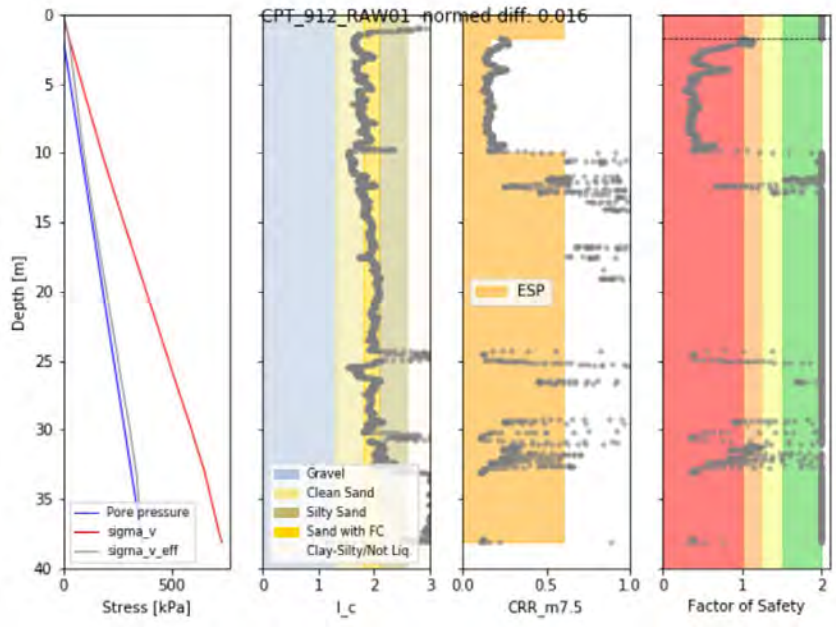

Figure 3-12 CPT profile #912, for which the equivalent soil profile method is consistent with the real soil profile (St.N.E.<0.05).

This project has received funding from the European Union's Horizon 2020 research and innovation programme under grant agreement No. 700748

The results are still acceptable but with a lesser extent, in the case of CPT catalogued with #2, characterised by a standard normed error of 0.111 (Figure 3-13). Here two distinct liquefiable layers can be identified within the first 20 m, an upper one at 7-12 meters depth and a lower at 15-20 metres depth. A non-liquefiable layer around 2-3 meters thick can be recognised between them. In the ESP method, the second layer is not considered and the CPT_002 is classified as SMX type: strong since it is characterized by a relatively high CRR (0.25-0.5) and midsize because the liquefiable thickness H_{liq} is around 5 meters.

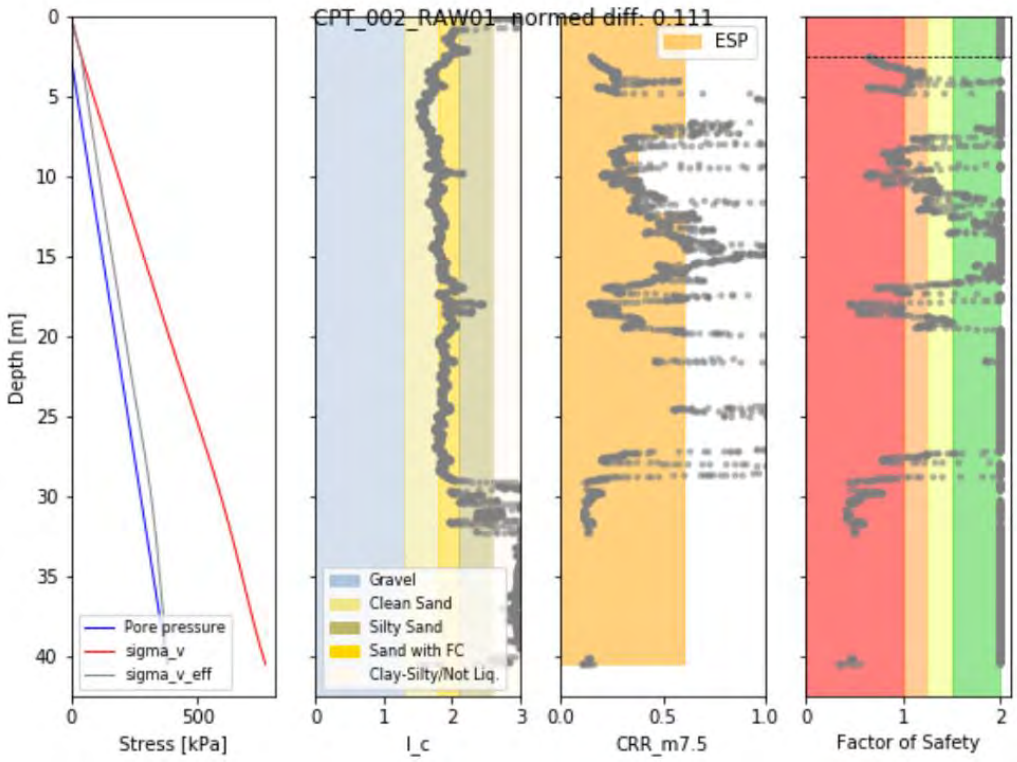

Figure 3-13 CPT profile #2 showing an average agreement between the equivalent soil profile and the real one (0.05<St.N.E.<0.15).

This project has received funding from the European Union's Horizon 2020 research and innovation programme under grant agreement No. 700748

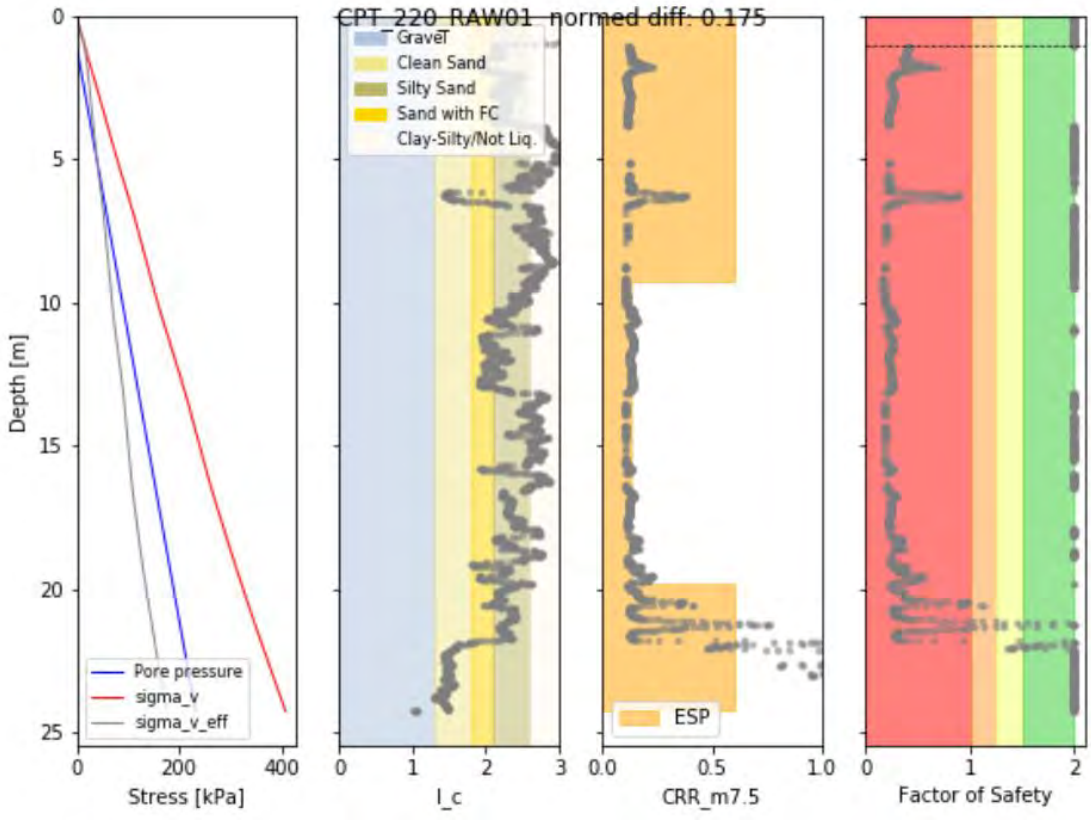

Figure 3-14 CPT profile #220 showing an example of profile where ESP equivalence is not acceptable, and a specific engineering evaluation is required (0.15<ST.N.E.).

Finally, the third example (CPT #220) concerns a test where the equivalence with the ESP is not acceptable and further analyses for liquefaction assessment are needed (Figure 3-14). In fact, the results of such CPT are characterized by an average error of 0.175. Here the profile is classified as WLD according to the presence of a large weak liquefiable layer, but the equivalence method does not account for the presence of a thick shallow liquefiable layer extended in the first 2-4 m of depth from the ground. Moreover, the same CPT profile highlights the presence of a second liquefiable lens 5-7m deep. The ESP method gives a thickness of the crust (H_{crust}) larger than 9 meters, that implies a deep liquefaction phenomenon. The large normed error clearly identifies a poor fit and engineering judgement would be required to generate a suitable equivalent profile.

The equivalent soil profile method is implemented into Liquefact toolbox to evaluate susceptibility. Figure 3-15 shows the results of this analysis over the city of Christchurch. It can be observed that the most of zones which experienced liquefaction during the Christchurch Earthquake Sequence are assessed by the ESP method as weak/mid resistant profiles (yellow and red areas in the map of Figure 3-15).

This project has received funding from the European Union's Horizon 2020 research and innovation programme under grant agreement No. 700748

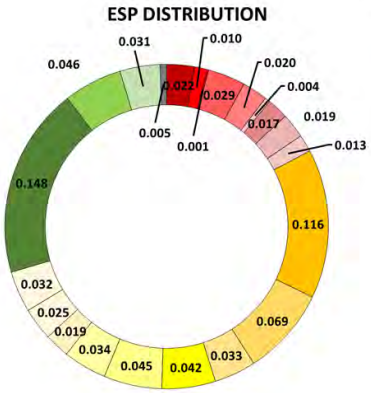

WLS WLM WLD WMS WMM WMD WTS WTM WTD MLS MLM
MLD MMS MMM MMD MTS MTM MTD SLX SMX STX RXX

		WEAK	%	MID	%	STRONG	%	RESIST	%
LARGE	Shallow	WLS	2.15	MLS	11.59	SLX	14.84	RXX	0.51
	Mid.	WLM	1.00	MLM	6.87				
	Deep	WLD	0.11	MLD	3.25				
MIDSIZE	Shallow	WMS	2.91	MMS	4.17	SMX	4.56		
	Mid.	WMM	1.98	MMM	4.52				
	Deep	WMD	0.40	MMD	3.38				
THIN	Shallow	WTS	1.66	MTS	1.94	STX	3.12		
	Mid.	WTM	1.92	MTM	2.54				
	Deep	WTD	1.34	MTD	3.20				

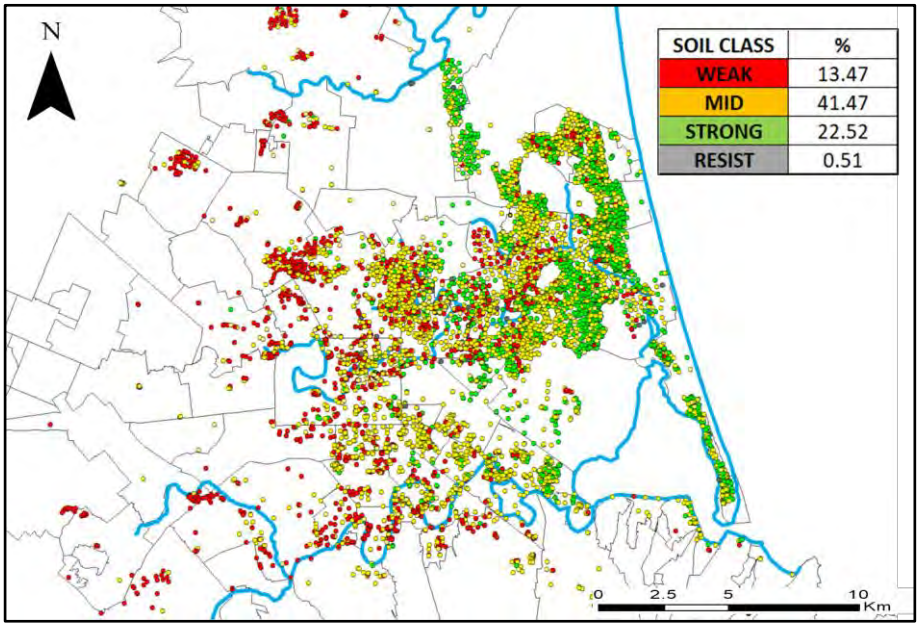

Figure 3-15 Statistical distribution of the Equivalent Soil Profile in Christchurch and overview of the spatial distribution of subsoil classes.

3.2.3 Mapping of liquefaction severity indicators

The hazard analysis has been based on the evaluation of some of the most widely adopted liquefaction severity indicators, namely LPI (Iwasaki et al., 1978), w (Zhang et al., 2002), LSN (Van Ballegooy et al., 2014) . It has been carried out over the whole territory of Christchurch considering the most damaging event of the 2010—2011 sequence, the (Mw 6.2) 22 February 2011 Christchurch earthquake. The factor of safety has been evaluated by applying the Boulanger & Idriss (2014) procedure, adopting a cutoff equal to 2.6 to the soil class indicator I_c as suggested for the regional assessment of liquefaction susceptibility by Tonkin & Taylor (2013 – Appendix A). In addition to the traditional "LPI" index, the Ishihara inspired "LPI_{ISH}" (Maurer, 2014) has also been calculated.

Before computing indicators, a filter was applied to the dataset of CPT profiles removing those not consistent with the spatial trend (outlier) in accordance with the procedure described in Chapter 1 (Figure 1-6). Then

the values of all indicators were computed correspondingly to the CPT positions and interpolated with geostatistical analyses to obtain maps covering the territory. Taking advantage of the possibility given by the geostatistical analysis to estimate uncertainty, the standard error distribution was studied and the area affected by errors larger than 25% have been removed from the present analysis (and represented with grey colour).

The maps of different indicators are reported in Figure 3-16, Figure 3-17, Figure 3-18 and Figure 3-19. Although with difference from each other, all maps highlight a heterogeneous distribution of values over the territory area with a stronger concentration of potentially liquefiable layers along the end portions of the (North East and South East portions). This trend reflects the geological and hydrogeological features of the territory, consisting of alluvial deposits of various composition, but having major sandy components along the watercourses.

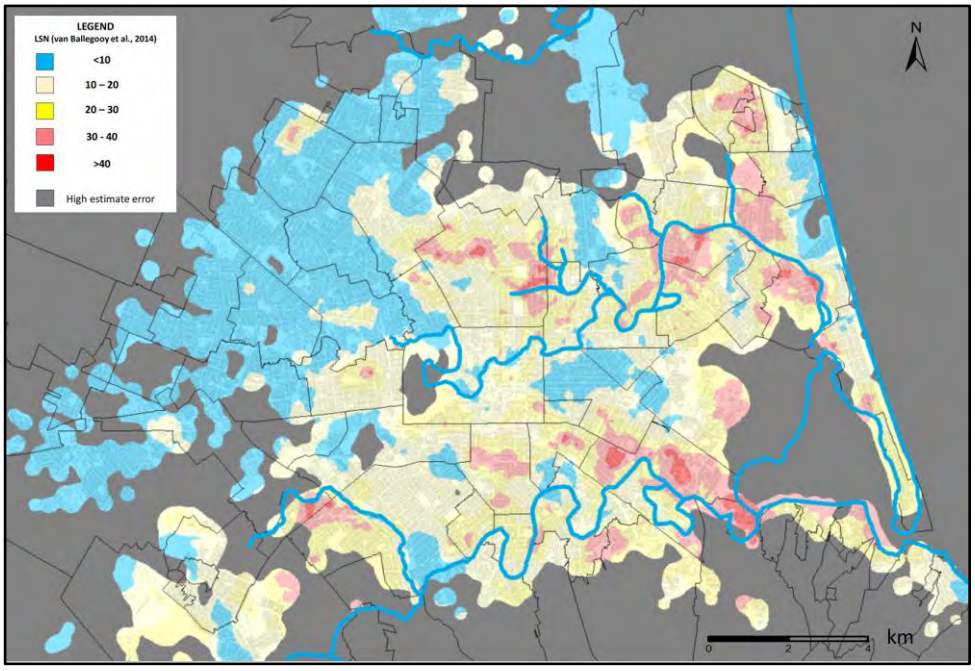

Figure 3-16 Geostatistical interpolation of "LSN" on the entire territory of Christchurch; estimate error map was overlaid to the indicator Map to cut the areas where knowledge is not adequate.

This project has received funding from the European Union's Horizon 2020 research and innovation programme under grant agreement No. 700748

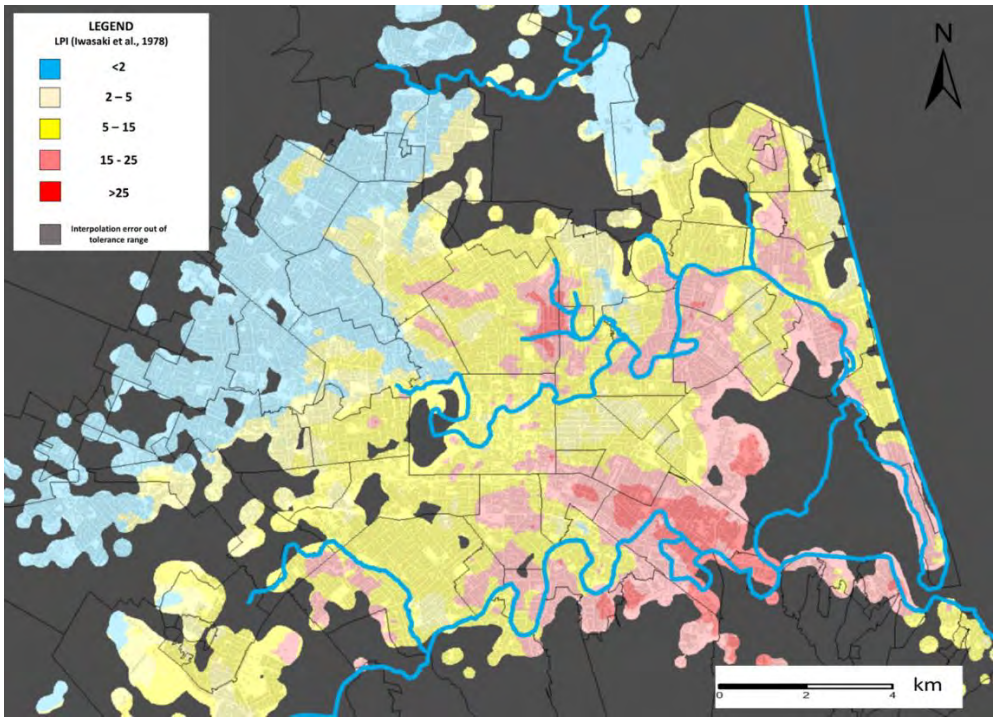

Figure 3-17 Geostatistical interpolation of "LPI" on the entire territory of Christchurch; estimate error map was overlaid to the indicator Map to cut the areas where knowledge is not adequate.

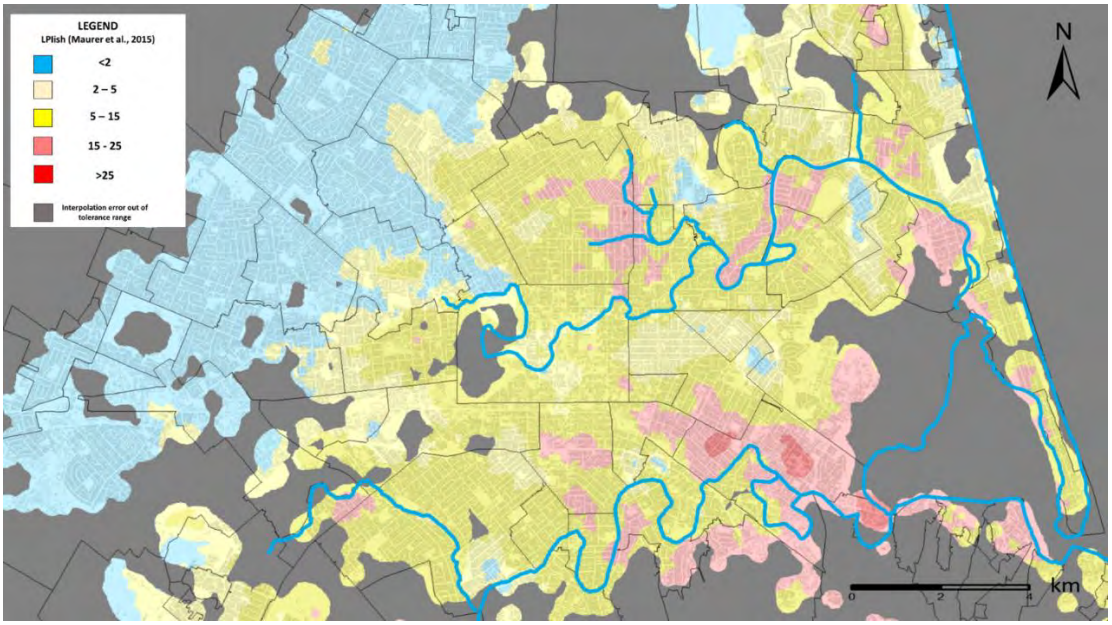

Figure 3-18 Geostatistical interpolation of "LPIish" on the entire territory of Christchurch; estimate error map was overlaid to the indicator Map to cut the areas where knowledge is not adequate.

This project has received funding from the European Union's Horizon 2020 research and innovation programme under grant agreement No. 700748

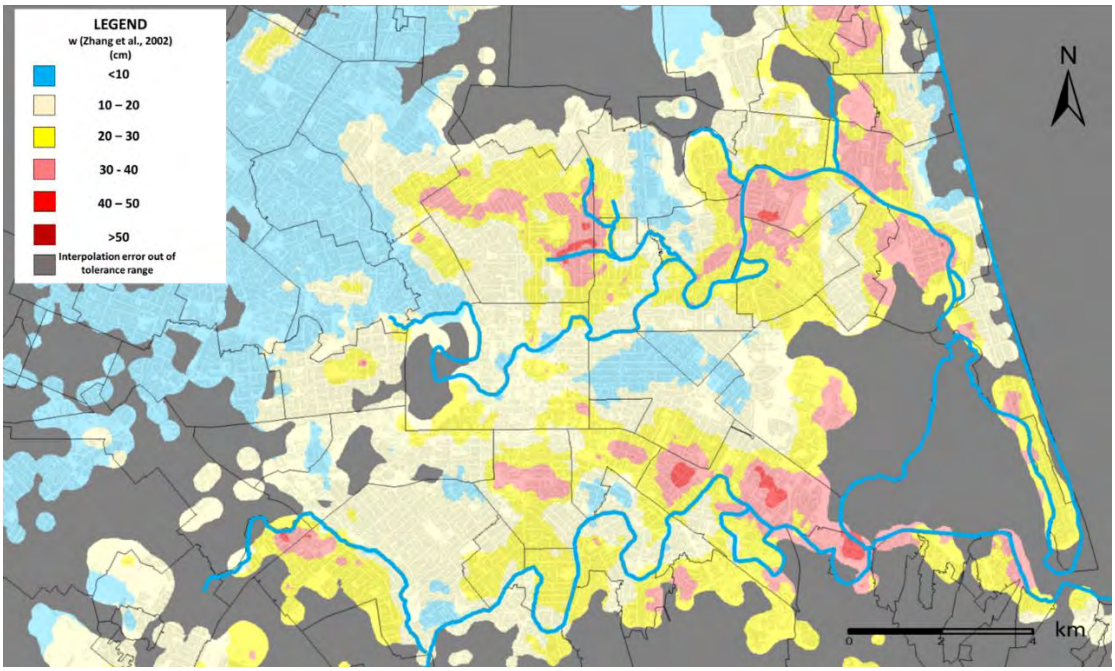

Figure 3-19 Geostatistical interpolation of liquefaction-induced 1D settlement "w" on the entire territory of Christchurch; estimate error map was overlaid to the indicator Map to cut the areas where knowledge is not adequate. Survey of liquefaction-induced ground damage.

Following the major Canterbury earthquake events, a survey of damage to land and dwelling foundation was undertaken as part of the coordinated response by the agencies of the NZ government. The mapping of liquefaction-induced land damage was carried out immediately after the September 2010, February 2011, and June 2011 earthquakes to assess the extent and severity of the surface effects. Observations were categorized according to the quantity of ejected material observed on the ground surface and to the presence/absence of cracks and lateral spreading. Each of these three categories was further subdivided according to its severity. In particular, the map of land damage recorded the incremental effects of earthquakes. The blue (damage level 1) and green areas (damage level 2, only shaking-induced) represent zones where no liquefaction was observed; yellow areas are characterized by minor to moderate sand ejecta and cracks, but no lateral spreading (level 3 of damage), while in the red zones (level 4 of damage) severe liquefaction, including major cracks and lateral spreading, occurred.

This map only identified phenomena that were visible on the ground surface at the time of inspection. It must thus be warned that liquefaction might have occurred at depth, without evidences on the ground surface, and that some traces of liquefaction might have been removed before the inspection. In fact, removed material was identified with aerial photographs taken a day or two after the earthquake. Figure 3-20 shows that the most severe liquefaction evidences, in terms of quantity of sand ejecta, ground subsidence and lateral movements occurs along the northern watercourse (Avon river) and along the southern sea shoreline. As a general comment from this overview, the effects of liquefaction tend to stronger near the rivers and to disappear when moving aside, although it must be considered that the watercourses might have moved with time in the plain.

This project has received funding from the European Union's Horizon 2020 research and innovation programme under grant agreement No. 700748

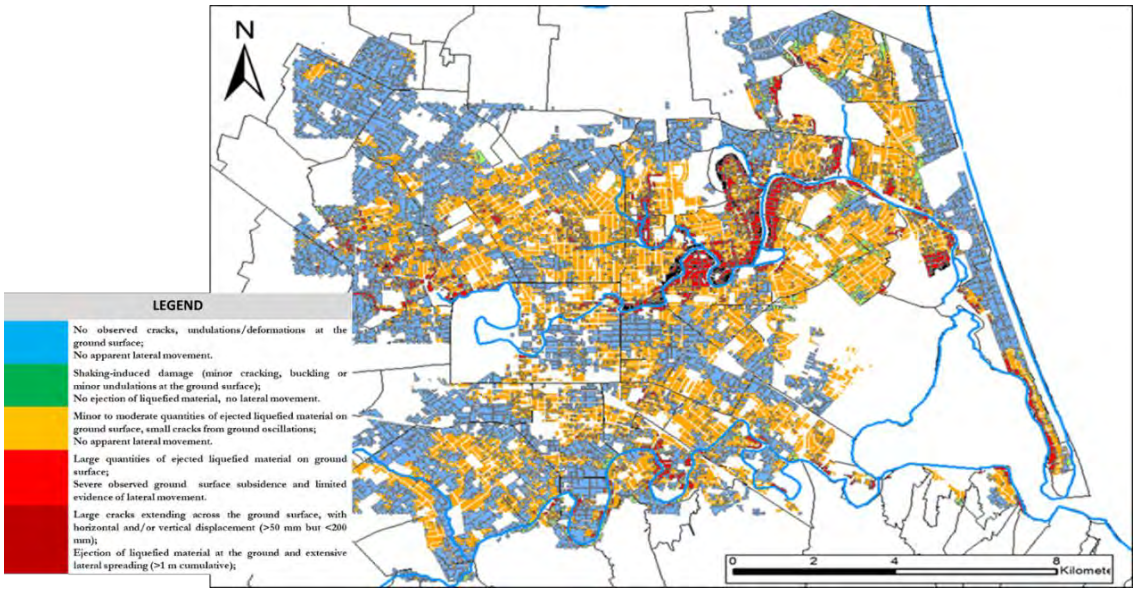

Figure 3-20 Liquefaction and Lateral Spreading Observations from Canterbury Geotechnical Database (2013). Map Layer CGD0300 - 22 September 2016, retrieved [date] from https://canterburygeotechnicaldatabase.projectorbit.com/.

3.2.4 Validation of Liquefaction Severity Indicators

The liquefaction severity indicators are here validated for the February 2011 (M_w 6.2) earthquake comparing the prediction obtained from each CPT profile with the damage level corresponding to the same position after the earthquake (Figure 3-21). According to the criterion adopted for validation, described in chapter 1 (Kongar et al., 2015), punctual values of the liquefaction severity indicators have been computed at each CPT location and the values have been compared with the event. Concerning the latter, yellow and red areas in Figure 3-20 represent zones affected by liquefaction (positive event). In the validation test, threshold values have been varied between the minimum and maximum observed values and the Receiver Operator Curve has been built (Kongar et al., 2015). Then the area under the curve AUC is calculated, by combining the True Positive/Negative Ratio and the False Positive/Negative Ratio. Finally, the Mathews Correlation Coefficient has been evaluated to identify the optimal treshold of each indicator in liquefaction-induced ground damage prediction.

This project has received funding from the European Union's Horizon 2020 research and innovation programme under grant agreement No. 700748

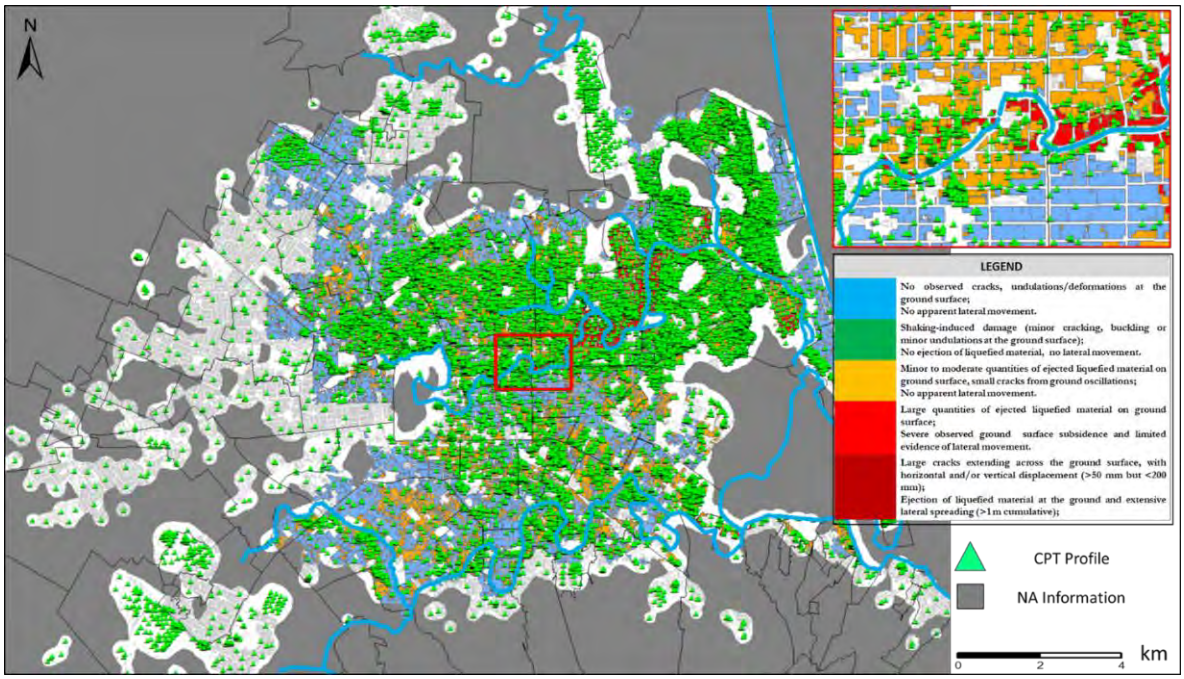

Figure 3-21 Map of liquefaction ground damage superposed to the location of CPT tests.

The results of this analysis, reported in Figure 3-22, show a fairly good predictive ability of all indicators, with minimal differences among the different methods. However, one of the critical issues points of the simplified analysis based on indicators is its representativeness in case of multiple liquefiable alternated with non-liquefiable layers. As pointed out by Cubrinovski and Van Ballegooy (2017), the dense alternation of liquefiable and non-liquefiable layers creates the conditions for a more complex dynamic response (called system response by the authors) of the deposit, where liquefaction does not affect all layers, as postulated by the indicators, but affects selectively some of them and propagates with time to closer layers. In the further step of the analysis a distinction has been made among the CPT tests considering only those fulfilling the equivalence criterion defined by the Equivalent Soil Profile (Deliverable D7.3.3 of the present project). In particular, a threshold of the normed error equal to 0.05 has been fixed, and the analysis has been repeated only for the CPT tests that can be assimilated to a three layer.

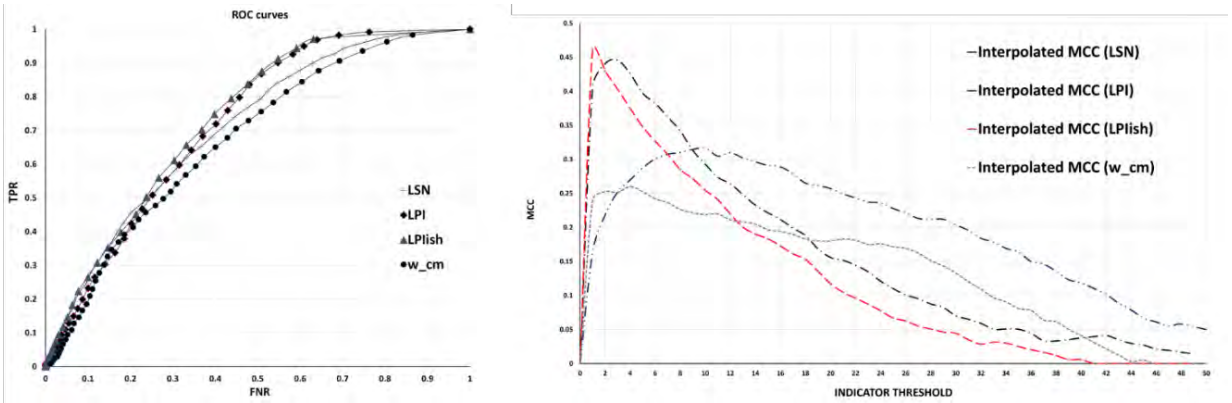

This project has received funding from the European Union's Horizon 2020 research and innovation programme under grant agreement No. 700748

INDICATOR	AUC	β	OPTIMAL THRESHOLD
LPI	0.74	0.491	≈3
LPIish	0.75	0.655	≈1-2
W (cm)	0.69	0.801	≈5
LSN	0.72	0.431	≈10

Figure 3-22 Roc curves and MCC after geostatistical error filtering.

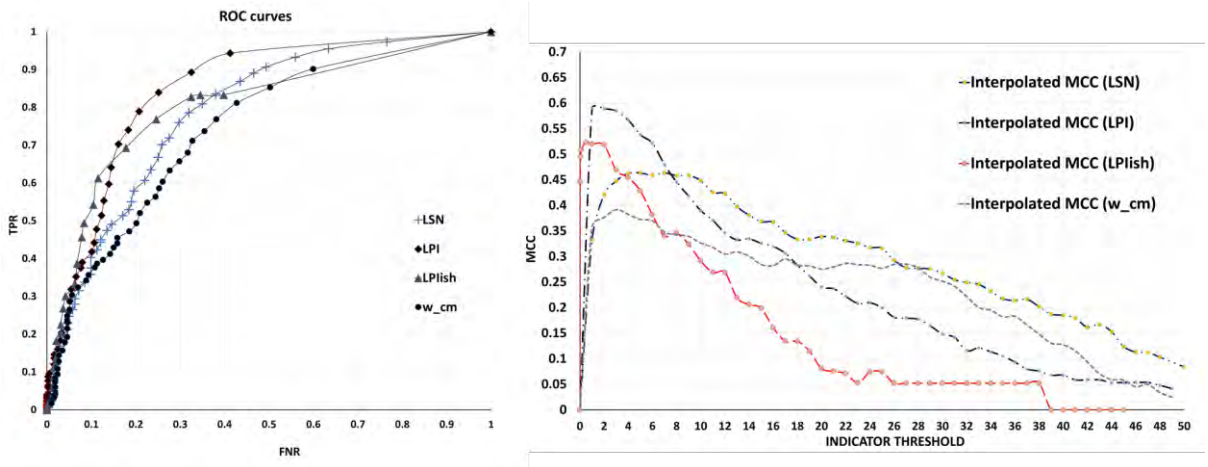

INDICATOR	AUC	β	OPTIMAL THRESHOLD
LPI	0.87	0.396	≈3-5
LPIish	0.80	0.633	≈2
W (cm)	0.77	0.357	≈3-5
LSN	0.80	0.301	≈8-10

Figure 3-23 Roc curves only for CPT tests consistent with the three-layers profiles.

Out of the entire database, around 1000 profiles (corresponding to the 13%) with a normed error< 0.05 have been selected. The repetition of the binary test considering only these profiles shows a remarkable improvement of the performance of traditional liquefaction severity indicators. It is also interesting to note that the optimal threshold values for each indicator, i.e. those better defining the prediction of positive/negative event, are consistent with the typical values defined by the authors of each method. Therefore, this analysis confirms the validity of all methods for the subsoil stratigraphy where a unique liquefiable layer can be identified.

This project has received funding from the European Union's Horizon 2020 research and innovation programme under grant agreement No. 700748

3.3 Building vulnerability and Damage Assessment

Out of the entire Christchurch building portfolio, through data provided by the University of Canterbury, around 6 000 buildings were characterized by collecting all the information required in Risk Assessment Procedures (i.e. ID, Location, Geometry, Model Building Type, Number of storeys, Use) (Figure 3-24).

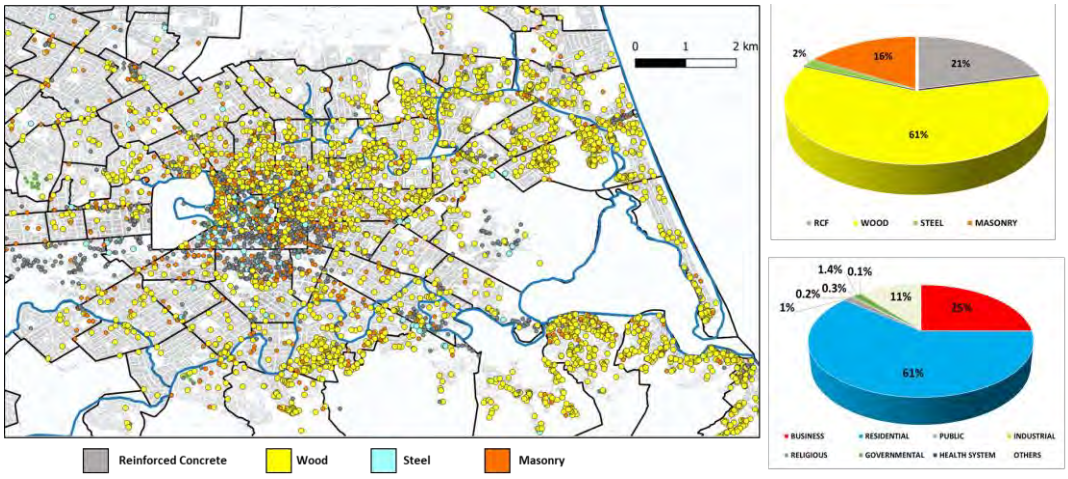

Figure 3-24 Distribution of the available building typologies over the entire Christchurch area. Pie diagrams show the percentage of each model building type and their use.

In addition to the buildings Database, a post-earthquake damage survey database was developed by applying the van Ballegooy et al. (2014) classification which distinguish the severity of liquefaction induced building damage based on the measured settlements. This information was collected from data stored in the CEBA Database which includes both post-earthquake rapid surveys and Detailed Engineering Evaluation (DEE).

In fact, immediately after the February 2011 earthquake, the Christchurch City Council (CCC) undertook post-earthquake building safety evaluation task as per the guidelines developed by New Zealand Society of Earthquake Engineering (NZSEE) and endorsed by the Department of Building and Housing (DBH, current Ministry of Business, Innovation and Employment, MBIE). The "Christchurch Eq RAPID Assessment Form" was designed and used to evaluate building damage and to place colour tags. The purpose of the rapid inspection was to quickly assess a building in order to identify its danger to the public safety. Following the rapid assessment, a "Detailed Engineering Evaluation" process, was issued to commercial and large buildings by the Canterbury Earthquake Recovery Authority (CERA), which purpose was to ensure public safety focused on the nonresidential (commercial) and large (multi-unit/multistorey residential) buildings.

3.3.1 Evaluation of liquefaction induced settlements on buildings

For the February 22nd 2011 seismic scenario, the potential of liquefaction-induced building damage in the area of Christchurch was assessed through three analytical procedures, namely: Karamitros et al. (2013), Bray and Macedo (2017) and Bullock et al. (2018).

Karamitros et al. (2013) gives a simplified analytical formula for the computation of the seismic settlements of strip and rectangle footings resting on a clay crust overlying a liquefiable layer, while Bray and Macedo (2017) proposed a method to evaluate the shear-induced building settlement (Ds) due to liquefaction below the building by combining in-situ observation, experimental tests and numerical analyses. After interpolating with a non-linear regression and latent variable analysis the results of an extensive fully coupled three-dimensional numerical parametric study of soil–structure systems, Bullock et al. (2018) presented a comprehensive predictive relation for the settlement of shallow-founded structures on liquefiable ground during earthquakes.

Intensity Measures and main features of the selected mechanical-based procedures are summarized in the following table.

Table 3-4 Methods adopted for the calculation of settlements.

INDEX	REFERENCE	IM	SUBSOIL	BUILDING
ρ	Karamitros et al., 2013	$a_{max}\,T^2 N = \pi^2 \int_{t=0}^{N\cdot T} \lvert v(t)\rvert dt$	Three-layer	Foundation bearing pressure
Ds	Bray and Macedo, 2017	CAVdp, Sa1	Three-layer	Building geometry, depth and contact pressure of foundation
Sadj	Bullock et al.,2018	CAV	Multi-layer Low/high permeability cap	Building geometry, Inertial mass, foundation embedment depth, foundation contact pressure

Aimed at applying such formulas, a database was created considering the footprint dimensions of each building, the number of storeys; the crust and liquefiable layer thickness, in addition to the mean CRR were interpolated below each building centroid after the application of the Equivalent Soil Profile Method. Traditional LSN was also interpolated after liquefaction hazard analysis of the selected scenario.

Relevant issues for calculation are the applied load, computed as a function of the above variables, and the foundation type and dimensions. To this aim it is considered that the building foundation is rather homogeneous for residential buildings, consisting in small math foundations. The applied unit load is then computed subdividing uniformly spreading on this area the total load, proportional to the number of floors and extension of the building.

The procedures of Karamitros et al. (2013), Bray & Macedo (2017) and Bullock et al. (2018) were implemented on the entire Christchurch area and results are separately shown on the following maps. From a qualitative viewpoint, all methods show a similar trend of settlements severity and the obtained results are consistent with the geotechnical susceptibility of the area, which was previously described. The maps of (Figure 3-25, Figure 3-26 and Figure 3-27) show that the analyses capture rather closely the liquefaction evidences, sand ejecta and ground fissures, noticed at the ground level soon after the earthquakes (Cubrinovski et al., 2011) and the spatial distribution of damaged buildings.

This project has received funding from the European Union's Horizon 2020 research and innovation programme under grant agreement No. 700748

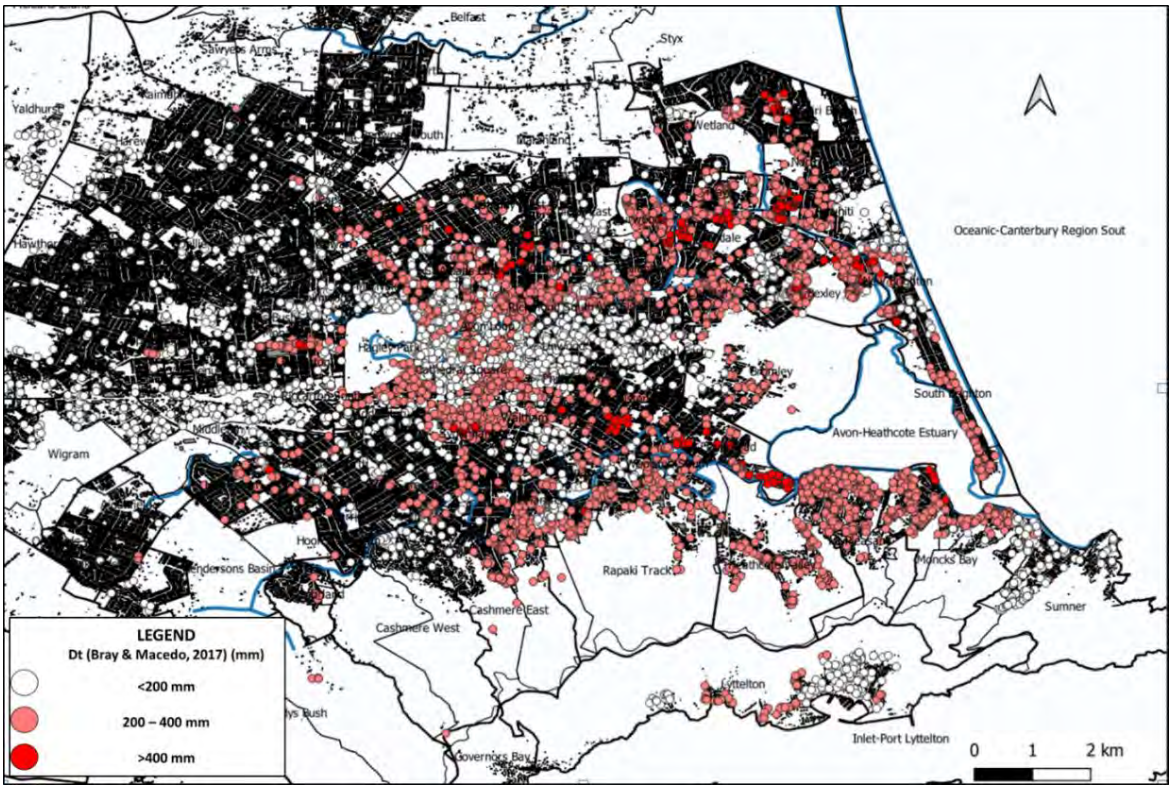

Figure 3-25 Evaluation of liquefaction-induced building settlements (Bray & Macedo, 2017).

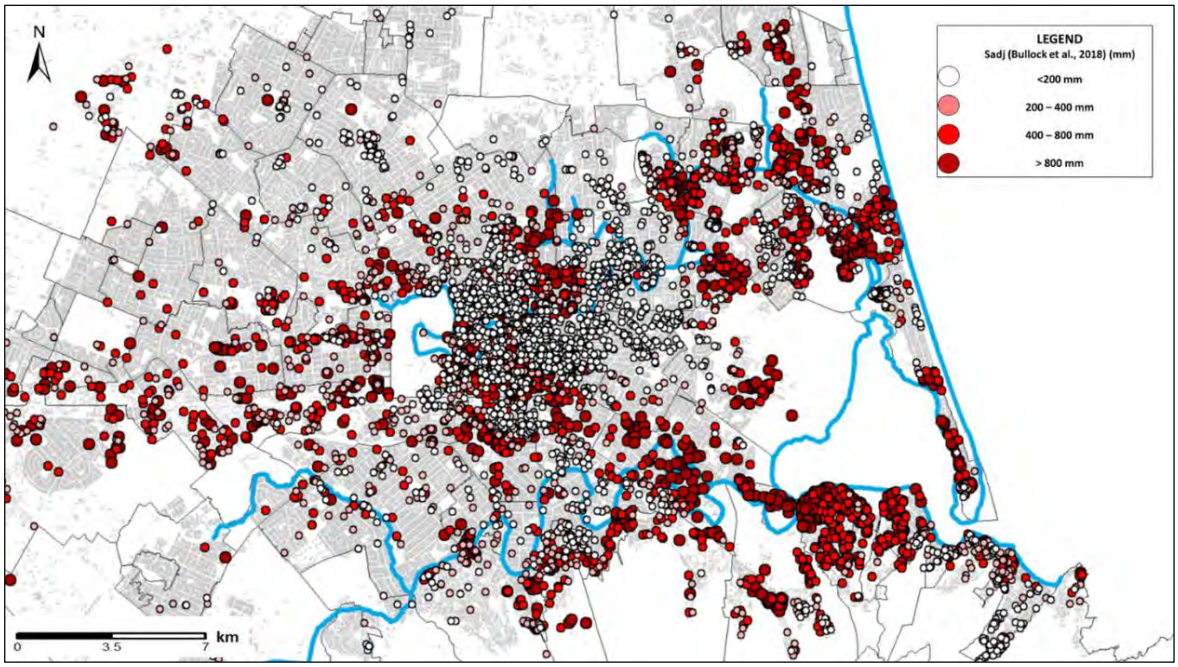

Figure 3-26 Evaluation of liquefaction-induced building settlements (Bullock et al., 2018).

This project has received funding from the European Union's Horizon 2020 research and innovation programme under grant agreement No. 700748

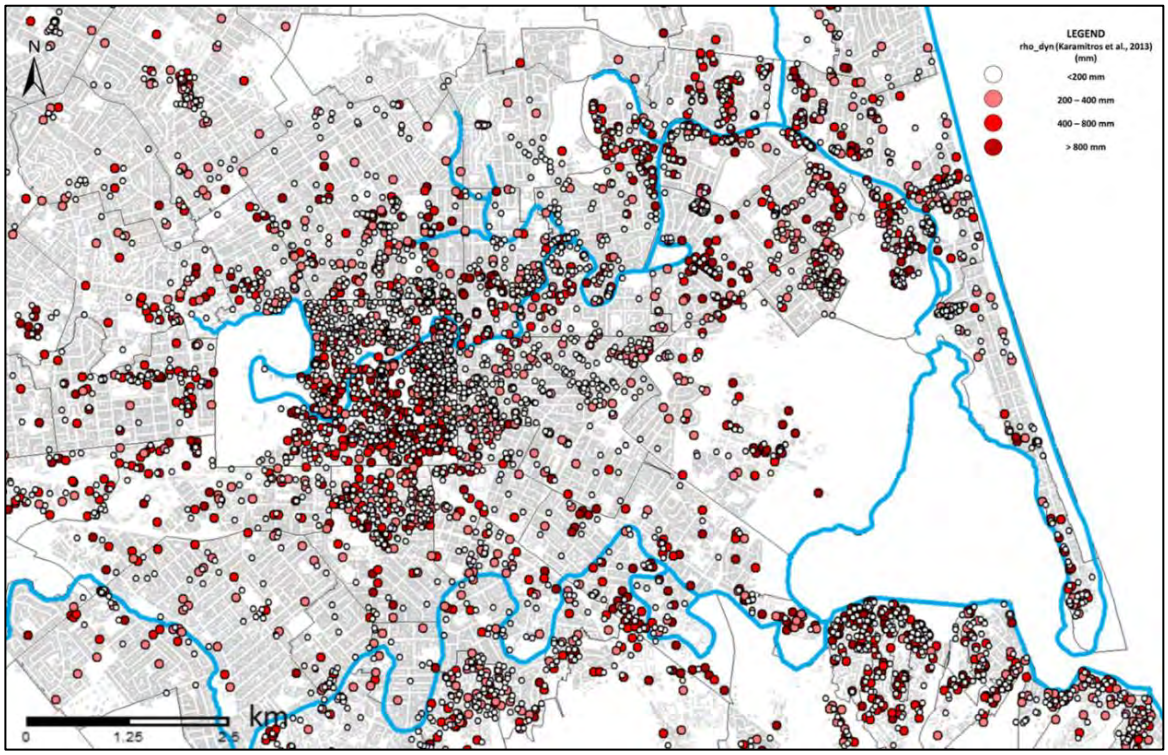

Figure 3-27 Evaluation of liquefaction-induced building settlements (Karamitros et al., 2013).

3.3.2 Damage Survey

The Canterbury earthquake sequence resulted in significant damage to the building structures, particularly in the central Christchurch. Christchurch City Council undertook rapid damage assessment of all types of buildings as Level 1 and Level 2 assessments, while another survey form, namely Detailed Engineering Evaluation (DEE) form, was used specifically for commercial and multi-storey residential buildings to collect details including structural, site and damage information (Lin et al., 2014).

The post-earthquake building safety evaluation survey, coordinated by CCC, was performed following the main event in September 2010 and again after the February 2011 event. The inspection included initial Level 1 RAPID Assessments and the more detailed Level 2 Assessments. A Level 2 assessment is required on all critical facility buildings, large (typically multi-storey) buildings, and any other buildings where Level 1 Assessment identifies the need for further – detailed inspection. The assessment forms capture fundamental building and damage data, including location, structural type, use category, overall hazard or damage (possibility of collapse or partial collapse, leaning, structural damage, overhead falling hazard, ground deformation, and hazard from building services), and repair/reconstruction/demolition recommendations. Structural damage is grouped into damage to foundations, roofs/floors, columns, bracings, connections, and beams, and damage to non-structural elements into parapets, claddings, ceilings, partitions, elevators, stairs, and utilities. Geotechnical damage or ground deformation is also assessed for slope failures, ground movements, and liquefaction. All the damage attributes are captured in a somewhat qualitative manner by ticking 'Minor', 'Moderate', or 'Severe'. Based on these damage evaluations, engineers will estimate the building overall damage ratio in percentage as well as assign placard.

This project has received funding from the European Union's Horizon 2020 research and innovation programme under grant agreement No. 700748

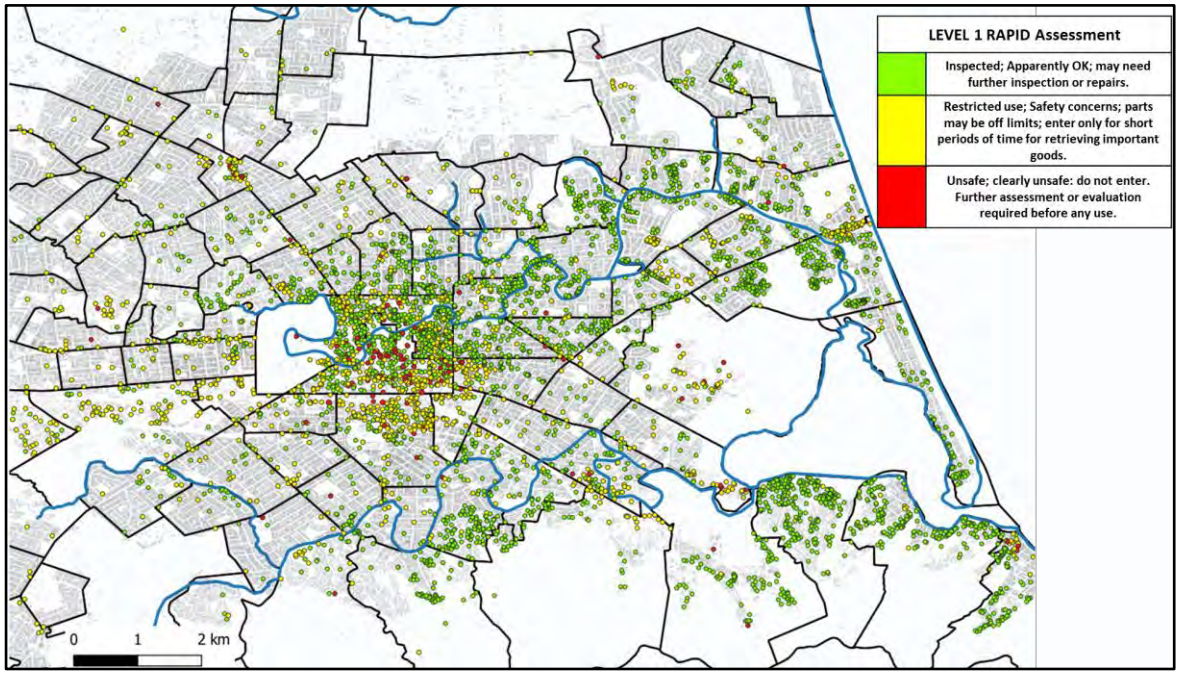

Figure 3-28 Definition of different building colour tagging categories after post-earthquake rapid inspections.

Ground deformations and failure associated with liquefaction contributed to widespread damage to residential buildings, commercial buildings, buried pipelines, bridges, roads, and stop banks. The extent and nature of the liquefaction-related damages for each type of infrastructure have been well documented in various publications and databases.

A Level 1 RAPID Assessment results in a building being tagged 'Green', 'Yellow' or 'Red', whereas Level 2 Assessments include further classifications into all the three colour tags. The different colour tags and their implied meanings are listed in Figure 3-28. Some buildings were red tagged as R3 despite little building damage because of threat from adjacent damaged buildings and ground liquefaction.

In addition to the land damage mapping and rapid properties inspections, a more detailed land damage inspection program was undertaken on each of some 65,000 insured residential properties by a team of approximately 400 engineers for insurance claim damage assessment purposes. Visually observed damage to the foundations of homes was recorded based on the criteria described in the van Ballegooy et al., 2014. These detailed property inspections were undertaken in areas where land damage claims were lodged with EQC between September 2010 and December 2012. Generally, all properties with land damage were inspected at least once during this period and many with a reassessment after subsequent events. Totally, about 100,000 inspections were made.

Damage to residential buildings depended on the magnitude and distribution of the ground surface subsidence and lateral spreading displacements across their foundations. Differential ground settlements or stretching (lateral extension) across a site were associated with cracking, tilting, or warping of building foundations, which were accompanied by architectural cracking and structural distress manifested as

This project has received funding from the European Union's Horizon 2020 research and innovation programme under grant agreement No. 700748

racking, hogging, twisting, or distortion of the building structure. Ground deformations also caused cracking and offsets in driveways, patios, and other landscaping features and damaged underground utility connections between the buildings and distribution mains. Building damage was generally repairable in areas of minor to moderate liquefaction effects but was often too extensive for economical repair in areas of severe liquefaction effects. There were no cases of liquefaction-induced ground deformations causing collapse of a residential building. However, some buildings in the areas of extensive lateral spreading in the Red Zone were severely deformed and close to partial collapse. In the following figure buildings higher than 2 storeys on which the liquefaction-induced global settlement was detected, are located.

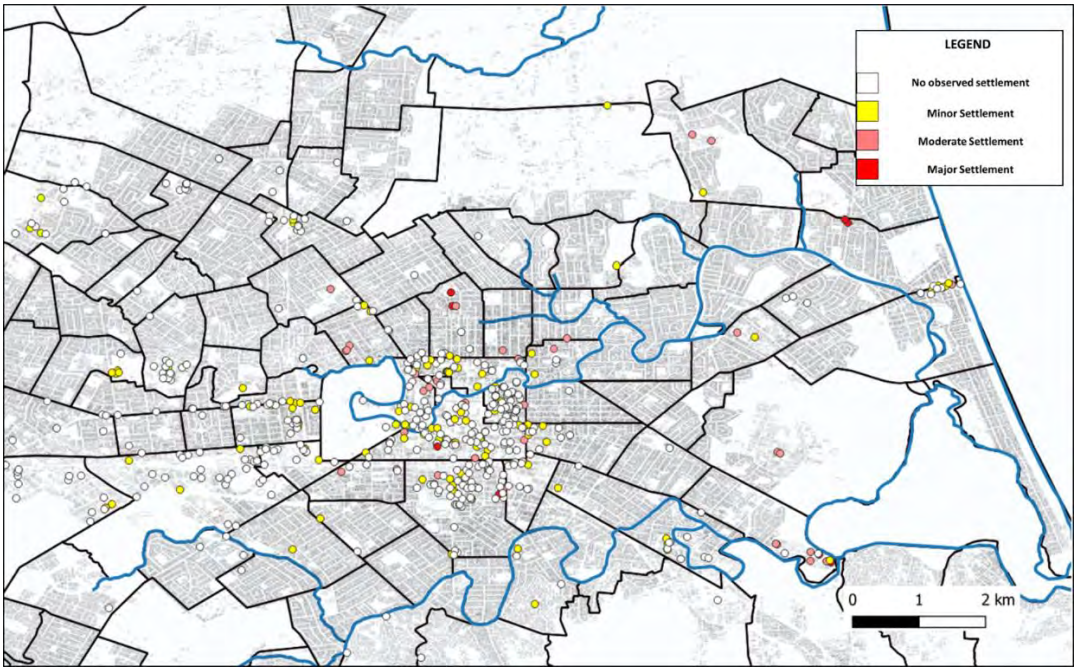

Figure 3-29 Localisation of buildings on which the global liquefaction-induced settlement was classified according the criteria defined in van Ballegooy (2014).

The observed impact of liquefaction on residential buildings in the entire Christchurch Earthquake Sequence was a primary consideration in the land zonation established by the New Zealand Government shown in Figure 3-30. The residential Red Zone is land identified by the New Zealand Government where the repair and rebuilding process is not judged to be practical, because the required land repair and improvement works would be difficult to implement, prolonged, and disruptive for landowners. The balance of the land was categorized into the three technical categories TC1-TC3 by the Ministry of Building, Innovation and Employment (MBIE). The TC1 area corresponds to areas where liquefaction damage is unlikely in future large earthquakes, and standard residential foundation assessment and construction is appropriate. The TC2 area corresponds to areas where liquefaction damage is possible in future large earthquakes and standard enhanced foundation repair and rebuild options per MBIE guidance (MBIE, 2012) are suitable for liquefaction mitigation. The TC3 area corresponds to areas where liquefaction damage is possible in future large earthquakes and individual engineering assessment with site specific geotechnical investigations is required

to select appropriate foundation repair or rebuild options. NA areas (white zones of the following map) represent non-residential/rural areas.

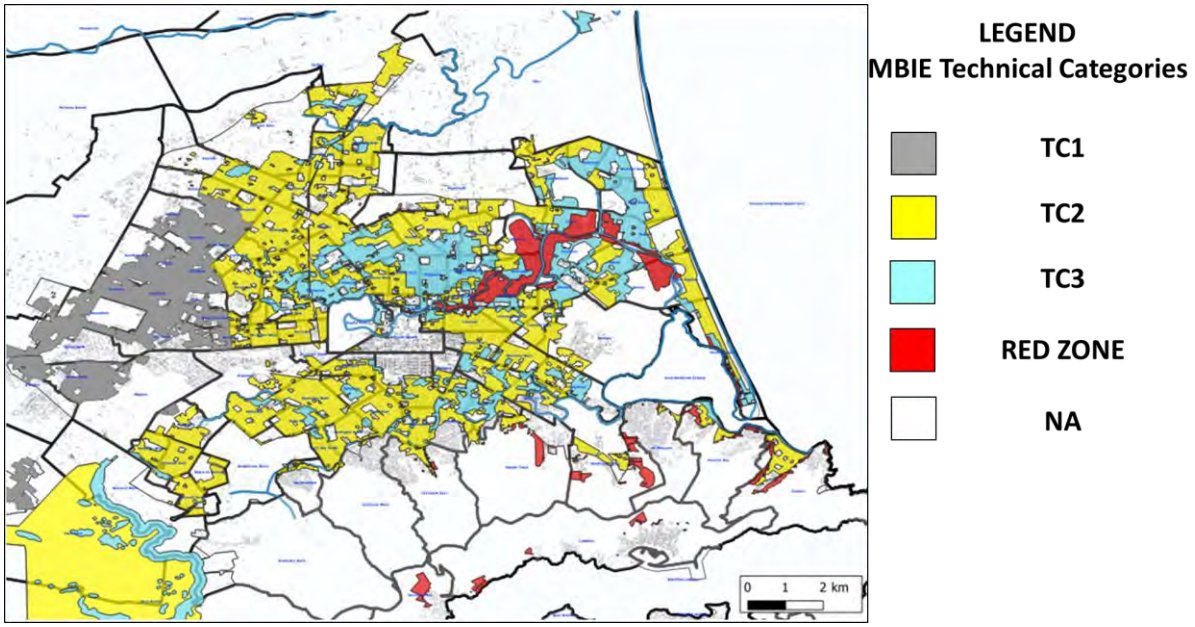

Figure 3-30 The Red Zone and Technical Categories zones established by the New Zealand government after the 2010 – 2011 Christchurch Earthquake Sequence.

3.3.3 Validation of liquefaction-induced building settlements

Predicting the damage of each building is a very difficult challenge since many relevant information, primarily the structural characteristics of the buildings and the mechanical properties of the foundation soil, are unknown and assumed as constant. For this reason, a statistical procedure was implemented to validate the effectiveness of each method in liquefaction-induced damage prediction. In fact, as for the free field conditions, a binary test was applied assuming variable thresholds for settlements and a synthetic parameter of performance (as a function of the assumed threshold) was evaluated by correlating the predictions to the observations. The computed settlement was used as a proxy of liquefaction-induced damage severity (van Ballegooy et al., 2014). The area under the curve AUC was then evaluated. In addition, for each of the threshold values, the Matthew correlation coefficient *"MCC"* was calculated. The MCC is more useful for cases where there is a large difference in the number of positive and negative observations (Matthews, 1975). It is proportional to the chi-squared statistic for a 2 x 2 contingency table and its interpretation is similar to Pearson's correlation coefficient, so it can be treated as a measure of the goodness-of-fit of a binary classification model (Powers, 2011). For each method, optimal thresholds for damage assessment were defined as maximum value of the MCC function and the TPR/FPR, TNR/FNR were calculated.

The validation test was preliminarily applied over the entire building database: the evaluated building settlements were related to the current placard assessments, which were mapped by engineers' team after post-earthquake rapid inspections. This analysis gave a random distribution of the true positives and false

negatives as a function of the thresholds assumed for settlement. In fact, considering that better predictive models locate points of the ROC curve towards the top left of the plot, the AUC is a generalized measure of model quality assuming no specific threshold. The diagonal of the plot is equivalent to random guessing (AUC = 0.5), while AUC = 1 is a good prediction. In this case, for each of the considered methods AUC results generally are around 0.50, thus the obtained results show lack of correlation between event and selected variables. This result is probably related with the purpose of rapid visive inspections which is to globally assess the safety of each building after an earthquake, both including shaking and liquefaction-induced damage on structures.

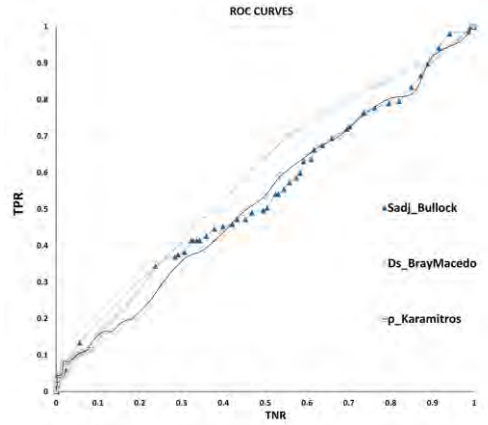

Liquefaction-Induced Settlement	Reference	AUC	OPTIMAL THRESHOLD
Sadj (mm)	Bullock et al. (2018)	0.57	80 mm
Ds+Dt (mm)	Bray & Macedo (2017)	0.60	170 mm
Pdyn (mm)	Karamitros et al. (2013)	0.55	150 mm

Bullock et al. (2018)		Bray & Macedo (2017)		Karamitros et al. (2013)	
MCC(THRESHOLD) = 0.10		MCC(THRESHOLD) = 0.13		MCC(THRESHOLD) = 0.16	
TPR = 98 %	TNR = 94%	TPR = 70 %	TNR = 56%	TPR = 9%	TNR = 2%
FPR = 2%	FNR = 6 %	FPR = 30%	FNR = 44 %	FPR = 91%	FNR = 98 %

Figure 3-31 Validation test between settlement predictive models and damage observations on buildings. For each of the implemented methods, optimal thresholds as a function of the MCC and the respective values of the TPR/TNR are shown.

The ROC test has then been repeated isolating only those buildings that manifested liquefaction-induced settlements. Therefore, the analysis has been restricted to the buildings having at least two floors, for which the load transferred onto the foundation is significant. Additionally, the test described in Figure 1-17 has been performed recovering the Equivalent Soil Profile and excluding from the database of buildings those resting on subsoil not respecting this test (with an error >10%). In this way, the test has been applied only to those situations that respecting the basic assumptions of the calculation methods. Finally, a different threshold has been considered for the test, assuming as positive event the buildings affected by moderate damage. The results of each analysis, shown in Figure 3-32, Figure 3-33 and Figure 3-34, record a progressive increase on the performance indicator, with AUC as high as 0.72-0.74 when predicting moderate damage and as high as 0.74-0.89 when predicting the major damage.

Therefore, it can be concluded that the building settlements can be assumed as a proxy of damage, provided the basic assumptions of the model are fulfilled. Among the considered methods, the formula proposed by Bray and Macedo (2017) shows a very good performance in the prediction of major damage of buildings.

This project has received funding from the European Union's Horizon 2020 research and innovation programme under grant agreement No. 700748

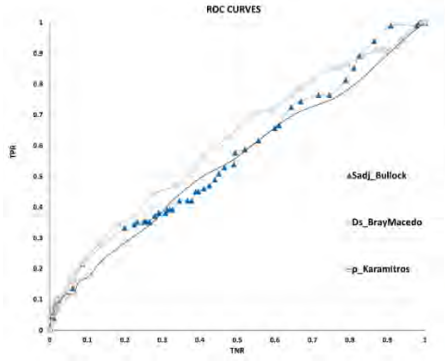

Liquefaction-Induced Settlement	Reference	AUC	OPTIMAL THRESHOLD
Sadj (mm)	Bullock et al. (2018)	0.60	80 mm
Ds+Dt (mm)	Bray & Macedo (2017)	0.63	170 mm
Pdyn (mm)	Karamitros et al. (2013)	0.60	150 mm

Bullock et al. (2018)		Bray & Macedo (2017)		Karamitros et al. (2013)	
MCC(THRESHOLD) = 0.14		MCC(THRESHOLD) = 0.14		MCC(THRESHOLD) = 0.18	
TPR = 99 %	TNR = 90%	TPR = 70 %	TNR = 55%	TPR = 9%	TNR = 1%
FPR = 1%	FNR = 10%	FPR = 30%	FNR = 45 %	FPR = 91%	FNR = 99 %

Figure 3-32 Validation test between settlement predictive models and damage observations on buildings, after ESP error filtering. For each of the implemented methods, optimal thresholds as a function of the MCC and the respective values of the TPR/TNR are shown.

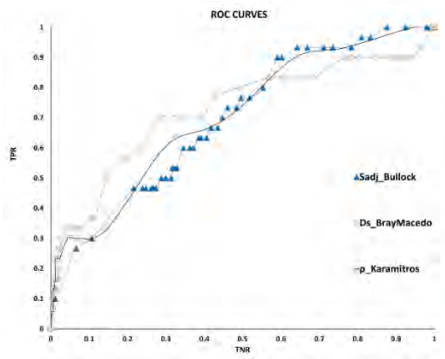

Liquefaction-Induced Settlement	Reference	AUC	OPTIMAL THRESHOLD
Sadj (mm)	Bullock et al. (2018)	0.72	180 mm
Ds+Dt (mm)	Bray & Macedo (2017)	0.74	300 mm
Pdyn (mm)	Karamitros et al. (2013)	0.74	180 mm

Bullock et al. (2018)		Bray & Macedo (2017)		Karamitros et al. (2013)	
MCC(THRESHOLD) = 0.17		MCC(THRESHOLD) = 0.27		MCC(THRESHOLD) = 0.35	
TPR = 90 %	TNR = 60%	TPR = 35 %	TNR = 6%	TPR = 24%	TNR = 1%
FPR = 10%	FNR = 40%	FPR = 65%	FNR = 94 %	FPR = 76%	FNR = 99 %

Figure 3-33 Validation test between settlement predictive models and minor/moderate damage observations on buildings, after ESP error filtering. For each of the implemented methods, optimal thresholds as a function of the MCC and the respective values of the TPR/TNR are shown.

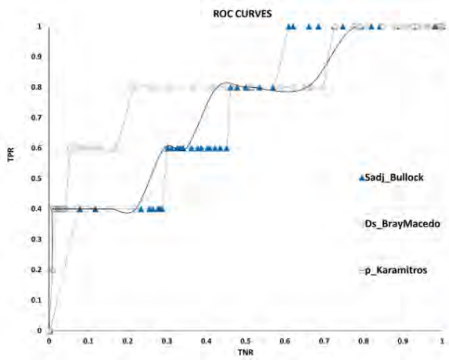

Liquefaction-Induced Settlement	Reference	AUC	OPTIMAL THRESHOLD
Sadj (mm)	Bullock et al. (2018)	0.74	180 mm
Ds+Dt (mm)	Bray & Macedo (2017)	0.89	320 mm
Pdyn (mm)	Karamitros et al. (2013)	0.75	280 mm

Bullock et al. (2018)		Bray & Macedo (2017)		Karamitros et al. (2013)	
MCC (THRESHOLD) = 0.10		MCC THRESHOLD) = 0.30		MCC (THRESHOLD) = 0.45	
TPR = 100 %	TNR = 61%	TPR = 60 %	TNR = 5%	TPR = 20%	TNR = 0%
FPR = 0%	FNR = 39%	FPR = 40%	FNR = 95 %	FPR = 80%	FNR = 100 %

Figure 3-34 Validation test between settlement predictive models and moderate/major damage observations on buildings, after ESP error filtering. For each of the implemented methods, optimal thresholds as a function of the MCC and the respective values of the TPR/TNR are shown.

This project has received funding from the European Union's Horizon 2020 research and innovation programme under grant agreement No. 700748

3.4 Evaluation of Liquefaction-induced physical impact on buildings

Recent strong seismic events have demonstrated that even moderate levels of earthquake intensity can cause liquefaction, potentially leading to induced soil settlements and lateral spreading that may result to severe physical damages and important economic and societal losses. However, the published literature in the evaluation of the induced physical damages to building structures is generally inadequate. Fotopoulou et al. (2018) developed an efficient analytical methodology for assessing the vulnerability of typical low-code reinforced concrete (RC) buildings, subjected to liquefaction-induced displacements.

Specifically, a series of nonlinear static time-history parametric analyses of representative structural typologies are carried out. The input to the structural model are various sets of displacement loads imposed quasi-statically directly at its supports (shallow foundations), to simulate the differential displacement demand of the structure impact by liquefaction. The building's response is then assessed using appropriate engineering demand parameters (EDPs) that are statistically correlated with predefined damage states to construct the fragility functions. Log-normally distributed fragility curves are finally derived for different damage states using nonlinear regression analysis, for the different structural typologies representative of typical seaport structures. They could be used in quantitative risk assessment studies to assess the vulnerability of typical low-code RC buildings and warehouses exposed to liquefaction hazard along European-Mediterranean and other regions of similar facilities worldwide.

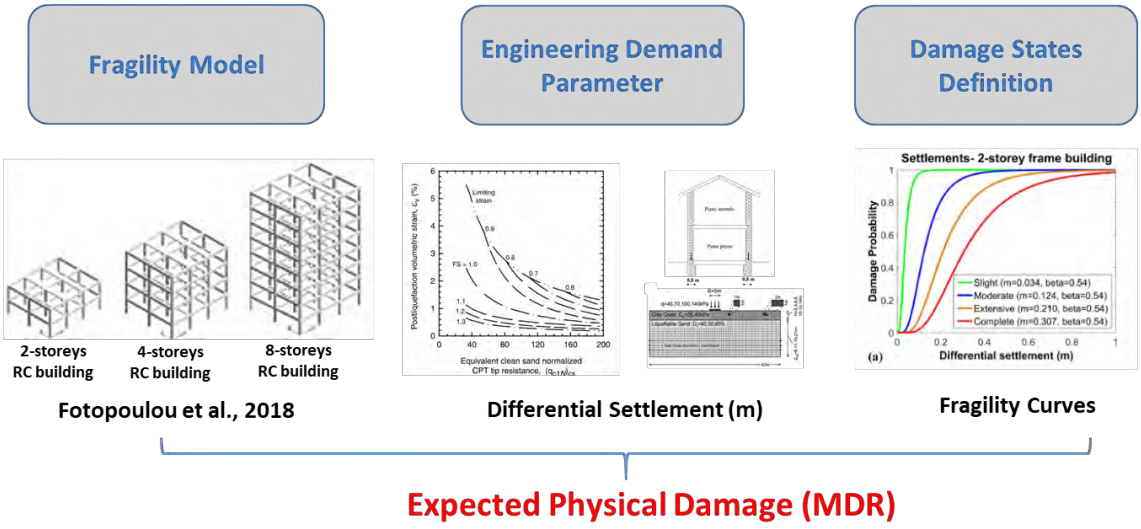

Figure 3-35 Conventional Liquefaction vulnerability and followed approach to evaluate the building loss ratio.

To assess the physical impact of liquefaction on buildings following the conventional approach, the fragility model defined by Fotopouolu et al. (2018) (which is also implemented in the Liquefact software) was used. This model was developed for low-rise, mid-rise and high-rise reinforced concrete buildings and considers the differential settlement as EDP. In this step, firstly the arithmetic mean settlement among the three above defined methods (Table 3-4) was computed as w_{max}. Then, looking at the results reported in Figure 1-30, a scaling factor equal 0.667 (i.e. 2/3) was applied to convert absolute into differential settlements, which were used to access the Fotopoulou et al. fragility curves.

Four damage limit states ranging from slight-to-complete are defined and the loss factors associated with each damage state are summarized in the following table. By combining the probability of reaching each damage state to the loss factor, the Mean Damage Ratio for the 22 February earthquake scenario was evaluated on the entire building portfolio.

DAMAGE LIMIT STATE	LOSS FACTOR
Slight	0.10
Moderate	0.30
Extensive	0.70
Complete	1.00

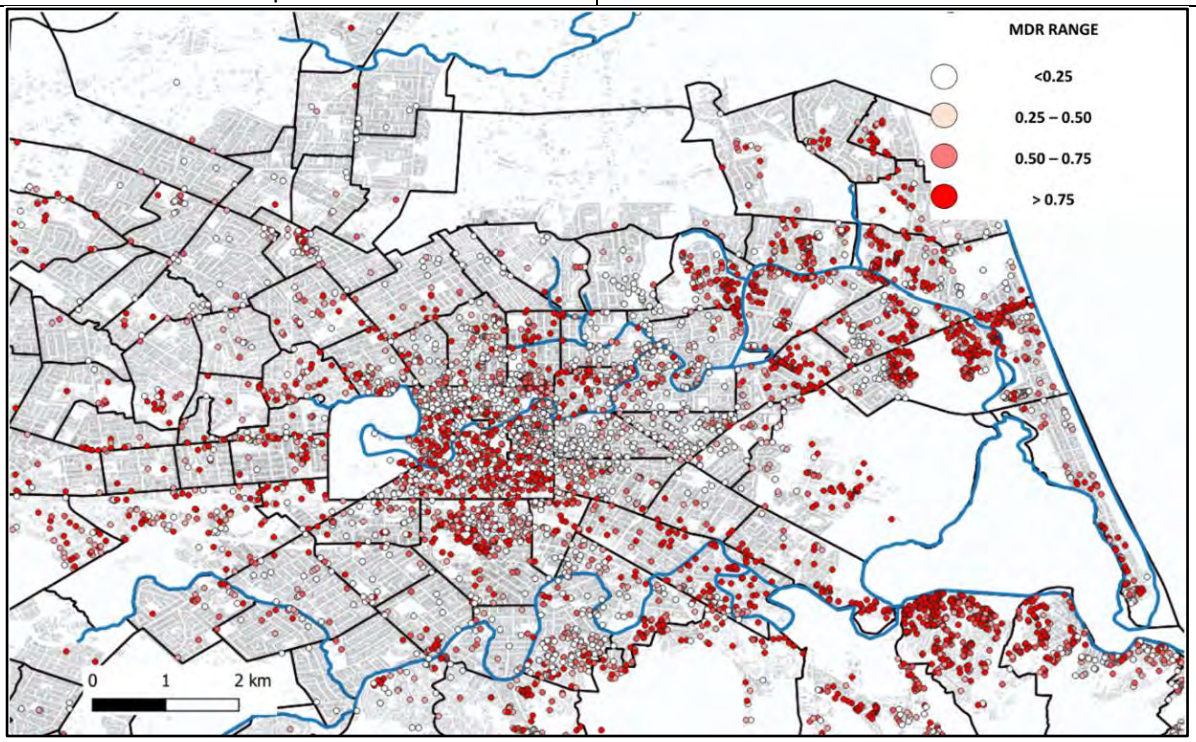

Figure 3-36 Map of Mean Damage Ratio evaluated for the entire set of buildings by applying the conventional fragility model.

The results summarized in Figure 3-36 demonstrate that, from a qualitative viewpoint, a good agreement exists with the map of the technical categories classified by the New Zealand government. In particular, both maps highlight that the most damaged areas are localised along the Avon River (North-East of Christchurch) which was defined as Red Zone in the Technical Categories Map and within the Central Building District.

The validation criterion (Figure 3-37) shows that the performance of the mean damage ratio in predicting the minor/moderate damage is adequate since AUC is found equal to 0.70 and optimal threshold of MDR ≈ 80% which maximize the MCC can be defined.

This project has received funding from the European Union's Horizon 2020 research and innovation programme under grant agreement No. 700748

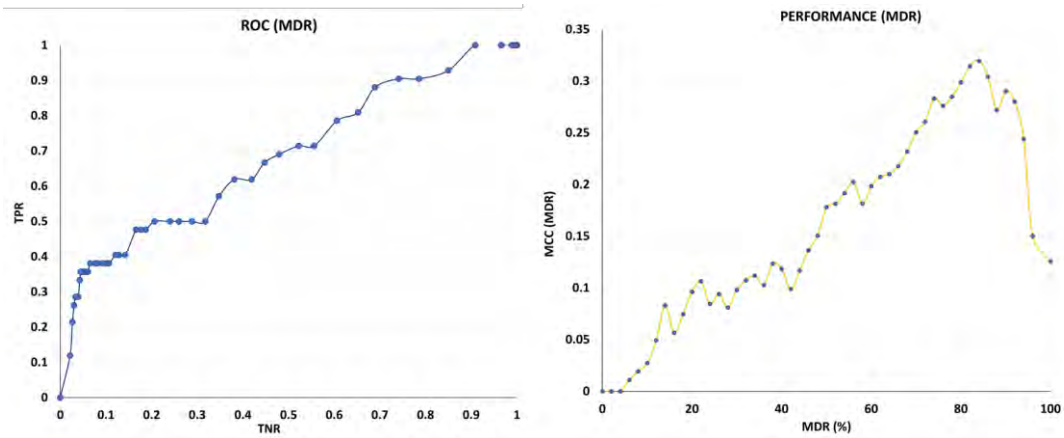

Figure 3-37 ROC validation criterion (Kongar et al., 2015) applied to the mean damage ratio vs moderate damage level, and MCC as a function of the Mean Damage Ratio.

3.5 Estimate of the economic losses and cost/benefit analysis

According to the procedure defined in deliverable D7.1, the obtained mean damage ratio (which is a proxy of the liquefaction-induced physical impact) can be combined with the loss of functionality and the recovery time to quantify the total loss induced by liquefaction on each building. An example of economic loss calculation is here implemented by setting 1000,00 €/mq as building unitary cost and 3000,00 €/mq as repair/replacement cost, which includes the costs for transportation and demolition; in addition, a monthly cost of 1000,00 € was used to transform the dwelling loss of functionality into a cost.

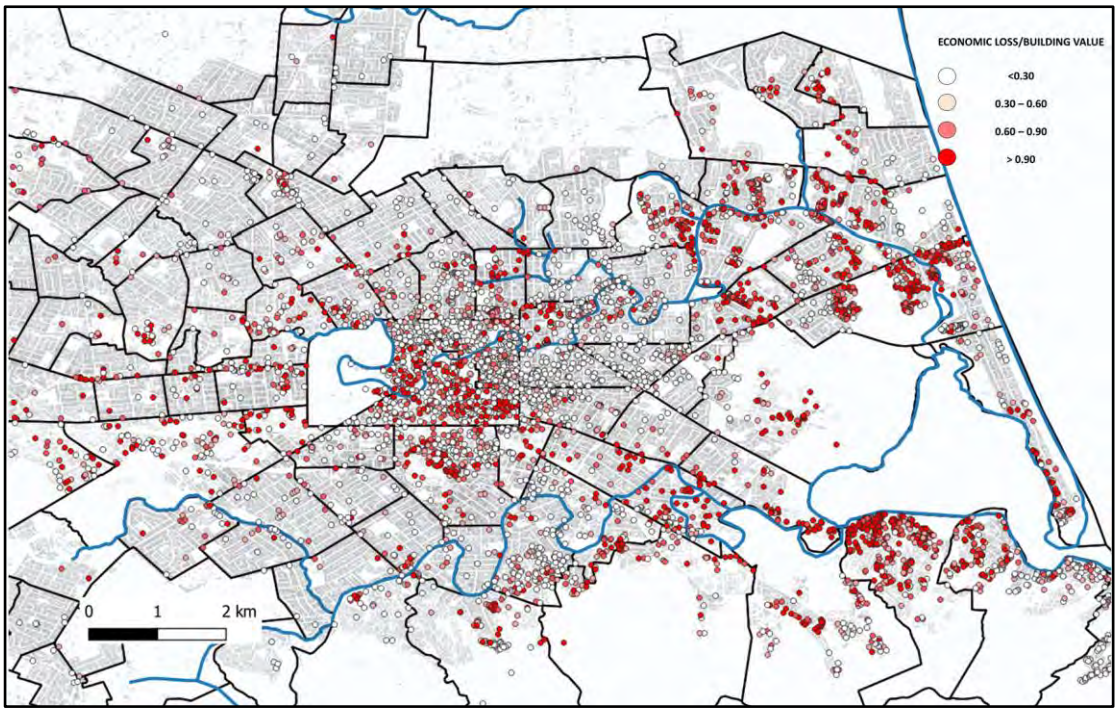

Figure 3-38 Economic loss estimated with the proposed methodology for the residential buildings of Christchurch after the 2011 Feb 22nd earthquake (Mw=6.2).

This project has received funding from the European Union's Horizon 2020 research and innovation programme under grant agreement No. 700748

Finally, the total economic loss due to liquefaction for the seismic scenario of February 22nd 2011 has been related to the value of each individual building and expressed as a percentage of the total building value (Figure 3-38).

Finally, the evaluation of liquefaction annual risk on the building portfolio has been performed by applying the Liquefact procedure. In particular, four seismic scenarios having Tr ranging in 25 to 2500 years (NZGD), have been considered. For each scenario, the MDR and the economic loss has been calculated; finally, the convolution of these terms with the respective Annual Frequence of Exceedance gives the annual liquefaction risk on buildings. Its reduction represents the benefit of a possible mitigating action.

The benefit/cost analysis has then been performed considering mitigation that has parametrically variable costs in the range of 10 to 100 € / m^3. For each solution, the cost of the treatment has been evaluated as product of a unit cost times the volume of potentially liquefiable sandy layer to be treated, the latter given by the thickness of liquefiable layer and the footprint area computed below each building. The calculation has been performed considering a lifecyle of 50 years and a 30-year time horizon for all buildings. This information serves to calculate the annual mitigation rate to be paid to support the investment. This term represents the cost of mitigation. The cost/benefit analysis has thus been performed on each building of Figure 3-38, considering different unit costs of mitigation and plotting the buildings for which the benefit is larger than cost. It is here assumed that, independently on the unit cost, mitigation is able to eliminate risk for all cases. The results obtained for unit mitigation costs equal to 10, 20, 50 and 100 € per cubic meter of soil are plotted in Figure 3-39. Obviously, once the liquefaction risk is defined on the study area, the more expensive the mitigation is and the smaller the number of buildings on which it is convenient.

The different plots show that mitigation with ground improvement is convenient for a larger number of buildings if its cost is low or very low (say 10 €/mc), while becomes less appealing when costs increase. For the larger considered cost (100 €/mc) only few buildings, most of them located in the Central Business District of the city, are worth of mitigation with ground improvement. For the other residential houses of the city affected by risk it is not convenient to undertake this kind of countermeasure. Other solutions should thus be considered for this class of buildings, such as the stipulation of insurance policies. The implemented risk assessment procedure provides in this case the possibility of establishing the cost of premium to be assigned for each building.

This project has received funding from the European Union's Horizon 2020 research and innovation programme under grant agreement No. 700748

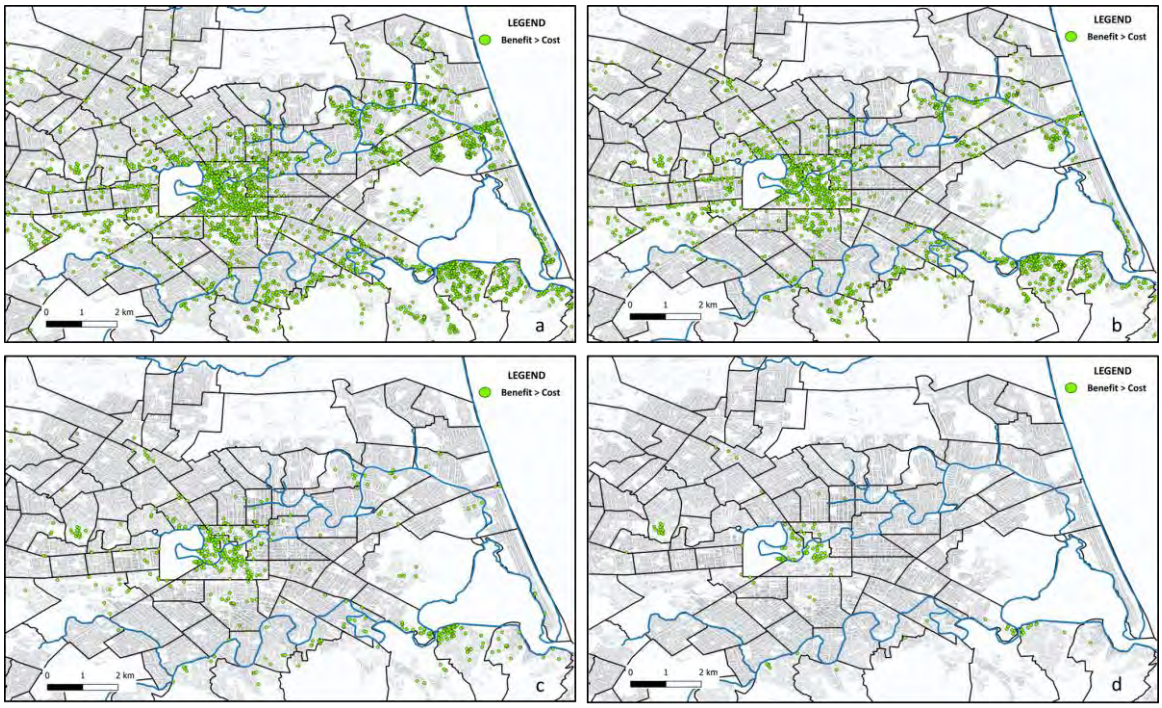

Figure 3-39 Benefit cost analysis considering a cost of mitigation equal to 10 €/mc (a), 20 €/mc (b), 50 €/mc (c), 100 €/mc (d).

3.6 Bibliography

Bradley BA. Strong ground motion characteristics observed in the 13 June Mw6.0 Christchurch, New Zealand earthquake. Soil Dynamics and Earthquake Engineering 2016, Vol. 91, pp. 23-38. Brown L.J. and Weeber J.H., 1992. "Geology of the Christchurch Urban Area", Scale 1:25 000. Institute of Geological & Nuclear Sciences Geological Map 1.

Boulanger R.W., & Idriss I.M., 2014: "CPT and SPT based liquefaction triggering procedures", Department of Civil and Environmental engineering, University of California at Davis.

Bray, J. & Macedo, J., 2017. 6th Ishihara lecture: "Simplified procedure for estimating liquefaction-induced building settlement". Soil Dynamics Earthquake Engng 102, 215–231.

Bullock Z., Karimi Z., Dashti S., Porter K., Liel A.B., Franke K. W., 2018: "A physics-informed semi-empirical probabilistic model for the settlement of shallow-founded structures on liquefiable ground". Géotechnique [https://doi.org/10.1680/jgeot.17.P.174].

Cubrinovski M., Bradley B., Wotherspoon L., Green R., Bray J., Wood C., Pender M., Allen J., Bradshaw A., Rix G., Taylor M., Robinson K., Henderson D., Giorgini S., Ma K., Winkley A., Zupan J., O'Rourke T., DePascale G., Wells D., 2011: "Geotechnical aspects of the 22 February 2011 Christchurch earthquake", "Bullettin of the New Zealand Society for earthquake engineering", Vol. 44, N. 4, December 2011.

Cubrinovski M., Rhodes M., Ntritsos N., van Ballegooy S., 2017: "System Response of liquefiable deposits". PBD III Earthquake Geotechnical Engineering, Vancouver.

Fotopoulou S., Karafagka S., Pitilakis K. 2018: "Vulnerability assessment of low-code reinforced concrete frame buildings subjected to liquefaction-induced differential displacements, Soil Dynamics and Earthquake Engineering, 110:173-184.

Goldsworthy H. M., 2012: "Lessons from the February 22nd Christchurch Earthquake", Australian Earthquake Engineering Society 2011 Conference, 18-20 November, Barossa Valley, South Australia.

Iwasaki T., Tatsuoka F., Tokida K., Yasuda S., 1978: "A Practical method for assessing soil liquefaction potential based on case studies at various sites in Japan", [conference] // 2nd International conference on Microzonation. - 1978. - pp. 885-896.

Karamitros, D.K., Bouckovalas, G. D., Chaloulos Y.K., 2013. Seismic settlements of shallow foundations on liquefiable soil with a clay crust. Soil Dynamics and Earthquake Engineering. 46. 64-76.

Kongar I., Rossetto T., Giovinazzi S., 2015: "Evaluating Simplified Methods for Liquefaction Assessment for Loss Estimation". Nat. Hazards Earth Syst. Sci. Discuss., doi:10.5194/nhess-2016-281, journal Nat. Hazards Earth Syst. Sci. Published: 15 September 2016.

Lin S.L., Ums S. R., Nayerloo M, Buxton R., King A., 2014: "Engineering characterisation of building performance with detailed engineering evaluation (DEE) data from the Canterbury Earthquake Sequence". ASEC 2014 Conference: structural engineering in Australasia, Auckland, New Zealand.

Matthews, B. W., (1975), Comparison of the predicted and observed secondary structure of T4 phage lysozyme, Biochimica et Biophysica Acta – Protein Structure, 405(2), 442-451.

Maurer, B. W., Green, R. A., Oliver, S., Taylor, O. S. 2015. "Moving Towards an Improved Index for Assessing Liquefaction Hazard: Lessons from Historical Data". Soils and Foundations, 55(4): 778-787.

Powers, D. M. W., 2011: "Evaluation: from precision, recall and F-measure to ROC, informedness, markedness and correlation", J. of Mach. Lear. Tech, 2(1), 37-63.

Quigley M.C., Bastin S. and Bradley B.A., 2013: "Recurrent liquefaction in Christchurch, New Zealand, during the Canterbury earthquake sequence", Geology 41, 419–422.

Quigley M, Hughes MW, Bradley BA, Van Ballegooy S, Reid C, Morgenroth J, Horton T, Duffy B, Pettinga J. The 2010-2011 Canterbury earthquake sequence: Environmental effects, seismic triggering thresholds and geologic legacy. Tectonophysics. 2016. Vol 672-673, pp 228-274.

Tonkin & Taylor, 2015: "Canterbury Earthquake Sequence: Increased Liquefaction Vulnerability Assessment Methodology". Prepared for Chapman Tripp acting on behalf of the Earthquake Commission (EQC).

van Ballegooy S., Malan P., Lacrosse V., Jacka M.E., Cubrinovski M., Bray J.D., O'Rourke T.D., Crawford S.A., Cowan H., 2014: "Assessment of Liquefaction-Induced Land Damage for Residential Christchurch", Earthquake Spectra, Volume 30, No. 1, pages 31–55, February 2014.

Zhang G., Robertson P.K., Brachman R.W.I., 2002: "Estimating liquefaction-induced ground settlements from CPT for level ground", Canadian Geotechnical Journal, 39, 1168–80.

This project has received funding from the European Union's Horizon 2020 research and innovation programme under grant agreement No. 700748

4 A MEDIUM TO LARGE CITY #2 – ADAPAZARI (TURKEY)

4.1 Introduction

Adapazari, which is the capital of Sakarya City in Turkey, was affected by a large earthquake in 17 August 1999 and widespread damage to buildings occurred throughout the city. Some of the damages were attributed to liquefaction, which caused excessive settlements, tilt and bearing capacity failures for several buildings on shallow foundations on saturated low plasticity silty soils and silt mixtures. Liquefaction was pervasive in some parts of the city, producing several phenomena ranging from minor settlement of buildings to complete toppling of structures (Bardet et al., 2000). Following the earthquake, an extensive field investigation was carried out in the city by different parties (Bay and Cox, 2001, Yoshida et.al, 2001, Sancio, 2003, U.C Berkeley et al., 2003). These investigations consisted of assessment of liquefaction-induced damage levels and conducting soil investigations in the area including CPT's, boreholes, in situ tests and laboratory tests in order to understand the underlying mechanisms for liquefaction. The results of these studies were published by several researchers (Sancio et al., 2004, Bray et al., 2001, Bol et al., 2010, Quintero et al. 2018). Ground failure in Adapazari was primarily observed adjacent to buildings (Bray et al, 2001) and Sancio et al. (2003) attributed this, among other factors to the detrimental effect of an increase in confining stress on the cyclic strength in terms of cyclic stress ratio. This may mean that effects of the structures on the liquefaction susceptibility of soils should be taken into account in liquefaction triggering analyses.

This report aims to present a full and detailed case study report for the application of the risk/resilience assessment toolbox for the Adapazari EILD cases. In this context, a detailed investigation for the buildings which were affected by the 1999 Adapazari earthquake was performed. The study consisted of gathering the damage data in the city center, which was severely affected by the earthquake both due to ground shaking and/or liquefaction. An extensive study was also carried out to determine the soil profiles in the studied area. The data was then used as input in the "LIQUEFACT software" and outputs were taken. These output files consisted of hazard analyses and hazard and risk analyses. Spatial distribution of risk analyses were then compared with the field liquefaction data. The results were also compared with the well-known liquefaction indicators; Liquefaction Potential Index (LPI) and Liquefaction Severity Number (LSN), which were used both in original and modified forms.

4.2 Methodology

The study carried out for this research consisted of several steps. The details about these stages are given below.

4.2.1 Literature Review

The first step was gathering the liquefaction induced ground damage (Fig. 2.1) database using the reports and documentation that were created after the 1999 Adapazari earthquake. This literature consisted of Bay and Cox (2001), Yoshida et. al (2001), Sancio (2003), Sancio et al. (2004) and Bray et al. (2001).

This project has received funding from the European Union's Horizon 2020 research and innovation programme under grant agreement No. 700748

4.2.2 Site visits to Adapazari city center

Several site visits were carried out by Istanbul University-Cerrahpasa team members to Adapazari city in years 2017 and 2018 to get a database of the damaged buildings in 1999 Adapazari earthquake. The locations given in the literature were visited, photographs were evaluated. Several visits were made to Sakarya Municipality offices in order to receive their database of damaged buildings in 1999 earthquake. The current situation of the damaged areas were evaluated. Some photographs regarding these visits are presented in **Figs. 2.2, 2.3 and 2.4**.

Figure 4-1: Typicalphotographs-1 for buildings with Liquefaction Induced Damage (LID) (Provided by Adapazari and Sakarya Municipalities and taken during site visits).

Figure 4-2: Typical photographs-3 taken during site visits to Adapazari city center.

This project has received funding from the European Union's Horizon 2020 research and innovation programme under grant agreement No. 700748

Figure 4-3: Typical photographs-3 taken during site visits to Adapazari city center.

Figure 4-4: Typical photographs-4 taken during site visits to Adapazari city center.

This project has received funding from the European Union's Horizon 2020 research and innovation programme under grant agreement No. 700748

4.2.3 Damaged building database

A damaged building database was created for Adapazari based on the Sakarya Municipality archives. The database consisted of buildings which were classified ranging from moderate damage to heavy damage in the post-earthquake investigations. This database from Sakarya Municipality consisted of 4550 buildings, 3504 of which were "heavily damaged" and 1406 were "moderately damaged". The buildings were reported as damaged, however the database did not differentiate whether the damage was due to ground shaking or due to liquefaction.

Figure 4-5 demonstrates the location of these buildings in Adapazari city center. The figure shows the two rivers running near the city from south to north. The Sakarya River lays on the east and flows into the Black Sea, whereas Cark River runs on the west of the city from the Sakarya Lake to Black Sea (Yoshida et al., 2001). The boundaries of the studied region is also presented in the figure.

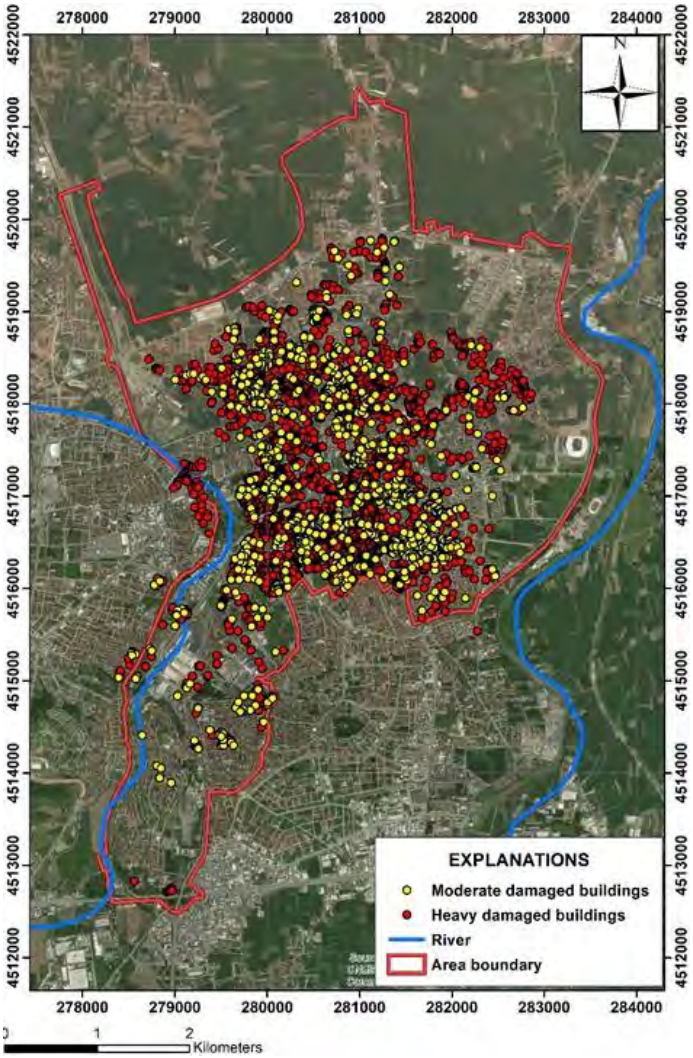

Figure 4-5: Database for damaged buildings in 1999 August Adapazari Earthquake.

4.2.4 Creation of a database for possible liquefaction induced damage buildings

In order to understand the areas where liquefaction occurred in the city, an extensive literature survey regarding the field liquefaction cases in Adapazari during the 1999 earthquake was carried out. One of the most important publications about this subject was prepared by Yoshida et al. (2001), who reported the results of a detailed investigation of the structural damage and its geotechnical condition in the Adapazari City by the Japanese Geotechnical Society Reconnaissance Team. They carried out a regional investigation, in which damage to buildings and houses was classified by cause, i.e.; inertia force (ground shaking) or ground deformation. Based on detailed investigation, they determined the limits of the liquefied area as given in Figure 4-6. The limits of the liquefied area was identified by settlement and tilt of buildings and houses. The authors stated that there was a non-liquefied area at the center of the map in the downtown area and a liquefied area surrounded this area and it was several hundred meters wide.

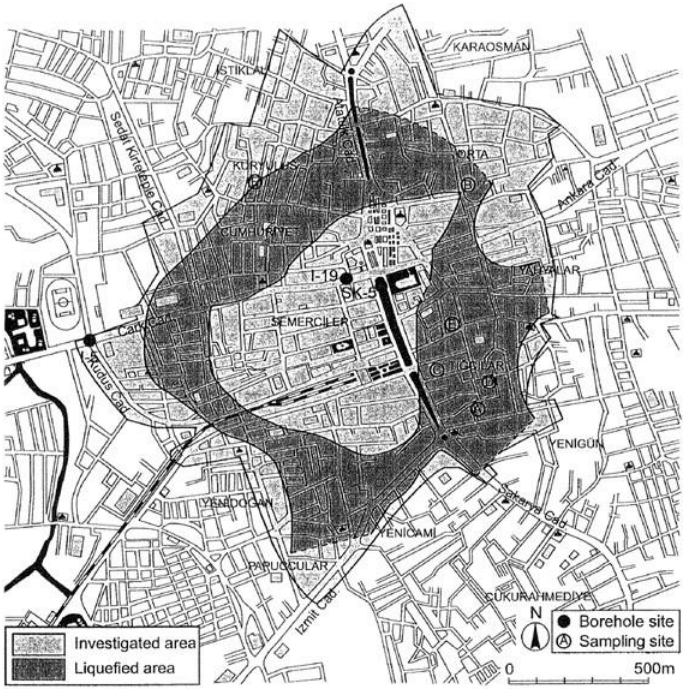

Figure 4-6: Liquefied area in Adapazari center as determined by Yoshida et al. (2001) in 1999 August Adapazari Earthquake

It should be recalled that total database from Sakarya Municipality consisted of 4550 buildings, 3504 of which were "heavily damaged" and 1406 were "moderately damaged". However, it should be emphasized that due to the vast amount of damaged buildings in the earthquake, it was not possible (or intended) by the municipality (governmental) post-earthquake reconnaissance teams to determine whether the damage was due to,

- Ground shaking,
- Liquefaction or
- Ground shaking and liquefaction.

This project has received funding from the European Union's Horizon 2020 research and innovation programme under grant agreement No. 700748

In this context, in order to determine the buildings which were possibly affected by liquefaction, a hybrid approach was followed. The buildings which are within the Yoshida et al. (2001) boundary were extracted from the total damaged building database of the municipality and it was accepted that the main damage making phenomenon might be the liquefaction for these buildings. This extracted database consisted of 1172 buildings and is given in Figure 4-7 below with black dots. Figure 4-7 also shows the areas where no or limited development was present during the 1999 earthquake.

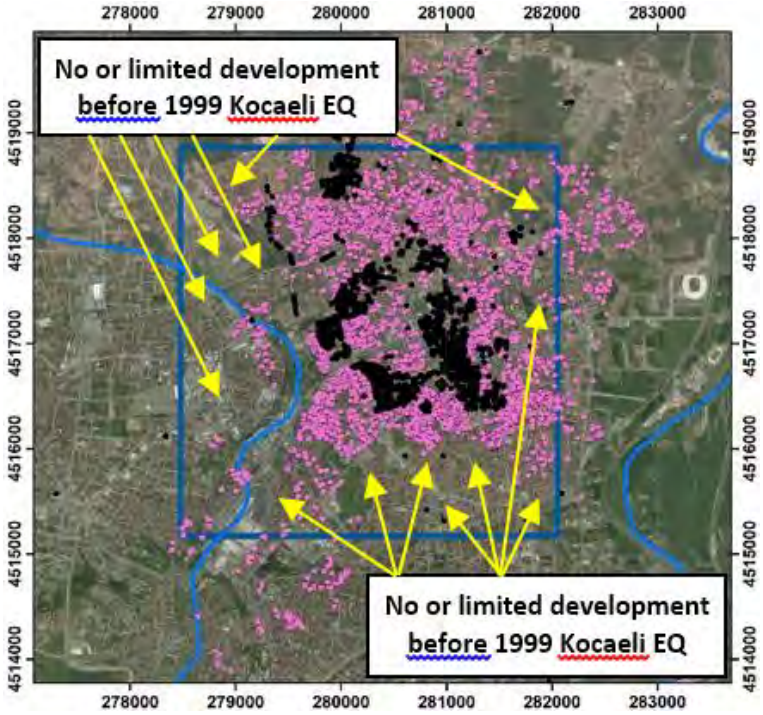

Figure 4-7: EILD buildings (black dots) in Yoshida et al. (2001)'s liquefied area

A detailed investigation was then carried out to determine the details about these 1172 buildings. Based on the information from the municipality, it was learned that 646 of these buildings were demolished after the earthquake and therefore there was no information was available about them. However, it was possible to reach the details for 526 of these buildings. The data for 526 of these buildings in this boundary were taken from the Sakarya Municipality and were listed in an EXCEL sheet. In Adapazari, the building stock consisted mainly of two to six story concrete frame buildings with a rigid raft foundations which are located at depths of typically 1.0 to 1.5 m. The details about the buildings included the plan area of the structure, number of stories and structural details such as building types; typology. These buildings were all reinforced concrete buildings (RFC), which were low rise (lr) or mid-rise (mr) and were all constructed before the latest Turkish earthquake codes of 1999 and were therefore of low code (LC) according to the classification developed in LIQUEFACT Software. These details are important because LIQUEFACT Software makes use of the fragility curves for the selected building typology.

4.2.5 Evaluation of LIQUEFACT Software and other evaluations

After all these data was gathered, different kinds of analyses were carried out using this data. The main aim was to evaluate the LIQUEFACT Software in means of liquefaction-induced damage (LID) assessment. The other studies carried out within the context of the study were to use liquefaction assessment indicators in spatial scale and to compare them with the field liquefaction cases. The analyses can be grouped as below.

A. LIQUEFACT software evaluation studies are listed below;

   i. Using LIQUEFACT to run hazard analyses: This includes running LIQUEFACT in Adapazari city center using the available CPT data and the seismic demand in the studied area. This was carried out for the 1172 buildings, the details of which are given in the above sections. Only hazard analyses could be carried out to evaluate these buildings because building information was not available for all of them as stated in the above section. Relevant maps are given in Istanbul University-Cerrahpasa section (Adapazari Case) in deliverable D7.2 of LIQUEFACT project.

   ii. Using LIQUEFACT to run hazard and risk analyses for 526 buildings: This includes running LIQUEFACT software in Adapazari city center using the CPT data and the data for the buildings. This was carried out for the 526 buildings. This type of analyses was repeated twice and was performed both for liquefaction and ground shaking plus liquefaction. Relevant maps are given in Istanbul University-Cerrahpasa section in D7.2 of LIQUEFACT project.

   iii. Using LIQUEFACT to run hazard and risk analyses for 55 buildings: This was carried out for the fifty five buildings which were determined to be affected by liquefaction based on post-earthquake surveys. Some of these buildings were listed in Yoshida et al (2001) and Sancio (2003). Other buildings were found during the city visits within the Liquefact project. Therefore, LIQUEFACT software was used to carry out hazard and risk analyses for liquefaction for these fifty five buildings in this database. Relevant maps are given in Istanbul University-Cerrahpasa section in D7.2 of LIQUEFACT project.

B. Spatial distribution of liquefaction assessment indicators to compare with the 1172 buildings (Oztoprak et al., 2019). It should be recalled that these buildings might have been damaged either due to ground shaking plus liquefaction or only due to liquefaction.

C. Evaluation of damage for selected 55 buildings with Earthquake Induced Liquefaction Damage (EILD) using liquefaction assessment indicators (Oztoprak et al., 2019). Some of these buildings were listed in Yoshida et al (2001) and Sancio (2003). However, as stated above, other buildings were found during the city visits within the Liquefact project.

4.2.6 The Studied Area – Adapazari City Center

4.2.6.1 Geology and geotechnical characterization

One of the crucial information for this study is the geology of the site and the geotechnical characterization of the soils below the foundations. This necessitated a large database. The soil data was gathered based on a very detailed literature study. Geotechnical investigations that were used in the analyses included the

CPTu's that had been carried out in the studies following the earthquake (Bay and Cox, 2001, Yoshida et. al, 2001, Sancio, 2003, Sancio et al., 2004, Bray et al., 2001). Some additional data (50 boreholes and 20 CPTu's) was provided by the Adapazari and Sakarya Municipalities and for the locations where the data was lacking, new CPTu's and boreholes (thirteen CPTu's and thirteen boreholes) were performed within the context of this study. This made a total of about 86 CPTu soundings and relevant soil data for the whole region.

In Adapazari, Holocene alluvial deposits of the Sakarya River overlie older lake bed sediments. Bardet et al. (2000) emphasize that due to active sedimentation and fluvial action, the subsurface conditions in Adapazari are such that large variations of soil type and state are to be expected in both the vertical and horizontal directions. The subsoil is heterogeneous and consists of fine sands, silty sands, silty clays and gravels. The typical soil profile consists of alternating layers of silty sand and silty clay and non-plastic silts. The groundwater table lies generally at 1 m to 2 m depth from the ground surface. In this context, the soil profile consists of potentially liquefiable soil layers.

Figure 4-8 and Figure 4-8 show typical profiles from the area. Figure 4-10 shows typical values from the soil profiles. These figures depict that the soil profiles consist of silty layers with different thicknesses ranging from 0.7 m to 7.8 m. The depths of the upper silty layer from the ground surface varies from 0.5 m to 4.4 m. The normalized clean sand equivalent cone tip resistance (q_{C1Ncs}) values in these silty layers are small, in the range of 40-80, generally less than 70 and the soil behavior type index (I_c) values ranges in the 1.2 – 3.2 spectrum. The soil profiles were obtained by idealizing q_c and f_s profiles and they were also evaluated from a system response point of view. These typical profiles were evaluated in terms of critical layer (L_{crit}) which has been defined by Cubrinovki et al. (2018), as the layer that is most likely to trigger and manifest liquefaction at the ground surface of a given site. The detailed evaluations showed that the candidate critical layers laid between 0.3 m and 4.2 m. The depth of the crust layer which is defined as the soil layers that do not liquefy ranged between 0.5 m and 4.4 m.

This project has received funding from the European Union's Horizon 2020 research and innovation programme under grant agreement No. 700748

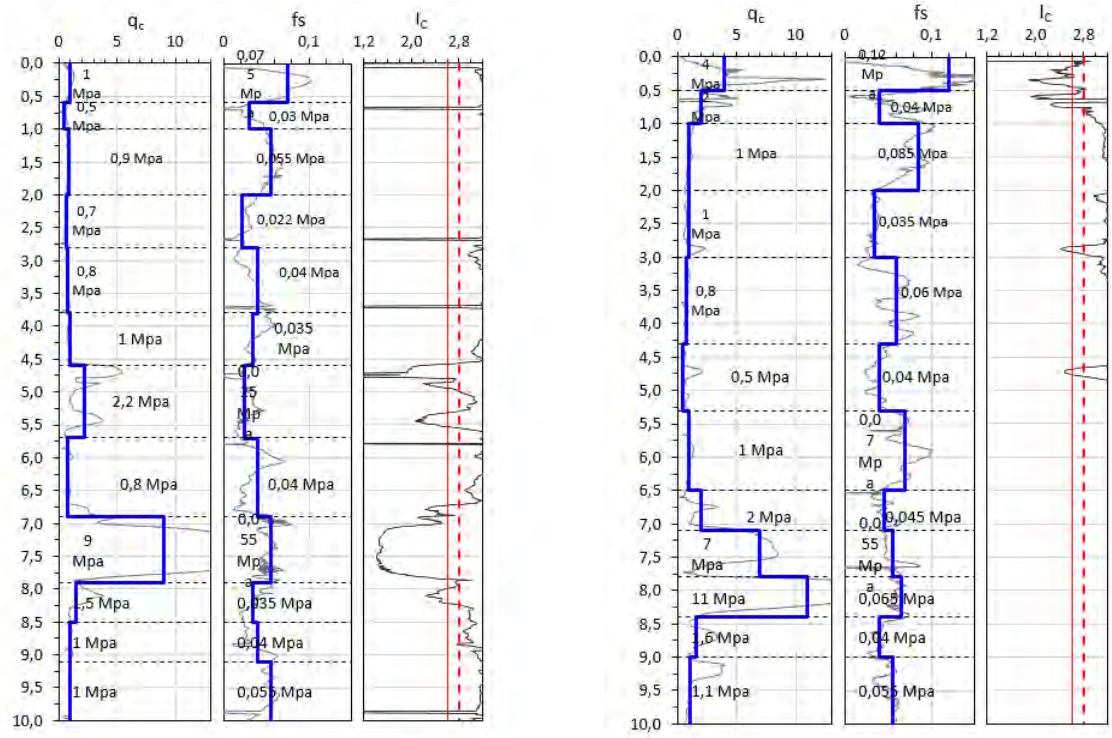

Figure 4-8: Typical CPTu profiles in Adapazari city center

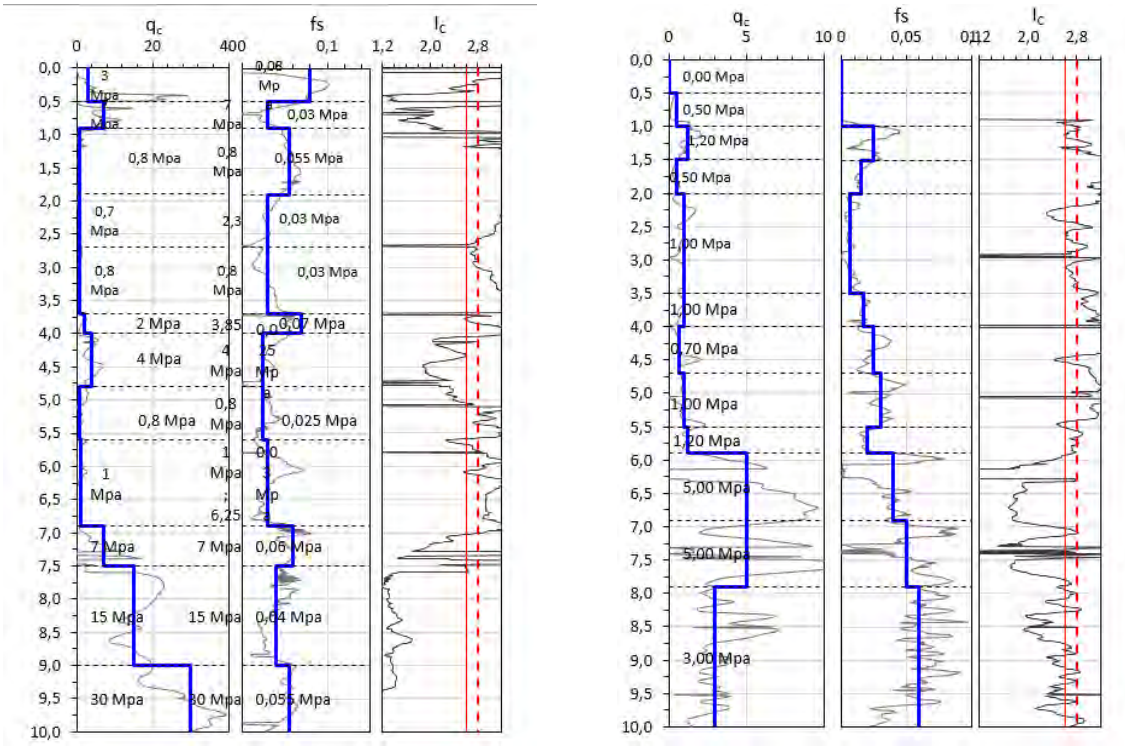

Figure 4-9: Typical CPTu profiles in Adapazari city center

This project has received funding from the European Union's Horizon 2020 research and innovation programme under grant agreement No. 700748

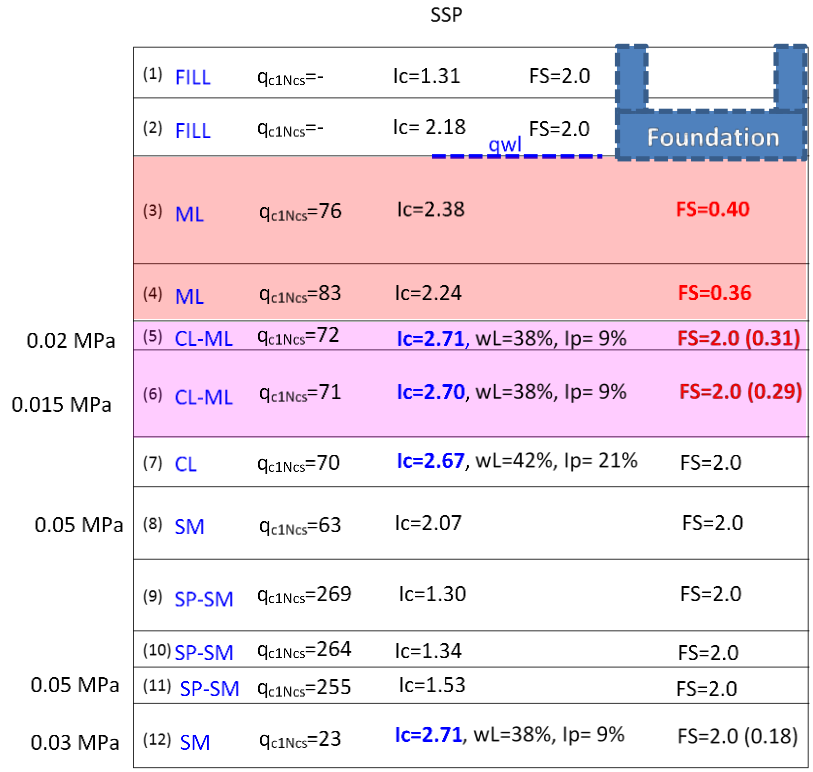

Figure 2. Soil profiles in Adapazari

Figure 4-10: Typical geotechnical characterization in Adapazari city center based on CPT data

4.2.7 Seismic demand in the studied area

The city of Adapazari is located 7 km north of the fault rupture which caused a 7.4 magnitude earthquake. As detailed in Rathje et al. (2000), the Sakarya strong motion in Adapazari is located on stiff soil in the southern part of city. The largest recorded maximum horizontal acceleration was 0.41g, however the softer sediments underlying the severely damaged sections in Adapazari is believed to amplify the intensity and increase the long period content of ground motions. In this study, an attempt was made to determine the maximum horizontal acceleration for each studied location. For this purpose, R-Crisis (Ordaz, M. and Salgado-Gálvez, M.A., 2017) software was implemented to deduce the bedrock accelerations and EERA (Bardet et al., 2000) software was used to obtain PGAs. Based on these calculations, the PGA values at the ground surface were found to range between 0.32g and 0.44g in the studied area and for each location, the corresponding PGA values were used in the liquefaction triggering analyses (Figure 2-11). These values are consistent with the peak ground acceleration (0.41g) that was measured during the earthquake.

This project has received funding from the European Union's Horizon 2020 research and innovation programme under grant agreement No. 700748

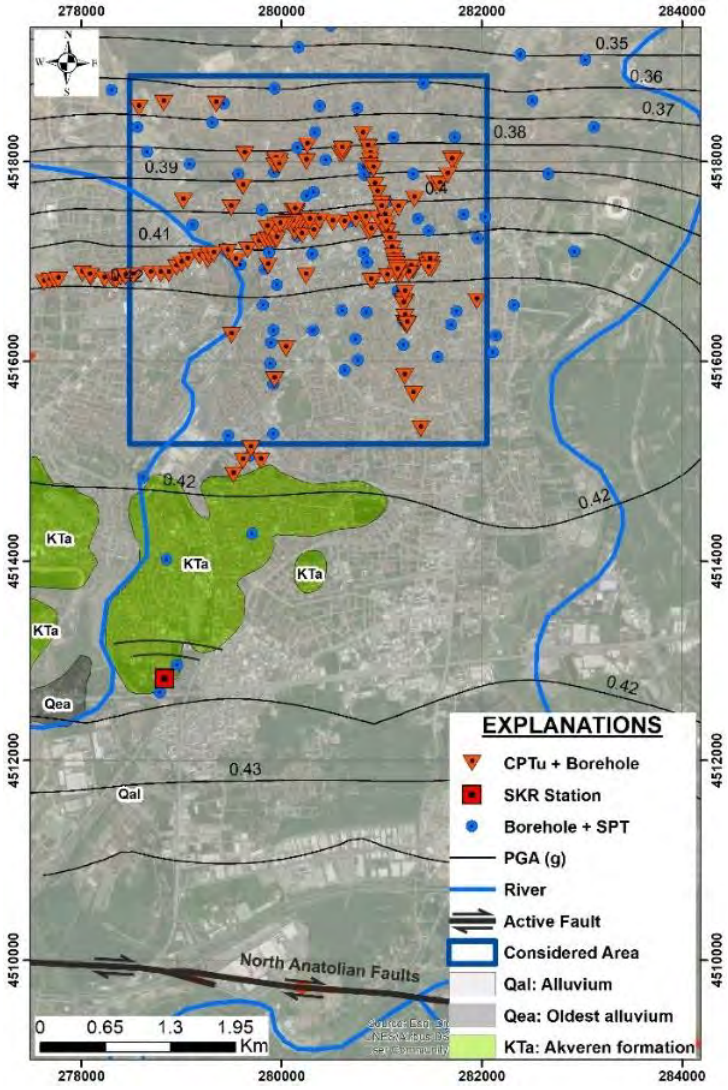

Figure 4-11: Geology of the studied region, field test locations and estimated peak ground accelerations (seismic demand).

The geology of the studied region, the locations of the CPTu's, boreholes, SPT's together with the estimated peak ground accelerations are presented in Figure 4-11. The figure shows that the studied area lies between two rivers and the main geological unit in the area is Alluvium. The location of the North Anatolian Fault is also located in the map and the distance of the fault to the studied area ranges from 5 km to 10 km.

4.2.8 Liquefaction verification methodologies

4.2.8.1 LIQUEFACT software

Using the LIQUEFACT Software begins with selection of the analysis type and identification of the location of the site. The building locations and soil data are then put as input. The next stage is defining the source causing the damage. Selection of the method for site response analysis is the following step. It may be code-

design and site specific. Selecting the appropriate fragility curves for the damaged buildings regarding their typology is another important step. These analyses can be carried out for liquefaction, liquefaction (built-in) or ground shaking and liquefaction. It is important to recall that LIQUEFACT necessitates the fragility curves for different typologies. The relevant data is also needed to calculate the loss due to the hazard. LIQUEFACT Software then runs the analyses lists the results as an EXCEL sheet and shows the results in GIS platform.

4.2.8.2 Comparison with liquefaction assessment indicators with soil-system response analysis point of view

Different liquefaction damage assessment indicators were evaluated in this study in order to compare with the observed liquefaction damage in Adapazari city center in 1999 earthquake. The indicators were calculated both from ground surface and from the foundation base. All the factor of safety values for liquefaction were calculated for free-field conditions. The indicators used in this study are Liquefaction Potential Index and Liquefaction Severity Index; applied in their original form and also from a system response point of view. The boundary value for soil behavior index (I_c) and the occurrence of seepage induced liquefaction in Adapazari silty soils above the groundwater level were also questioned.

In this context, classical and modified approaches for liquefaction vulnerability assessment were compared based on their capability to assess the liquefaction-induced building damage level. The results were then mapped in GIS platform and spatial distribution of damage levels were compared with the actual damage levels. Probable underlying mechanisms for the liquefaction induced damages in Adapazari were also briefly presented.

Context and reasoning behind the selected methodology

Following the Christchurch earthquakes in 2010 and 2011, Cubrinovski et al. (2018) recommended "soil-system response" to evaluate the liquefaction-induced damage. In this concept, main considerations are as below:

a) Liquefaction occurs in the first ten meters.

b) The liquefaction is dominated by the critical layers (L_{crit}) and in this context, the shallowest critical layer is of outmost importance. In this approach critical layer is defined as the layer which is most likely to trigger and manifest liquefaction at the ground surface of a given site. The critical layer and the layers of low liquefaction resistance that are vertically continuous form the critical zone.

c) The critical layer is characterized by q_{c1Ncs}<85.

d) The liquefiable layers between the critical layers and even the thin layers which are not liquefiable may contribute to the liquefaction. However, interbedded deposits of liquefiable and non-liquefiable soils were accepted to result in vertical discontinuity in soils that did not liquefy.

e) The first 2.5 m layer from the ground surface which does not liquefy is called the crust layer and the presence of a crust layer prevents liquefaction.

f) The soils above the groundwater table can liquefy due to seepage induced liquefaction. When liquefaction occurs in the critical zone, due to vertical communication of excess pore water pressures,

the soil above the water table at shallow depths liquefies due to an upward flow from the critical zone.

Within the context of this study, the applicability of these considerations for Adapazari cases was investigated through the studied database. Well known liquefaction damage assessment tools; Liquefaction Potential Index (LPI) and Liquefaction Severity Index (LSN) were applied to evaluate their capability of capturing the real damage. These approaches were implemented through CPTu test data and it was also aimed to see the applicability of these methodologies to saturated silts and silty sands which are dominant in the studied area.

Some modifications were also made regarding the soil behavior index, in order to include the soils with soil behavior index greater than 2.6 as being liquefiable depending on the Plasticity Index value. In this context, soils with soil behavior index greater than 2.6 and lower than 2.8 were accepted to liquefy in case their Plasticity Index (PI) values were less than 15. The PI criteria was based partially on the literature on the subject. Chinese criteria (Wang, 1979) classifies the soils with PI <12 and w_c/LL>0.85 (where w_c is natural water content) as liquefiable soils. Sancio et al. (2003) classifies the soils with PI <12 and w_c/LL>0.85 as liquefiable soils. Sancio et al. (2003) determined that soils with PI>20 did not generate significant cyclic strains after a large number of cycles at low confining stresses representing the mean effective stress for soils under the corner of the mat foundation of typical 4 to 5 story structures in Adapazari. In this context, PI of 15 can be a reasonable boundary (Oztoprak et al., 2019). Following Cubrinovski et al. (2018), seepage induced liquefaction may occur in a soil layer above groundwater level, therefore in this study, seepage induced liquefaction was considered as one of the factors within the damage assessment indicators. The indicators used in this study can be classified as classical approaches, and modified approaches. The details are given below.

Classical approaches

The approaches in this category are named as LPI-1 and LSN-1. Liquefaction Potential Index (LPI) developed by Iwasaki (1978), indicates vulnerability to liquefaction effects and evaluates the liquefaction potential of the soil using the factor of safety, the thickness of the layer and the depth of the relevant layer. Liquefaction Potential Index is estimated as;

$$\mathrm{LPI} = \int \mathrm{F_1 W(z) dz} \quad LPI = \int F_1 W(z) dz \tag{1}$$

where F1=1-FS for FS ≤1.0, F1=0 for FS>1.0 and W(z)=10-0.5z. The calculations are carried out for the top 20 m as it is accepted that liquefaction effect on the building is negligible at depths greater than 20 m. Liquefaction potential categories related to LPI are given in Table 2-1.

Table 4-1: Liquefaction Potential Index (LPI) – Iwasaki et al (1982) & Sonmez (2003).

LPI	Expected Damage Level
0	No liquefaction
0 - 2	Low
2 - 5	Moderate
5 - 15	High
≥ 15	Very high

This project has received funding from the European Union's Horizon 2020 research and innovation programme under grant agreement No. 700748

Liquefaction Severity Index (LSN), is a recent parameter which defines the liquefaction related vulnerability of structures. It was developed by Tonkin and Taylor Ltd. (2013) based on the liquefaction damage observations resulting from 2010 and 2011 New Zealand earthquakes. This value depends on the volumetric densification values and the depth weighted factor. The volumetric strains are calculated for layers with FS less than 2.0 and these values are then used to calculate the LSN values as given in Eq. 2.

$$LSN = 1000 \int \frac{\varepsilon_v}{z} dz \quad (2)$$

In this equation, ε_v is the volumetric densification or strain for 1D post-liquefaction reconsolidation and is calculated using Zhang et al. (2002) or Idriss and Boulanger (2008). z is the depth to the layer of interest in meters below the ground surface. With 1/z depth weighing factor, the effect of the depth is much more influenced compared to LPI. The liquefaction potential categories based on LSN are given in Table 4-2.

Table 4-2: Liquefaction Severity Number (LSN) by Tonkin and Taylor Ltd. (2013).

LSN	Expected Damage Level
< 10	None to Little
10 - 20	Minor
20 - 30	Moderate to Severe
30 - 40	Severe
40 - 50	Major
>50	Extensive

LPI and LSN for the first ten meters

The approaches in this category are LPI-2 and LSN-2. In this approach, the analyses were carried out for the first 10 meters as suggested by Cubrinovski et al. (2018).

Modified approaches

The last group of analyses were based on some modifications for I_c value boundary and seepage induced liquefaction concept recommended by Cubrinovski et al. (2018). These approaches were developed by Istanbul University-Cerrahpasa team within the context of the Liquefact project. The approaches in this category are named LPI-3, LPI-4, LSN-3 and LSN-4.

LPI-3 and LSN-3 values consider an upper boundary of 2.8 for I_c values coupled with a Plasticity Index of 15%. These modification was made in order to capture the actual observed damage levels. This meant that the boundary for liquefiable soils was elevated in order to include silty soils with low plasticity indices. These indicators considered the top ten meters.

For LPI-4 and LSN-4 values, seepage induced liquefaction was accepted to occur in soil layers above the ground water table. However, seepage induced liquefaction was accepted to occur in a soil layer only in cases where it satisfied the following criteria; the soil behavior type index (I_c) causing liquefaction is less than 2.8 coupled with a Plasticity Index of 15 and normalized clean sand equivalent cone tip resistance value is less than 85. It is clear that the depth of the GWL (with respect to the layer bottom) should affect this seepage induced liquefaction mechanism. In the studied cases, this depth ranged from 50 cm to 150 cm.

Application of the liquefaction assessment indicators

In order to perform liquefaction damage assessment indicators, liquefaction triggering analyses have to be performed in the first place. In this context, Cyclic Stress Ratio (CSR) and normalized clean sand equivalent cone tip resistances (q_{C1Ncs}) were used to calculate the factor of safety values through the depth using the procedures given by Boulanger and Idriss (2016) and Robertson and Wride (1998). The method developed by Robertson and Wride (1998) uses soil behavior index (I_c) which is based on cone tip resistance (q_c) and sleeve friction (f_s). Soils with higher I_c values behave more like fine-grained materials and those with lower values like granular materials. In this context, this methodology accepts that soils with I_c values greater than 2.6 are too clay rich to liquefy and therefore these soil layers are accepted to not to liquefy. This I_c value of 2.6 has also been accepted by Cubrinovski et al. (2018) as the upper boundary of liquefiable soils. The presence of I_c values greater than 2.6 in the shallow depths in typical Adapazari profiles where significant liquefaction-induced damage makes this boundary values open to discussion and this is one of the points considered in this study.

4.2.8.3 Comparison of damage in selected 55 buildings with Earthquake Induced Liquefaction Damage (EILD) with liquefaction assessment indicators

The other issue within the context of this work package was to evaluate the liquefaction induced damage in Adapazari based on the latest state of the art on the subject. In this context, fifty five buildings with well documented liquefaction induced damage performances were investigated in detail.

For these fifty five cases, the liquefaction damage assessment tools were applied to the most rigorous level and the expected damage levels were determined. The locations of these buildings are given in **Figure 2.12.** Ground Failure Indices (GFI) developed by Bray et al. (2001) were also used as a guide. This classification system is given in

This project has received funding from the European Union's Horizon 2020 research and innovation programme under grant agreement No. 700748

Table 4-3. This damage evaluation system uses an index for observed damage ranging from "no observable ground failure" to "significant ground failure" level. For each building, "Observed" ground damage level was also evaluated based on the LPI and LSN classifications given in Table 4-8 and Table 4-9. The relevant grades and damage levels were assigned based on all these classifications. It should be recalled that the majority (50) of the buildings in the 55 building database suffered from GF2 and GF3 level ground damage. Based on these classifications, the distribution of the damage states was as given in Figure 4-13.

Table 4-3: Ground Failure Index (GFI) classification system (Bray and Stewart, 2000).

Index	Description	Interpretation
GF0	No observable ground failure	No vertical movement, tilt, lateral movement or boils
GF1	Minor ground failure	Δ<10 cm; tilt of >3-story buildings <1°; no lateral movements
GF2	Moderate ground failure	10<Δ<25 cm; tilts of 1°-3°; small lateral movements (<10cm)
GF3	Significant ground failure	Δ>15 cm; tilts of>3°; lateral movements>25 cm

Note: Δ=Vertical movements

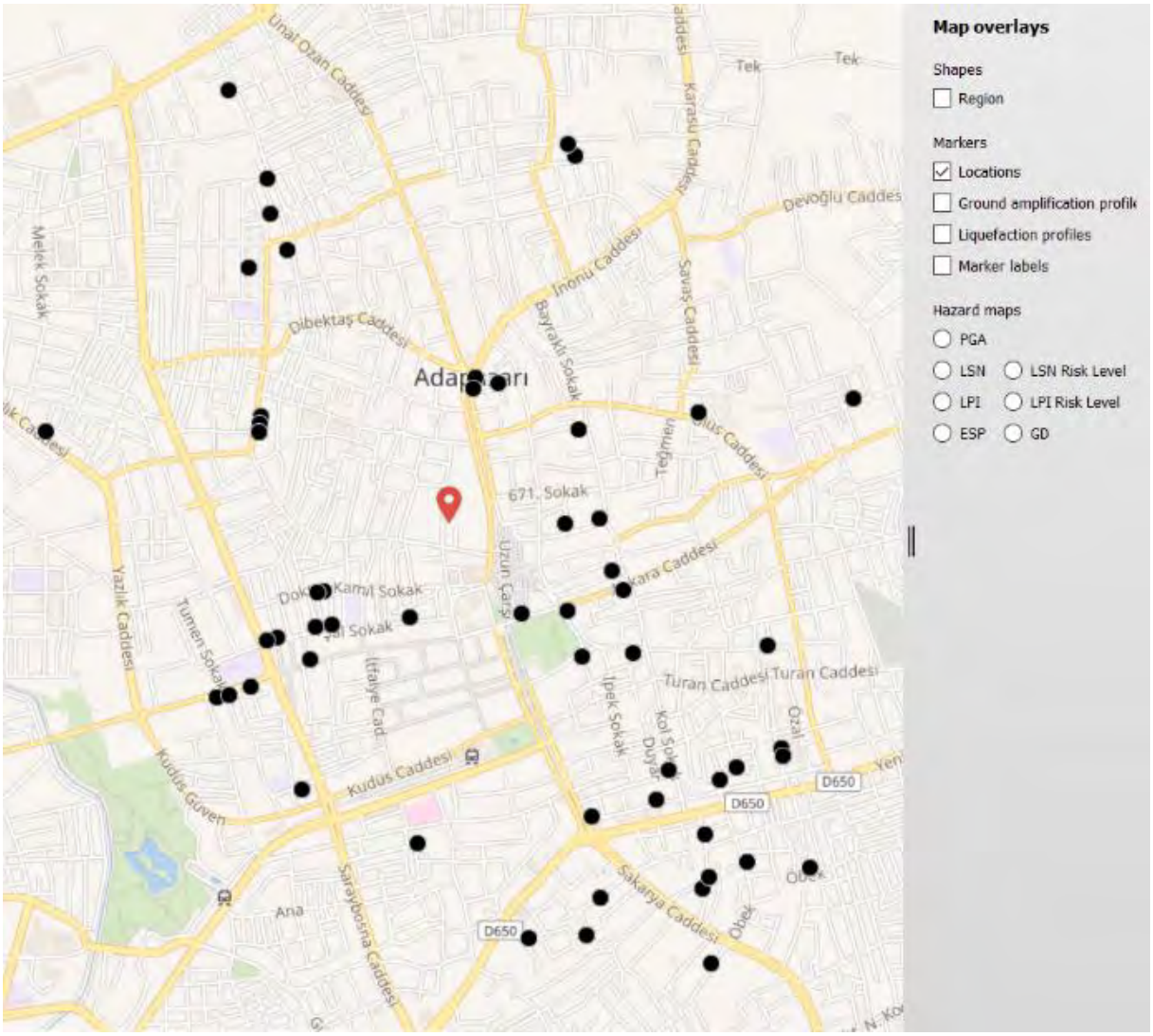

Figure 4-12: Detailed investigation for the fifty-five buildings.

This project has received funding from the European Union's Horizon 2020 research and innovation programme under grant agreement No. 700748

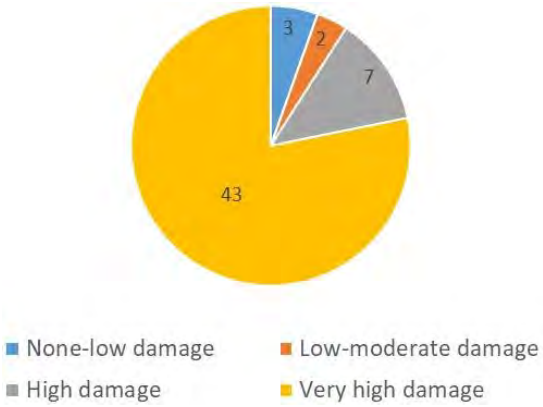

Figure 4-13: Distribution of the damage states for fifty-five studied buildings.

CPTu data that were adjacent to the buildings where liquefaction induced damage was observed were coupled with these buildings. The whole CPTu data that was compiled in this study was used in creating the spatial distribution of the damage assessment indicators and GIS mapping. 55 of these CPTU data that were adjacent to the buildings where liquefaction induced damage was observed were coupled with these buildings.

The evaluation of the results from a system response point of view revealed that almost all of the findings by Cubrinovski et al. (2018) were valid for Adapazari liquefaction cases in this study. The critical layers in Adapazari dominated the liquefaction damage and q_{c1ncs}<85. While the system response evaluations by Cubrinosvski et al. (2018) defines that a top 2.5 m crust prevents the liquefaction-induced ground damage in Christchurch cases, in Adapazari cases, it was observed that a 3.0 m crust layer below the foundation base prevented liquefaction-induced damage. This was observed in five cases, where the liquefaction damage was not observed. Considering the crust layer depth from the foundation base level is consistent with the shear induced type of liquefaction that occurred in Adapazari.

4.3 Results

4.3.1 Microzonation Works

4.3.1.1 Hazard and Risk Analyses in LIQUEFACT Software

The results for various analyses are presented in detail in Istanbul University-Cerrahpasa section in D7.2 of LIQUEFACT project. They will not be presented here for the sake of simplicity. Only some examples will be given here.

The results of hazard analyses for the 1172 buildings are given below in Figure 2-14. Obtained LSN and LPI microzonation maps were overlapped with 1172 damaged buildings in Figure 2-14. As seen from the figure, LPI demonstrates a better performance than the LSN methodology. In addition to this, selected 55 cases which correspond to only liquefaction damage, were overlapped with the microzonation maps (Figure 2-15). LPI technique leads to better performance again for estimating the damage.

4.3.2 Spatial comparison of field liquefaction with liquefaction assessment indicators

4.3.2.1 Spatial distribution of liquefaction assessment indicators to compare with the 1172 buildings

When the simplified profiles of CPT data were used for liquefaction triggering analyses, different LPI and LSN indicators could be obtained. The spatial distribution of liquefaction assessment indicators are given in Figure 4-16 for LPI indicators and in Figure 4-17 for LSN indicators. It should be recalled here that the analyses were carried out for both form the ground surface and from the foundation base.

For LPI indicators, the damage levels ranges from "Low to very high", while for LSN indicators, the range was between "None to little" to "Extensive". For LPI values calculated from the ground surface and from the foundation base, the maps were generally similar, with the "foundation base" maps being slightly superior in capturing the liquefaction damage data. LPI-4 gives the most successful estimations spatially. For LSN values, the spatial distributions give significant differences for ground surface and foundation level calculations, with the superiority being with the foundation level calculations. LSN-3 and LSN-4 maps give the most successful predictions. In all cases, LSN seems to be a better indicator for liquefaction damage assessment for Adapazari soils provided that the calculations are made from the foundation base.

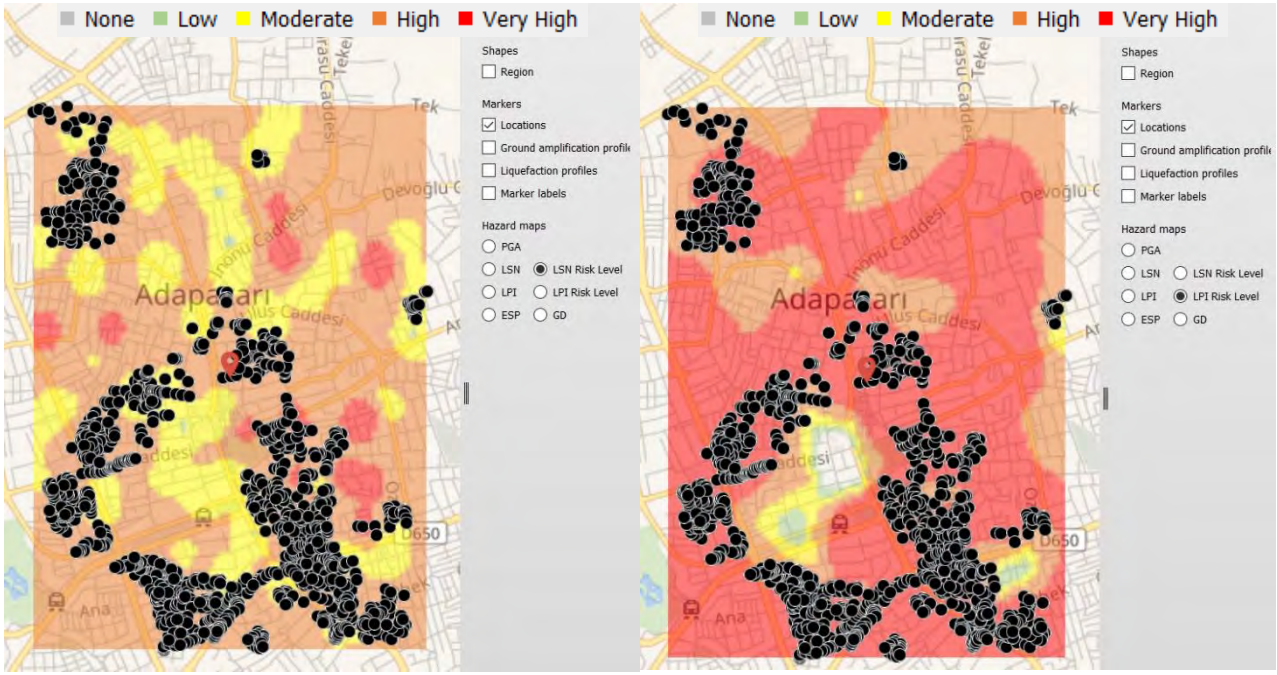

Figure 4-14: LSN and LPI microzonation maps of LIQUEFACT software with 1172 damaged buildings.

This project has received funding from the European Union's Horizon 2020 research and innovation programme under grant agreement No. 700748

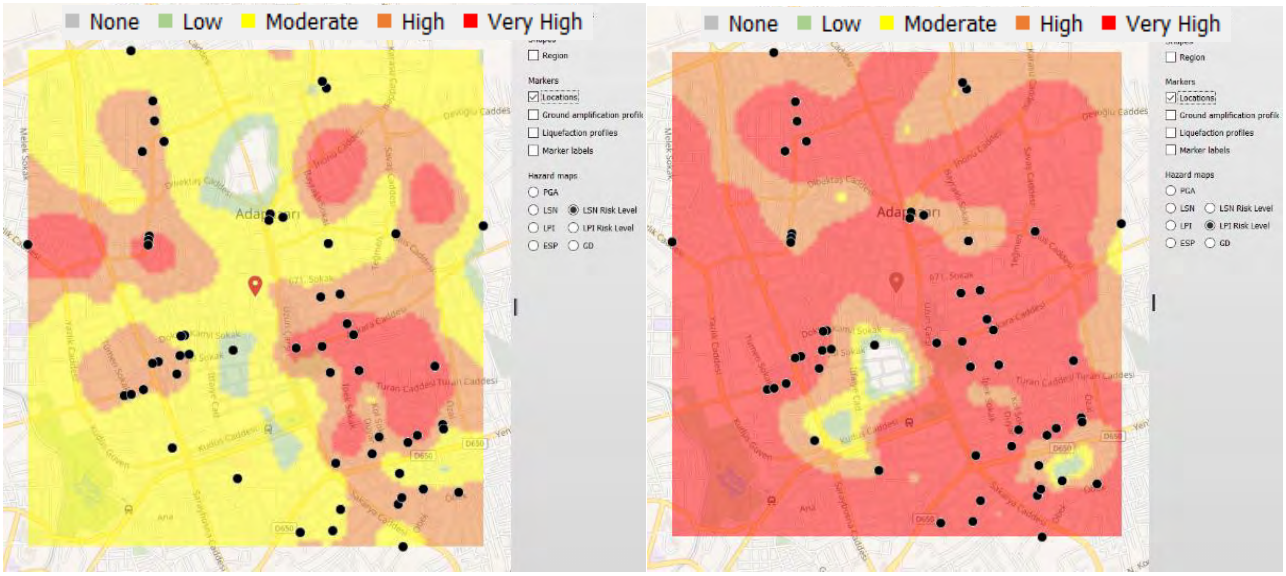

Figure 4-15: LSN and LPI microzonation maps of LIQUEFACT software with 55 damaged buildings.

This project has received funding from the European Union's Horizon 2020 research and innovation programme under grant agreement No. 700748

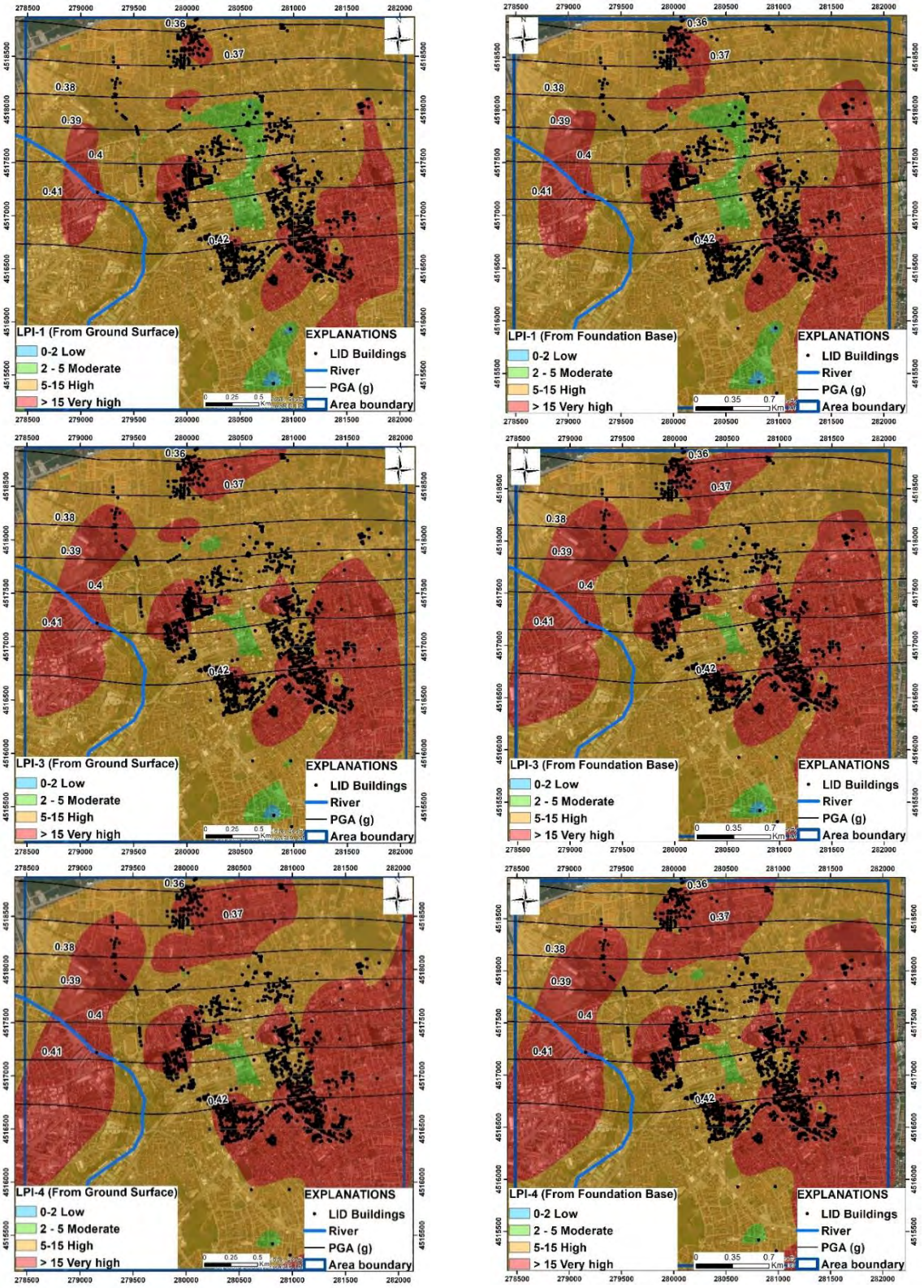

Figure 4-16: Comparison of LID buildings and Liquefaction Potential Index (LPI) maps for Adapazari considered from ground surface and foundation base.

This project has received funding from the European Union's Horizon 2020 research and innovation programme under grant agreement No. 700748

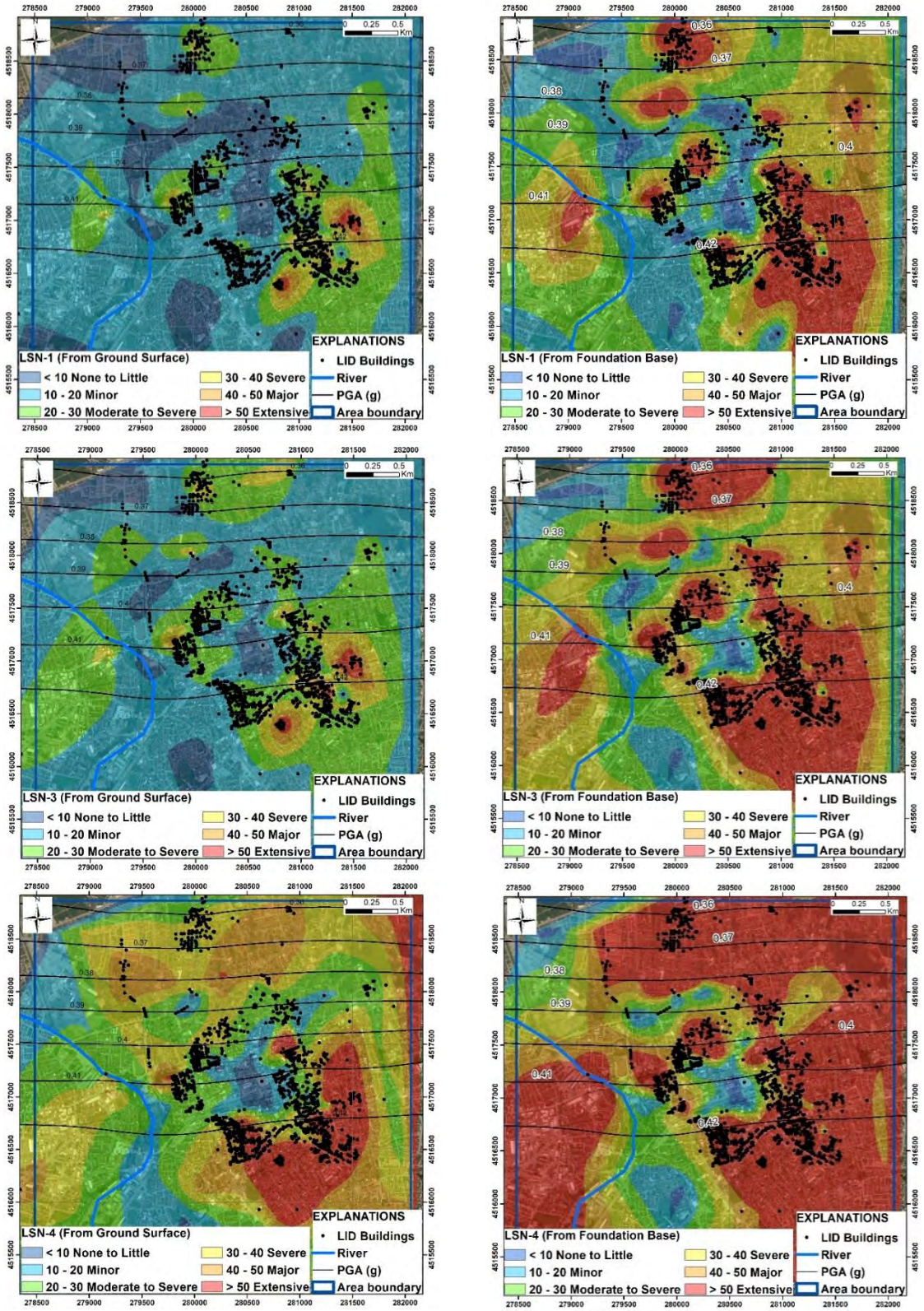

Figure 4-17: Comparison of LID buildings and Liquefaction Severity Number (LSN) maps for Adapazari considered from ground surface and foundation base.

This project has received funding from the European Union's Horizon 2020 research and innovation programme under grant agreement No. 700748

4.3.3 EILD Buildings Individually

Observed and estimated damage of selected 55 buildings were carried out. The results can be seen in **Tables 2-4, 2-5, 2-6 and 2-7**. In addition to this, output of LPI, LSN, LSN(ESP) tabulated for 526 and 55 buildings following the hazard and risk analyses were obtained.

The estimation capability of LPI and LSN methodologies for 55 buildings was evaluated in three categories. The estimation can either be a successful estimation of the damage level, an overestimation damage level or an underestimation of the damage level. After this evaluation was performed for each building, the percentages of these estimations in the whole database were calculated for each category, as a percentage. The findings are given below in Table 4-8. It should be recalled that the calculation were made both from the ground surface and from the foundation base level.

As seen in Table 4-8, when the estimations for LPI values calculated from the ground surface and foundation base are compared, the estimation percentages are found to be very close. The LPI values calculated from the ground surface and from the foundation level can predict the correct damage level as high as 50-70%. The "overestimation" percentage is about 18% for all approaches. LPI-1 and LPI-2 give similar performances in "successful estimation" percentages. The results reveal that there is not much difference if the LPI values are calculated for the first 10 m or 20 m, since the soils are generally not liquefiable for depths under 10 m in the studied area. There is slight increase in "successful" prediction percentages with LPI-4, with an estimation rate of 67%. It seems that extending the liquefiable criteria with modified I_c value coupled with a PI value increased the estimation rate. In this group, LPI-4 shows the best performance with the lowest "underestimation" percentage and highest "successful estimation" percentage. It should be recalled that for LPI-4, seepage-induced liquefaction phenomenon together with the modified I_c values coupled with a PI value is taken into account.

When the LSN results obtained from Table 4-9 are studied, it is seen that no overestimation is obtained in all cases. The main difference in the values obtained for "underestimation" and "successful estimation" rates is due to the considered level of the analyses; whether from the ground surface or from foundation base. Foundation base analyses have significantly higher "successful estimation" rates, compared to ground surface estimation rates. With LSN values from ground surface calculations, the "successful estimation" are only as high as 16%, while with the foundation base, the "successful estimation" rates increase to about 64% with LSN-1 and LSN-2 approaches. The indicators calculated with LSN-3 and LSN-4 from the foundation base, have very high successful estimation rates, 87% and 96% respectively. It is clear that when the estimations are made based on the foundation level, the LSN becomes a much better indicator as compared to ground surface calculations. The superiority of the LSN approach when the calculations are performed for the foundation level is indisputable. This may be a proof that, with the foundation level closer to the shallow liquefiable layers, the effect of "z", in Equation 2 dominates the results and therefore the correct depth to the shallowest layer of any thickness is of outmost importance. The superiority of LSN-3 approach over LSN-1 and LSN-2 may be attributed to the modified I_c and PI criteria. However, consideration of seepage induced liquefaction together with the relevant I_c and PI criteria defined in this study also seems a proper approach to estimate damage level.

Table 4-4: Observed and calculated LPI values considered from ground surface.

This project has received funding from the European Union's Horizon 2020 research and innovation programme under grant agreement No. 700748

Case #	CPT #	Building #	$D_{vertical}$ (cm)	$D_{lateral}$ (cm)	Tilt	Ground Damage Level	LPI (From Ground Surface)						Successful Estimation (Y/UE/OE)			
							Observed		LPI-1	LPI-2	LPI-3	LPI-4	LPI-1	LPI-2	LPI-3	LPI-4
							LPI	D.Level								
1	CPT-BE-A4	A-1	150	N/A	3.0	GF3-VH	15	VH	11.8	11.8	11.8	11.8	UE	UE	UE	UE
2	CPT-BE-A5	A-2	35	N/A	N/A	GF3-VH	15	VH	16.6	16.6	22.2	24.7	Y	Y	Y	Y
3	CPT-BE-B1	B-1	N/A	N/A	5.0	GF3-VH	15	VH	6.9	6.9	6.9	14.8	UE	UE	UE	Y
4	CPT-BE-B3	B-5	>25	N/A	N/A	GF3-VH	15	VH	1.5	1.5	13.2	13.2	UE	UE	UE	UE
5	CPT-BE-C1	C-3	0-10	N/A	N/A	GF0-NO	0	NL	2.5	2.5	2.5	2.5	OE	OE	OE	OE
6	CPT-BE-C3	C-1	N/A	N/A	N/A	GF3-VH	15	VH	20.6	20.6	20.6	20.6	Y	Y	Y	Y
7	CPT-BE-C4	C-2	35	57	N/A	GF3-VH	15	VH	20.4	20.4	26.3	26.3	Y	Y	Y	Y
8	CPT-BE-D1	D-1	44	N/A	2.0	GF3-VH	15	VH	10.9	10.9	10.9	19	UE	UE	UE	Y
9	CPT-BE-E1	E-1	25	N/A	2.0	GF3-VH	15	VH	14.5	14.5	14.5	14.5	Y	Y	Y	Y
10	CPT-BE-F1	F-1	45/90	N/A	N/A	GF3-VH	15	VH	21.5	21.5	21.5	22	Y	Y	Y	Y
11	CPT-BE-G2	G-1	20-25	N/A	N/A	GF2-HI	10	HI	15.5	15.5	15.5	15.5	OE	OE	OE	OE
12	CPT-BE-H2	H-1	30-35	N/A	N/A	GF3-VH	15	VH	15.8	13.4	13.4	13.4	Y	UE	UE	UE
13	CPT-BE-I4	I-4	>35	N/A	N/A	GF3-VH	15	VH	23.8	23.8	23.8	23.8	Y	Y	Y	Y
14	CPT-BE-J2	J-1	>25	N/A	N/A	GF3-VH	15	VH	28.8	28.8	28.8	28.8	Y	Y	Y	Y
15	CPT-BE-J4	J-2	21-26	N/A	N/A	GF3-VH	15	VH	29.4	29.4	34.5	34.5	Y	Y	Y	Y
16	CPT-BE-K2	K-2	20-25	N/A	N/A	GF2-HI	10	HI	15.6	15.6	15.6	15.6	OE	OE	OE	OE
17	CPT-BE-L1	L-1	>50	N/A	N/A	GF3-VH	15	VH	22.7	22.7	27	27	Y	Y	Y	Y
18	CPT-BE-LINE 1-28	KAM-11S	?	N/A	4-5	GF3-VH	15	VH	18.3	18.3	26	26	Y	Y	Y	Y
19	CPT-BE-LINE 1-30	CIN-1S	20-30	N/A	2-6	GF3-VH	15	VH	18.4	18.4	19.5	21.5	Y	Y	Y	Y
20	CPT-BE-LINE 1-34	PAP-1	10	N/A	N/A	GF1-LO	1	LO	8.2	8.2	8.2	10.5	OE	OE	OE	OE
21	CPT-BE-LINE 1-38	SER-4	0-5	N/A	1	GF2-MO	3.5	MO	6.9	6.9	6.9	6.9	OE	OE	OE	OE
22	CPT-BE-LINE 1-39	SOG-1S/L1	>50	N/A	N/A	GF3-VH	15	VH	18.1	18.1	31	35.8	Y	Y	Y	Y
23	CPT-BE-LINE 2-02	2-BE-22	>25	N/A	N/A	GF3-VH	15	VH	13.8	13.8	19.2	19.2	Y	Y	Y	Y
24	CPT-BE-LINE 2-06	2-BE-16	<10	N/A	N/A	GF1-LO	1	LO	7.2	7.2	11.6	11.6	OE	OE	OE	OE
25	CPT-BE-LINE 2-07	2-BE-13	>25	N/A	N/A	GF3-VH	15	VH	16.5	16.5	32.6	32.6	Y	Y	Y	Y
26	CPT-BE-LINE 2-10	2-BE-7	<10	N/A	N/A	GF0-NO	0	NL	5.8	5.8	5.8	5.8	OE	OE	OE	OE
27	CPT-BE-LINE 2-11	2-BE-6	>25	N/A	N/A	GF3-VH	15	VH	27.2	27.2	27.2	27.2	Y	Y	Y	Y
28	CPT-BE-LINE 3-06	3-BE-6	>25	N/A	N/A	GF3-VH	15	VH	22.9	22.9	25.2	25.2	Y	Y	Y	Y
29	CPT-BE-LINE 3-07	3-BE-2	>25	N/A	N/A	GF3-VH	15	VH	24	24	24	24	Y	Y	Y	Y
30	CPT-BE-LINE 4-05	4-O-9	>25	N/A	N/A	GF3-VH	15	VH	11.7	11.7	11.7	11.7	UE	UE	UE	UE
31	CPT-BE-LINE 4-08	4-M-1	<10	N/A	1	GF2-MO	3.5	MO	11.5	11.5	11.5	11.5	OE	OE	OE	OE
32	CPT-BE-LINE 4-10	4-K-1	10-25	N/A	1	GF2-HI	10	HI	11.8	11.8	11.8	11.8	Y	Y	Y	Y
33	CPT-BE-LINE 4-16	4-B-5	10-25	N/A	N/A	GF2-HI	10	HI	5	5	5	5	Y	Y	Y	Y
34	CPT-IUC-01	IUC-01	>40	N/A	N/A	GF3-VH	15	VH	24.7	24.7	24.7	27.5	Y	Y	Y	Y
35	CPT-IUC-03	IUC-03	>40	N/A	N/A	GF3-VH	15	VH	19.3	19.3	19.3	23.6	Y	Y	Y	Y
36	CPT-IUC-05	IUC-05	>50	N/A	N/A	GF3-VH	15	VH	29.1	29.1	42.5	48.2	Y	Y	Y	Y
37	CPT-IUC-14	IUC-14	>40	N/A	N/A	GF3-VH	15	VH	11.1	11.1	19.8	29.8	UE	UE	Y	Y
38	CPT-IUC-15	IUC-15	>40	N/A	N/A	GF3-VH	15	VH	12.8	12.8	12.8	12.8	UE	UE	UE	UE
39	CPT-IUC-16	IUC-16	>50	N/A	N/A	GF3-VH	15	VH	5	5	5	13	UE	UE	UE	UE
40	CPT-IUC-22	IUC-22	>50	N/A	N/A	GF3-VH	15	VH	8.4	8.4	10.7	16.7	UE	UE	UE	Y
41	CPT-IUC-28	IUC-28	>50	N/A	N/A	GF3-VH	15	VH	12.8	12.8	23.8	26.2	UE	UE	Y	Y
42	CPT-IUC-29	IUC-29	>50	N/A	N/A	GF3-VH	15	VH	29.5	29.5	29.5	33.7	Y	Y	Y	Y
43	CPT-IUC-31	IUC-31	>50	N/A	N/A	GF3-VH	15	VH	8.2	8.2	15.4	15.4	UE	UE	Y	Y
44	CPT-IUC-32	IUC-32	>50	N/A	N/A	GF3-VH	15	VH	20	20	20	25.6	Y	Y	Y	Y
45	CPT-IUC-33	IUC-33	<10	N/A	N/A	GF0-NO	0	NL	2.8	2.8	2.8	2.8	OE	OE	OE	OE
46	CPT-IUC-34	IUC-34	>10	N/A	N/A	GF2-MO	3.5	MO	7.3	7.3	7.3	7.3	OE	OE	OE	OE
47	CPT-IUC-35	IUC-35	>40	N/A	N/A	GF3-VH	15	VH	15.1	15.1	15.1	15.1	Y	Y	Y	Y
48	CPT-IUC-38	IUC-38	>40	N/A	N/A	GF3-VH	15	VH	11.5	11.5	18.2	19.7	UE	UE	Y	Y
49	CPT-IUC-40	IUC-40	>50	N/A	N/A	GF3-VH	15	VH	34.6	34.6	34.6	37.3	Y	Y	Y	Y
50	CPT-IUC-42	IUC-42	>50	N/A	N/A	GF3-VH	15	VH	24.5	24.5	24.5	24.5	Y	Y	Y	Y
51	CPT-IUC-43	IUC-43	>50	N/A	N/A	GF3-VH	15	VH	7.3	7.3	12.8	12.8	UE	UE	UE	UE
52	CPT-IUC-44	IUC-44	>50	N/A	N/A	GF3-VH	15	VH	3.8	3.8	12.3	14.6	UE	UE	UE	Y
53	CPT-IUC-45	IUC-45	>40	N/A	N/A	GF3-VH	15	VH	7.4	7.4	9	9	UE	UE	UE	UE
54	CPT-IUC-48	IUC-48	>50	N/A	N/A	GF3-VH	15	VH	15	15	15	15	Y	Y	Y	Y
55	CPT-IUC-50	IUC-50	>30	N/A	N/A	GF3-VH	15	VH	6.7	6.7	6.7	14	UE	UE	UE	Y

Table 4-5: Observed and calculated LPI values considered from foundation base.

This project has received funding from the European Union's Horizon 2020 research and innovation programme under grant agreement No. 700748

Case #	CPT #	Building #	$D_{vertical}$ (cm)	$D_{lateral}$ (cm)	Tilt	Ground Damage Level	LPI (From Foundation Base)						Successful Estimation (Y/UE/OE)			
							Observed		LPI-1	LPI-2	LPI-3	LPI-4	LPI-1	LPI-2	LPI-3	LPI-4
							LPI	D.Level								
1	CPT-BE-A4	A-1	150	N/A	3	GF3-VH	15	VH	12.7	12.7	12.7	12.7	UE	UE	UE	UE
2	CPT-BE-A5	A-2	35	N/A	N/A	GF3-VH	15	VH	18.4	18.4	24.5	24.5	Y	Y	Y	Y
3	CPT-BE-B1	B-1	N/A	N/A	5	GF3-VH	15	VH	7.6	7.6	7.6	15.5	UE	UE	UE	Y
4	CPT-BE-B3	B-5	20-30	N/A	N/A	GF3-VH	15	VH	1.7	1.7	14.4	14.4	UE	UE	UE	UE
5	CPT-BE-C1	C-3	0-10	N/A	N/A	GF0-NO	0	NL	2.8	2.8	2.8	2.8	OE	OE	OE	OE
6	CPT-BE-C3	C-1	N/A	N/A	N/A	GF3-VH	15	VH	22.7	22.7	22.7	22.7	Y	Y	Y	Y
7	CPT-BE-C4	C-2	35	57	N/A	GF3-VH	15	VH	22.2	22.2	28.7	28.7	Y	Y	Y	Y
8	CPT-BE-D1	D-1	44	N/A	2	GF3-VH	15	VH	11.9	11.9	11.9	19.3	UE	UE	UE	Y
9	CPT-BE-E1	E-1	25	N/A	2	GF3-VH	15	VH	15.3	15.3	15.3	15.3	Y	Y	Y	Y
10	CPT-BE-F1	F-1	45/90	N/A	N/A	GF3-VH	15	VH	23.6	23.6	23.6	23.2	Y	Y	Y	Y
11	CPT-BE-G2	G-1	20-30	N/A	N/A	GF2-HI	10	HI	17	17	17	17	OE	OE	OE	OE
12	CPT-BE-H2	H-1	30-35	N/A	N/A	GF3-VH	15	VH	17.5	17.5	17.5	17.5	Y	Y	Y	Y
13	CPT-BE-I4	I-4	>35	N/A	N/A	GF3-VH	15	VH	26	26	26	26	Y	Y	Y	Y
14	CPT-BE-J2	J-1	>25	N/A	N/A	GF3-VH	15	VH	27.7	27.7	27.7	27.7	Y	Y	Y	Y
15	CPT-BE-J4	J-2	21-26	N/A	N/A	GF3-VH	15	VH	29.7	29.7	34.7	34.7	Y	Y	Y	Y
16	CPT-BE-K2	K-2	20-30	N/A	N/A	GF2-HI	10	HI	17.1	17.1	17.1	17.1	OE	OE	OE	OE
17	CPT-BE-L1	L-1	>50	N/A	N/A	GF3-VH	15	VH	24.3	24.3	29	29	Y	Y	Y	Y
18	CPT-BE-LINE 1-28	KAM-11S	?	N/A	4-5	GF3-VH	15	VH	19.1	19.1	27.1	27.1	Y	Y	Y	Y
19	CPT-BE-LINE 1-30	CIN-1S	20-30	N/A	2-6	GF3-VH	15	VH	21.3	20.1	21.3	21.3	Y	Y	Y	Y
20	CPT-BE-LINE 1-34	PAP-1	10	N/A	N/A	GF1-LO	1	LO	9.1	9.1	9.1	9.1	OE	OE	OE	OE
21	CPT-BE-LINE 1-38	SER-4	0-5	N/A	1	GF2-MO	3.5	MO	6.9	6.9	6.9	6.9	OE	OE	OE	OE
22	CPT-BE-LINE 1-39	SOG-1S/L1	>50	N/A	N/A	GF3-VH	15	VH	19.8	19.8	34.2	34.2	Y	Y	Y	Y
23	CPT-BE-LINE 2-02	2-BE-22	>25	N/A	N/A	GF3-VH	15	VH	15.1	15.1	20.9	20.9	Y	Y	Y	Y
25	CPT-BE-LINE 2-07	2-BE-13	>25	N/A	N/A	GF3-VH	15	VH	18.5	18.5	36.1	36.1	Y	Y	Y	Y
26	CPT-BE-LINE 2-10	2-BE-7	<10	N/A	N/A	GF0-NO	0	NL	6.4	6.4	6.4	6.4	OE	OE	OE	OE
27	CPT-BE-LINE 2-11	2-BE-6	>25	N/A	N/A	GF3-VH	15	VH	30	30	30	30	Y	Y	Y	Y
28	CPT-BE-LINE 3-06	3-BE-6	>25	N/A	N/A	GF3-VH	15	VH	24.8	24.8	27.2	27.2	Y	Y	Y	Y
29	CPT-BE-LINE 3-07	3-BE-2	>25	N/A	N/A	GF3-VH	15	VH	25.9	25.9	25.9	25.9	Y	Y	Y	Y
30	CPT-BE-LINE 4-05	4-O-9	>25	N/A	N/A	GF3-VH	15	VH	12.8	12.8	12.8	12.8	UE	UE	UE	UE
31	CPT-BE-LINE 4-08	4-M-1	<10	N/A	1	GF2-MO	3.5	MO	12.6	12.6	12.6	12.6	OE	OE	OE	OE
32	CPT-BE-LINE 4-10	4-K-1	10-25	N/A	1	GF2-HI	10	HI	12.8	12.8	12.8	12.8	Y	Y	Y	Y
33	CPT-BE-LINE 4-16	4-B-5	10-25	N/A	N/A	GF2-HI	10	HI	5.5	5.5	5.5	5.5	Y	Y	Y	Y
34	CPT-IUC-01	IUC-01	>40	N/A	N/A	GF3-VH	15	VH	26.5	26.5	26.5	26.5	Y	Y	Y	Y
35	CPT-IUC-03	IUC-03	>40	N/A	N/A	GF3-VH	15	VH	19.9	19.9	19.9	19.9	Y	Y	Y	Y
36	CPT-IUC-05	IUC-05	>50	N/A	N/A	GF3-VH	15	VH	28.6	28.6	43.6	43.6	Y	Y	Y	Y
37	CPT-IUC-14	IUC-14	>40	N/A	N/A	GF3-VH	15	VH	12.2	12.2	21.9	30.7	UE	UE	Y	Y
38	CPT-IUC-15	IUC-15	>40	N/A	N/A	GF3-VH	15	VH	14.1	14.1	14.1	14.1	UE	UE	UE	UE
39	CPT-IUC-16	IUC-16	>50	N/A	N/A	GF3-VH	15	VH	5.5	5.5	5.5	11.6	UE	UE	UE	UE
40	CPT-IUC-22	IUC-22	>50	N/A	N/A	GF3-VH	15	VH	9.2	9.2	11.8	15.1	UE	UE	UE	Y
41	CPT-IUC-28	IUC-28	>50	N/A	N/A	GF3-VH	15	VH	14.4	14.4	26.3	26.3	UE	UE	Y	Y
42	CPT-IUC-29	IUC-29	>50	N/A	N/A	GF3-VH	15	VH	31	31	31	31	Y	Y	Y	Y
43	CPT-IUC-31	IUC-31	>50	N/A	N/A	GF3-VH	15	VH	9.1	9.1	16.7	16.7	UE	UE	Y	Y
44	CPT-IUC-32	IUC-32	>50	N/A	N/A	GF3-VH	15	VH	21.8	21.8	21.8	21.8	Y	Y	Y	Y
45	CPT-IUC-33	IUC-33	<10	N/A	N/A	GF0-NO	0	NL	2.8	2.8	2.8	4.6	OE	OE	OE	OE
46	CPT-IUC-34	IUC-34	10-20	N/A	N/A	GF2-MO	3.5	MO	8	8	8	8	OE	OE	OE	OE
47	CPT-IUC-35	IUC-35	>40	N/A	N/A	GF3-VH	15	VH	16.5	16.5	16.5	16.5	Y	Y	Y	Y
48	CPT-IUC-38	IUC-38	>40	N/A	N/A	GF3-VH	15	VH	12.8	12.8	19.5	19.5	UE	UE	Y	Y
49	CPT-IUC-40	IUC-40	>50	N/A	N/A	GF3-VH	15	VH	35.7	35.7	35.7	35.7	Y	Y	Y	Y
50	CPT-IUC-42	IUC-42	>50	N/A	N/A	GF3-VH	15	VH	24.9	24.9	24.9	24.9	Y	Y	Y	Y
51	CPT-IUC-43	IUC-43	>50	N/A	N/A	GF3-VH	15	VH	6.3	6.3	9.6	9.6	UE	UE	UE	UE
52	CPT-IUC-44	IUC-44	>50	N/A	N/A	GF3-VH	15	VH	4.2	4.2	13	13	UE	UE	UE	UE
53	CPT-IUC-45	IUC-45	>40	N/A	N/A	GF3-VH	15	VH	8.1	8.1	9.7	9.7	UE	UE	UE	UE
54	CPT-IUC-48	IUC-48	>50	N/A	N/A	GF3-VH	15	VH	16.3	16.3	16.3	16.3	Y	Y	Y	Y
55	CPT-IUC-50	IUC-50	>30	N/A	N/A	GF3-VH	15	VH	7.7	7.7	7.7	15	Y	Y	Y	Y

This project has received funding from the European Union's Horizon 2020 research and innovation programme under grant agreement No. 700748

Table 4-6: Observed and calculated LSN values considered from ground surface.

Case #	CPT #	Building #	$D_{vertical}$ (cm)	$D_{lateral}$ (cm)	Tilt	Ground Damage Level	LSN (From Ground Surface)						Successful Estimation (Y/UE/OE)			
							Observed		LSN-1	LSN-2	LSN-3	LSN-4	LSN-1	LSN-2	LSN-3	LSN-4
							LSN	D.Level								
1	CPT-BE-A4	A-1	150	N/A	3	GF3-EX	50	EX	32.1	32.1	32.1	32.1	UE	UE	UE	UE
2	CPT-BE-A5	A-2	35	N/A	N/A	GF3-EX	50	EX	16.2	16.2	29.1	41.4	UE	UE	UE	UE
3	CPT-BE-B1	B-1	N/A	N/A	5	GF3-EX	50	EX	13.3	13.3	13.3	44.5	UE	UE	UE	UE
4	CPT-BE-B3	B-5	20-30	N/A	N/A	GF3-EX	50	EX	2	2	25.6	25.6	UE	UE	UE	UE
5	CPT-BE-C1	C-3	0-10	N/A	N/A	GF0-NO	5	NO	3.1	3.1	3.1	3.1	Y	Y	Y	Y
6	CPT-BE-C3	C-1	N/A	N/A	N/A	GF3-EX	50	EX	33.5	33.5	33.5	33.5	UE	UE	UE	UE
7	CPT-BE-C4	C-2	35	57	N/A	GF3-EX	50	EX	33.5	33.5	38.1	38.1	UE	UE	UE	UE
8	CPT-BE-D1	D-1	44	N/A	2	GF3-EX	50	EX	20.1	20.1	20.1	71.7	UE	UE	UE	Y
9	CPT-BE-E1	E-1	25	N/A	2	GF3-EX	50	EX	37.6	37.6	37.6	37.6	UE	UE	UE	UE
10	CPT-BE-F1	F-1	45/90	N/A	N/A	GF3-EX	50	EX	33.9	33.9	33.9	40.6	UE	UE	UE	UE
11	CPT-BE-G2	G-1	20-25	N/A	N/A	GF2-SE	35	SE	17.7	17.7	17.7	17.7	UE	UE	UE	UE
12	CPT-BE-H2	H-1	30-35	N/A	N/A	GF3-EX	50	EX	23.3	21.5	21.5	21.5	UE	UE	UE	UE
13	CPT-BE-I4	I-4	>35	N/A	N/A	GF3-EX	50	EX	29.9	29.9	29.9	29.9	UE	UE	UE	UE
14	CPT-BE-J2	J-1	>25	N/A	N/A	GF3-EX	50	EX	66.8	66.8	66.8	66.8	Y	Y	Y	Y
15	CPT-BE-J4	J-2	21-26	N/A	N/A	GF3-EX	50	EX	51.5	51.5	68.8	68.8	Y	Y	Y	Y
16	CPT-BE-K2	K-2	20-30	N/A	N/A	GF2-SE	35	SE	18.9	18.9	18.9	18.9	UE	UE	UE	UE
17	CPT-BE-L1	L-1	>50	N/A	N/A	GF3-EX	50	EX	31.3	31.3	38.2	38.2	UE	UE	UE	UE
18	CPT-BE-LINE 1-28	KAM-11S	?	N/A	4-5	GF3-EX	50	EX	43.6	43.6	53.1	53.1	UE	UE	Y	Y
19	CPT-BE-LINE 1-30	CIN-1S	20-30	N/A	2-6	GF3-EX	50	EX	25.8	25.8	28.6	38.7	UE	UE	UE	UE
20	CPT-BE-LINE 1-34	PAP-1	10	N/A	N/A	GF1-MI	15	MI	20.1	20.1	12.2	12.2	Y	Y	Y	Y
21	CPT-BE-LINE 1-38	SER-4	0-5	N/A	1	GF2-MO	15	MI	17.3	17.3	17.3	17.3	Y	Y	Y	Y
22	CPT-BE-LINE 1-39	SOG-1S/L1	>50	N/A	N/A	GF3-EX	50	EX	31.8	31.8	48.6	165	UE	UE	UE	Y
23	CPT-BE-LINE 2-02	2-BE-22	>25	N/A	N/A	GF3-EX	50	EX	17.5	17.5	29.9	29.9	UE	UE	UE	UE
24	CPT-BE-LINE 2-06	2-BE-16	<10	N/A	N/A	GF1-MI	15	MI	5.9	5.9	9.9	9.9	UE	UE	UE	UE
25	CPT-BE-LINE 2-07	2-BE-13	>25	N/A	N/A	GF3-EX	50	EX	15.8	15.8	36.8	36.8	UE	UE	UE	UE
26	CPT-BE-LINE 2-10	2-BE-7	<10	N/A	N/A	GF0-NO	5	NO	5.6	5.6	7.7	7.7	Y	Y	Y	Y
27	CPT-BE-LINE 2-11	2-BE-6	>25	N/A	N/A	GF3-EX	50	EX	28.5	28.5	28.5	28.5	UE	UE	UE	UE
28	CPT-BE-LINE 3-06	3-BE-6	>25	N/A	N/A	GF3-EX	50	EX	38.1	38.1	40.6	40.6	UE	UE	UE	UE
29	CPT-BE-LINE 3-07	3-BE-2	>25	N/A	N/A	GF3-EX	50	EX	38.3	38.3	38.3	38.3	UE	UE	UE	UE
30	CPT-BE-LINE 4-05	4-O-9	>25	N/A	N/A	GF3-EX	50	EX	22.2	22.2	22.2	22.2	UE	UE	UE	UE
31	CPT-BE-LINE 4-08	4-M-1	<10	N/A	1	GF2-MO	25	MO	14.3	14.3	14.3	14.3	UE	UE	UE	UE
32	CPT-BE-LINE 4-10	4-K-1	10-25	N/A	1	GF2-MA	45	MA	19.4	19.4	19.4	19.4	UE	UE	UE	UE
33	CPT-BE-LINE 4-16	4-B-5	10-25	N/A	N/A	GF2-SE	35	SE	10.1	10.1	10.1	10.1	UE	UE	UE	UE
34	CPT-IUC-01	IUC-01	>40	N/A	N/A	GF3-EX	50	EX	35.9	35.9	35.9	55.4	UE	UE	UE	Y
35	CPT-IUC-03	IUC-03	>40	N/A	N/A	GF3-EX	50	EX	36.4	36.4	36.4	64.4	UE	UE	UE	Y
36	CPT-IUC-05	IUC-05	>50	N/A	N/A	GF3-EX	50	EX	48.9	48.9	62.7	130	UE	UE	Y	Y
37	CPT-IUC-14	IUC-14	>40	N/A	N/A	GF3-EX	50	EX	14.4	14.4	22.9	62.8	UE	UE	UE	Y
38	CPT-IUC-15	IUC-15	>40	N/A	N/A	GF3-EX	50	EX	17.4	17.4	17.4	17.4	UE	UE	UE	UE
39	CPT-IUC-16	IUC-16	>50	N/A	N/A	GF3-EX	50	EX	10	10	10	49.9	UE	UE	UE	Y
40	CPT-IUC-22	IUC-22	>50	N/A	N/A	GF3-EX	50	EX	11.6	11.6	15.8	49.7	UE	UE	UE	Y
41	CPT-IUC-28	IUC-28	>50	N/A	N/A	GF3-EX	50	EX	11.4	11.4	31.5	49.5	UE	UE	UE	Y
42	CPT-IUC-29	IUC-29	>50	N/A	N/A	GF3-EX	50	EX	49.8	49.8	49.8	107	Y	Y	Y	Y
43	CPT-IUC-31	IUC-31	>50	N/A	N/A	GF3-EX	50	EX	6.3	6.3	28.6	28.6	UE	UE	UE	UE
44	CPT-IUC-32	IUC-32	>50	N/A	N/A	GF3-EX	50	EX	29.4	29.4	29.4	63.9	UE	UE	UE	Y
45	CPT-IUC-33	IUC-33	<10	N/A	N/A	GF0-NO	5	NO	4.5	4.5	4.5	4.5	Y	Y	Y	Y
46	CPT-IUC-34	IUC-34	>10	N/A	N/A	GF2-MO	25	MO	14	14	14	14	UE	UE	UE	UE
47	CPT-IUC-35	IUC-35	>40	N/A	N/A	GF3-EX	50	EX	24.7	24.7	24.7	24.7	UE	UE	UE	UE
48	CPT-IUC-38	IUC-38	>40	N/A	N/A	GF3-EX	50	EX	13.5	13.5	38.5	50.4	UE	UE	UE	Y
49	CPT-IUC-40	IUC-40	>50	N/A	N/A	GF3-EX	50	EX	63.6	63.6	63.6	123	Y	Y	Y	Y
50	CPT-IUC-42	IUC-42	>50	N/A	N/A	GF3-EX	50	EX	42.9	42.9	42.9	42.9	UE	UE	UE	UE
51	CPT-IUC-43	IUC-43	>50	N/A	N/A	GF3-EX	50	EX	13.8	13.8	31.3	31.3	UE	UE	UE	UE
52	CPT-IUC-44	IUC-44	>50	N/A	N/A	GF3-EX	50	EX	6.6	6.6	33.9	53	UE	UE	UE	Y
53	CPT-IUC-45	IUC-45	>40	N/A	N/A	GF3-EX	50	EX	17.6	17.6	21.5	21.5	UE	UE	UE	UE
54	CPT-IUC-48	IUC-48	>50	N/A	N/A	GF3-EX	50	EX	28.6	28.6	28.6	28.6	UE	UE	UE	UE
55	CPT-IUC-50	IUC-50	>30	N/A	N/A	GF3-EX	50	EX	5.4	5.4	5.4	33.3	UE	UE	UE	UE

Table 4-7: Observed and calculated LSN values considered from foundation base.

This project has received funding from the European Union's Horizon 2020 research and innovation programme under grant agreement No. 700748

Case #	CPT #	Building #	$D_{vertical}$ (cm)	$D_{lateral}$ (cm)	Tilt	Ground Damage Level	LSN (From Foundation Base)						Successful Estimation (Y/UE/OE)			
							Observed		LSN-1	LSN-2	LSN-3	LSN-4	LSN-1	LSN-2	LSN-3	LSN-4
							LSN	D.Level								
1	CPT-BE-A4	A-1	150	N/A	3	GF3-EX	50	EX	135	135	135	135	Y	Y	Y	Y
2	CPT-BE-A5	A-2	35	N/A	N/A	GF3-EX	50	EX	21.6	21.6	54.8	54.8	UE	UE	Y	Y
3	CPT-BE-B1	B-1	N/A	N/A	5	GF3-EX	50	EX	25.8	25.8	25.8	85.1	UE	UE	UE	Y
4	CPT-BE-B3	B-5	30	N/A	N/A	GF3-EX	50	EX	3.1	3.1	57.2	57.2	UE	UE	Y	Y
5	CPT-BE-C1	C-3	0-10	N/A	N/A	GF0-NO	5	NO	4.8	4.8	4.8	4.8	Y	Y	Y	Y
6	CPT-BE-C3	C-1	N/A	N/A	N/A	GF3-EX	50	EX	108	108	108	108	Y	Y	Y	Y
7	CPT-BE-C4	C-2	35	57	N/A	GF3-EX	50	EX	107	107	113	113	Y	Y	Y	Y
8	CPT-BE-D1	D-1	44	N/A	2	GF3-EX	50	EX	55.2	55.2	55.2	96.5	Y	Y	Y	Y
9	CPT-BE-E1	E-1	25	N/A	2	GF3-EX	50	EX	87.4	87.4	87.4	87.4	Y	Y	Y	Y
10	CPT-BE-F1	F-1	45/90	N/A	N/A	GF3-EX	50	EX	76.1	76.1	76.1	66.3	Y	Y	Y	Y
11	CPT-BE-G2	G-1	20-30	N/A	N/A	GF2-SE	35	SE	32.1	32.1	32.1	32.1	Y	Y	Y	Y
12	CPT-BE-H2	H-1	30-35	N/A	N/A	GF3-EX	50	EX	54.8	54.8	54.8	54.8	Y	Y	Y	Y
13	CPT-BE-I4	I-4	>35	N/A	N/A	GF3-EX	50	EX	53.4	53.4	53.4	53.4	Y	Y	Y	Y
14	CPT-BE-J2	J-1	>25	N/A	N/A	GF3-EX	50	EX	113	113	113	113	Y	Y	Y	Y
15	CPT-BE-J4	J-2	21-26	N/A	N/A	GF3-EX	50	EX	72.8	72.8	103	103	Y	Y	Y	Y
16	CPT-BE-K2	K-2	20	N/A	N/A	GF2-SE	35	SE	33.9	33.9	33.9	33.9	Y	Y	Y	Y
17	CPT-BE-L1	L-1	>50	N/A	N/A	GF3-EX	50	EX	46.2	46.2	58.7	58.7	UE	UE	Y	Y
18	CPT-BE-LINE 1-28	KAM-11S	?	N/A	4-5	GF3-EX	50	EX	83.8	83.8	95.3	95.3	Y	Y	Y	Y
19	CPT-BE-LINE 1-30	CIN-1S	20-30	N/A	2-6	GF3-EX	50	EX	45.4	45.4	55.1	55.1	UE	UE	Y	Y
20	CPT-BE-LINE 1-34	PAP-1	10	N/A	N/A	GF1-MI	15	MI	12.2	12.2	12.2	12.2	Y	Y	Y	Y
21	CPT-BE-LINE 1-38	SER-4	0-5	N/A	1	GF2-MO	15	MI	17.3	17.3	17.3	17.3	Y	Y	Y	Y
22	CPT-BE-LINE 1-39	SOG-1S/L1	>50	N/A	N/A	GF3-EX	50	EX	77.4	77.4	101	101	Y	Y	Y	Y
23	CPT-BE-LINE 2-02	2-BE-22	>25	N/A	N/A	GF3-EX	50	EX	30	30	76.4	76.4	UE	UE	Y	Y
24	CPT-BE-LINE 2-06	2-BE-16	<10	N/A	N/A	GF0-NO	5	NO	5.9	5.9	12.7	12.7	UE	UE	Y	Y
25	CPT-BE-LINE 2-07	2-BE-13	>25	N/A	N/A	GF3-EX	50	EX	20.1	20.1	51.3	51.3	UE	UE	Y	y
26	CPT-BE-LINE 2-10	2-BE-7	<10	N/A	N/A	GF0-NO	5	NO	5.6	5.6	7.7	7.7	Y	Y	Y	Y
27	CPT-BE-LINE 2-11	2-BE-6	>25	N/A	N/A	GF3-EX	50	EX	42.7	42.7	42.7	42.7	UE	UE	UE	UE
28	CPT-BE-LINE 3-06	3-BE-6	>25	N/A	N/A	GF3-EX	50	EX	92.1	92.1	95.5	95.5	Y	Y	Y	Y
29	CPT-BE-LINE 3-07	3-BE-2	>25	N/A	N/A	GF3-EX	50	EX	83.9	83.9	83.9	83.9	Y	Y	Y	Y
30	CPT-BE-LINE 4-05	4-O-9	>25	N/A	N/A	GF3-EX	50	EX	71.3	71.3	71.3	71.3	Y	Y	Y	Y
31	CPT-BE-LINE 4-08	4-M-1	<10	N/A	1	GF2-MO	25	MO	25.4	25.4	25.4	25.4	Y	Y	Y	Y
32	CPT-BE-LINE 4-10	4-K-1	10-25	N/A	1	GF2-MA	45	MA	48.6	48.6	48.6	48.6	Y	Y	Y	Y
33	CPT-BE-LINE 4-16	4-B-5	10-25	N/A	N/A	GF2-SE	35	SE	33.6	33.6	33.6	33.6	Y	Y	Y	Y
34	CPT-IUC-01	IUC-01	>40	N/A	N/A	GF3-EX	50	EX	81.3	81.3	81.3	81.3	Y	Y	Y	Y
35	CPT-IUC-03	IUC-03	>40	N/A	N/A	GF3-EX	50	EX	121	121	121	121	Y	Y	Y	Y
36	CPT-IUC-05	IUC-05	>50	N/A	N/A	GF3-EX	50	EX	81.2	81.2	101	101	Y	Y	Y	Y
37	CPT-IUC-14	IUC-14	>40	N/A	N/A	GF3-EX	50	EX	25.1	25.1	36.1	85.7	UE	UE	UE	Y
38	CPT-IUC-15	IUC-15	>40	N/A	N/A	GF3-EX	50	EX	29.8	29.8	29.8	29.8	UE	UE	UE	UE
39	CPT-IUC-16	IUC-16	>50	N/A	N/A	GF3-EX	50	EX	19.2	19.2	19.2	82.7	UE	UE	UE	Y
40	CPT-IUC-22	IUC-22	>50	N/A	N/A	GF3-EX	50	EX	17	17	24.5	71.2	UE	UE	UE	Y
41	CPT-IUC-28	IUC-28	>50	N/A	N/A	GF3-EX	50	EX	14.3	14.3	51.3	51.3	UE	UE	Y	y
42	CPT-IUC-29	IUC-29	>50	N/A	N/A	GF3-EX	50	EX	76.4	76.4	76.4	76.4	Y	Y	Y	Y
43	CPT-IUC-31	IUC-31	>50	N/A	N/A	GF3-EX	50	EX	8	8	74.6	74.6	UE	UE	Y	Y
44	CPT-IUC-32	IUC-32	>50	N/A	N/A	GF3-EX	50	EX	82.3	82.3	82.3	82.3	Y	Y	Y	Y
45	CPT-IUC-33	IUC-33	<10	N/A	N/A	GF0-NO	5	NO	4.5	4.5	4.5	4.5	Y	Y	Y	Y
46	CPT-IUC-34	IUC-34	>10	N/A	N/A	GF2-MO	25	MO	28.1	28.1	28.1	28.1	Y	Y	Y	Y
47	CPT-IUC-35	IUC-35	>40	N/A	N/A	GF3-EX	50	EX	51.7	51.7	51.7	51.7	Y	Y	Y	Y
48	CPT-IUC-38	IUC-38	>40	N/A	N/A	GF3-EX	50	EX	25.2	25.2	85.7	85.7	UE	UE	Y	Y
49	CPT-IUC-40	IUC-40	>50	N/A	N/A	GF3-EX	50	EX	88.7	88.7	88.7	88.7	Y	Y	Y	Y
50	CPT-IUC-42	IUC-42	>50	N/A	N/A	GF3-EX	50	EX	87.8	87.8	87.8	87.8	Y	Y	Y	Y
51	CPT-IUC-43	IUC-43	>50	N/A	N/A	GF3-EX	50	EX	5.9	5.9	65	65	UE	UE	Y	Y
52	CPT-IUC-44	IUC-44	>50	N/A	N/A	GF3-EX	50	EX	11.8	11.8	88.2	88.2	UE	UE	Y	Y
53	CPT-IUC-45	IUC-45	>40	N/A	N/A	GF3-EX	50	EX	45.3	45.3	51.7	51.7	UE	UE	Y	Y
54	CPT-IUC-48	IUC-48	>50	N/A	N/A	GF3-EX	50	EX	103	103	103	103	Y	Y	Y	Y
55	CPT-IUC-50	IUC-50	>30	N/A	N/A	GF3-EX	50	EX	6.4	6.4	6.4	80	UE	UE	UE	Y

Table 4-8: LPI results for 55 buildings in Adapazari.

This project has received funding from the European Union's Horizon 2020 research and innovation programme under grant agreement No. 700748

	From ground surface				From foundation base			
	LPI-1	*LPI-2*	*LPI-3*	*LPI-4*	*LPI-1*	*LPI-2*	*LPI-3*	*LPI-4*
Successful estimation (%)	52.7	50.9	58.2	67.3	54.5	54.5	61.8	67.3
Underestimation (%)	29.1	30.9	23.6	14.5	27.3	27.3	20.0	14.5
Overestimation (%)	18.2	18.2	18.2	18.2	18.2	18.2	18.2	18.2

Table 4-9: LSN results for 55 buildings in Adapazari.

	From ground surface				From foundation base			
	LSN-1	*LSN-2*	*LSN-3*	*LSN-4*	*LSN-1*	*LSN-2*	*LSN-3*	*LSN-4*
Successful estimation (%)	16.4	16.4	20.0	40.0	63.6	63.6	87.3	96.4
Underestimation (%)	83.6	83.6	80.0	60.0	36.4	36.4	12.7	3.6
Overestimation (%)	0.0	0.0	0.0	0.0	0.0	0.0	0.0	0.0

Hazard and Risk analyses in LIQUEFACT captured the 411 of 526 of damaged cases (%78) for ESP method. This should be accepted as a good estimate. It should be recalled that ESP method was developed within the context of LIQUEFACT Project. However, LIQUEFACT was not able to discriminate the complete failure cases and less severe cases for the 47 buildings. This means that all the buildings were estimated to have very damage, while the observed damage levels ranged in the field.

For the 526 buildings and hazard analyses in LIQUEFACT, the results are listed below in Table 2-10. LSN (Classic) approach estimated the percent of no damage as 37%, while LSN(ESP) and LPI(Classic) estimations for no damage were both 22%. LSN(ESP) was a better indicator in the sense that it estimated damage levels ranging from low to very high for all buildings and there was no estimation for "no damage, none".

The results for hazard analyses in LIQUEFACT for 55 buildings are listed below in Table 2-11. LSN (Classic) approach estimated the percent of no damage as 33%, while LSN(ESP) and LPI(Classic) estimations for no damage were both 15%. LSN(ESP) and LPI(Classic) were better indicators in the sense that they estimated damage ranging from low to very high for all buildings and there was no estimation for "no damage, none".

For these 55 buildings, for hazard and risk analyses, LIQUEFACT Software estimated that 15% of the buildings would be not damaged, this is an underestimation. However, for 85% of the cases, the estimation was complete damage. It should be recalled that, complete damage estimation for all the buildings can be an overestimation, since the damage levels ranged from low to very high. However, for a spatial study, 85% correct estimation of damage should be accepted a very good estimation.

Table 4-10: Comparison of Hazard analyses for 526 buildings.

LSN (Classic)		
Damage	Observed	Liquefact Software
None	**0**	148
Low	**0**	68
Moderate	**526**	186
High		101
Very High		23
Percent of No Damage	0/526 **0%**	196/526 **37%**

LSN (ESP)		
Damage	Observed	Liquefact Software
None	**0**	0
Low	**0**	114
Moderate	**526**	39
High		58
Very High		315
Percent of No Damage	0/526 **0%**	114/526 **22%**

LPI (Classic)		
Damage	Observed	Liquefact Software
None	**0**	114
Low	**0**	0
Moderate	**526**	17
High		108
Very High		287
Percent of No Damage	0/526 **0%**	114/526 **22%**

Table 4-11: Hazard analyses for 55 buildings.

LSN (Classic)		
Damage	Observed	Liquefact Software
None	**0**	11
Low	**3**	7
Moderate	**2**	23
High	**7**	13
Very High	**43**	1
Percent of No Damage	3/55 **5%**	18/55 **33%**

LSN (ESP)		
Damage	Observed	Liquefact Software
None	**0**	0
Low	**3**	8
Moderate	**2**	4
High	**7**	5
Very High	**43**	38
Percent of No Damage	3/55 **5%**	8/55 **15%**

LPI (Classic)		
Damage	Observed	Liquefact Software
None	**0**	0
Low	**3**	8
Moderate	**2**	1
High	**7**	13
Very High	**43**	33
Percent of No Damage	3/55 **5%**	8/55 **15%**

4.4 Conclusions

This report aims to present a full and detailed case study report for the application of the risk/resilience assessment toolbox for the Adapazari EILD cases. Within the context of the project, an extensive investigation for the buildings which were affected by the 1999 Adapazari earthquake was performed. The study consisted of gathering the damage data in the city center, which was severely affected by the earthquake both due to ground shaking and/or liquefaction. In this context, several site visits were carried out by Istanbul University-Cerrahpasa team members to Adapazari city in years 2017 and 2018 to get a database of the damaged buildings in 1999 Adapazari earthquake. All the relevant literature was investigated. A damaged building database was created for Adapazari based on the Sakarya Municipality archives. The database consisted of buildings which were classified ranging from moderate damage to heavy damage in the post-earthquake investigations. This database from Sakarya Municipality consisted of 4550 buildings, 3504 of which were

"heavily damaged" and 1406 were "moderately damaged". The buildings were reported as damaged, however the database did not differentiate whether the damage was due to ground shaking or due to liquefaction. Using Yoshida et al. (2001)'s database, a region in Adapazari city center was determined as a liquefied area and then a hybrid approach was used to extract the total of 1172 buildings in this region. 526 of these buildings were identified in detail based on the Sakarya Municipality archives, while for the rest of them no data was available. These buildings were possibly affected by liquefaction. For 55 buildings, damage due to liquefaction was obvious, and these buildings constructed another database. A detailed study was also carried out to determine the soil profiles in the Adapazari city center.

The data was then used in LIUEFACT Software for hazard analyses and hazard and risk analyses. Spatial distribution of risk analyses were then compared with the field liquefaction data. The results were also compared with the well-known liquefaction indicators, which are Liquefaction Potential Index (LPI) and Liquefaction Severity Number (LSN), which were used both in original and modified forms.

For the 526 buildings and hazard and risk analyses, an evaluation was carried out for the LIQUEFACT Software results. Hazard and Risk analyses captured the 78% of the damaged cases for ESP method, which should be accepted as a good estimate. It should be recalled that ESP method was developed within the context of LIQUEFACT Project. For the 526 buildings and hazard analyses, while LSN(ESP) and LPI(Classic) estimations were better in estimating the damage than LSN(Classic). LSN(ESP) was a better indicator in the sense that it estimated damage levels ranging from low to very high for all buildings and there was no estimation for "no damage, none". The results for hazard analyses for 55 buildings, LSN(ESP) and LPI(Classic) were better indicators in the sense that they estimated damage ranging from low to very high for all buildings and there was no estimation for "no damage, none". For these 55 buildings, for hazard and risk analyses, LIQUEFACT Software estimated that 15% of the buildings would be not damaged, this is an underestimation. However, for a spatial study, 85% correct estimation of damage should be accepted a very good estimation.

The comparison with the liquefaction assessment indicators is as follows. The results showed that LSN was a better indicator for estimating the liquefaction induced damage levels in Adapazari, in case the values are calculated from the foundation base. Among the LSN approach, the best estimation rates were obtained with LSN-3 and LSN-4 approaches, which took into account the modified I_c and PI values and seepage induced liquefaction in weak layers overlying the groundwater level. This may be an evidence that, the unsaturated, shallow, weak silty layers (with normalized clean sand equivalent cone tip resistance less than 85) coupled with modified soil behavior index (I_c<2.8 and PI<15) contributed to liquefaction in 1999 Adapazari earthquake. The study carried out in this paper showed that system response approach developed by Cubrinovski et al. (2018) could be applied with great success to Adapazari silty soils. In Adapazari, liquefaction occurred in the first 10 m as described in the system response approach, however with the effect of foundation and shear stresses. The critical layers dominated the liquefaction occurrence and the shallowest critical layer was of critical importance. The saturated silty layers below the foundation levels affected to the liquefaction damage considerably no matter how thin they were. The critical layers in Adapazari were characterized by q_{c1ncs} values between 40 and 85 in all 55 cases. Seepage induced liquefaction was shown to occur in Adapazari cases, in cases where tip resistance, soil behavior index and Plasticity Index criteria were met. While the system response approach defines that a top 2.5 m crust prevents the liquefaction-induced ground damage in Christchurch cases, in Adapazari it was observed that a 3.0 m crust layer below foundation base prevented liquefaction-induced damage. These findings brought novel contributions to the literature.

This project has received funding from the European Union's Horizon 2020 research and innovation programme under grant agreement No. 700748

4.5 Bibliography

Bardet, J. P., Çetin, K. Ö., Lettis, W., Rathje, E., Rau, G., Seed, R. B., & Ural, D. 2000. Chapter 7: Soil Liquefaction, Landslides and Subsidences. Earthquake Spectra, Supplement A to Volume 16, 141–162.

Bardet, J. P., Ichii, K., & Lin, C. H. 2000. EERA, A Computer Program for Equivalent-linear Earthquake site Response Analyses of Layered Soil Deposits, August 2000, California.

Bay, J. A., & Cox, B. R. 2001. Shear Wave Velocity Profiling and Liquefaction Assesment of Sites Shaken by The 1999 Kocaeli, Turkey Earthquake. Logan: Utah State University.

Bol, E., Onalp , A., Arel, E., Sert, S., & Ozocak, A. 2010. Liquefaction of Silts: The Adapazari Criteria. Bull. Earthquake Engineering, 859-873. doi:10.1007/s10518-010-9174-x

Boulanger, R. W., & Idriss, M. 2016. CPT-Based Liquefaction Triggering Procedure. Journal of Geotechnical and Geoenvironmental Engineering, February 2016, 142(2), 1-11. doi:https://doi.org/10.1061/(ASCE)GT.1943-5606.0001388

Bray, J. D., & Stewart, J. P. 2000. Damage patterns and foundation performance in Adapazari. (T. L. Youd, J. P. Bardet, & J. D. Bray, Eds.) Earthquake Spectra, Supplement A to 16, 163-189.

Bray, J. D., Sancio, B. R., Durgunoglu, T., Onalp, A., & et al. 2004. Subsurface Characterization at Ground Failure Sites in Adapazari, Turkey. Journal of Geotechnical and Geoenvironmental Engineering, 673-685.

Bray, J. D., Sancio, R. B., Durgunoglu, H. T., Onalp, A., Seed, R. B., Stewart, J. P., Emrem C. 2001. Ground Failure in Adapazari, Turkey. Proc.of the 15th International Conference on Sol Mechanics and Geotechnical Engineering, p. 3200, Istanbul: Taylor & Français.

Cubrinovski , M., Rhodes, A., Ntritsos, N., & Ballegooy, S. V. 2018. System response of liquefiable deposits. Soil Dynamics and Earthquake Engineering, Pressed online. May 2018, https://doi.org/10.1016/j.soildyn.2018.05.013

Idriss, I. M., & Boulanger, R. W. 2008. Soil Liquefaction During Earthquakes. Oakland: Earthquake Engineering Research Institute; 2nd edition.

Iwasaki, T., Arakawa, T., & Tokida , K. 1982. Simplified procedures for assessing soil liquefaction during earthquakes. Proceedings of the Conference on Soil Dynamics and Earthquake Engineering, pp. 925-939, Southampton.

Iwasaki, T., Tatsuoka, F., Tokida, K., & Yasuda, S. 1978. A practical method for assessing soil liquefaction potential based on case studies at various sites in Japan. Proc., 2nd Int. Conf. on Microzonation, pp. 885-896, San Francisco.

Ordaz, M. and Salgado-Gálvez, M.A. 2017. R-CRISIS Validation and Verification Document. Technical Report. Mexico City, Mexico

Quintero, J., Saldanha, S., Millen, M., Viana da Fonseca, A., Sargin, S., Oztoprak, S., & Kelesoglu, M. K. 2018. Investigation into the settlement of a case study building on liquefiable soil in Adapazari, Turkey. Geotechnical and Earthquake Engineering and Soil Dynamics V, pp. 321-336, Austin, Texas: ASCE.

Oztoprak, S., Oser, C., Sargin, S., Bozbey, I., Aysal, N., Ozcep, F., Kelesoglu, M.K., Almasraf, M. 2019. Evaluation of system response approach and liquefaction damage assessment tools applied to Adapazari cases in Kocaeli 1999 Earthquake, 7th ICEGE Conference, Rome, 17-20 June.

Rathje, E., Idriss, I. M., Somerville, P., Ansal, A., Bachhubber, J., Baturay, M., Ugras, T. 2000. Strong Ground Motions and Site Effects. Earthquake Spectra, December 2000, 16(1), 65-96. doi:10.1193/1.1586147

Robertson, P. K., & Wride, C. E. 1998. Evaluating cyclic liquefaction potential using the cone penetration test. Canadian Geotechnical Journal, 442-459. doi:10.1139/t98-017

Sakarya Municipality Archives (2017-2018), Personal communication

Sancio, R. 2003. Ground Failure and Building Performance In Adapazari, Turkey. Phd. Thesis. Universtiy of California.

Sancio, R. B., Bray, J. D., Riemer, M. F., & Durgunoglu, T. 2003. An assessment of the liquefaction susceptibility of Adapazari Silt. Proc. of the7th Pacific Conference on Earthquake Engineering, pp. 172-179, Christchurch: New Zealand Society for Earthquake Engineering.

Sancio, R., Onalp, A., & Durgunoglu, H. T. 2004. Performance Of Buildings Over Liquefiable Ground In Adapazari, Turkey. 13th World Conference on Earthquake Engineering, 2. Vancouver, Canada.

Sonmez, H. 2003. Modification of the liquefaction potential index and liquefaction susceptibility mapping for a liquefaction-prone area (Inegol, Turkey). Environmental Geology, 44, 862-871.

Tonkin & Taylor Ltd. 2013. Liquefaction Vulnerability Study. Canterbury: EARTHQUAKE COMMISSION. doi:https://www.eqc.govt.nz/sites/public_files/documents/liquefaction-vulnerability-study-final.pdf

U.C Berkeley, Brigham Young Univ., UCLA, ZETAS,. 2003. Documenting Incidents of Ground Failure Resulting from the August 17, 1999 Kocaeli, Turkey Earthquake. Retrieved from https://apps.peer.berkeley.edu/publications/turkey/adapazari/index.html

Wang, W. (1979). Some findings in soil liquefaction. Beijing: Water conservancy and hydroelectric power scientific research Institute.

Yoshida, N., Tokimatsu, K., Yasuda, S., Kokusho, T., & Okimura, T. 2001. Geotechnical Aspects of Damage In Adapazari City During 1999 Kocaeli, Turkey Earthquake. Soils And Foundations, 25-45.

Zhang, G., Robertson, P. K., & Brachman, R. W. 2002. Estimating liquefaction induced ground settlements from CPT for level ground. Canadian Geotechnical Journal, 39(5), 1168-1180. doi:10.1139/T02-047

This project has received funding from the European Union's Horizon 2020 research and innovation programme under grant agreement No. 700748

This project has received funding from the European Union's Horizon 2020 research and innovation programme under grant agreement No. 700748

5 A SMALL TOWN AND INDUSTRIAL DISTRICT: TERRE DEL RENO (EMILIA ROMAGNA - ITALY)

5.1 Introduction

In May-June 2012 an intense seismic sequence hit a wide area of the southern Po Plain in Emilia Romagna (Italy) (Figure 1). Due to the high susceptibility of some deposits contained in alluvial plain, the earthquakes produced extensive liquefaction phenomena, probably the most impactant in the last century in Italy (Berardi et al., 1991). Two mainshocks were particularly severe (Figure 5-1): the first one, with ML 5.9, occurred on May 20th with epicenter between Finale Emilia, S. Felice sul Panaro and S. Martino Spino; the second one, with ML 5.8, occurred in May 29th about twelve km southwest of the previous mainshock. Both mainshocks occurred on about E-W trending, S dipping blind thrust faults; the whole aftershocks area extends in an E-W direction for more than 50 km and includes five ML≥5.0 events and more than 1800 ML>1.5 events. Ground cracks and liquefactions evidences (sand boils, settlement and tilting of structures) were among the most relevant coseismic effects observed during the Emilia sequence. Totally, the area affected by liquefaction during the May 20th and May 29th events covered about 1200 km^2.

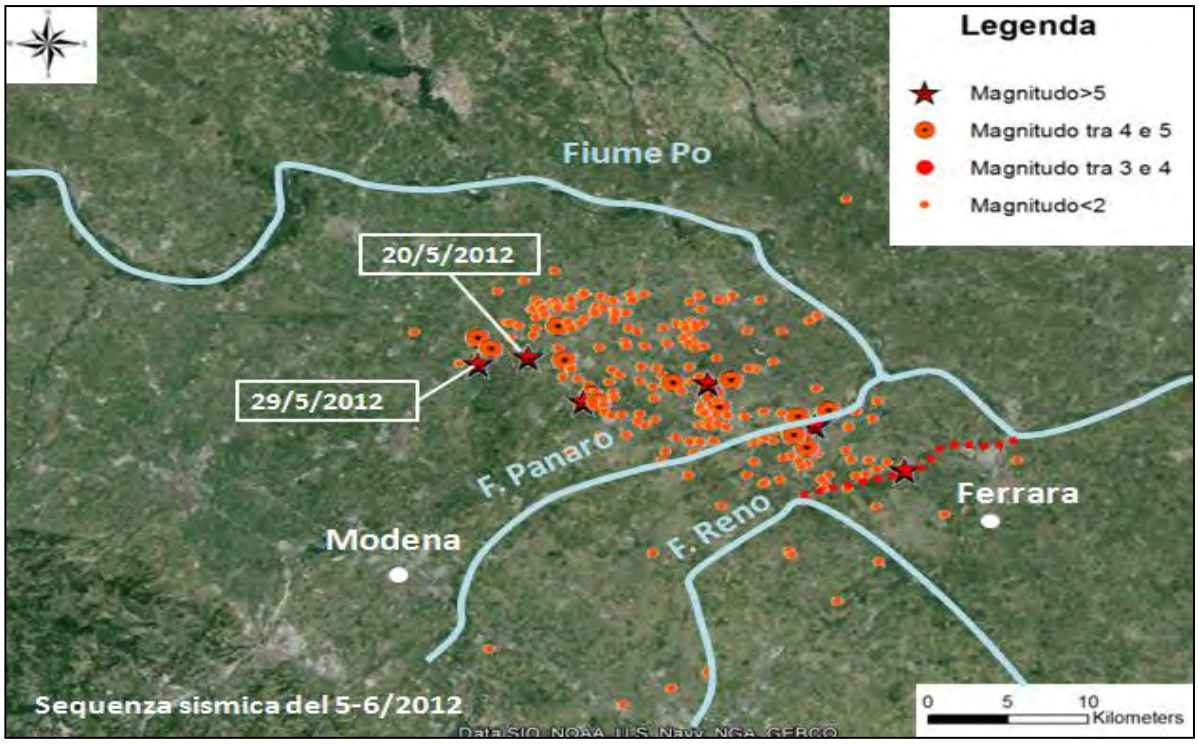

Figure 5-1 The earthquake sequence of May – June 2012 in Emilia.

The Emergeo Working Group (2013) performed a systematic survey of the earthquake sequence area through field, aerial and interview approaches. Data regarding 1362 observation were collected, stored in a

geographical information system, and made partially available at the address http://www.esriitalia.it/emergeo/. The observations were grouped into three categories: (i) liquefaction; (ii) fracture/liquefaction; and (iii) fracture. On the whole number of 1362 sites with coseismic effects identified and surveyed over more than 1200 km^2; 768 were classified as fracture/ liquefaction, 485 as liquefaction, and 109 as fracture (Figure 5-2). Soon it appeared that liquefaction evidences were not evenly distributed over the area, but tended to concentrate along preferential alignments, mostly dictated by the presence of paleo-riverbeds, levees, out-flow channels and fans (Figure 5.4) that are characterised by the presence of sandy layers a relatively shallow depths. The maximum distance of observed liquefaction phenomena from epicentres is about 30 km, in agreement with the regional empirical relations proposed by Galli (2000). In terms of liquefaction hazard, the spatial distribution reflects the combined effects of soil susceptibility (loose cohesionless soil with shallow water table) and ground motion intensity. The area affected by liquefaction can be roughly represented as the projection to the surface of the seismogenic source (e.g. the area affected by surface deformation); stratigraphic and hydrological conditions in the upper 5–10m are then the discriminator to identify the areas subjected to liquefaction.

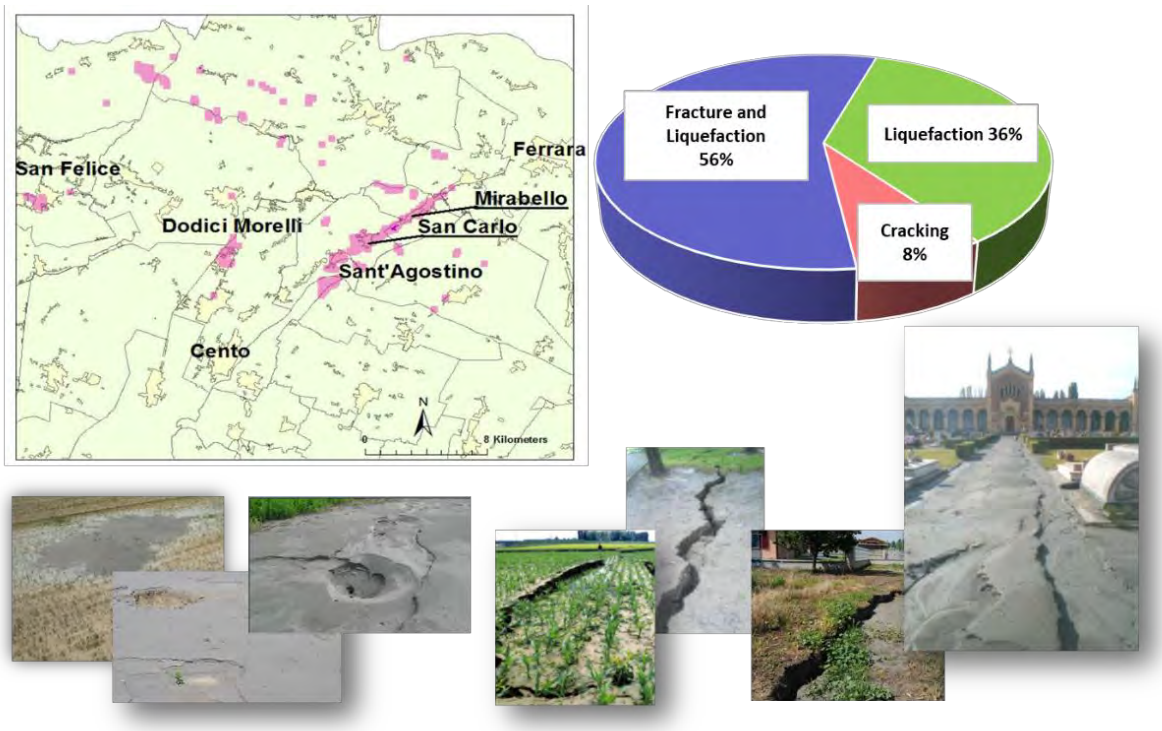

Figure 5-2 Liquefaction evidences after 2012 earthquakes in Emilia.

The area affected by liquefaction is also one of the most productive in Italy, hosting a high concentration of agricultural production, agri-food, industrial and handicraft units. Several industrial plants of international relevance are located in the area. For 2011, Italian Institute of Statistics (ISTAT, 2018) recognised for this area a gross product of 19.6 billion euro that generated 12.2 billion euros of exports. Only in the crater of the

This project has received funding from the European Union's Horizon 2020 research and innovation programme under grant agreement No. 700748

earthquakes, that included 33 municipalities, there are about 48 thousand companies and 187.000 employees (Figure 5-3).

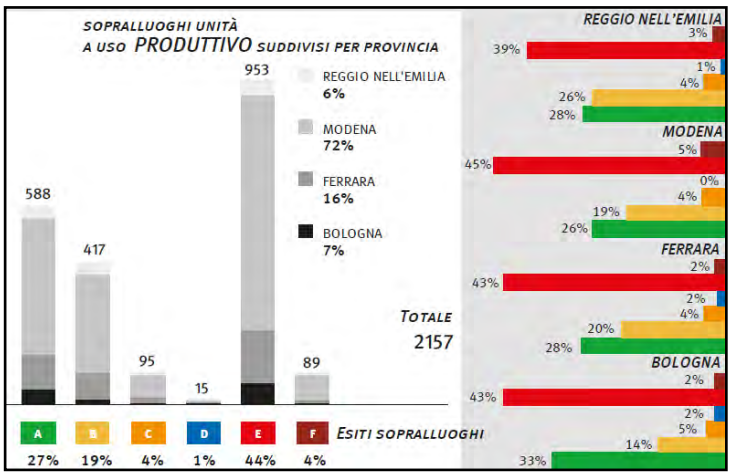

Figure 5-3 Outcome of post-earthquake damage inspections on productive activities ("Servizio Geologico, Sismico e dei Suoli, 2012").

5.1.1 The Municipality of Terre del Reno

The municipalities of Mirabello and Sant'Agostino, the latter including the village of San Carlo, were merged in 2017 to form a unique municipality named Terre del Reno. Here, the M_w6.1 earthquake of May 20th caused extensive damages due to liquefaction: only in the village of San Carlo 186 buildings of a total of 660 were damaged at different levels (ISTAT, 2018). In this area Galli (2000) and Romeo et al. (2012) highlighted the presence of hidden paleochannels and paleo-levees (Figure 5-4), as can be seen from the Digital Elevation Model of the area.

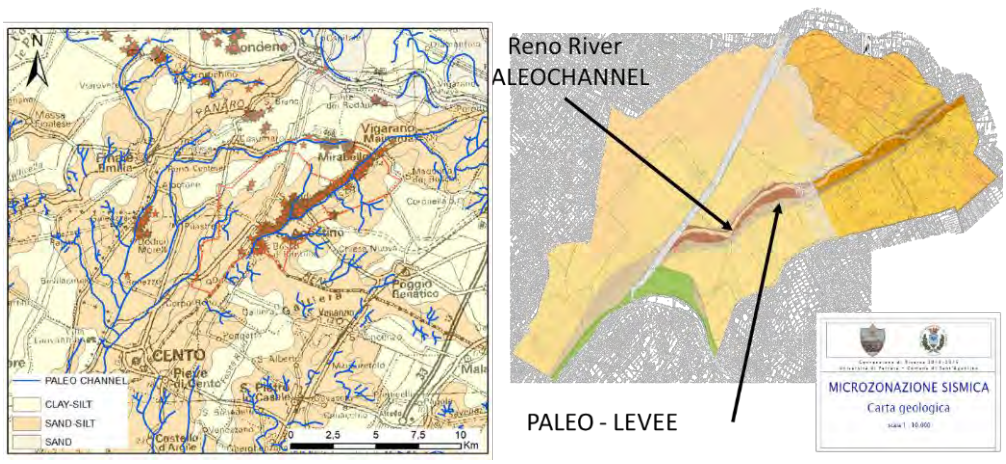

Figure 5-4 Geological features and paleochannels of the study area (on the left). Geological Map on the right shows that the district of Terre del Reno is located along the old Reno River Paleochannel.

After the May-June 2012 seismic sequence, the Emilia Romagna Region encouraged the collection of all available geological and geotechnical data to form a database accessible from all involved parties. Since then,

the database has been constantly updated and nowadays (datum at January 2018) it includes more than 85.000 tests (boreholes, various penetrometer tests etc.), distributed over the entire regional territory (Figure 5.5.a). Additionally, a database has been created accessing the Geoportale Nazionale (http://www.pcn.minambiente.it), collecting information on the buildings present in the area (Figure 5.5.b). A collection of effects recorded after the 2012 Emilia seismic sequence in northern Italy is available from Emergeo Working Group of INGV (Figure 5-5c), while post-earthquake rapid inspections (Aedes format, Baggio 2009) and detailed engineering evaluation on damaged-buildings were undertaken both to assess the safety of structures after the sequence and to plan the rebuilt.

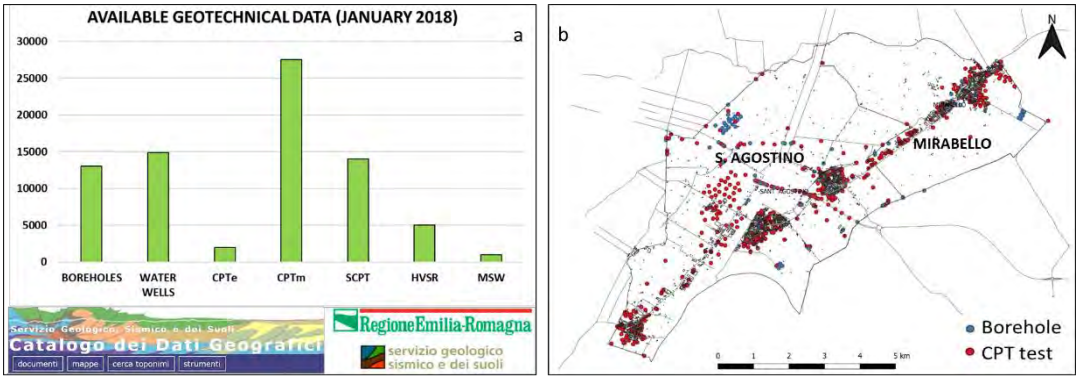

BUILDING LOCATION			MODEL BUILDING TYPE MBT							
BUILDING ID	LONG.	LAT.	BUILDING TYPOLOGY	SLABS	ROOF	TYPE OF FOUNDATION	NUMBER OF STOREYS (ABOVE THE GROUND)	NUMBER OF UNDERGROUND STOREYS	STOREY HEIGHT [m]	PERIOD OF CONSTRUCTION

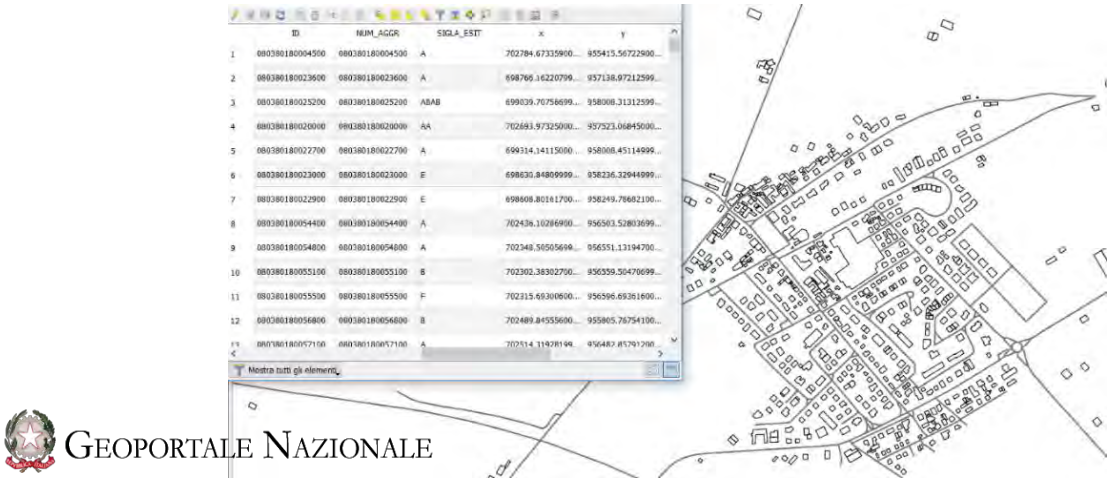

Figure 5-5 Summary of the available investigations in the Emilia Romagna Region Geotechnical Database (a); position of available CPTs (around 1000) and boreholes (≈200) in Terre del Reno (b); example of buildings data from the Geoportale Nazionale (http://www.pcn.minambiente.it) (c).

This project has received funding from the European Union's Horizon 2020 research and innovation programme under grant agreement No. 700748

5.2 Liquefaction hazard assessment

The assessment of liquefaction hazard for the Municipality of Terre del Reno has been performed following the flow chart ofFigure 5-6. According to this scheme, liquefaction hazard is given by the combination of seismic hazard and liquefaction susceptibility, that are the two subjects shown in the next paragraphs.

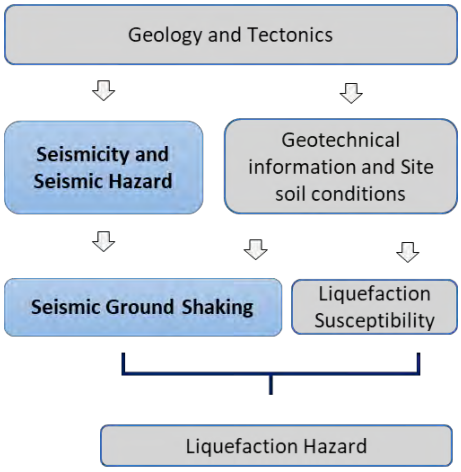

Figure 5-6 Flowchart describing the hazard assessment for the study area.

5.2.1 Seismicity

The present analysis is focused on the seismic scenario of May 20th earthquake. Figure 5-7shows a map of the area affected by earthquakes in 2012 (Emergeo, 2013) reporting the main active faults determining the seismic events (a, b and c). The position of historical events recorded in the area is also reported (d) showing that liquefaction already affected the area in Ferrara (1570) and Finale Emilia (1639).

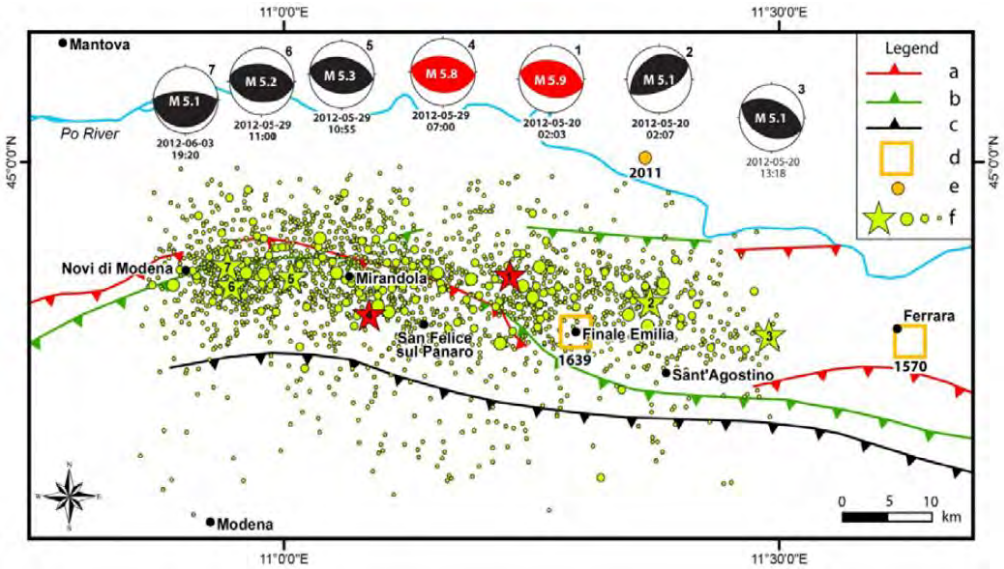

Figure 5-7 Epicenters of the 2012 Emilia seismic sequence and location of historical liquefaction ground observations (Emergeo, 2013).

The yellow dots (f) represent the epicenter position of all seismic events of the sequence, while the events with Magnitude greater than 5.5 are highlighted with red cross. The list of earthquakes with Magnitudes higher than 5 is also summarized in Table 5-1.

In the Liquefact toolbox software, the 20th May 2012 seismic scenario is reproduced giving the fault location, strike/dip, the magnitude and the fault mechanism. Here it is seen that mean PGA estimated in the municipality of Terre del Reno was around 0.24 g (Figure 5-8).

The characteristics of the subsoil include values of $Vs_{,30}$ generally less than 200 m/s (Martelli et al., 2013, Stefani et al., 2014, Università di Ferrara, 2014).

Table 5-1 Magnitude and location of Earthquakes with Magnitude greater than 5..

Tempo Origine (UTC)	Latitudine	Longitudine	Profondità (Km)	Magnitudo
2012-05-20 02:03:52	44,89	11,23	6,3	5,9
2012-05-20 02:07:31	44,86	11,37	5	5,1
2012-05-20 13:18:02	44,83	11,49	4,7	5,1
2012-05-29 07:00:03	44,85	11,09	10,2	5,8
2012-05-29 10:55:57	44,89	11,01	6,8	5,3
2012-05-29 11:00:25	44,88	10,95	5,4	5,2
2012-06-03 19:20:43	44,9	10,94	9,2	5,1

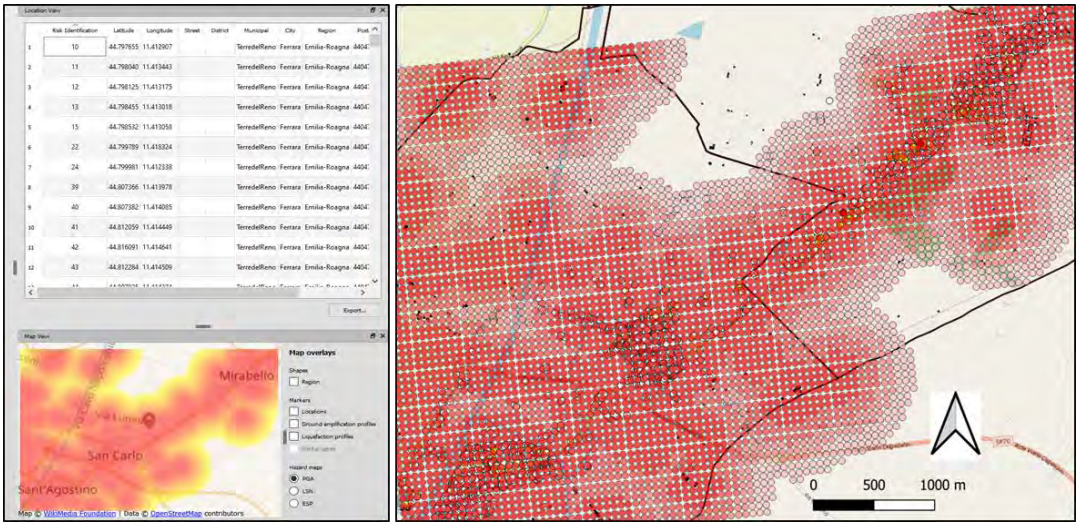

Figure 5-8 The 20 May 2012 (M_w6.1) Earthquake scenario was reproduced in Liquefact software toolbox and a mean PGA of 0.24g was calculated on the study area.

This project has received funding from the European Union's Horizon 2020 research and innovation programme under grant agreement No. 700748

5.2.2 Liquefaction Susceptibility

From a geological viewpoint, Youd and Perkins (1978) classify the Holocene deposit of the territory of Terre del Reno as moderately to highly susceptible of liquefaction.

Table 5-2 Liquefaction susceptibility of sedimentary deposits (Youd & Perkins, 1978).

Type of deposit (1)	General distribution of cohesionless sediments in deposits (2)	Likelihood that Cohesionless Sediments, When Saturated, Would Be Susceptible to Liquefaction (by Age of Deposit)			
		<500 yr (3)	Holocene (4)	Pleistocene (5)	Pre-pleistocene (6)
(a) Continental Deposits					
River channel	Locally variable	Very high	High	Low	Very low
Flood plain	Locally variable	High	Moderate	Low	Very low
Alluvial fan and plain	Widespread	Moderate	Low	Low	Very low
Marine terraces and plains	Widespread	—	Low	Very low	Very low
Delta and fan-delta	Widespread	High	Moderate	Low	Very low
Lacustrine and playa	Variable	High	Moderate	Low	Very low
Colluvium	Variable	High	Moderate	Low	Very low
Talus	Widespread	Low	Low	Very low	Very low
Dunes	Widespread	High	Moderate	Low	Very low
Loess	Variable	High	High	High	Unknown
Glacial till	Variable	Low	Low	Very low	Very low
Tuff	Rare	Low	Low	Very low	Very low
Tephra	Widespread	High	High	?	?
Residual soils	Rare	Low	Low	Very low	Very low
Sebka	Locally variable	High	Moderate	Low	Very low
(b) Coastal Zone					
Delta	Widespread	Very high	High	Low	Very low
Esturine	Locally variable	High	Moderate	Low	Very low
Beach					
High wave energy	Widespread	Moderate	Low	Very low	Very low
Low wave energy	Widespread	High	Moderate	Low	Very low
Lagoonal	Locally variable	High	Moderate	Low	Very low
Fore shore	Locally variable	High	Moderate	Low	Very low
(c) Artificial					
Uncompacted fill	Variable	Very high	—	—	—
Compacted fill	Variable	Low	—	—	—

Additionally, data from geotechnical investigation have been interpreted for this analysis. Out of 1 000 CPT profiles available for the whole area of Sant'Agostino and Mirabello, more than 700 CPT profiles have been used after filtering data with the geostatistical tools described in Figure 1.6 to reconstruct the geotechnical model of the area, about 150 of them are located in the village of S. Carlo. The liquefaction susceptibility has been evaluated adopting the Equivalent Soil Profile methodology defined in the deliverable D3.2 (par.2.3.4). Together with a classification in 22 different classes, the method provides an error index (the standard normed error) that quantifies the difference of the real profile with an equivalent three-layer model.Figure 5-9, showing a summary of results for Terre del Reno, confirms that almost 88% of the subsoil profiles investigated with CTPs can be considered as three-layer models, i.e. a single liquefiable layer separated by large non-liquefiable layers. About 70% of the stratified subsoil can be classified as weak from the viewpoint of liquefaction. This result stem from the geological history of the site, given by the presence of the paleo-river of Fiume Reno (Fioravante et al., 2013), that for a period of three centuries crossed the Territory of Terre del Reno (Bondesan & Bondesan, 2017).

This project has received funding from the European Union's Horizon 2020 research and innovation programme under grant agreement No. 700748

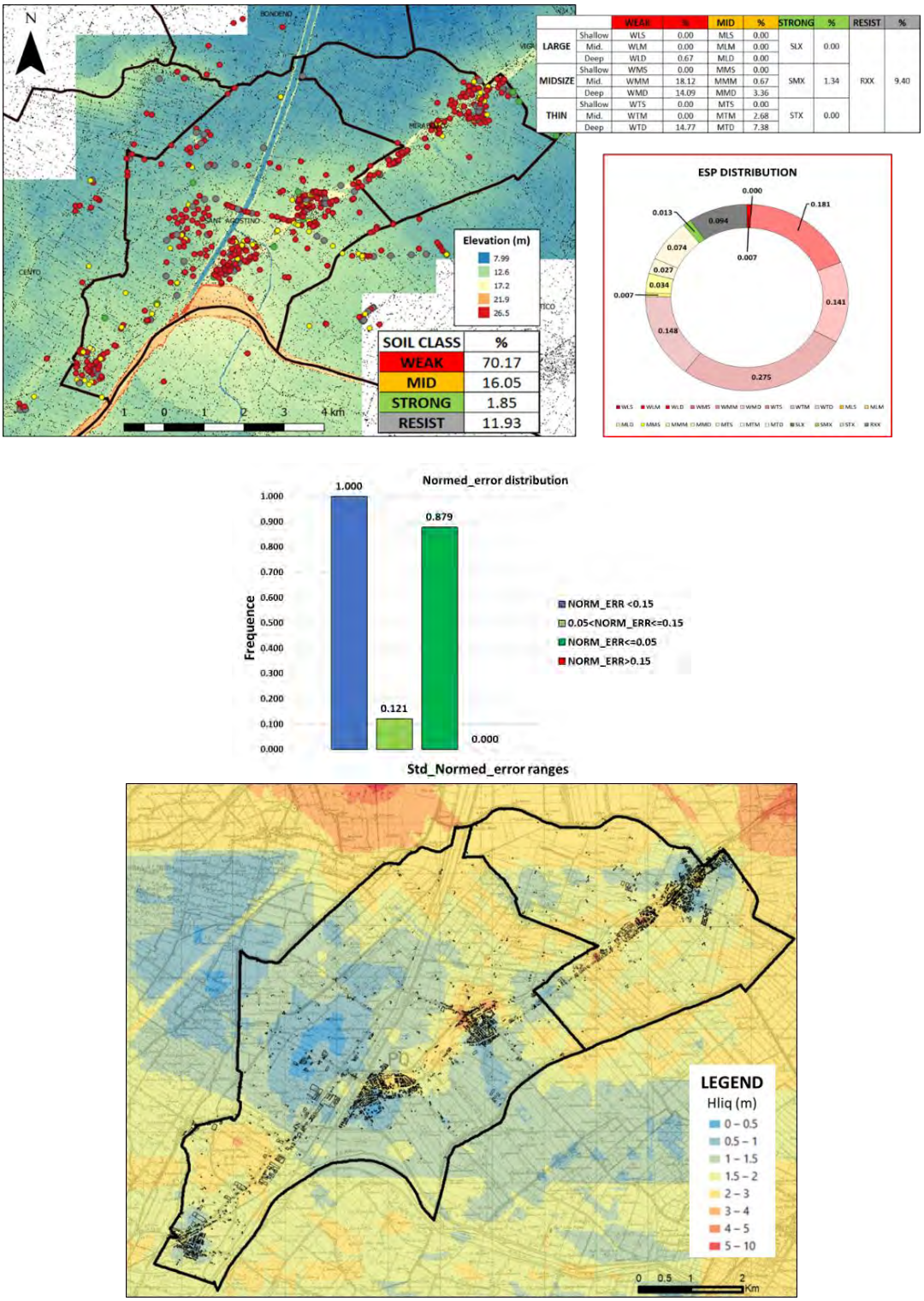

Figure 5-9 Overview of the ESP distribution over the territory of Terre del Reno(a); Histograms of the ESP Standard _Normed_Error ($Std\ Normed\ Err = Normed\ error * 20/Max\ depth$) (b); Map of the thickness of liquefiable layer evaluated through the ESP method (c).

This project has received funding from the European Union's Horizon 2020 research and innovation programme under grant agreement No. 700748

The recalled ESP method identifies the best combination of (H_crust, H_liq, CRR) that gives the lowest normed error compared with the real profile. An example of result the Municipality of Terre del Reno is here represented (Figure 5-10 .c) as thickness of liquefiable layer (H_liq) evaluated from the available CPT profiles. It can be seen that, the geotechnical model highlights the presence of liquefiable layers with variable thickness from 2 to 5 m and more variously concenrated below the three districts of Sant'Agostino, San Carlo and Mirabello.

Concerning the groundwater conditions, monitoring of the hydraulic head was undertaken by the Emilia-Romagna region over the districts where liquefaction was estensively observed from June 2012. The conditions existing at May 2012 have been reconstructed from information and reports published by the Emilia-Romagna working group (Regione Emilia-Romagna, PG.2012.0134978 del 31/5/2012a; Regione Emilia-Romagna, PG.2012.0134978 del 31/5/2012b;) integrated with monitoring wells (Figure 5-10).

In the present analysis the position of the groundwater table has been fixed averageing over each discrict the values from the maps of Figure 5-10 and considering a rise due to the hydraulic connection between contiguous layers (Cubrinovski & van Ballegooy (2017) call this effect system response). This effect noticed in this case during the major earthquakes (Martelli, 2012), but also in other examples (e.g. Christchurch) has been broadly quantified in 1.5 metres.

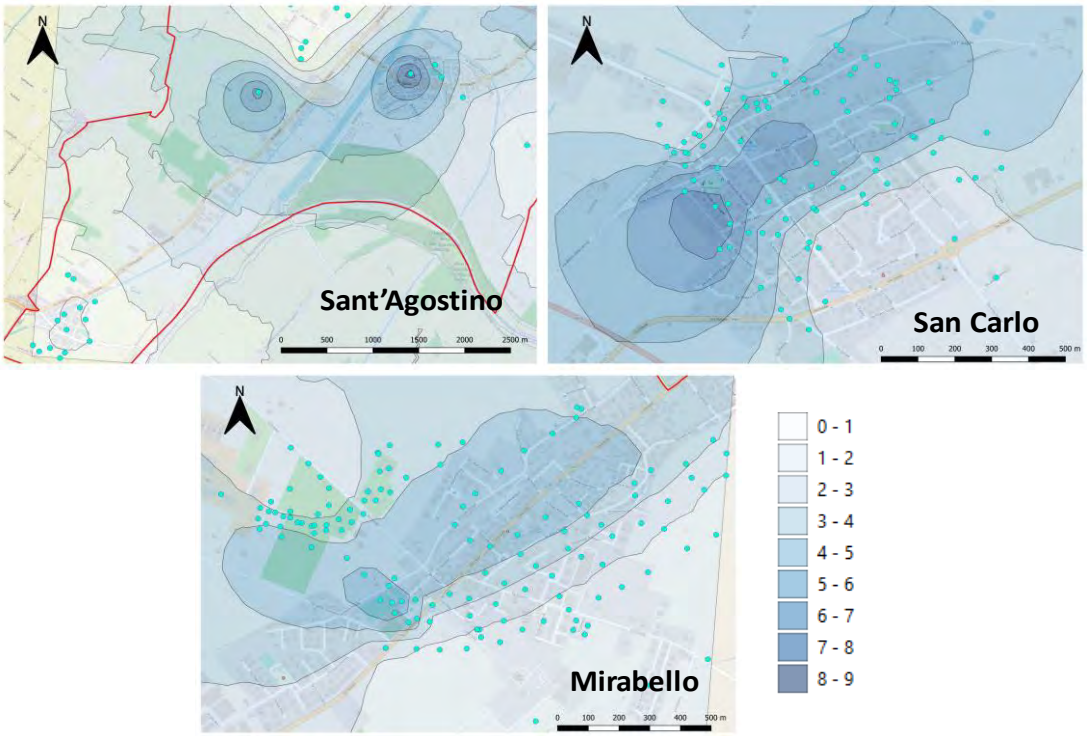

Figure 5-10 Map of groundwater depth over the districts of S. Agostino, S. Carlo and Mirabello.

5.2.3 Liquefaction severity indicators

The analysis of the traditional liquefaction hazard, carried out on the entire municipality of Terre del Reno, is reported here for the (Mw 6.1) May 20th 2012 earthquake. The liquefaction safety factor evaluated with the Boulanger & Idriss (2014) procedure forms the basis for computing the Liquefaction Potential Index (LPI-Iwasaki et al., 1978), the Ishihara inspired Liquefaction Potential Index (LPI_{ISH} - Maurer, 2015), the post liquefaction settlement (w - Zhang et al., 2002) and the Liquefaction Severity Number (LSN – Van Ballegooy et al., 2014). The values of such indicators have been interpolated with geostatistical tools in order to obtain a map for each indicator. Before computing indicators, a filter was applied to the dataset of CPT profiles removing those not consistent with the spatial trend (outlier) in accordance with the procedure described in chapter 1 (Figure 1.6). Then the values of all indicators were computed correspondingly to the CPT positions and interpolated with geostatistical analyses to obtain maps covering the territory. The estimate error was also considered in this calculation to remove from the maps those areas where knowledge is not adequate (areas with standard deviations higher than 25% of the estimated values have been removed). Examples of the obtained results are reported in Figure 5-11.

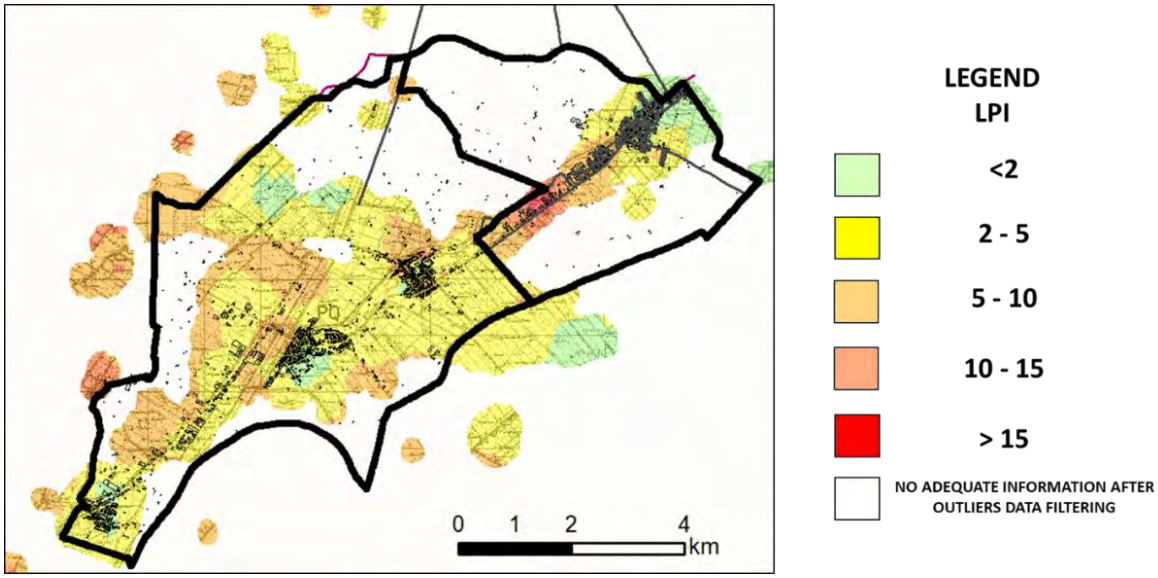

Figure 5-11.a Geostatistical interpolation of "LPI" on the entire territory of Terre del Reno;

This project has received funding from the European Union's Horizon 2020 research and innovation programme under grant agreement No. 700748

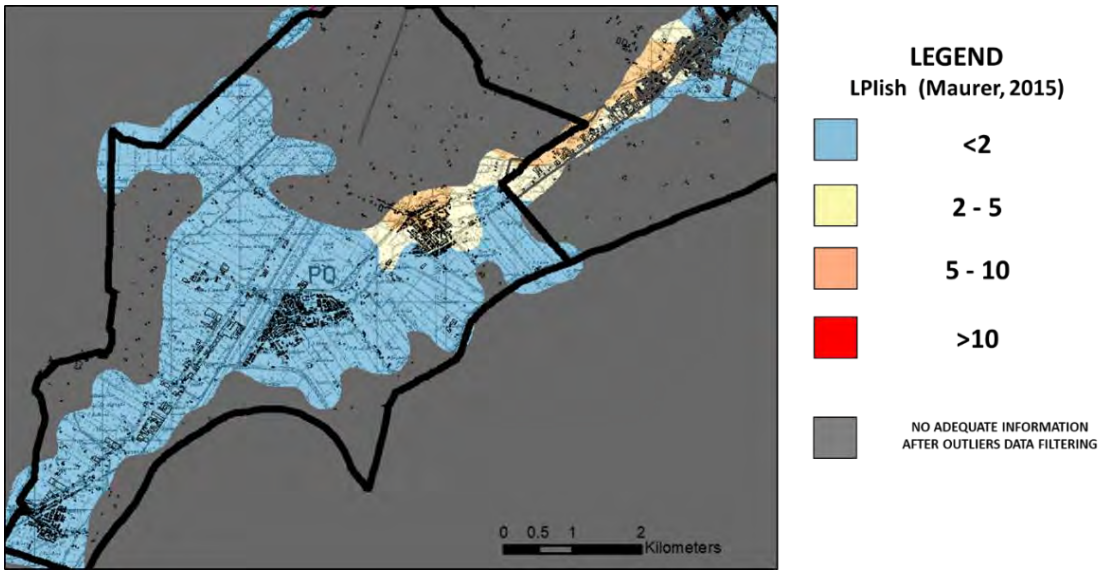

Figure 5-11.b Geostatistical interpolation of "LPI $_{ISH}$" on the entire territory of Terre del Reno; estimate error map (grey area) was overlaid to the indicator Map to cut the areas where knowledge is not adequate.

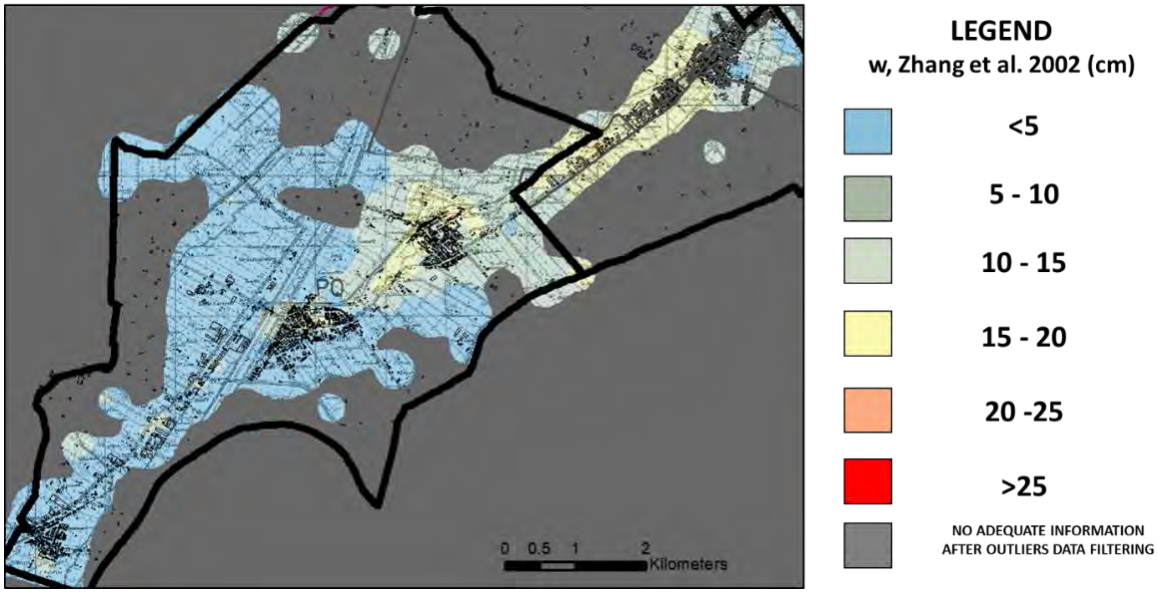

Figure 5-11.c Geostatistical interpolation of "w" on the entire territory of Terre del Reno; estimate error map (grey area) was overlaid to the indicator Map to cut the areas where knowledge is not adequate.

This project has received funding from the European Union's Horizon 2020 research and innovation programme under grant agreement No. 700748

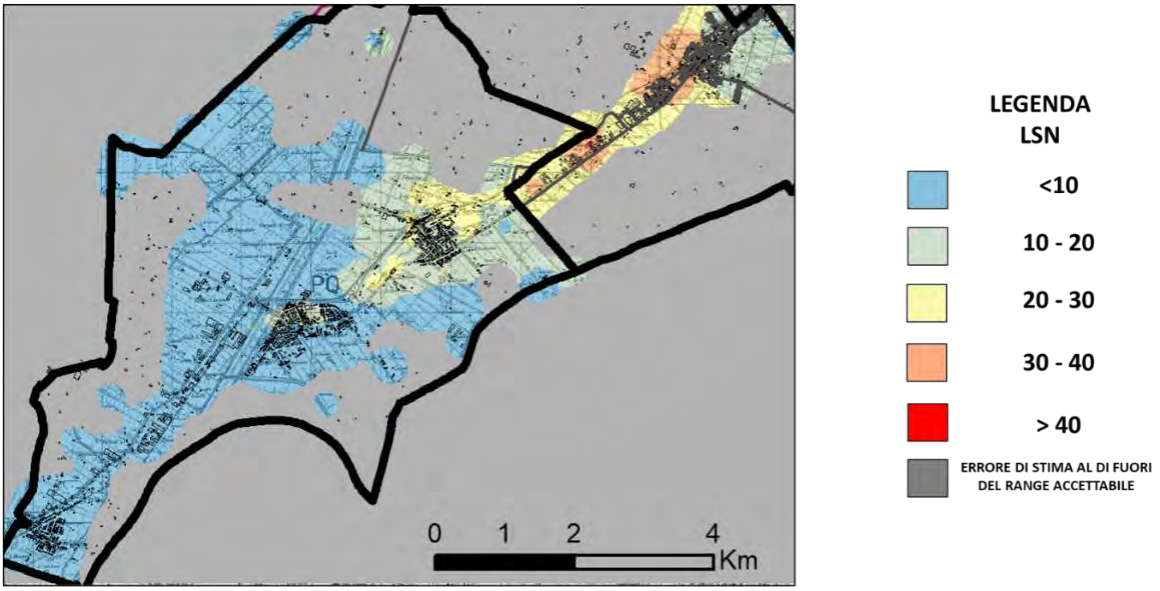

Figure 5-11 d Geostatistical interpolation of "LSN" on the entire territory of Terre del Reno; estimate error map (grey area) was overlaid to the indicator Map to cut the areas where knowledge is not adequate.

Although with some difference from each other, all maps highlight a heterogeneous distribution of values over the territory area with a stronger concentration of potentially liquefiable layers along the North-East/ South-West direction. This trend reflects the geological and hydrogeological features of the territory, consisting of alluvial deposits of various composition, but having major sandy components along the old Reno River channel. It is also worth noting that the spatial distribution of indicators reflects the distribution of ESP categories (Figure 5-9).

5.2.4 Survey of land damage

After the May 20th Earthquake, within the area of Mirabello, Sant'Agostino, San Prospero, Cento, and Finale Emilia, a detailed survey of damage was carried out classifying the liquefaction evidences in three categories: liquefaction, fracture/liquefaction, fracture. Over a total of 478 observations, 45% were liquefactions, 40% fracture/liquefactions, and 15% fractures. The highest density of evidences is located in San Carlo and Mirabello where large portions of the inhabitated villages are affected. The liquefaction manifestation in Sant'Agostino is more concentrated in a single portion of the village (Figure 5-12). The thickness of the ejected sand in open fields reached about 40 cm, whereas at sites in the San Carlo village garages or ground-floor apartments were filled with 1 m-thick sand boils.

This project has received funding from the European Union's Horizon 2020 research and innovation programme under grant agreement No. 700748

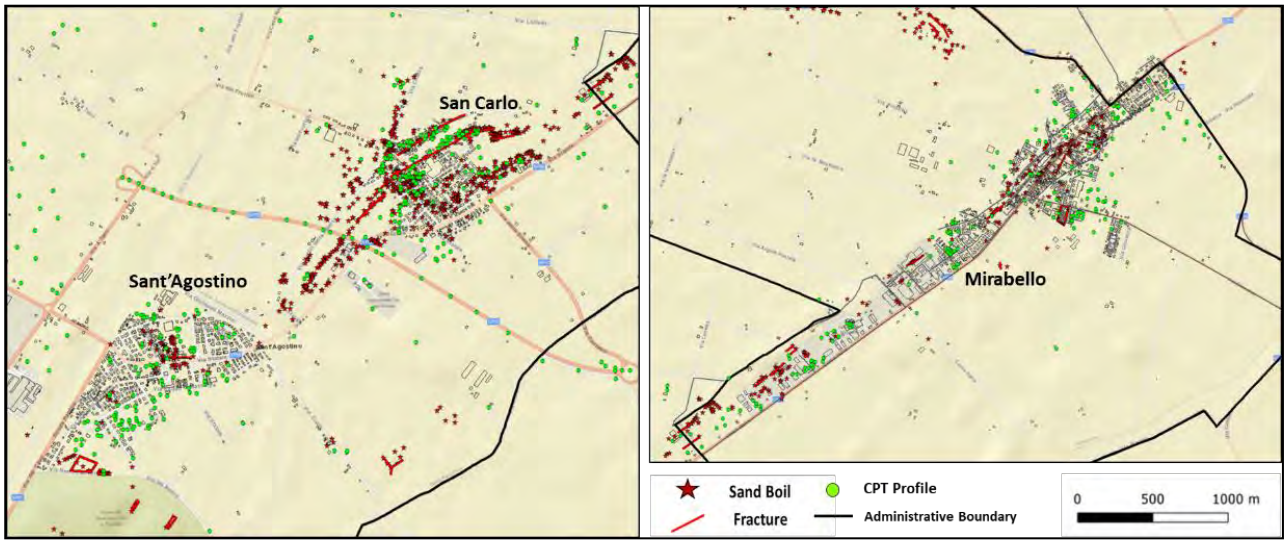

Figure 5-12 Liquefaction-induced land damage observations across Terre del Reno municipality after the May 20th 2012.

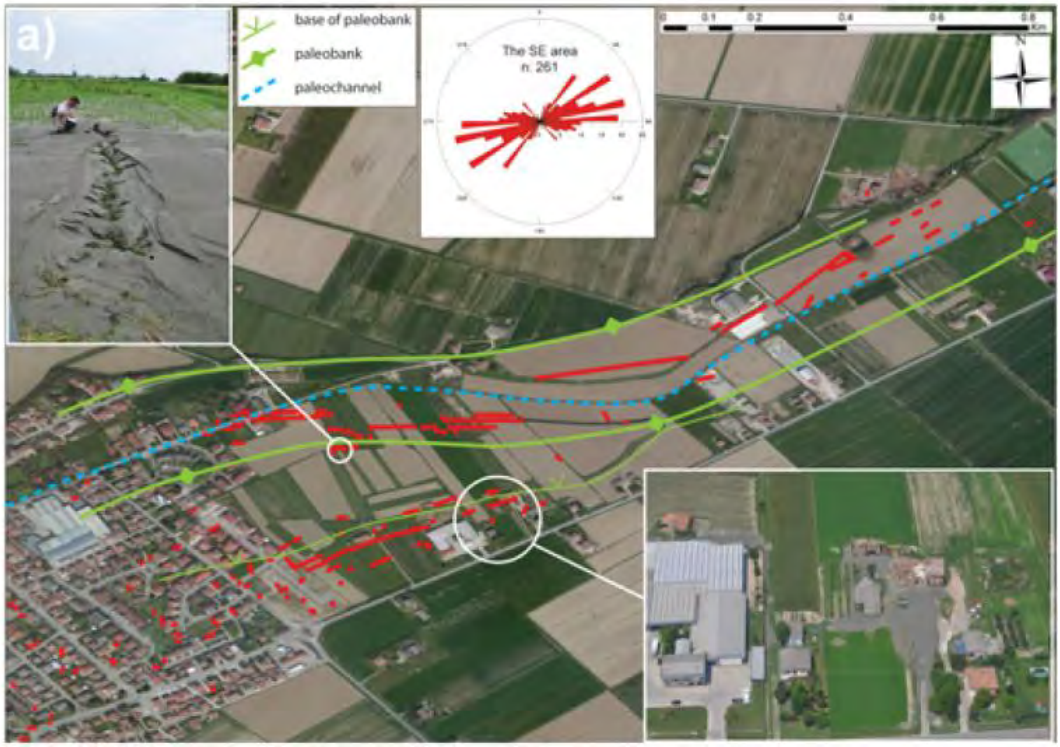

Figure 5-13 Examples of coseismic geological effects of the four study areas at different scales of observation (satellite view from Bing Maps; aerial and field view from Emergeo survey, 2013).

The maximum observed diameter of single sand ejecta was about 10 m. Many fractures, mostly in the NE–SW direction were noticed many of them extending for a maximum length of 50 m. Cracks were formed with gaps more than 20 cm wide and sometimes 20 cm of vertical step. Fractures without sand ejection had similar strikes, but had length up to a few hundred-metres, gaps up to 30 cm wide, and vertical steps up to 20 cm

with both SE and NW downthrown. In Figure 5-13 the Red dots indicate liquefaction manifestations, lines indicate fractures/liquefactions following the morphology of paleochannels. In some artificial cuts open to repair pipes, grey sand was noticed as a proof that even where sand didn't reach the surface, the driving phenomenon was liquefaction. The large amount of ejected sand in San Carlo produced important cavities undergournd that turned into localised subsidence, sometimes accompanied by ponding. Subsidence started with the occurrence of liquefactions but, because settling and recompaction of sediments is a slow process, it kept increasing day by day, representing a further hazard for the involved man-made structures (Alessio et al., 2013).

5.2.5 Validation of Liquefaction Severity Indicators

The liquefaction severity indicators are here validated for the May 20th 2012 (M_w 6.1) earthquake comparing the prediction obtained from each CPT profile with the local observation of liquefaction ground evidence. According to the criterion adopted for validation, described in chapter 1 (Kongar et al., 2015), punctual values of the liquefaction severity indicators have been computed at each CPT location and compared with the event. For the whole municipality of Terre del Reno, punctual liquefaction (sand boils) and extensive cracking observations have been taken to obtain the map liquefaction-induced damage (Figure 5-14), which was used to validate the performance of liquefaction severity indicators.Concerning the latter, a distance of 15 m was considered to define the influence area of the CPT profile: according to this assumption, the event is considered as positive if land damage evidences have occurred at a distance lower than 15 m from the CPT location (Figure 5.14). In this validation test, increasing threshold values have been fixed and the Receiver Operator Curve has been built and the True Positive/Negative Ratio and the False Positive/Negative Ratio have been computed each time and plotted. The goodness of prediction is quantified by the Area Under the Curve AUC, with 0.5 meaning nil, 1 perfect prediction capacity. Finally, the Mathews Correlation Coefficient has been evaluated to identify the optimal threshold value of indicators.

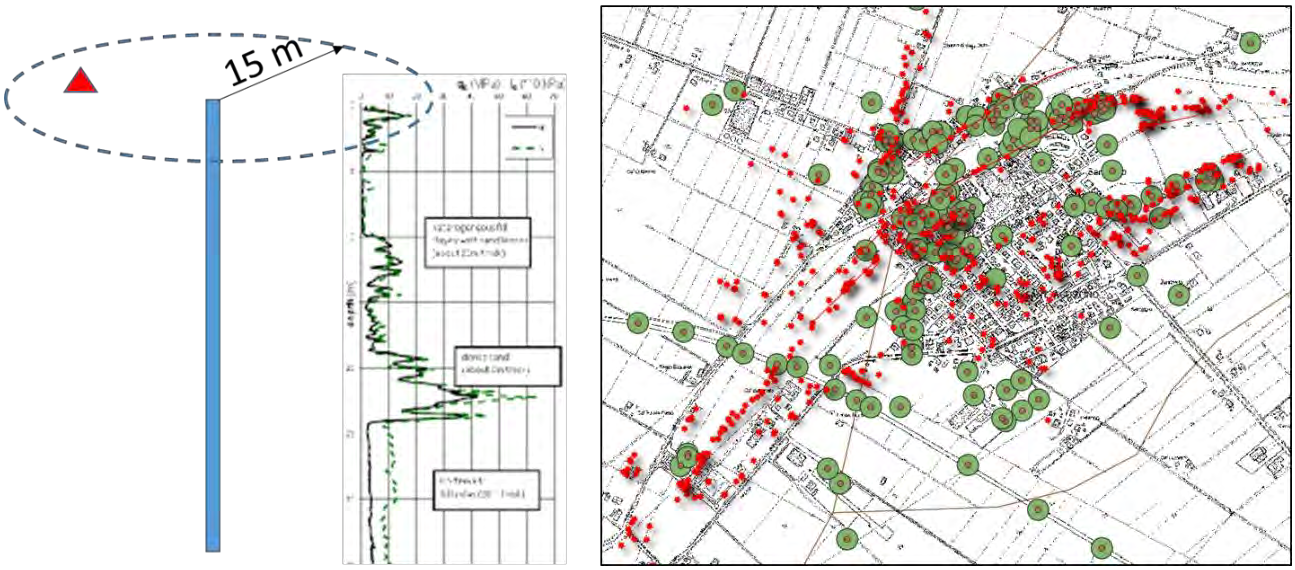

Figure 5-14 Example of validation criterion of liquefaction ground severity indicators applied to the San Carlo district by merging CPT profiles to liquefaction ground observations after the 20 May 2012 Earthquake.

The test results, plotted in Figure 5-15, reveal a fairly good performance of the prediction with slight differences among all indicators. This result can be motivated with the validity of a three-layer model to represent the stratigraphic features of the studied area and is consistent with the results of the Equivalent Soil Profile method, that showed normed error almost always lower than 0.05. Consequently, it can be concluded that the general performance of soil damage indicators is adequate. Additionally, the Mathews Correlation Coefficient shows optimal threshold values in accordance with the suggestions given by the authors.

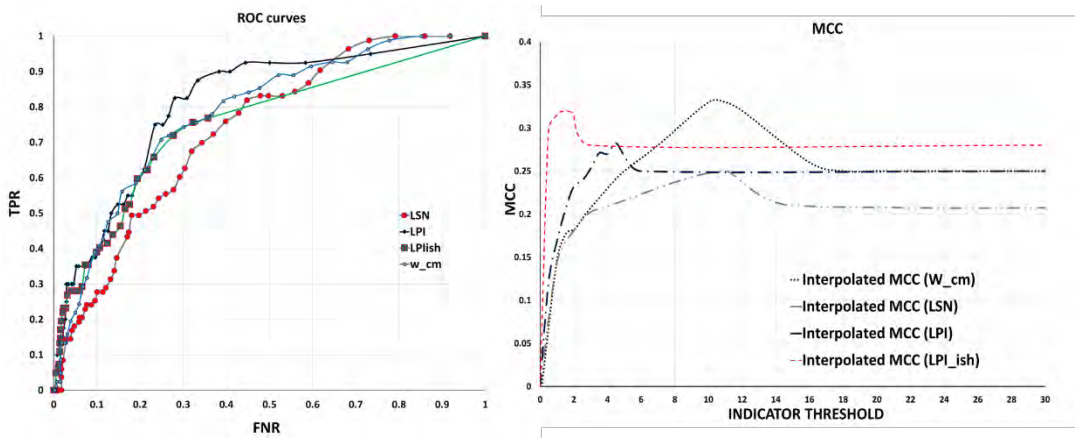

INDICATOR	AUC	β	OPTIMAL THRESHOLD
LPI	0.82	0.123	≈5
LPIish	0.84	0.106	1-2
W_cm	0.71	0.192	≈10
LSN	0.66	0.151	≈10-12

Figure 5-15 ROC test of Liquefaction severity indicators for the May 20th 2012 earthquake in Terre del Reno.

5.3 Building vulnerability and Damage Assessment

A database of residential buildings has been herein built combining information from various sources: ISTAT (https://www.istat.it/), Regione Emilia-Romagna (http://geoportale.regione.emilia-romagna.it/it/mappe) and Geoportale Nazionale (http://www.pcn.minambiente.it/mattm/servizio-wms/). A number of about 3 000 buildings have been characterized by collecting information required for the Risk Assessment Procedures (i.e. ID, Location, Geometry, Model Building Type, Number of storeys, Use). Additionally, aerial photographs available from Emilia-Romagna Region archives have been analysed to study the evolution of the building asset, establish the construction age of buildings and subdivide buildings in homogeneous classes for the vulnerability analysis (Figure 5-16).

This project has received funding from the European Union's Horizon 2020 research and innovation programme under grant agreement No. 700748

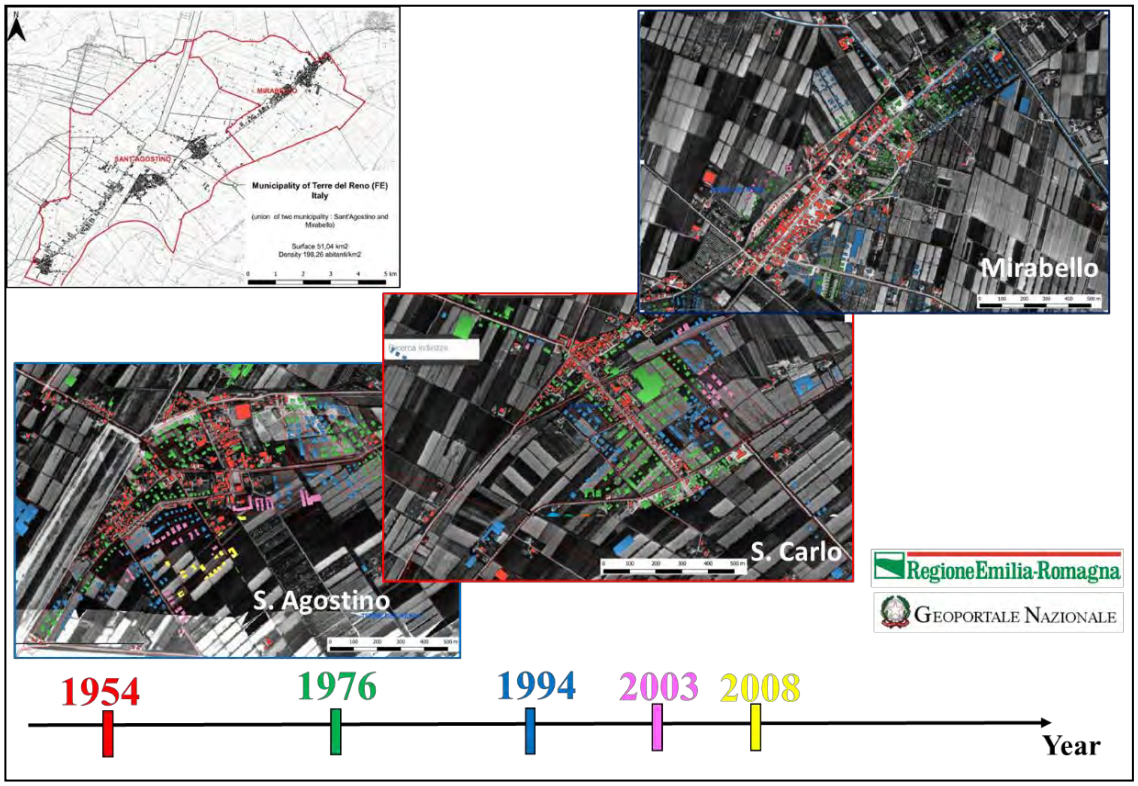

Figure 5-16 Documented urban development of Terre del Reno with aerial imagery.

Starting from this database, a post-earthquake damage survey database has been created deriving damage from the post-earthquake reports collected by the Emilia Romagna Region in a specific platform (MUDE). Following the procedure described in the next paragraph 5.3.3, damage on each building has been classified applying the van Ballegooy et al. (2014) classification criterion which distinguishes the severity of liquefaction induced building damage based on the measured settlements.

5.3.1 Evaluation of liquefaction induced settlements on buildings

The potential of liquefaction-induced building damage has been assessed considering three analytical procedures available in the literature: Karamitros et al. (2013), Bray and Macedo (2017) and Bullock et al. (2018) and considering the arithmetic mean settlement as indicator w_{max}. These methods compute the settlements of structures equivalent to buildings with simplified formulas that fit large number of calculations. The methods differ each other for the schematization of the subsoil-structure system. Relevant issues for calculation are applied load, foundation type and dimensions. To this aim it is considered that the building foundation is rather homogeneous for residential buildings, consisting in small math foundations. The applied unit load is then computed subdividing uniformly spreading on this area the total load, proportional to the number of floor and extension of the building. To apply these formulas, a database has been created reporting for each building the footprint dimensions, the number of storeys; the crust and liquefiable layer thickness, in addition to the mean CRR were interpolated below each building centroid after the application of the Equivalent Soil Profile Method. Traditional LSN was also interpolated after liquefaction

hazard analysis of the selected scenario. Further assumptions on subsoil features were made based on existing literature (Fioravante et al., 2013).

The three procedures of Karamitros et al. (2013), Bray & Macedo (2017) and Bullock et al. (2018) have been implemented on the entire residential building portfolio and results are separately shown on the maps of

Figure 5-17 5-18 and 5-19. From a qualitative viewpoint, the methods show different trends of settlements and the obtained results are consistent with the previously described hazard analysis.

The damage on each building has been computed with adopting the fragility curves defined by Fotopoulou et al. (2018). However, considering that this method adopts the differential settlements as Engineering Demand Parameter, while the above calculations provide absolute settlements. Therefore, a scaling factor equal 0.667 (i.e. 2/3) has been applied to convert absolute into differential settlements, following the results described in par.1.5.1 of the present deliverable. Additionally, being the Fotopoulou et al. fragility model developed for low-rise, mid-rise and high-rise reinforced concrete buildings, the median values of the fragility curves have been scaled by 3 to apply such model to masonry buildings which represent around the 90% of Terre del Reno building portfolio.

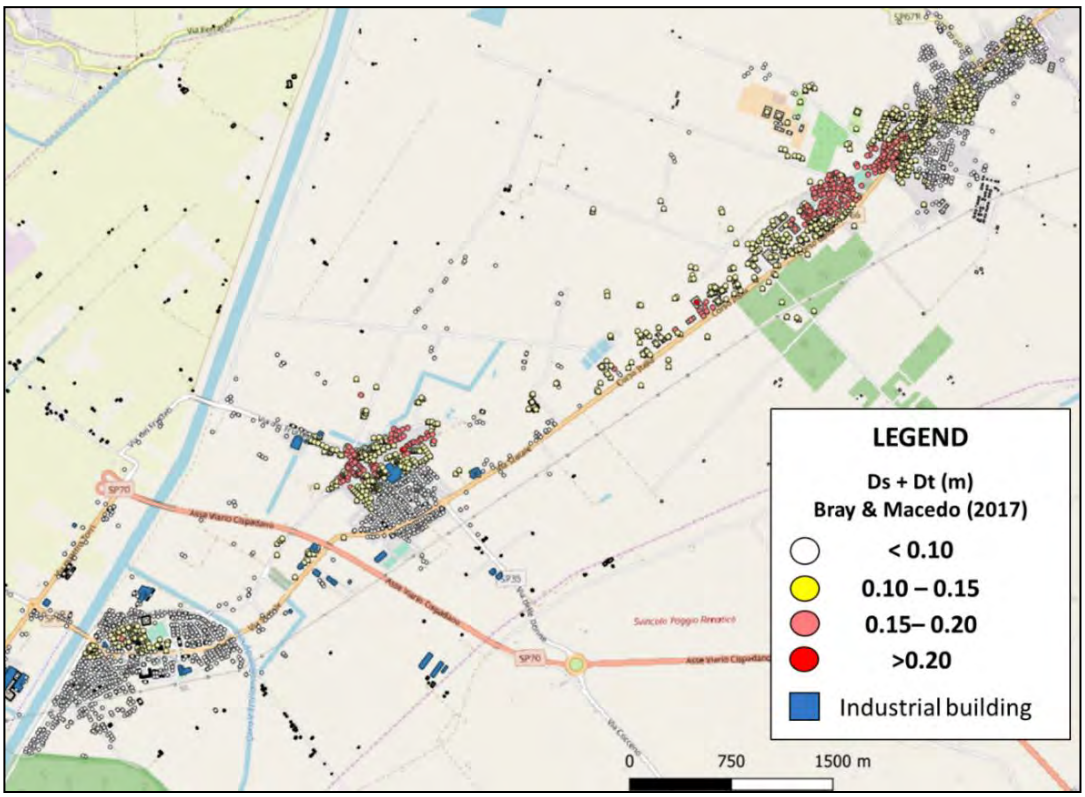

Figure 5-17 Evaluation of liquefaction-induced building settlements (Bray & Macedo, 2017).

This project has received funding from the European Union's Horizon 2020 research and innovation programme under grant agreement No. 700748

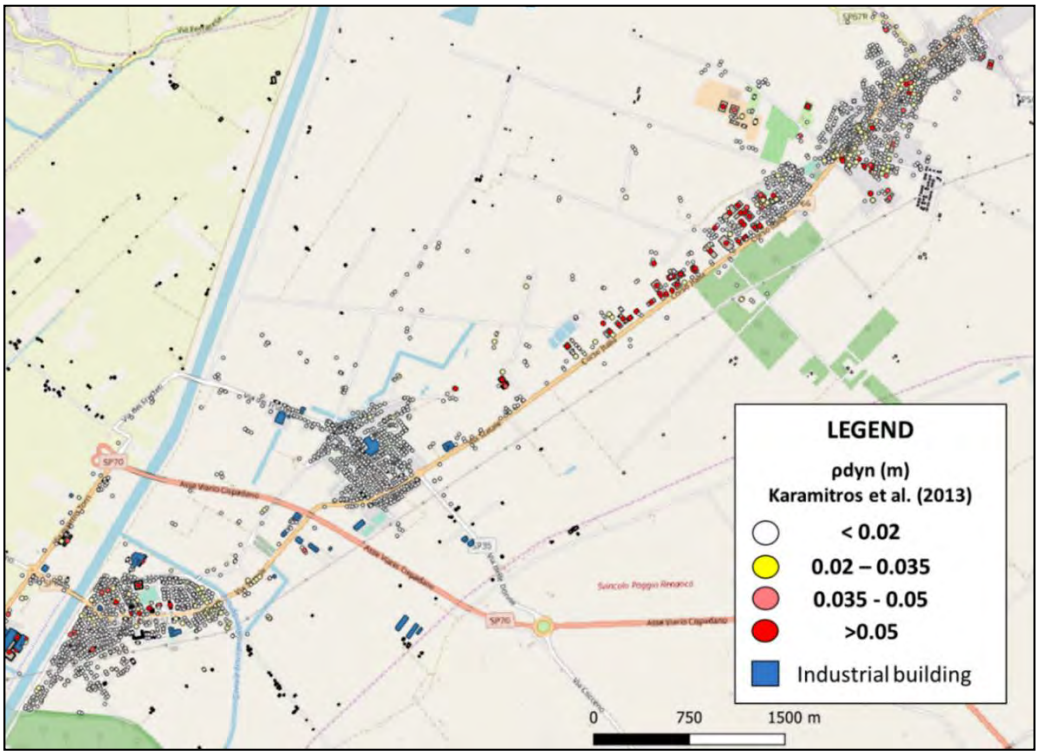

Figure 5-18 Evaluation of liquefaction-induced building settlements (Karamitros et al., 2013).

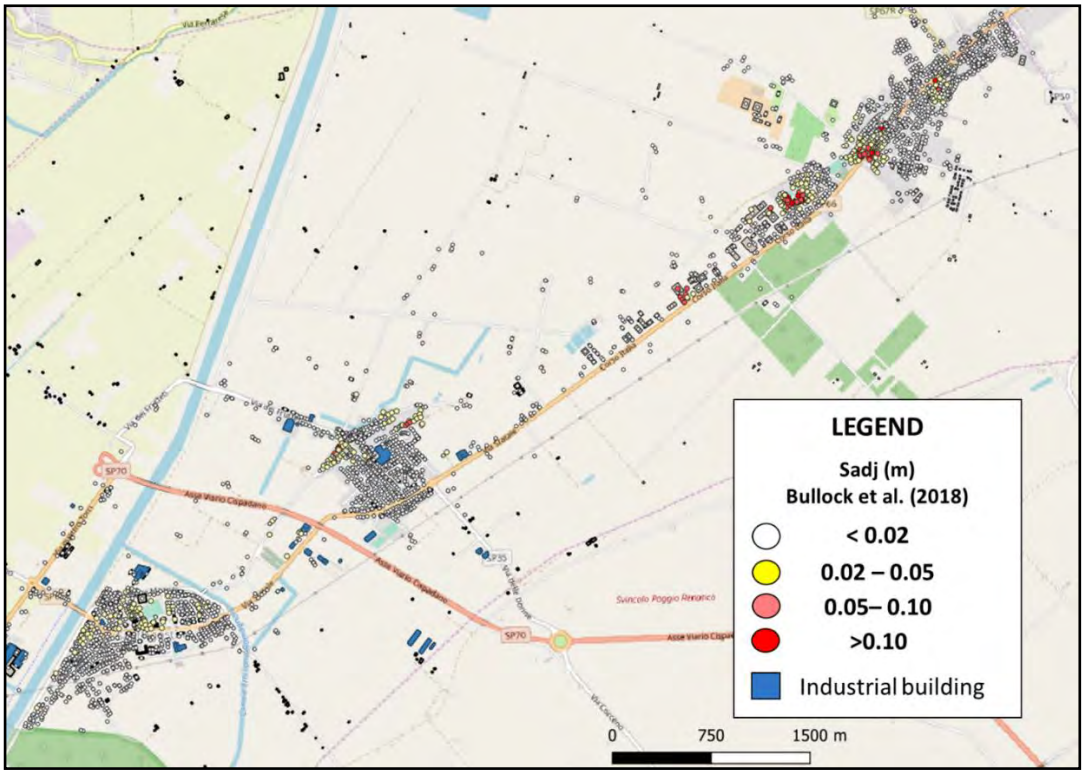

Figure 5-19 Evaluation of liquefaction-induced building settlements (Bullock et al., 2018).

5.3.2 Survey of building damage

The interaction of liquefaction effects with man-made structures was particularly strong, especially in the village of San Carlo where many buildings, roads, fenced walls, and lifelines were severely affected and damaged by fractures and liquefaction phenomena. Notably, a high percentage of the water wells in the area were filled by the liquefied sand, often up to the top. The ejected sand (liquefaction and fracture/liquefaction category) was mainly grey medium-to-fine sand and, but in minor amount, hazel sand, suggesting that liquefaction could come from two distinct layers. Immediately after the seismic sequence of May June 2012, the Emilia-Romagna Region in collaboration with technicians, engineers, and the Department of Civil Protection coordinated more then 40,000 inspections to assess the safety of buildings through the Aedes board format (Servizio Geologico, Sismico e dei Suoli 2012).

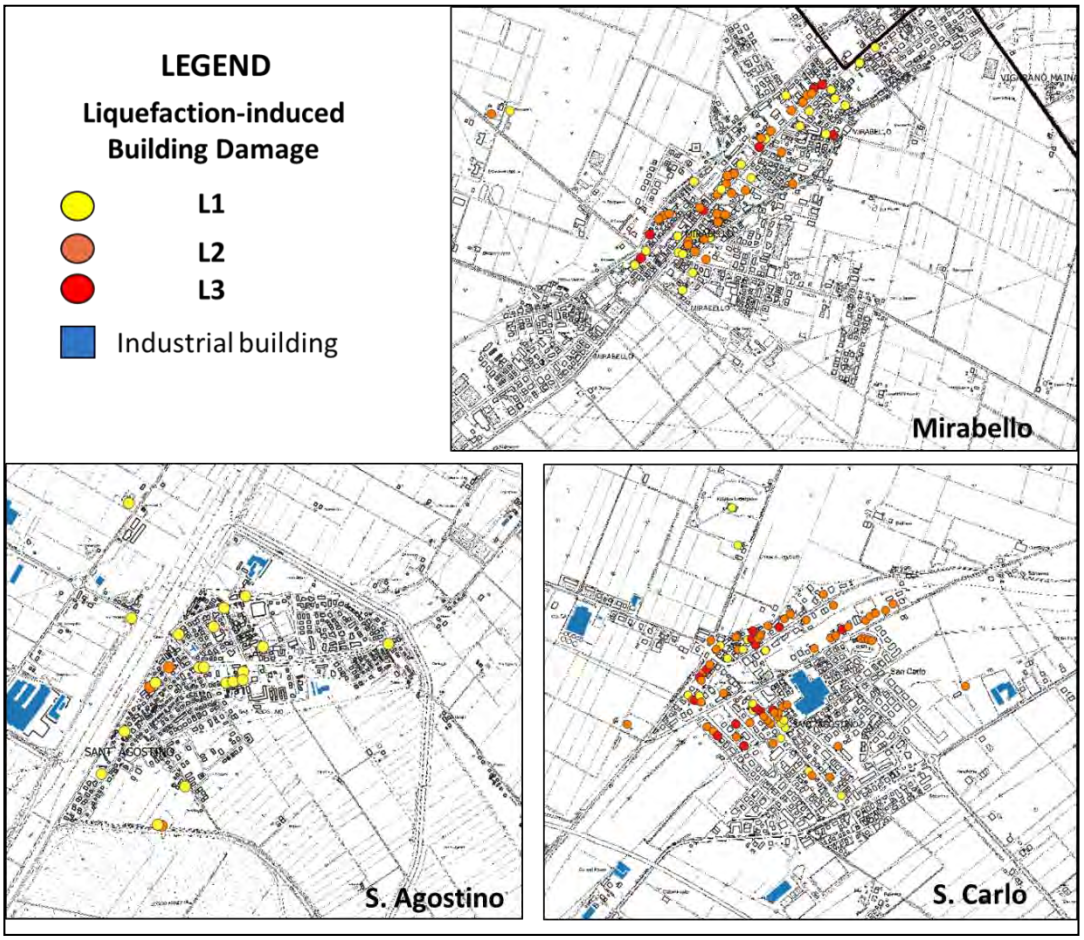

Figure 5-20 Localisation of the liquefaction-induced damage on buildings classified with the criteria of van Ballegooy et al. (2014).

The liquefaction-induced damage on residential buildings was classified through the analysis of post seismic surveys (Aedes format) and over 400 Mude reports, relating to buildings that required contributions for reconstruction following the 2012 earthquake. In fact, the Mude platform was established by the Emilia Romagna Region (https://www.regione.emilia-romagna.it/terremoto/mude-modello-unico-digitale-per-

This project has received funding from the European Union's Horizon 2020 research and innovation programme under grant agreement No. 700748

ledilizia) to manage with the same procedure the building repair or reconstruction and the request for contributions. One of the key points in damage database creation is to distinguish the liquefaction-induced damage from the shaking-induced and combined damage. For each of the existing Mude file, the liquefaction-induced damage was assessed by analyzing the photographic and technical reports and applying the criteria defined by van Ballegooy et al. (2014). The damage classification shows that slight/moderate damage was experienced by buildings in S. Agostino, while severe and moderate/severe liquefaction-induced building damage was respectively observed in the districts of S. Carlo and Mirabello (Figure 5-20). The major evidence of liquefaction-induced damage the municipality of Terre del Reno are: presence of sand ejecta and cracks on the basement floor, building rotation, differential and absolute settlements (Figure 5-21).

(a)

Dwelling Foundation Damage Categories

Type of Damage	Minor	Moderate	Major
Stretching	0 to 5mm	5 to 30mm	>30mm
Hogging	0 to 20mm	20 to 50mm	>50mm
Dishing	0 to 20mm	20 to 50mm	>50mm
Racking/Twisting	0 to 10mm	10 to 30mm	>30mm
Tilting	0 to 20mm	20 to 50mm	>50mm
Abrupt Differential Movement	0 to 10mm	10 to 20mm	>20mm
Global Settlement	0 to 50mm	50 to 100mm	>100mm

(b)

Figure 5-21 Examples of the most typical liquefaction-induced building damage in the municipality of Terre del Reno (a) and criterium adopted for the classification of damage (b) from van Ballegooy et al., 2014.

The analysis of economic costs of liquefaction damage following the seismic sequence of May / June 2012 was performed by comparing the Mude files and the data available from the Emilia-Romagna regional platform for reconstruction (https://openricostruzione.regione.emilia-romagna.it/). The distribution of

This project has received funding from the European Union's Horizon 2020 research and innovation programme under grant agreement No. 700748

liquefaction-induced damage on residential buildings is also reflected in the costs associated with reconstruction (Figure 5-22).

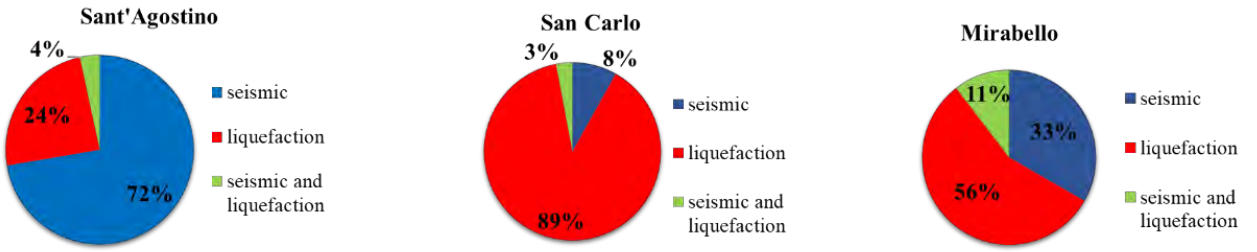

Figure 5-22 Once the data was collected, a statistical analysis of the costs was carried out, analyzing separately the three districts of S. Agostino, S. Carlo and Mirabello.

5.3.3 Validation of liquefaction-induced building settlements

Like for the free field analysis, a statistical procedure has been implemented to validate the effectiveness of each method in liquefaction-induced damage prediction. A binary test (Kongar et al., 2015) has been performed assuming settlements and engineering demand parameter (with variable threshold) and attempting its correlation with damage (Figure 5-23, b and c). The settlement, computed with the methods defined in par5.3.1 has been compared with the liquefaction-induced damage severity (van Ballegooy et al., 2014). The area under the curve AUC has been then evaluated for the building affected by minor, moderate and major damage. In addition, for each of the threshold values, the Matthew correlation coefficient *"MCC"* has ben e calculated. The MCC is more useful for cases where there is a large difference in the number of positive and negative observations (Matthews, 1975). It is proportional to the chi-squared statistic for a 2 x 2 contingency table and its interpretation is similar to Pearson's correlation coefficient, so it can be treated as a measure of the goodness-of-fit of a binary classification model (Powers, 2011). For each method, the optimal thresholds for damage assessment have been defined as the value maximising the MCC function and the corresponding TPR/FPR, TNR/FNR have been calculated. Considering that the validity of the three-layer model has been proven on the entire study area, the validation test has been applied over the entire building database: the evaluated building settlements have been related to the liquefaction-induced damage classification, which has been assessed from post-earthquake rapid inspections and detailed engineering evaluations available in the Mude platform. This analysis gives a reasonable distribution of the true positives and false negatives as a function of the thresholds assumed for settlement. In fact, considering that better predictive models locate points of the ROC curve towards the top left of the plot, the AUC is a generalized measure of model quality assuming no specific threshold. The diagonal of the plot is equivalent to random guessing (AUC = 0.5), while AUC = 1 is a good prediction. In this case, for each of the considered methods AUC results generally are greater than 0.50, thus the obtained results show good correlation between event and selected variables.

This project has received funding from the European Union's Horizon 2020 research and innovation programme under grant agreement No. 700748

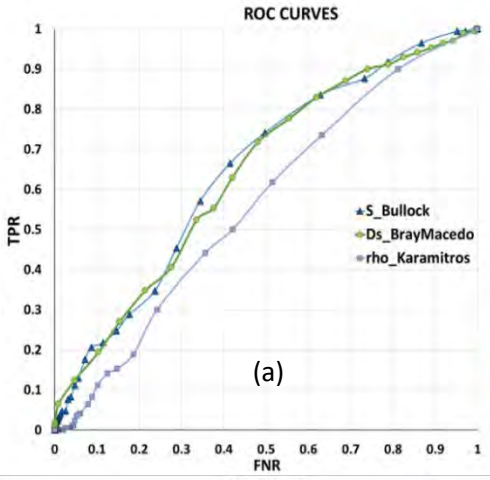

Liquefaction-Induced Settlement	Reference	AUC	OPTIMAL THRESHOLD
Sadj (mm)	Bullock et al. (2018)	0.68	≈15 mm
Ds+Dt (mm)	Bray & Macedo (2017)	0.67	≈85 mm
Pdyn (mm)	Karamitros et al. (2013)	0.60	≈5 mm

Bullock et al. (2018)		Bray & Macedo (2017)		Karamitros et al. (2013)	
MCC (THRESHOLD) = 0.12		MCC (THRESHOLD) = 0.12		MCC (THRESHOLD) = 0.06	
TPR = 75 %	TNR = 50%	TPR = 72 %	TNR = 52%	TPR = 45%	TNR = 64%
FPR = 25%	FNR = 50%	FPR = 28%	FNR = 48 %	FPR = 55%	FNR = 36 %

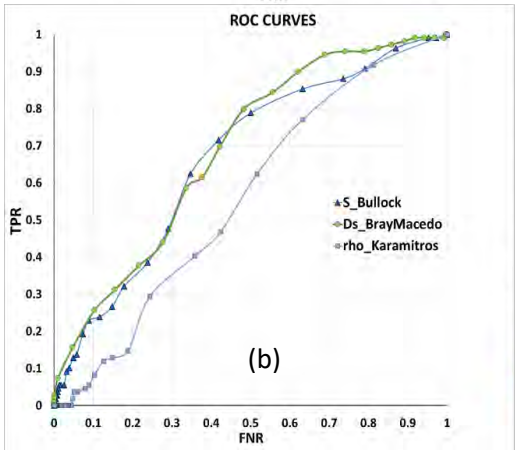

Liquefaction-Induced Settlement	Reference	AUC	OPTIMAL THRESHOLD
Sadj (mm)	Bullock et al. (2018)	0.70	≈15 mm
Ds+Dt (mm)	Bray & Macedo (2017)	0.71	≈85 mm
Pdyn (mm)	Karamitros et al. (2013)	0.62	≈5 mm

Bullock et al. (2018)		Bray & Macedo (2017)		Karamitros et al. (2013)	
MCC (THRESHOLD) = 0.12		MCC (THRESHOLD) = 0.13		MCC (THRESHOLD) = 0.06	
TPR = 80 %	TNR = 50%	TPR = 80 %	TNR = 52%	TPR = 40%	TNR = 64%
FPR = 20%	FNR = 50%	FPR = 20%	FNR = 48 %	FPR = 60%	FNR = 36 %

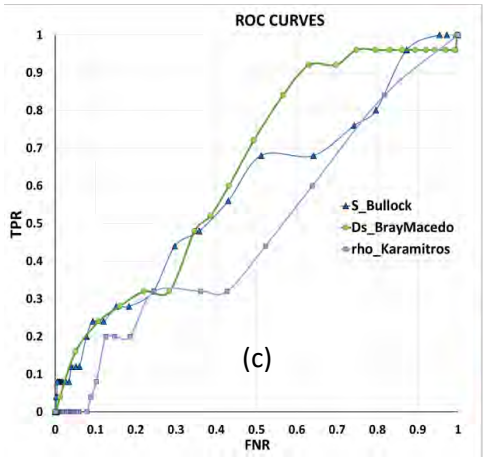

Liquefaction-Induced Settlement	Reference	AUC	OPTIMAL THRESHOLD
Sadj (mm)	Bullock et al. (2018)	0.61	≈45 mm
Ds+Dt (mm)	Bray & Macedo (2017)	0.67	≈85 mm
Pdyn (mm)	Karamitros et al. (2013)	0.55	≈15 mm

Bullock et al. (2018)		Bray & Macedo (2017)		Karamitros et al. (2013)	
MCC (THRESHOLD) = 0.10		MCC (THRESHOLD) = 0.06		MCC (THRESHOLD) = 0.02	
TPR = 8%	TNR = 99%	TPR = 92%	TNR = 37%	TPR = 40%	TNR = 64%
FPR = 92%	FNR = 1%	FPR = 8%	FNR = 63%	FPR = 60%	FNR = 36 %

Figure 5-23 Validation test between settlement predictive models and damage observations on residential buildings, in the hypothesis of ESP normed_error lower than 0.0.5 Optimal thresholds and respective values of the TPR/TNR are given (a. minor damage; b. moderate damage; c. major damage).

This project has received funding from the European Union's Horizon 2020 research and innovation programme under grant agreement No. 700748

5.4 Evaluation of Liquefaction-induced physical impact on buildings

To assess the physical impact of liquefaction on buildings following the conventional approach, the fragility model defined by Fotopouolu et al. (2018) (which is also implemented in the Liquefact software) have been used. Four damage limit states, ranging from slight-to-complete, are defined in the method and the loss factors associated with each damage state are summarized in the following table. These loss factors represent the fraction between the repair cost associate with each damage state and the replacement cost. Other similar tables exist for the non-structural damage, i.e. the loss associated to the damaged content of buildings or to the missed of the structure during the repair period.

Table 5-3 Assigned Loss Factors in the fragility model used to assess the liquefaction-induced physical damage.

DAMAGE LIMIT STATE	LOSS FACTOR
Slight	0.10
Moderate	0.30
Extensive	0.70
Complete	1.00

By combining the probability of reaching each damage state to the loss factor, the Mean Damage Ratio for the May 20th 2012 earthquake scenario has been evaluated on the entire residential building portfolio and the results are presented in Figure 5-24. The Figure shows a qualitative agreement with the map of the liquefaction-induced damage levels (shown in Figure 5-21), obtained applying the van Ballegooy et al., 2014 criteria.

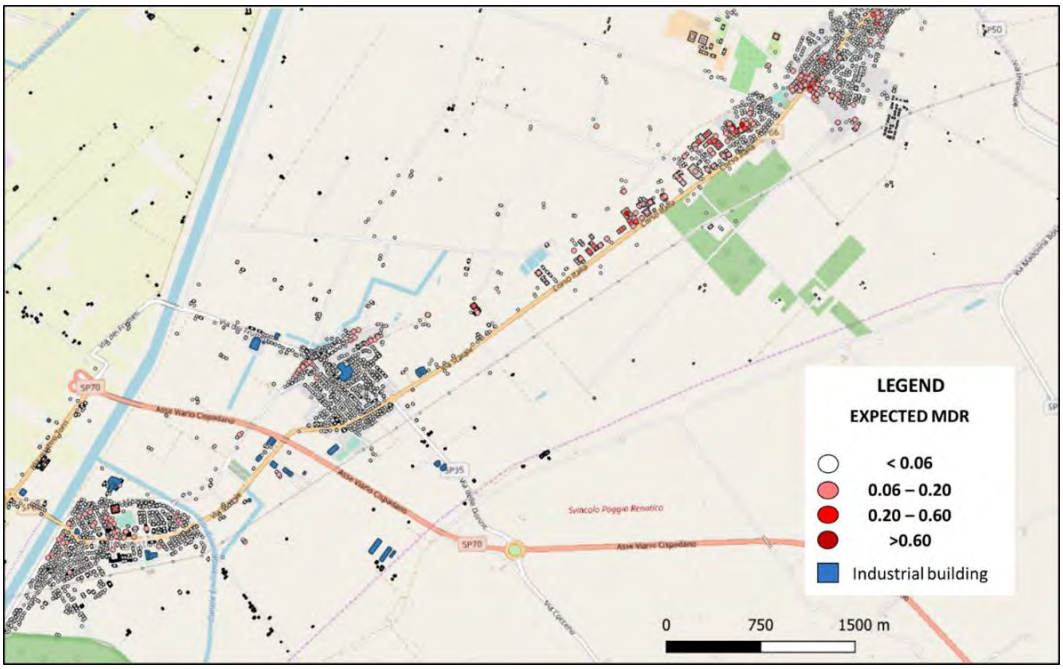

Figure 5-24 Expected Mean Damage Ratio on residential buildings for the 20 may 2012 Earthquake scenario.

5.5 The industrial district of Terre del Reno

The size of the area affected by the 2012 earthquake and the importance of economic activities present in this area seriously increased the severity of the earthquake-induced economic losses. In fact, it is well acknowledged that most of the earthquake-induced economic losses on business activities are due to the reduced or lost income, instead of the physical damage on structures. Studies concerning the economic situation in the region led to estimate the loss of Gross Domestic Product caused by the Emilia earthquake in 3.1 billion euros, distributed on 2012-2013. The typical structure of industrial buildings in the area is created with one floor prefabricated reinforced concrete modules. The vertical structure consists of pillars while the horizontal structure is made up of beams on which reinforced concrete roofing tiles rest. The building is closed with masonry or, in more recent buildings, with reinforced concrete panels (Figure 5-25).

Figure 5-25 Example of industrial buildings in the district of S. Agostino and observed collapse.

Before 2005, when the new seismic classification established by Annex 1 of the OPCM 3274/2003 was issued, the Emilia Plain areas were not classified as seismic; therefore, buildings were not subject to compliance with earthquake regulations. Concerning the industrial buildings, the beam-column and beam-tile connections are generally made up of a simple support without any mechanical connection. Furthermore, the pillars were designed to carry only the weights of the structure and the modest action of the wind. For these reasons, it was noted that most of the physical damage on industrial buildings was shaking-induced instead of liquefaction-induced. As observed by the methods of collapse and damage, it clearly emerged that the main cause of the collapses themselves was due to the loss of the support of the structural elements main changes due to the movement caused by the shaking seismic and therefore to the lack of effective connections between the structural elements themselves. In some cases, also the pillars collapsed (Figure 5-25).

Since the municipality of Terre del Reno hosts a series of factories (mostly located in S. Agostino district) capable of producing the 2% of the Italian Gross Domestic Product, it offers the possibility of assessing the liquefaction risk on a small industrial district. In particular, the liquefaction risk and the economic loss due to the May 20th 2012 earthquake were evaluated on 40 industrial buildings belonging to the 12 largest companies, for which the annual revenue are known (https://www.reportaziende.it/emilia_romagna). As can be seen from Figure 5-26 the annual revenue of the companies ranged between 5 to 60 million euros.

According to the Liquefact software economic model, the liquefaction risk assessment on industrial buildings must be performed once the company's annual revenue and the average value of the equipment (contents)

This project has received funding from the European Union's Horizon 2020 research and innovation programme under grant agreement No. 700748

are known. On business activities the economic losses connected to the building loss of functionality, loss of income and damage to specific equipment is much more impactant compared to the physical damage associated costs. The industrial buildings database for liquefaction risk assessment of the 12 selected companies was built collecting all the required information (ID, location, geometry, MBT, annual business revenue). In the absence of a detailed evaluation of the content (equipment, machineries etc.) for the company, the economic value of the content has been assumed equal to half of the annual business revenue.

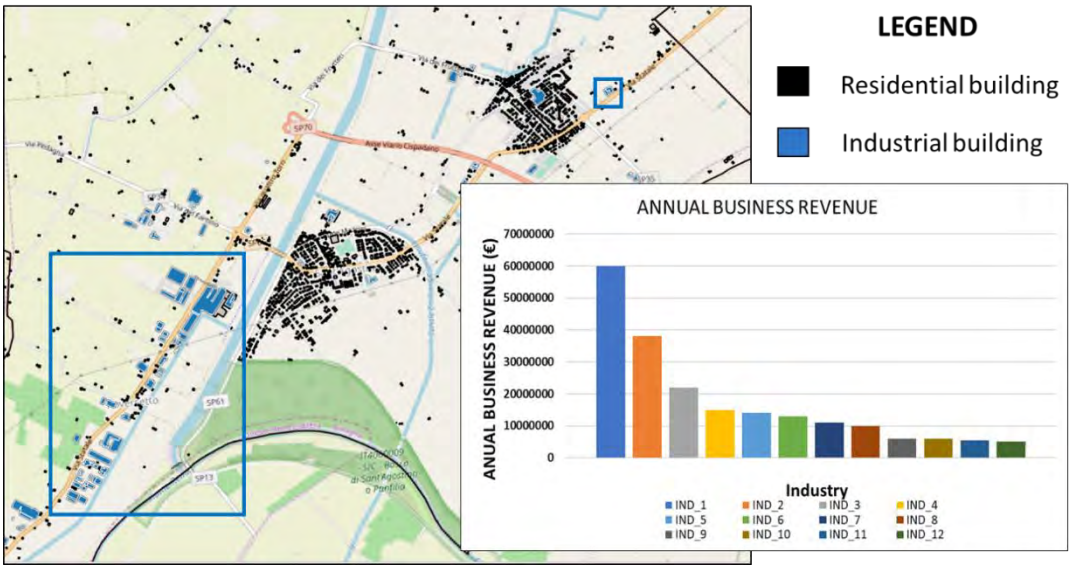

Figure 5-26 Map of the studied industrial district and annual revenue of the considered factories.

5.5.1 Liquefaction assessment of the May 20th 2012 Earthquake scenario

The analysis of the May 20th 2012 earthquake has been performed in the Liquefact software for 40 selected buildings identified in the industrial district of Sant'Agostino. The main steps of the implemented analysis are summarized in the flowchart ofFigure 5-27). The liquefaction susceptibility of the area has been firstly evaluated through the application of the Equivalent Soil Profile method, then the seismic input defined in the toolbox has been used to reproduce the M_w 6.1 earthquake of May 20th 2012. The fragility model based on the Equivalent Soil Profile (D3.2 of this project), which relates the seismic input to both the soil stratigraphy (in term of equivalent soil class) and the above structure, was applied. This model was developed for low rise and low code RC buildings and defines 4 damage limit states, which are: inter-story drift, probability of structural collapse, foundation damage and residuals. Thus 4 set of fragility curves exist for each of the 22 Equivalent Soil Profile class. The spectral acceleration Sa was used as Intensity Measure to access the curve. An example of the existing fragility curves sets is shown in Figure 5-28 for WTS soil class.

This project has received funding from the European Union's Horizon 2020 research and innovation programme under grant agreement No. 700748

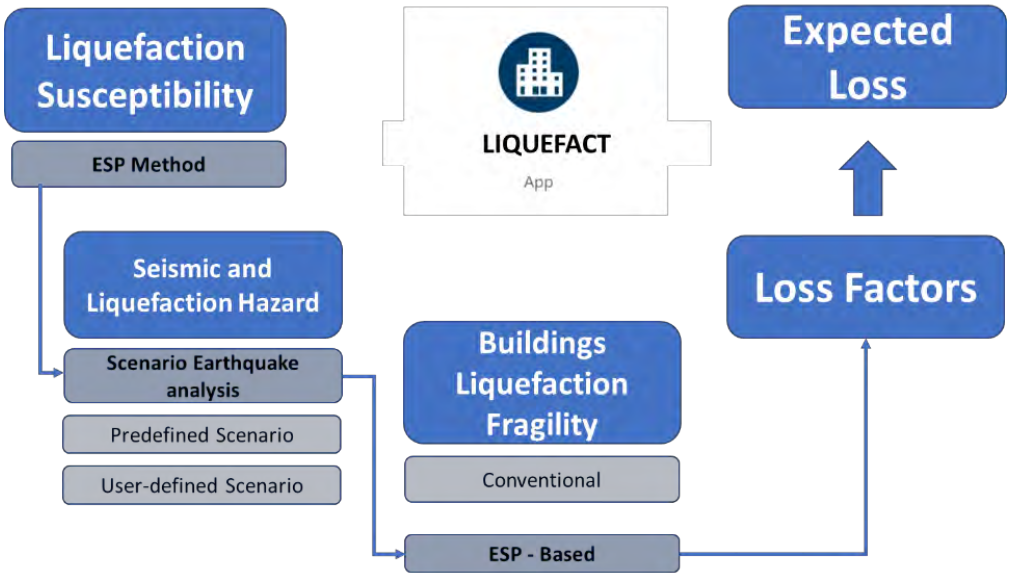

Figure 5-27 Simplified flowchart of the Liquefact implemented procedure.

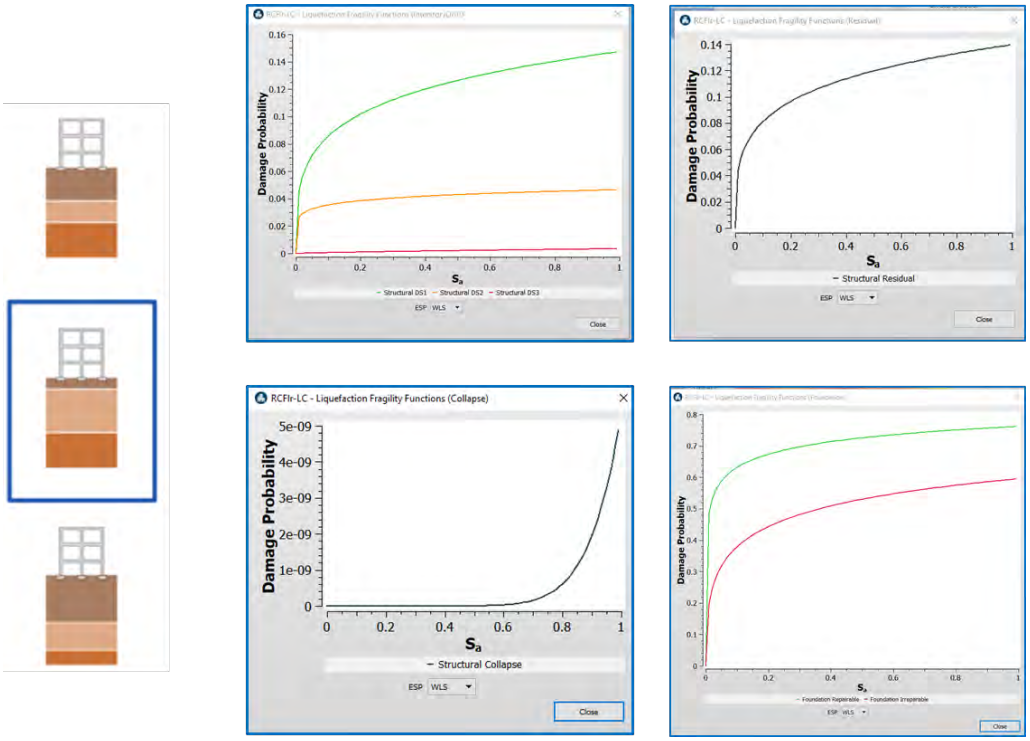

Figure 5-28 Example of fragility curves for low rise and low code RC buildings, coupled with the assessed soil class (e. g. WTS).

The probability of reaching each of the defined damage limit states has then been evaluated with the fragility model. Figure 5-29 shows that, for the May 20th 2012 earthquake, a probability of liquefaction-induced structural collapse smaller than 15% and a probability of residual limit state lower than 5% are estimated.

This project has received funding from the European Union's Horizon 2020 research and innovation programme under grant agreement No. 700748

Combining the probability of reaching each damage state to the associated loss factor given inTable 5-4, the expected building Loss Ratio can be evaluated on the industrial building portfolio.

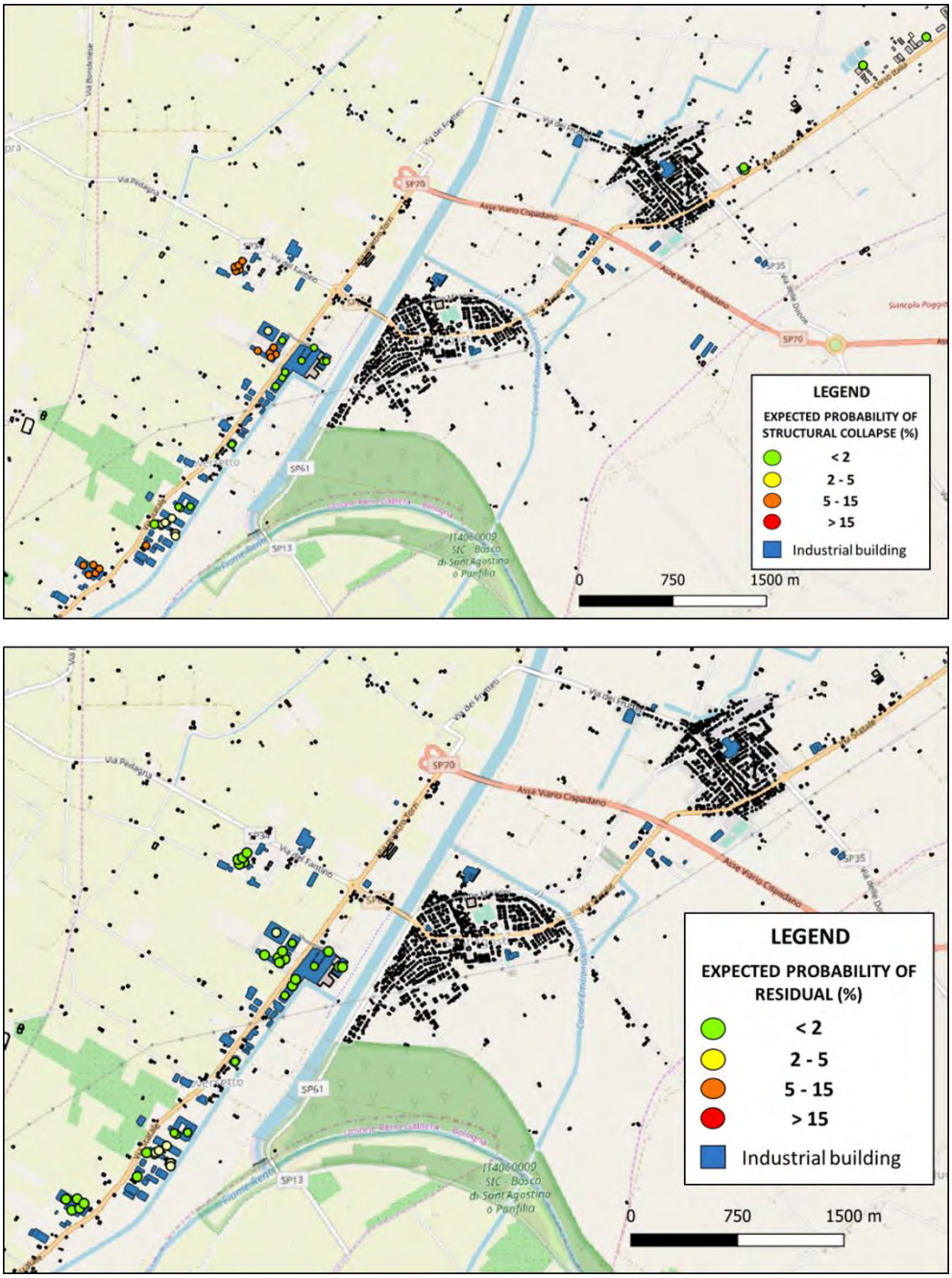

Figure 5-29 Expected probability of structural collapse on the industrial buildings of Terre del Reno due to May 20th 2012 earthquake.

Table 5-4 Assigned Loss Factors in the fragility model used to assess the liquefaction-induced physical damage.

This project has received funding from the European Union's Horizon 2020 research and innovation programme under grant agreement No. 700748

	DS1 (Structural)	DS2 (Structural)	DS3 (Structural)	Foundation Repairable	Foundation Irrepairable	Demolition Replacement
Building	0.1	0.2	0.5	0.3	1	1
Contents	0.2	0.5	0.7	0.4	1	1
Business	0	0.15	1	0.1	1	1

The following step is to apply the economic model defined inside the Liquefact software (D6.6 of this project) to assess the liquefaction-induced economic impact. Such a procedure provides an estimate of losses, both in terms of rates and monetary values. Since loss ratios are defined in term of structure repair, content and business revenue, the obtained results can be computed separately for each of these classes (Figure 5-30 and Figure 5-31).

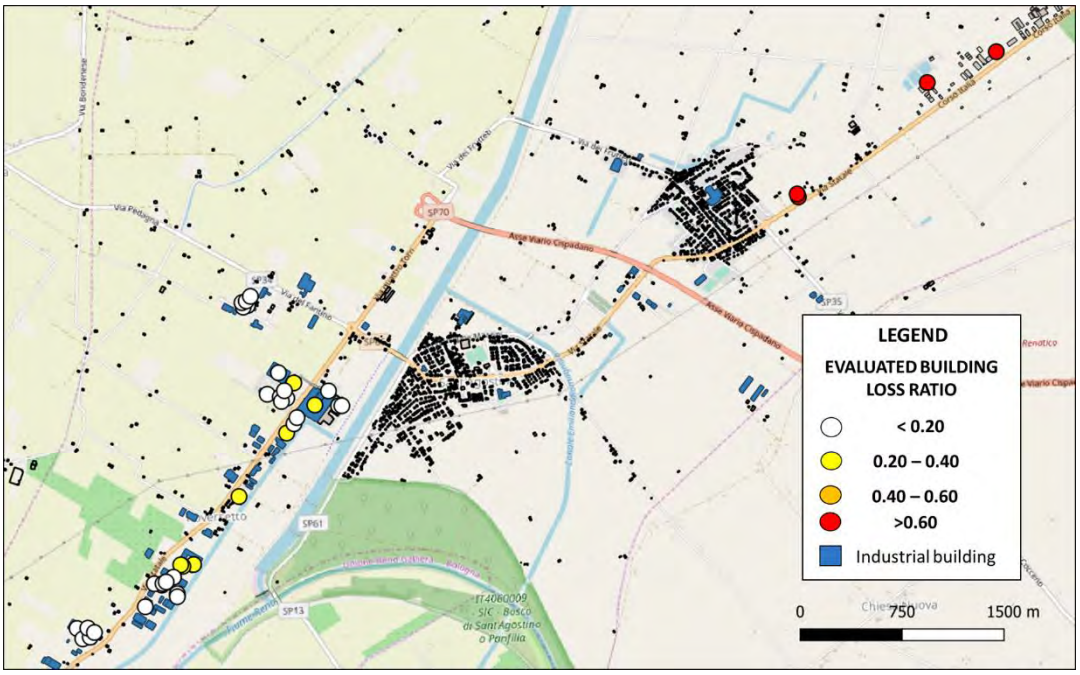

Figure 5-30 Expected building Loss Ratio on industrial buildings for the 20 may 2012 Earthquake scenario.

	Mean Loss Ratio (%)	Loss (€)
BUILDING	25.4	460'588.71
CONTENTS	27.6	4'011'579.71
BUSINESS INTERRUPTION	22.2	5'886'474.89

Figure 5-31 Summary of expected Mean Loss Ratios and Mean economic losses for industrial buildings, contents and loss of income.

This project has received funding from the European Union's Horizon 2020 research and innovation programme under grant agreement No. 700748

5.5.2 Mitigation

The applicability of mitigation options defined in the Deliverables 4.5, 6.5 and 7.4 has been evaluated performing a benefit cost analysis. There are different criteria to compute the annualized cost of mitigation, one of the most adopted is to equally distribute the invested capital over the lifecycle of the structure adding the interest rate (fixed or variable). The question can be seen as equivalent to borrow the capital necessary for mitigation from a bank at a fixed rate mortgage and pay it back with a constant annual amount. In this way the annualized cost sustained for mitigation is the amount paid by the borrower every year that ensures that the loan is paid off, in full of interest, at the end of its term. This cost should be compared with the annualized benefit, i.e. the earthquake losses saved per each year which in probabilistic assessment can be computed integrating the product between losses given by earthquakes of different intensity and their annual occurrence probability. Within the Liquefact software, 10 among the existing liquefaction mitigation options are implemented. For each of them a cost/cubic meter and the expected mitigation solution level (which is a proxy of the efficiency) must be defined in order to evaluate the cost-benefit ratio. Out of the 10 available mitigation options, the benefit cost analysis has been performed considering the most applicable on existing structures, i.e.: earthquake drains, induced partial saturation, compaction grouting, low pressure grouting, jet grouting and deep soil mixing (Table 5-5).

Table 5-5 Evaluated mitigation techniques in cost/benefit analysis.

Technology	Mitigation Cost €/mc	Expected Mitigation Solution Level
Earthquake Drains	30	80
Vibro Replacement	20	55
Induced Partial Saturation	30	45
Compaction Grouting	70	70
Low Pressure Grouting	100	65
Jet Grouting	50	75
Deep Soil Mixing	50	60

The applicability of these mitigation techniques has been evaluated on the buildings whose estimated building loss ratio is greater than 35% (Table 5-6), while a time horizon of 30 years (representative of a structure in the middle of its life) and an mortgage rate equal to 3% have been defined.

Table 5-6 Assigned Loss Factors in the fragility model used to assess the liquefaction-induced physical damage.

This project has received funding from the European Union's Horizon 2020 research and innovation programme under grant agreement No. 700748

Risk Identification	Latitude	Longitude	EARTHQUAKE DRAINS (CBR)	VIBRO REPLACEMENT (CBR)	INDUCED PARTIAL SATURATION (CBR)	COMPACTION GROUTING (CBR)	LOW PRESSURE GROUTING (CBR)	JET GROUTING (CBR)	DEEP SOIL MIXING (CBR)
1465	44.7892	11.370318	0.369	0.358	0.657	0.985	1.515	0.657	0.821
1466	44.7925	11.371141	0.461	0.447	0.820	1.231	1.893	0.820	1.025
1469	44.791	11.372969	2.380	2.308	4.231	6.346	9.764	4.231	5.289
1909	44.7807	11.361334	1.447	1.404	2.573	3.860	5.938	2.573	3.216
1910	44.7806	11.360338	0.087	0.084	0.155	0.232	0.357	0.155	0.194
1911	44.7807	11.360102	0.066	0.064	0.118	0.177	0.272	0.118	0.148
328	44.8038	11.418495	0.011	0.010	0.019	0.028	0.044	0.019	0.024
335	44.804	11.418369	0.063	0.061	0.112	0.168	0.259	0.112	0.140
1985	44.7851	11.365688	2.312	2.242	4.110	6.165	9.484	4.110	5.137
2844	44.813	11.437303	0.055	0.053	0.097	0.146	0.225	0.097	0.122
3177	44.8111	11.430819	0.042	0.041	0.074	0.111	0.171	0.074	0.093

5.5.3 Probabilistic risk assessment

The liquefaction risk assessment on the industrial district of Terre del Reno has also been performed in probabilistic terms. Eight seismic scenarios, with return periods ranging between 30 to 4975 years have been considered. The annual liquefaction risk has been calculated convoluting the losses corresponding to each scenario times the annual exceedance frequency (Figure 5-32).

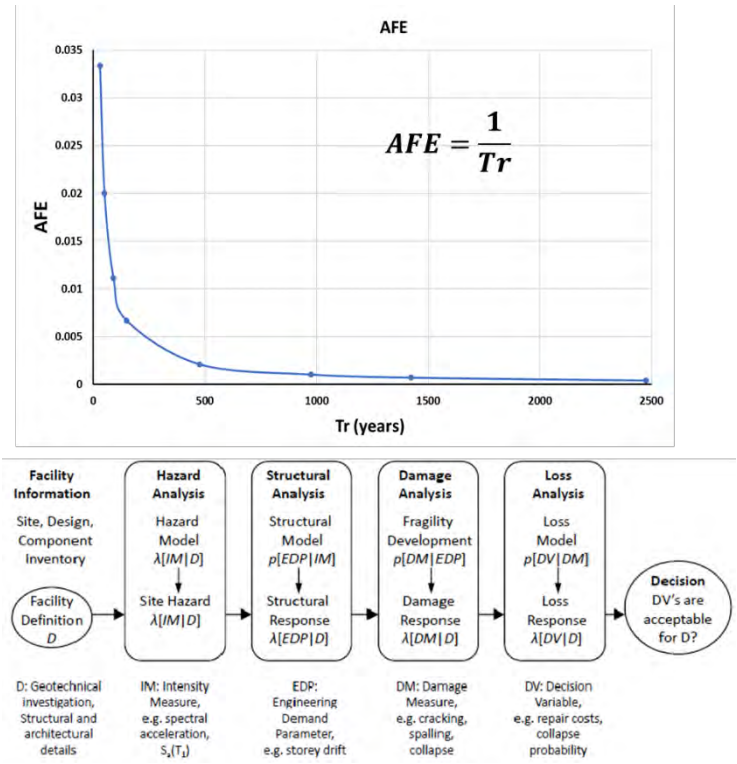

Figure 5-32 Seismic Annual Frequency of Exceedance and probabilistic definition of risk assessment (Cornell and Krawinkler, 2000).

In details the hazard, expressed as PGA, spectral acceleration for periods T equal to 1 sec and required intensity measures are evaluated for different return periods (30, 50, 90, 150, 475, 975, 1423, 2475 years). For each of them, the conventional procedure to evaluate liquefaction hazard and building settlements have been applied on each building and combined with the annual frequency of exceedance following the procedure summarized in Figure 5-33.

This project has received funding from the European Union's Horizon 2020 research and innovation programme under grant agreement No. 700748

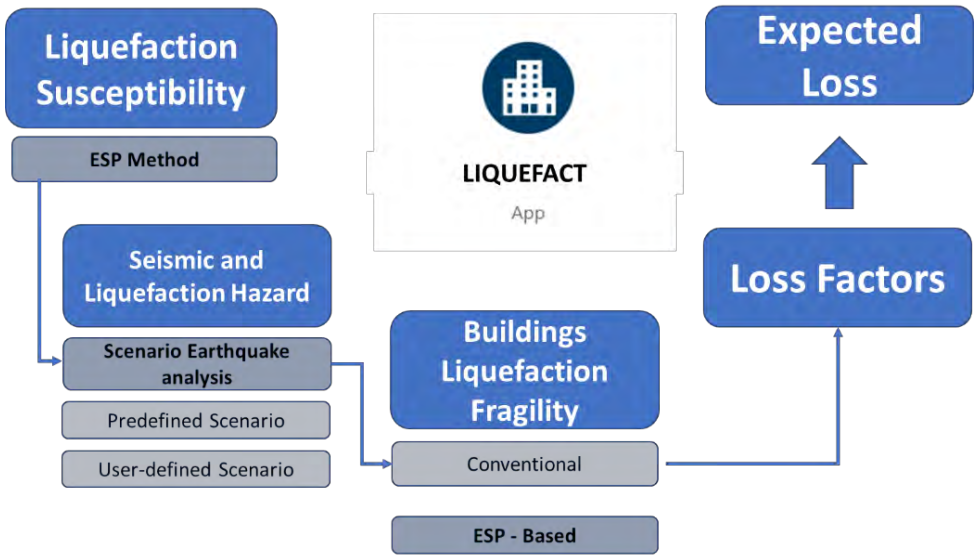

Figure 5-33 Flowchart of the applied Liquefact procedure to evaluate the impact of liquefaction on industrial buildings.

Once the liquefaction susceptibility was preliminarly defined, the arithmetic mean settlement among the three above defined methods (Karamitros, 2013; Bray & Macedo, 2017; Bullock et al., 2018) has been computed for each scenario. The physical impact of liquefaction on industrial buildings has been estimated with the fragility model defined by Fotopouolu et al. (2018) adopting the Liquefact conventional approach. In particular, the curves for low-rise reinforced concrete buildings have been used to quantify the damage of industrial buildings undergoing liquefaction-induced effects. Since these curves assume differential settlement as EDP, a scaling factor equal 0.667 (i.e. 2/3) was applied to convert absolute into differential settlements. Four damage limit states ranging from slight-to-complete are defined and the loss factors associated with each damage state are summarized in the following table. By combining the probability of reaching each damage state to the loss factor, the Mean Damage Ratio has been evaluated on the portfolio of industrial buildings.

This project has received funding from the European Union's Horizon 2020 research and innovation programme under grant agreement No. 700748

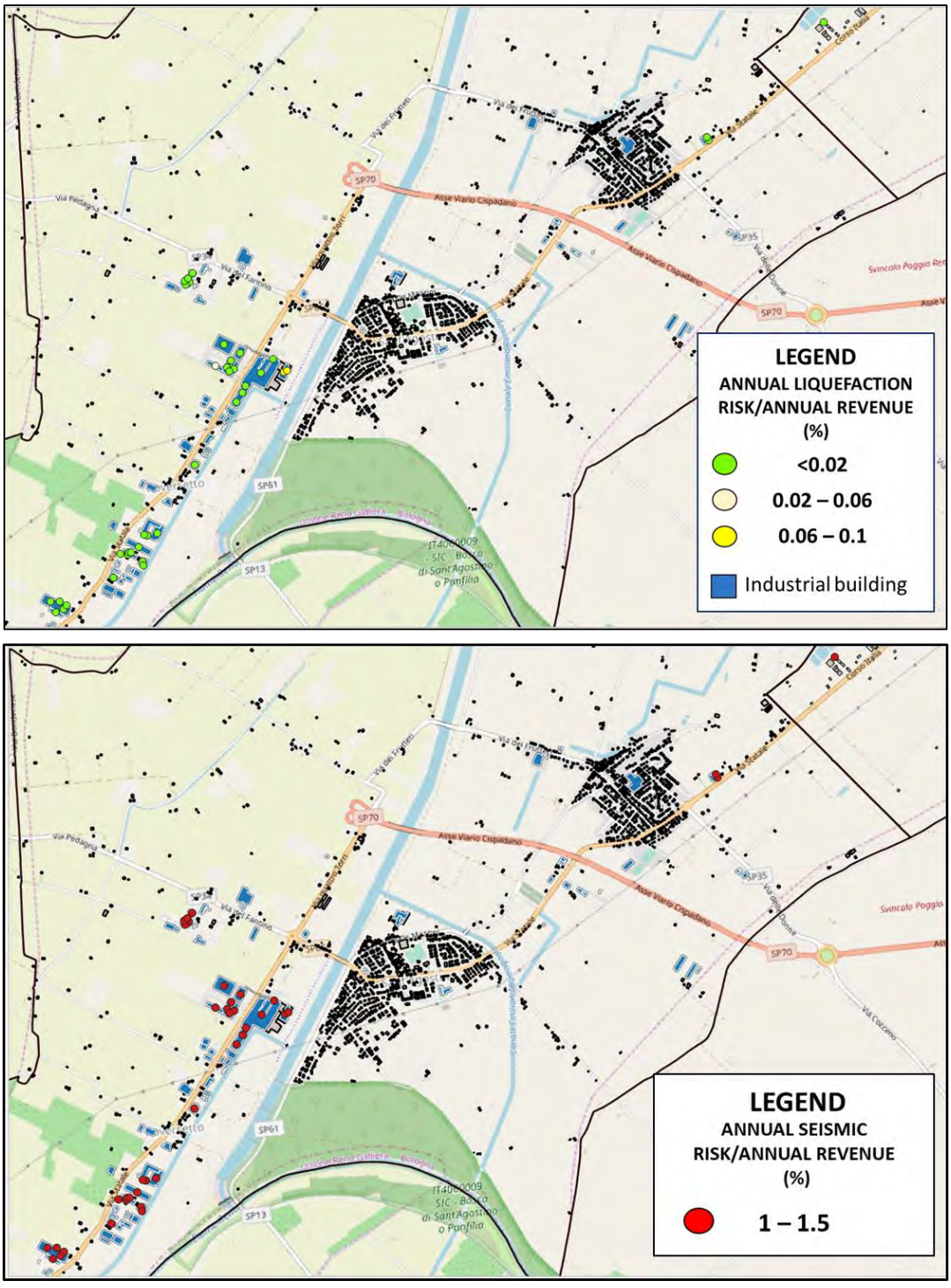

Figure 5-34 Map reporting the liquefaction (a) and traditional (b) Seismic Risk Assessment for the industrial district of Terre del Reno.

On the selected industrial district, the results of probabilistic liquefaction risk analysis show an expected annual loss lower than 1% of the annual business revenue (Figure 5-34). Various mitigation options have

been considered over a 30-years time horizon, assuming 3% mortgage rate for the annualized cost-benefit analysis.

An example of output is given in Figure 5-35, assuming a mitigation solution that costs € 100.00 per cubic meter soil. In this analysis, it must be considered that the annualized liquefaction risk is always lower than 1% of the annual business revenue. Therefore, it can be concluded that mitigation is advantageous only for the factories having the highest annual revenue (i.e. 60'000'000,00 €).

At the same time, the traditional seismic risk has been run considering the same eight seismic scenarios. The available seismic fragility curves (Syner-G fragility function manager, http://www.vce.at/SYNER-G/) for low rise and low code RC buildings have been used to perform such analysis. Here it can be observed that seismic risk is 10 times higher than for liquefaction.

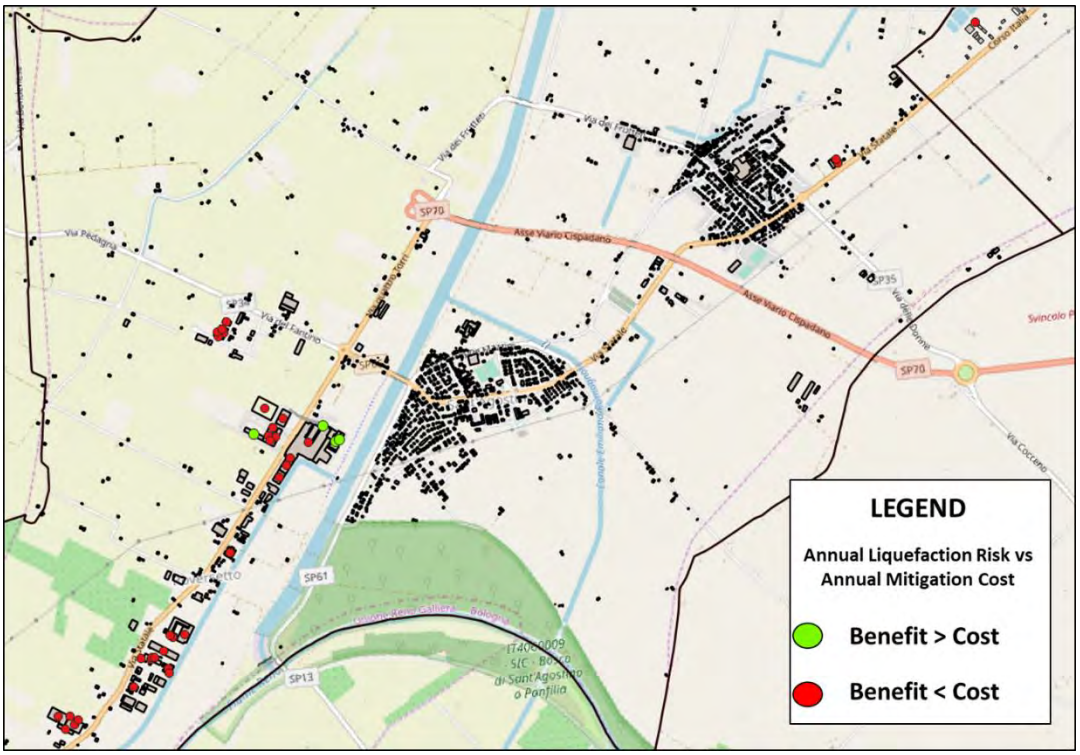

Figure 5-35 Output of Benefit/Cost analysis assuming a mitigation cost equal to 100.00 €/mc.

5.6 Bibliography

Alessio G. et al., 2013: "Liquefaction phenomena associated with the Emilia earthquake sequence of May–June 2012 (Northern Italy)". Nat. Hazards Earth Syst. Sci., 13, 1–13, 2013.

Baggio C., Bernardini A., Colozza R., Corazza L., Della Bella M., Di Pasquale G., Dolce M., Goretti A., Martinelli A, Orsini G., Papa F., Zuccaro G., 2009: "Manuale per la compilazione della scheda di 1° livello di rilevamento danno, pronto intervento e agibilità per edifici ordinari nell'emergenza post-sismica (AeDES)". Dipartimento della Protezione Civile.

Berardi R., Margottini C., Molin D. and Parisi A., 1991: "Soil liquefaction: case histories in Italy". Tectonophysics, 193 (1991) 141-164.

Bondesan A., Bondesan M., 2017: "Breve storia idrografica del territorio ferrarese", http://www.naturalistiferraresi.org/wp-content/uploads/2017/03/Storia-Idrografica-del-Ferrarese.pdf

Boulanger R.W., & Idriss I.M., 2014: "CPT and SPT based liquefaction triggering procedures", Department of Civil and Environmental engineering, University of California at Davis.

Bray, J. & Macedo, J., 2017. 6th Ishihara lecture: "Simplified procedure for estimating liquefaction-induced building settlement". Soil Dynamics Earthquake Engng 102, 215–231.

Bullock Z., Karimi Z., Dashti S., Porter K., Liel A.B., Franke K. W., 2018: "A physics-informed semi-empirical probabilistic model for the settlement of shallow-founded structures on liquefiable ground". Géotechnique [https://doi.org/10.1680/jgeot.17.P.174].

Cornell, C.A., and Krawinkler, H. 2000: "Progress and Challenges in Seismic Performance Assessment". PEER Center News, 3, 1-3.

Cubrinovski M., Rhodes M., Ntritsos N., van Ballegooy S., 2017: "System Response of liquefiable deposits". PBD III Earthquake Geotechnical Engineering, Vancouver.

Emergeo Working Group, 2012: "Technologies and new approaches used by the INGV EMERGEO Working Group for real-time data sourcing and processing during the Emilia Romagna (northern Italy) 2012 earthquake sequence". ANNALS OF GEOPHYSICS, 55, 4, 2012; doi: 10.4401/ag-6117.

Emergeo Working Group, 2013, G. Alessio, L. Alfonsi, C. A. Brunori, P. Burrato, G. Casula, F. R. Cinti, R. Civico, L. Colini, L. Cucci, P. M. De Martini, E. Falcucci, F. Galadini, G. Gaudiosi, S. Gori, M. T. Mariucci, P. Montone, M. Moro, R. Nappi, A. Nardi, R. Nave, D. Pantosti, A. Patera, A. Pesci, G. Pezzo, M. Pignone, S. Pinzi, S. Pucci, S. Salvi, C. Tolomei, P. Vannoli, A. Venuti, and F. Villani, Liquefaction phenomena associated with the Emilia earthquake sequence of May–June 2012 (Northern Italy), Nat. Hazards Earth Syst. Sci., 13, 935–947, 2013.

Fioravante, V. et al., 2013: "Earthquake geotechnical engineering aspects: the 2012 Emilia Romagna earthquake (Italy)". Seventh international Conference on Case Histories in Geotechnical Engineering, April 29 th – May 4th, 2013. Chicago (US).

Fotopoulou S., Karafagka S., Pitilakis K., 2018: "Vulnerability assessment of low-code reinforced concrete frame buildings subjected to liquefaction-induced differential displacements, Soil Dynamics and Earthquake Engineering, 110:173-184.

Galli, P. 2000: "New empirical relationships between magnitude and distance for liquefaction". Tectonophysics 324, 169-187.

Iwasaki T., Tatsuoka F., Tokida K., Yasuda S., 1978: "A Practical method for assessing soil liquefaction potential based on case studies at various sites in Japan", [conference] // 2nd International conference on Microzonation. - 1978. - pp. 885-896.

Karamitros, D.K., Bouckovalas, G. D., Chaloulos Y.K., 2013: "Seismic settlements of shallow foundations on liquefiable soil with a clay crust". Soil Dynamics and Earthquake Engineering. 46. 64-76.

Kongar I., Rossetto T., Giovinazzi S., 2015: "Evaluating Simplified Methods for Liquefaction Assessment for Loss Estimation". Nat. Hazards Earth Syst. Sci. Discuss., doi:10.5194/nhess-2016-281, journal Nat. Hazards Earth Syst. Sci. Published: 15 September 2016.

Martelli L., 2012: "The 2012 May 20 earthquake in the Emilia plain. The geologic point of view". 7th European Congress on Regional Geoscientific Cartography and Information Systems. Bologna 12th – 15th June 2012.

Martelli L., Calabrese L., Ercolessi G., Severi P., Romani M., Tarabusi G., Pileggi D., Rosselli S., Minarelli L., Pergalani F., Compagnoni M., Vannucchi G., Madiai C., Facciorusso J., Fioravante V., Giretti D., Mucciarelli M., Priolo E., Laurenzano G., Bramerini F., Speranza E., Conte C., Di Salvo G., Giuffrè M., Zuppiroli M., Guidi F., Vona V., Manicardi A., Mengoli B., Ugoletti C., Ricci L.; 2013: "Microzonazione Sismica dell'area Epicentrale Del Terremoto Della Pianura Emiliana Del 2012 (Ord. 70/2012)". Atti 32° Convegno Nazionale Gngts, Trieste. Isbn: 978-88-902101-7-4.

Matthews, B. W., 1975: "Comparison of the predicted and observed secondary structure of T4 phage lysozyme, Biochimica et Biophysica Acta – Protein Structure", 405(2), 442-451.

Maurer, B. W., Green, R. A., Oliver, S., Taylor, O. S., 2015: "Moving Towards an Improved Index for Assessing Liquefaction Hazard: Lessons from Historical Data". Soils and Foundations, 55(4): 778-787.

Papathanassiou G., Riccardo Caputo R., Rapti-Caputo D., 2012: "Liquefaction phenomena along the paleo-Reno River caused by the May 20, 2012, Emilia (northern Italy) earthquake". ANNALS OF GEOPHYSICS, 55, 4, 2012; doi: 10.4401/ag-6147.

Powers, D. M. W., 2011: "Evaluation: from precision, recall and F-measure to ROC, informedness, markedness and correlation", J. of Mach. Lear. Tech, 2(1), 37-63.

Regione Emilia-Romagna, PG.2012.0134978 del 31/5/2012a). "Primo rapporto sugli effetti della liquefazione osservati a S. Carlo, frazione di S. Agostino (Provincia di Ferrara)". A cura del gruppo di lavoro per la valutazione degli effetti di iquefazione a seguito dei terremoti del 20 e 29 maggio 2012.

Regione Emilia-Romagna, PG.2012.0134978 del 31/5/2012b. "Rapporto sugli effetti della liquefazione osservati a Mirabello (Provincia di Ferrara)". A cura del gruppo di lavoro per la valutazione degli effetti di iquefazione a seguito dei terremoti del 20 e 29 maggio 2012.

Romeo R.W., 2012: "Emilia (Italy) M5.9 earthquake on 20 May 2012: an unusual pattern of liquefaction". Italian Journal of Engineering Geology and Environment, 2 (2012).

Servizio Geologico, Sismico e dei Suoli Regione Emilia Romagna, 2012: "Terremoto 2012 geologia, rilievi agibilità, analisi dei danni".

Stefani M., Minarelli L., Pavanati A., Furin S., Tarabusi G., Gamberi S.: "Studio di microzonazione sismica di dettaglio dell'area del comune di mirabello (fe) basata sull'interpolazione tridimensionale di dati geologici e geofisici puntuali", Conference Paper · November 2014, DOI: 10.13140/2.1.5183.5681

Università di Ferrara, 2014: "Microzonazione sismica del Comune di Sant'Agostino", Rapporto di convenzione di ricerca.

van Ballegooy S., Malan P., Lacrosse V., Jacka M.E., Cubrinovski M., Bray J.D., O'Rourke T.D., Crawford S.A., Cowan H., 2014: "Assessment of Liquefaction-Induced Land Damage for Residential Christchurch", Earthquake Spectra, Volume 30, No. 1, pages 31–55, February 2014.

Zhang G., Robertson P.K., Brachman R.W.I., 2002: "Estimating liquefaction-induced ground settlements from CPT for level ground", Canadian.

This project has received funding from the European Union's Horizon 2020 research and innovation programme under grant agreement No. 700748

6 A PIPELINE NETWORK – URAYASU (JAPAN)

6.1 Introduction

The applicability of the liquefaction risk assessment procedure defined in the project and outlined in deliverable D7.1 has been here analysed for the case of Urayasu, a city geographically located in the bay of Tokyo, pertaining from an administrative viewpoint to the prefecture of Chiba (Japan). For this case study, data available on National Research Institute for Earth Science and Disaster Resilience (NIED) website and from the Chiba Information Map have been used. The format of data has been homogenised and processed automatically to calculate traditional indicators of liquefaction ground severity for the (Mw 9.0) 11th March 2011 Earthquake, occurred offshore of the Tōhoku Region, in northern Japan at 2.46 pm local time, at a depth of 29 kilometers (Suzuki et al., 2011; Kunugi et al., 2012). This earthquake is the most powerful earthquake ever recorded in Japan and among the strongest five even recorded in the world since 1900. Urayasu hosts a population of 164 024 inhabitants (2015) and is divided into three zones: Motomachi, Nakamachi and Shinmachi (in Japanese old, middle and new town). Despite a great distance (≈400km) from the hypocenter of the March 11th 2011 Great East Japan Earthquake, widespread and severe evidences of liquefaction were noticed in the city that affected buildings, roads, water supply and sewage lines (NPAJ, 2011; Bhattacharya S. et al., 2011). An example showing the uplift of manholes is given in Figure 6-2. The present chapter is dedicated to the assessment of risk on sewage pipelines exploiting the available information. To this aim databases have been created focusing on this category of infrastructures.

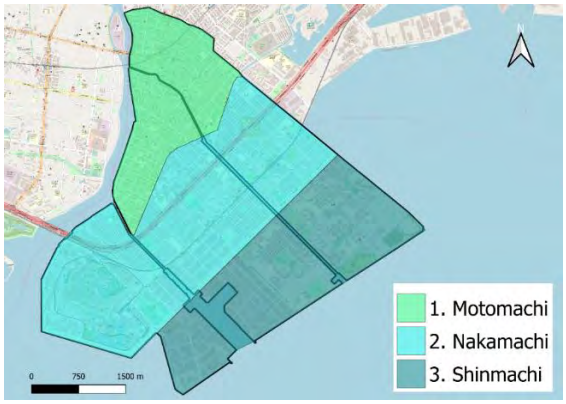

Figure 6-1 Map of Urayasu with indication of the three main areas forming the city.

This project has received funding from the European Union's Horizon 2020 research and innovation programme under grant agreement No. 700748

Figure 6-2 Uplift of sewage manholes caused by liquefaction.

6.2 The 2011 Great East Japan Earthquake sequence

The M_w=9.0 earthquake of Sendai and Tōhoku occurred on 11 March 2011 offshore of the Tōhoku Region in northern Japan at 2.46 pm local time, at a depth of 29 kilometers. Strong ground movements during the earthquake were observed on almost all the country, as confirmed by the three stations that observed seismic intensity of 7 on the scale of the Japan Meteorological Agency (JMA) and the 18 stations observed peak horizontal accelerations higher than 9.80 m/s^2 (Kamiyama, 2011).

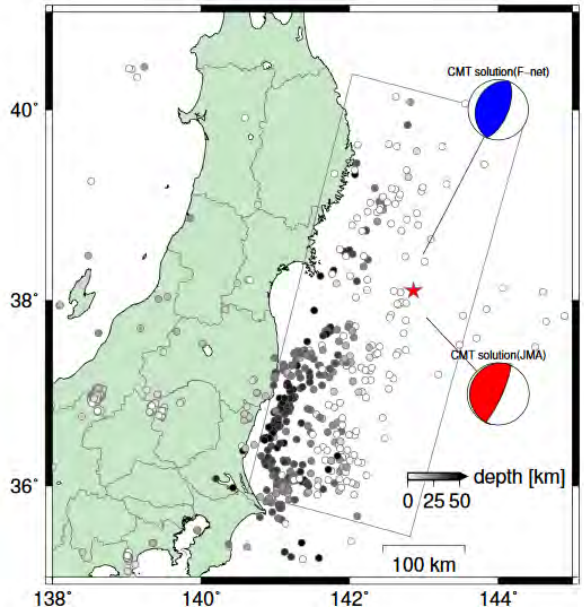

Figure 6-3 Aftershock distribution within 24 hours after the main shock, the rectangle area indicates the seismic fault (NIED).

Aftershocks occurred following the initial one (e.g. M_w7.0 at 3.06 pm, M_w 7.4 at 3.15 pm, M_w7.2 at 3.26 pm), and there were more than forty earthquakes of magnitude greater than 5.0 which took place in the hours following the initial shock. The distribution of aftershocks occurring within 24 hours after the main shock almost covers the fault zone.

At the dawn of March 13th, other shocks of 6.8 and 6.0 occurred in the north east of the country. On March 14th there was another great shock of magnitude 6.2. On March 15th, another shock of the same magnitude occurred 120 kilometers south-west of Tokyo, near Mount Fuji with its epicenter in Shizuoka. On March 16th, a quake of 6.0 shakes the Chiba prefecture. On March 17th, a new magnitude 5.8 quake occurred just outside Tokyo, with its epicenter off the coast of Ibaraki prefecture, north of the capital.

The March 11th earthquake was preceded by a series of large foreshocks over the previous 2 days, beginning on March 9 with a M_w = 7.4 event approximately 40 km from the epicenter of the March 11th earthquake and continuing with another three earthquakes greater than Mw = 6 on the same day.

The gigantic earthquake triggered powerful tsunami waves that may have reached as high as 40.5 metres in Miyako in Tōhoku Iwate Prefecture and inland in the Sendai area traveling up to 10 km. The tsunami caused the failure of the cooling system at the Fukushima Daiichi Nuclear Power Plant, which resulted in a level-7 nuclear meltdown and release of radioactive materials. The electrical power and backup generators were overwhelmed by the tsunami and the plant lost its cooling capabilities.

The number of confirmed deaths is 15,894 as of March 8, 2019, according to the reconstruction agency. More than 2,500 people are still reported missing. It is the most powerful earthquake ever recorded in Japan and the five even recorded in the world since 1900.

The 2011 Gigantic earthquake was an interface subduction earthquake with a low-angle reverse mechanism and was caused by tectonic movements of the North American (Okhotsk) plate and the Pacific plate (Figure 6.4). The Pacific plate dips under Okhotsk's underlying plate at a rate of 8 to 9 cm/year. This motion pushes the upper plate down until the accumulated stress causes a seismic slip-rupture event. Models of the rupture of this earthquake indicates that the fault moved as much as 50–60 m and slipped over an area approximately 500 km long (along strike) by 200 km wide (in the down-dip direction) (Figure 6.5). The rupture zone is approximately centred on the earthquake epicentre. The moment tensor solution gives two nodal planes, one dipping northwest at 81 degrees and one dipping southeast at 9 degrees.

Similar mechanisms have been observed in the off-shore Miyagi Prefecture (where the rupture was initiated) with a cyclical nature of about 30 years, as in the case of the M_w = 7.7 earthquake occurred in 1978, but the Great East Japan Earthquake differs from the others because it has involved an area significantly larger than the previous ones and it is the result of a coupled co-seismic rupture between different faults segments, such-as offshore Fukushima Prefecture and offshore Ibaraki Prefecture to south and offshore Iwate Prefecture to north. On July 13, 869 the last shock with this focal mechanism was observed and has been estimated as having a magnitude of at least M_w = 8.4.

This project has received funding from the European Union's Horizon 2020 research and innovation programme under grant agreement No. 700748

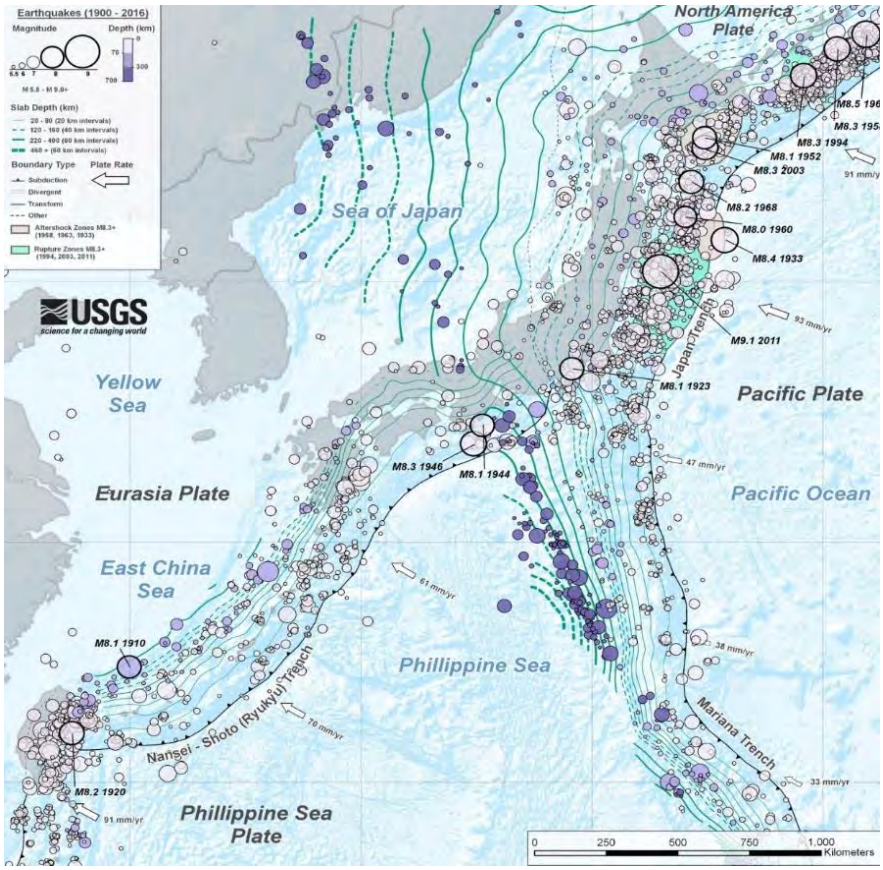

Figure 6-4 Map of tectonic summary region (source USGS)

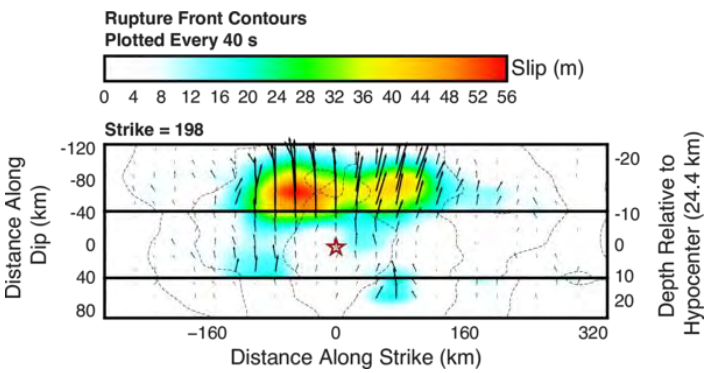

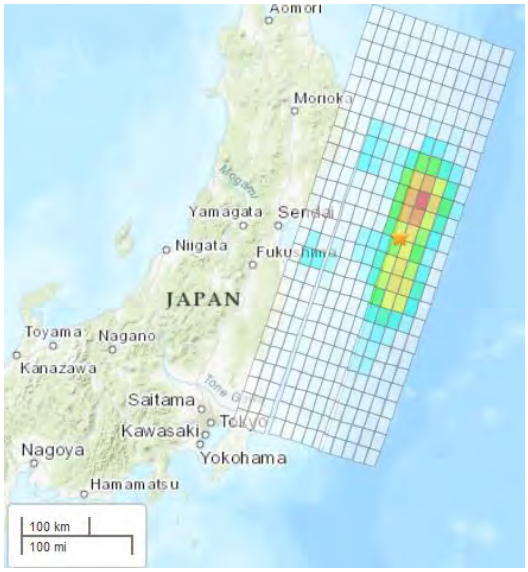

Figure 6-5 Cross-section and map of slip distribution. The strike direction is indicated above each fault plane and the hypocentre location is denoted by a star. Slip amplitude is shown in colour and the motion direction of the hanging wall relative to the footwall (rake angle) is indicated with arrows. Contours show the rupture initiation time in seconds. (source USGS).

Together with the severe damage caused by the tsunami and ground motions, the 2011 earthquake caused liquefaction as secondary seismic effect (Ishikawa et al., 2017). Kantö Region was largely affected by this phenomenon, in this region is possible to identify two areas affected by liquefaction: the first is situated near Naka river and Tone river in the northern part of the region, the second in the manmade peninsula along the Tokyo Bay area (Figure 6-6 Sites of liquefaction evidences in the Kanto Region after the 2011 earthquake sequence (Towhata et al., 2014).). Considering the particular density of human activities concentrated in the latter area and the susceptibility of the subsoil to liquefaction, assessment of risk becomes compulsory.

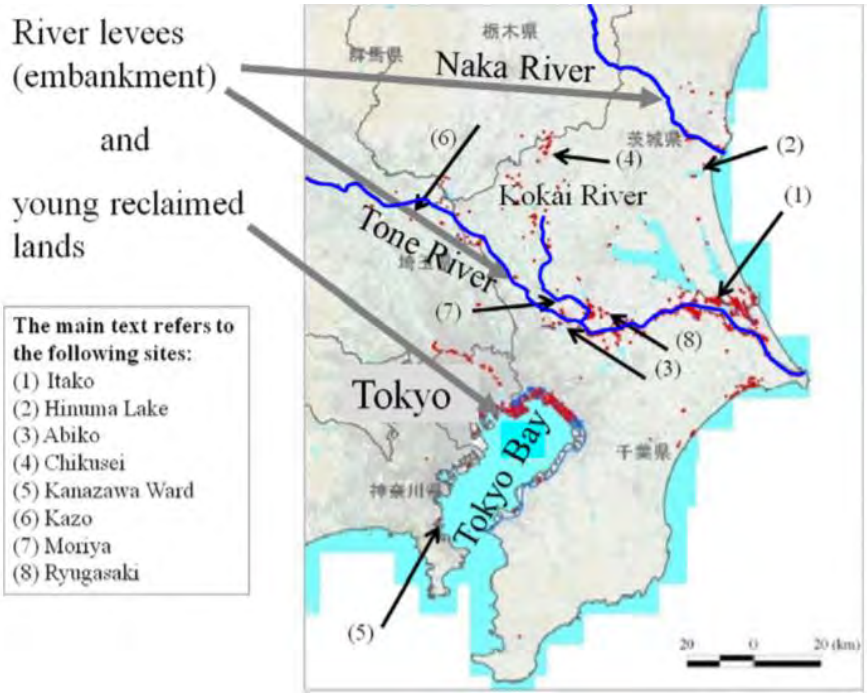

Figure 6-6 Sites of liquefaction evidences in the Kanto Region after the 2011 earthquake sequence (Towhata et al., 2014).

6.3 The case study of Urayasu

The Kanto Region consists mainly of a planar topography, its surface being the product of the Holocene era, during which the sea level rose over 100 m and reached the peak a few thousand years ago, and then lowered a few meters: the lowering of the ocean level jointly with the action of river erosion led to the formation of valleys, the most important of them located in the eastern part of Tokyo. Consequently, in the southern part, the rising of the water level created bays and lakes, subsequently filled by the natural and artificial deposition of sediments. In the geological map of Kantō Region's, Urayasu is defined a reclaimed area.

This project has received funding from the European Union's Horizon 2020 research and innovation programme under grant agreement No. 700748

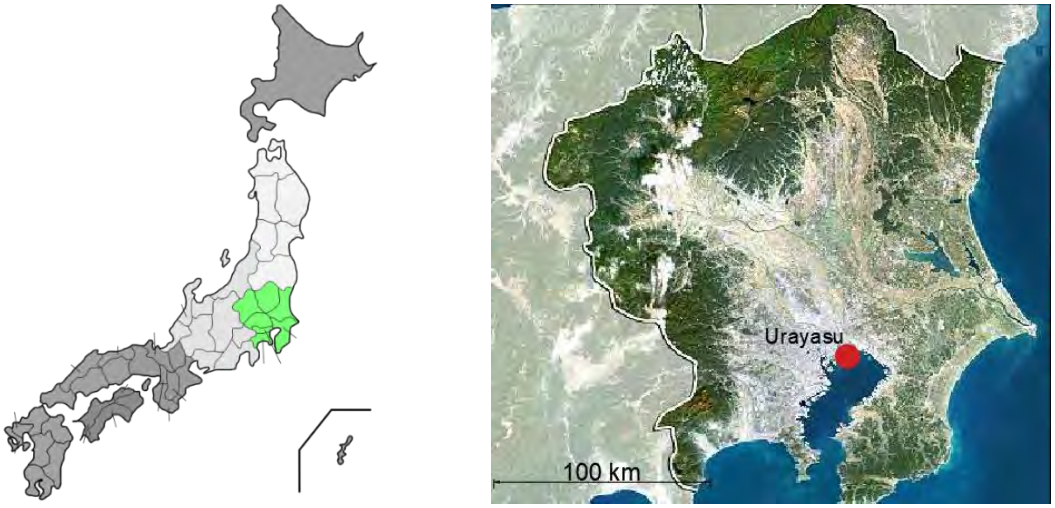

Figure 6-7 Recognition of Kantō Region and the geographical characters on the physical map.

The city arose on the east of the estuary of the Edo River, in the Chiba Prefecture. It can be ideally subdivided in two parts, one formed naturally by the sedimentation of river deposits, the second reclaimed in the last century by dredging materials from the sea. At 2015 the city, occupying a total area of 17.30 km^2, had an estimated population of 163.258 inhabitants, with a population density of 9490 persons/km^2. Urayasu city is divided into three zones (Figure 6-1): Motomachi, Nakamachi and Shinmachi, which literally, in Japanese, mean old town, middle town and new town. Motomachi is naturally formed on the banks of the Edo River, while Nakamachi and Shinmachi are reclaimed zones.

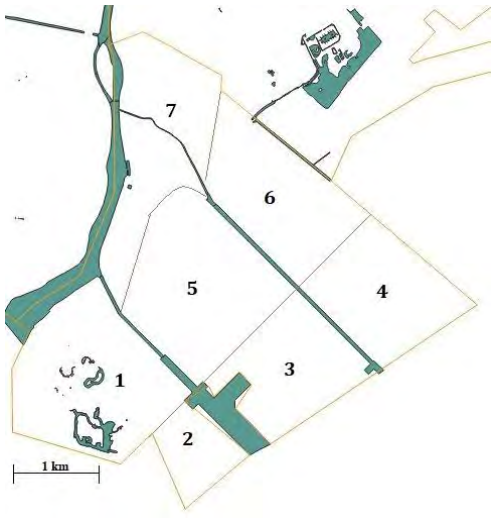

Figure 6-8 Map of Urayasu districts.

The reclaimed portion is about 75% of the total area of Urayasu City and the history of reclamation proceeded as follows: the area #2 was reclaimed between 1948 and 1975; subsequently, the reclamation of area #3 was accomplished between 1976 and 1980. The ground dredged by the seabed was used to fill the areas up to

the mean sea level, then a cover made of hill sand was applied on the top. Actually it's possible to distinguish seven zones In the city, labelled with numbers from 1 to 7 (Figure 6-8):

1. In the district of Maihama;
2. In the districts of Chidori;
3. In the district of Takasu;
4. In the districts of Akemi and Hinode;
5. In the districts of Imagawa, Benten, Tomioka, Higashino and Tekko-dori;
6. In the districts of Irifune, Mihama and Kairaku;
7. In the districts of Fujimi, Horie, Nekozane, Kitasakae and Todaijima.

The reclaimed area occupies about 75% of the total area of Urayasu City and the history of reclamation is the following: area 5 was reclaimed between 1948 and 1968, subsequently, areas 1 and 6 were reclaimed between 1968 and 1975 and, lastly, between 1976 and 1980, the realization of areas 2, 3 and 4 was concluded. The ground dredged from the seabed was used to fill the areas until it reached sea level. Then, the upper portion was covered with hill sand from the close Boso Peninsula.

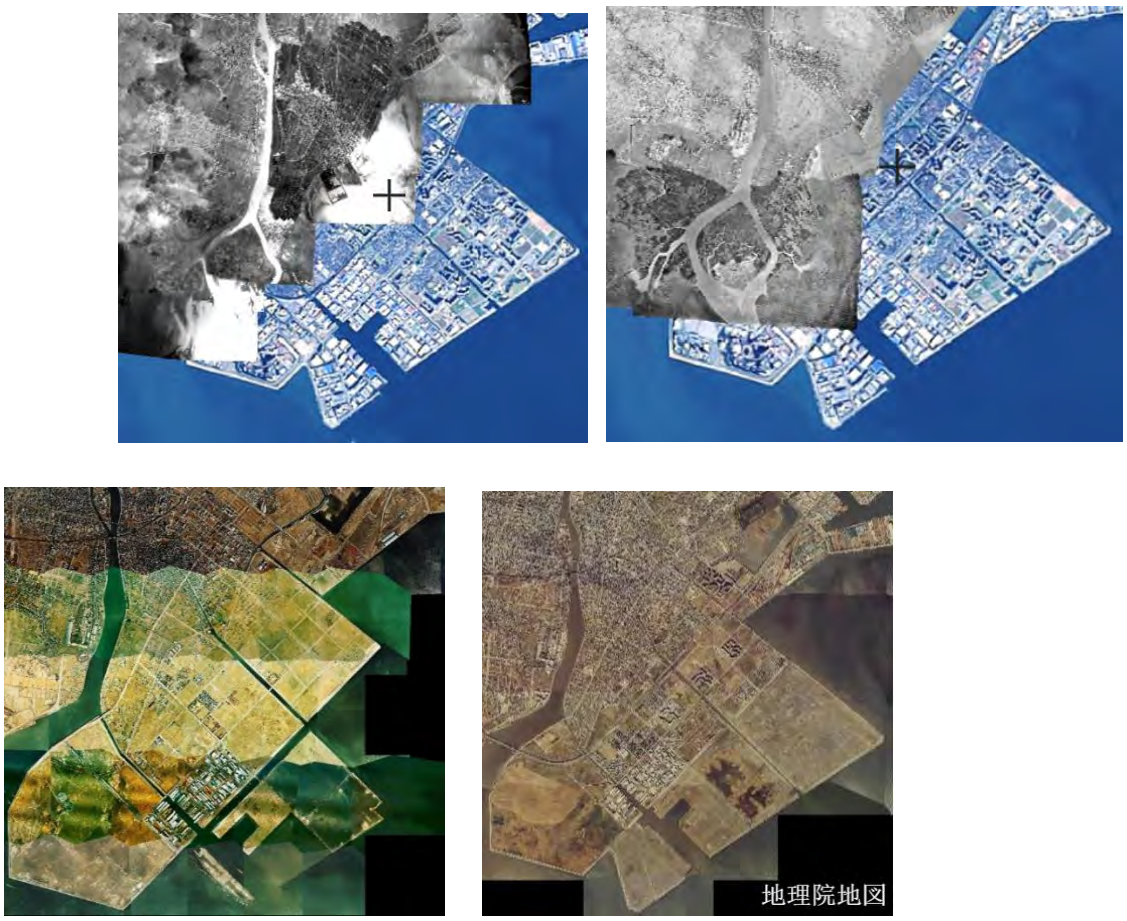

Figure 6-9 Aerial views of Urayasu, (a. in 1936; b in 1945-1950; c. in 1974-1978, d. 1979-1983 Source GSI).

6.3.1 The seismic event

Despite the earthquake's hypocentre is located about 400 km away from Urayasu City, the records of the CHB008 station, located in the city (Figure 6-10), were available for the present study (Goto et al., 2013). The station is located on soft soils (typically, average shear wave velocity in the upper 30 m VS30 is less than 200m/s) (Hayes et al., 2016) and the recorded ground acceleration time-series data at K-NET station are presented in Figure 6-10. With regard to local seismic amplification, the maps of mean shear wave velocity in the upper 30m and seismic amplification factors provided by the Japanese Seismic Hazard Information Station (J-SHIS) has been considered (Figure 6-12). These maps are available online in .kml format and can be accessed with the Google Earth software.

Origin time					
Date	Hour	Source Lat	Source Long	Source depth	Magnitude
11/3/2011	14:46:00	38.1	142.9	24.0 km	M9.0

			max acceleration (g)			Compositing of three vectors (g)
Lat	Long	Intensity	N-S	E-W	U-D	
35.654	139.902	5.1	0.127	0.16	0.076	0.177

Figure 6-10 Location of the seismometer in Urayasu City, data of the hypocenter data and of the CHB008 K-NET station (source J-SHIS).

This project has received funding from the European Union's Horizon 2020 research and innovation programme under grant agreement No. 700748

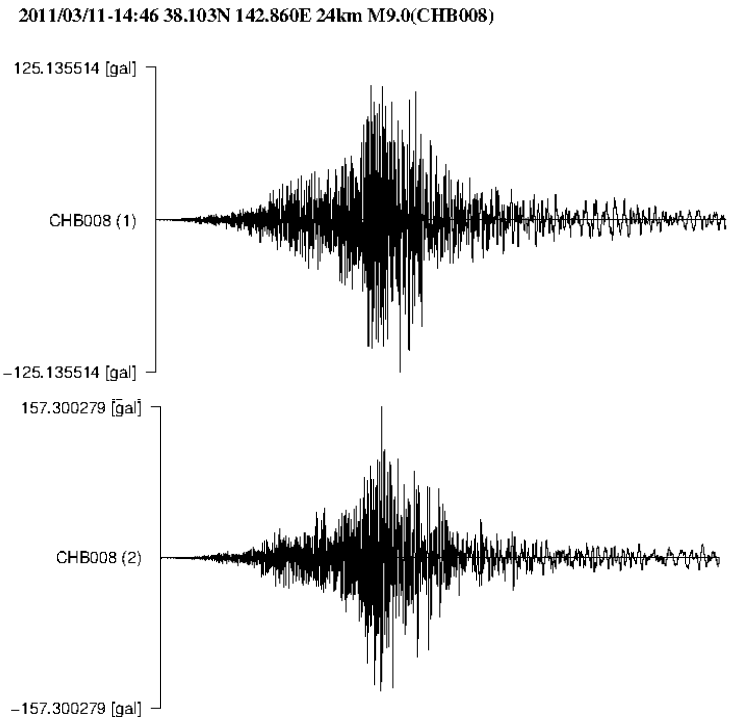

Figure 6-11 Time-series data at K-NET CHB008 station along the N-S, E-W alignments.

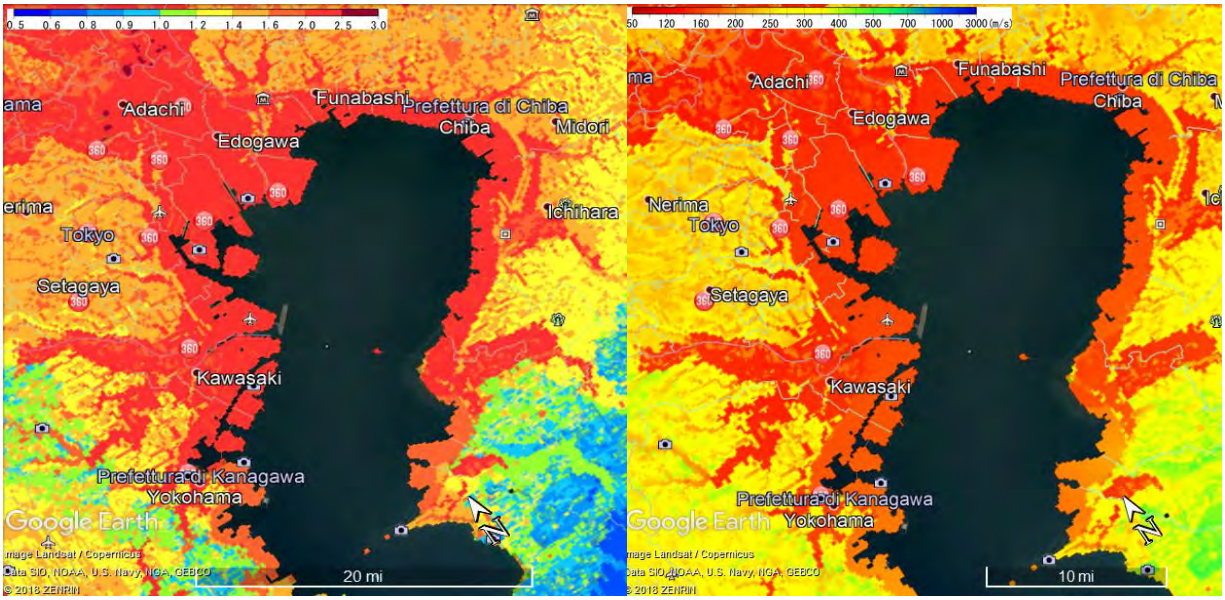

Figure 6-12 Amplification factors and mean shear wave velocity in the upper 30 m for Urayasu city (Source J-SHIS).

This project has received funding from the European Union's Horizon 2020 research and innovation programme under grant agreement No. 700748

6.3.2 Databases adopted for the study

The database of Urayasu has been built with a stepwise procedure, dividing the entire dataset into different categories:

- geotechnical database: containing data about subsoil stratigraphy, mechanical properties and groundwater depth;
- structural database: containing data on the characteristics of infrastructures;
- damage database: containing information on the surveyed evidences of liquefaction and damage.

All collected data have been combined into a geographic information system (GIS), using the open source software QGIS 3.4, and representing data on the Coordinate Reference System (CRS) WGS 84, UTM 54N projection.

6.3.2.1 Geotechnical Database

The boreholes and in situ tests available online for the case study of Urayasu city are taken from the web site of Chiba Prefecture and of the National Research Institute for Earth Science and Disaster Resilience (NIED). Basically, the available mechanical investigation of the subsoil was carried out by means of Standard Penetration Tests.

The SPT database contains 222 profiles divided as follows:

- 206 profiles taken from Chiba Prefecture Information map (Figure 6-13);
- 16 additional tests from the National Research Institute for Earth Science and Disaster Resilience (NIED) (Figure 6-14).

Among the above list, 22 SPTs have been neglected as they were performed at too shallow depth to be considered representative of the subsoil stratigraphy.

This project has received funding from the European Union's Horizon 2020 research and innovation programme under grant agreement No. 700748

Figure 6-13 Position of the Standard Penetration Tests downloaded from the Chiba Information Map.

Figure 6-14 Standard Penetration Tests location (Source NIED).

All considered SPTs were available in pdf format and have thus been digitized (Figure 6.14) transcribing values in a spreadsheet. In order to make all data consistent with the standard procedure (JGS, 2013) , each measured N_{SPT} blow count has been corrected as follows to obtain the values corresponding to a released energy ER=60% (Skempton, 1986):

- $$N_{60} = \frac{ER_m}{ER} N_m \quad (1)$$

The coefficients ER_m depend on the adopted equipment and were derived from Table 6.1. Being present in the literature two different corrections for the Japanese SPT, it was decided to apply the Tombi correction to

the tests carried out after the 1960s, because most of recent SPT data should have been obtained using semi or fully automatic release method that is equivalent to Tombi method in terms of the energy correction; instead, for the tests dating back to the 60s, the "Rope and Pulley with special throw release" correction was applied (Figure 6-15). Finally, the liquefiable layers were identified from the boreholes and an average number of blows was attributed to each of them (Figure 6-16).

Table 6-1 Released energy ERm of the most common equipment for SPT tests (Canadian Foundation Engineering Manual, 1992, in italian).

Paese	Tipo di maglio	Sgancio del maglio	Rilascio energia stimata ER_m (%)	Fattore di correzione per 60% di rilascio energia ER_m/ER
Giappone	*Donut*	*Tombi*	78	1.30
	Donut	*Rope and pulley with special throw release*	67	1.12 1.2 (media)
U.S.A.	*Safety*	*Rope and pulley*	60	1.00
	Donut	*Rope and pulley*	45	0.75
Argentina	*Donut*	*Rope and pulley*	45	0.75
Cina	*Donut*	*Free-fall*	60	1.00
	Donut	*Rope and pulley*	50	0.83
U.K.	*Pilcon*	*Trip*	60	1.00
	Old standard	*Rope and pulley*	60	1.00

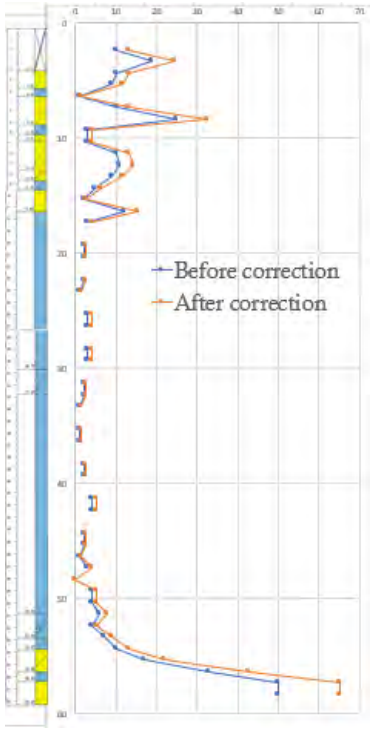

Figure 6-15 Comparison of the SPT data before and after correction.

This project has received funding from the European Union's Horizon 2020 research and innovation programme under grant agreement No. 700748

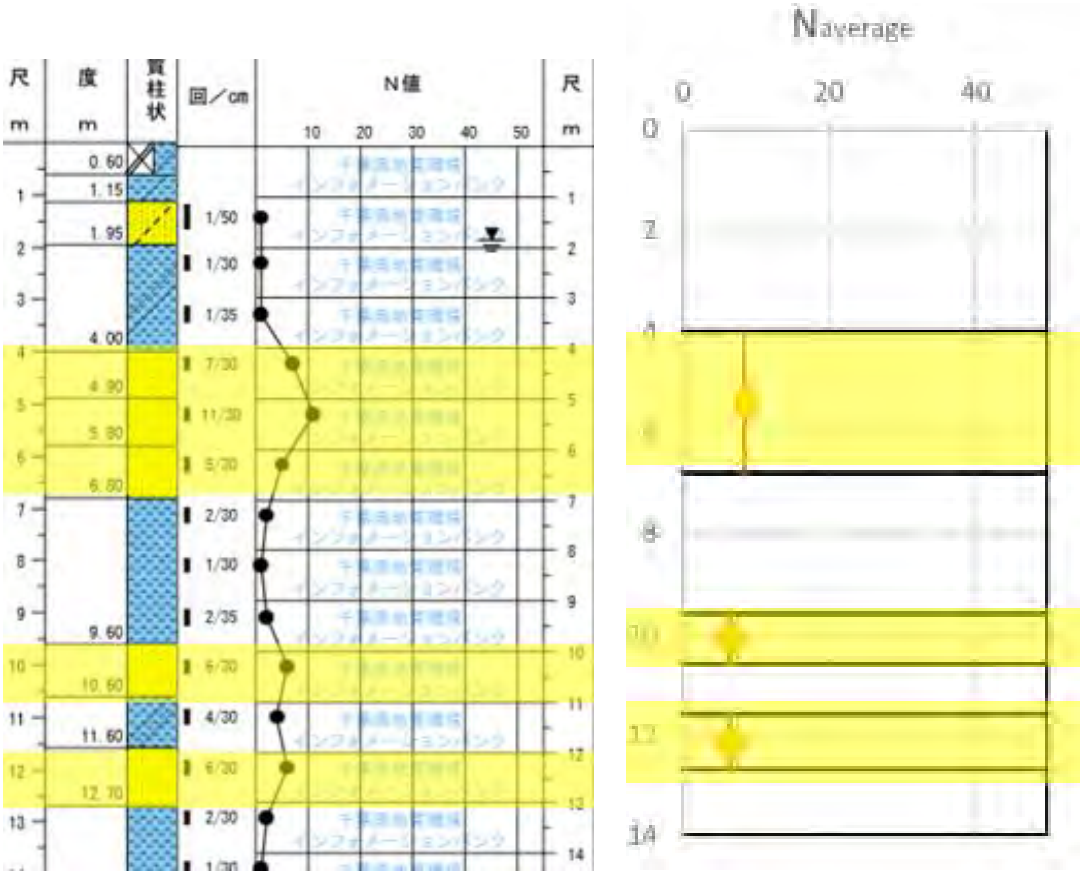

Figure 6-16 Example of discretized SPT with identification of liquefiable layers.

The information on the groundwater depth comes from the post-earthquake reports of Urayasu City. From Figure 6-17, it is seen that the groundwater table is uniformly deep over the entire area, being positioned almost everywhere a couple of metres below the ground level and reaching a maximum depth of about four metres only in some positions. These few singularities have been removed in the present study considering the closeness to the sea and that there is no particular justification like water feeding or extraction. The map, available in pdf format, was converted into a .png file, uploaded onto QGIS and georeferenced. The values of water level necessary to perform liquefaction assessment close to SPT profiles have been taken manually from this map.

The stratigraphy of Urayasu is very regular and it is quite immediate to distinguish the different layers of soil. Individual layers were identified combining in situ investigations with information found in the literature: reference has been particularly made to Yasuda et al., (2012 and 2013) that provides a typical section of the Urayasu stratigraphy (Figure 6-18).

Six different soil portions can be identified in the cross section of Figure 6.18: an upper layer of hill sand (B); a layer of dredged sandy soil (F) with low SPT N-values of 2-8 and a thickness of 6-9 m; an alluvial sand layer

This project has received funding from the European Union's Horizon 2020 research and innovation programme under grant agreement No. 700748

(As) having SPT N-values between 10-20 and a thickness of 4-8 m; a very soft alluvial clay layer (Ac) having a thickness of 10-40 m; a deeper diluvial dense sandy layer (Ds) having SPT N-values larger than 50.

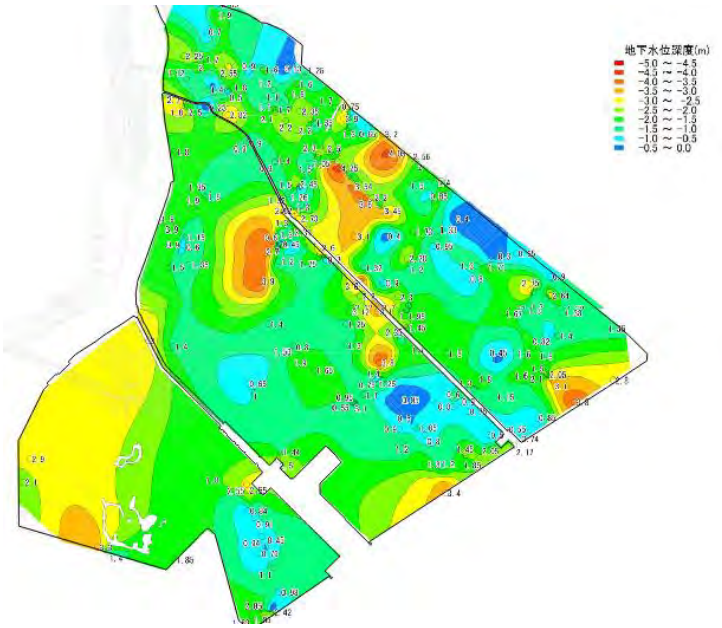

Figure 6-17 Map of groundwater table (source Urayasu aftershock report).

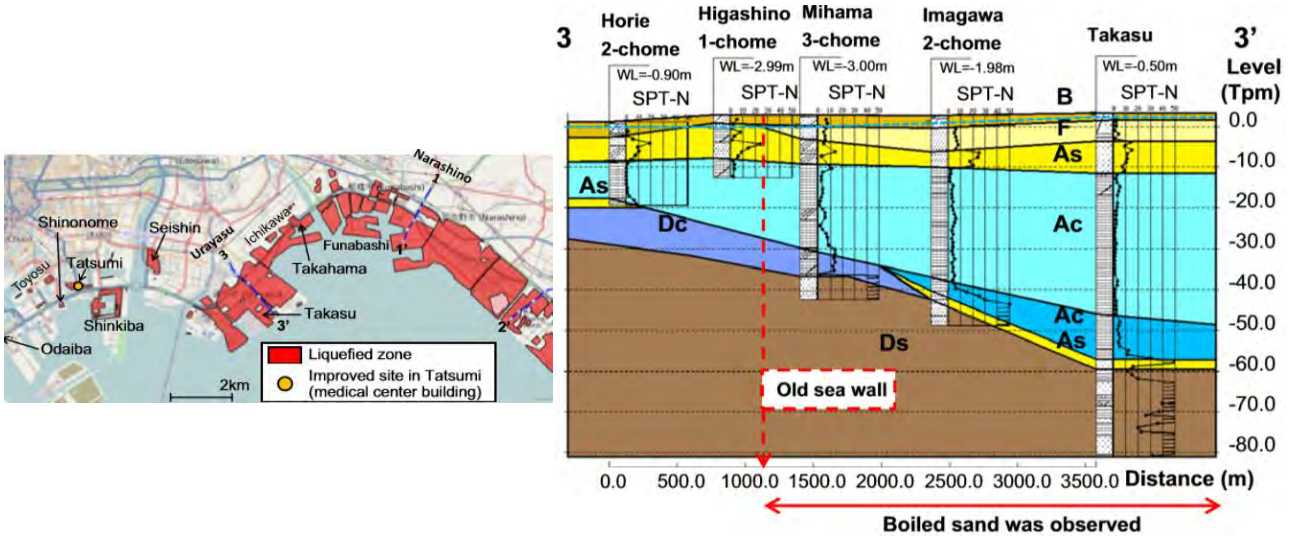

Figure 6-18 Cross sections of the subsoil in Urayasu. B: Fill, F: Dredged soil, As: Alluvial sand, Ac: Alluvial clay, Ds: Diluvial sand, Dc: Diluvial clay.

This project has received funding from the European Union's Horizon 2020 research and innovation programme under grant agreement No. 700748

6.3.2.2 Structural Database

This database consists of a collection of shapefiles containing the location of buildings and infrastructures present in Urayasu City. In particular, the available files contain:

1. Buildings

Figure 6-19 Map showing Buildings situated in Urayasu (source Geofabrick).

2. Roads:

Figure 6-20 Map showing Roads situated in Urayasu (source Geofabrick).

This project has received funding from the European Union's Horizon 2020 research and innovation programme under grant agreement No. 700748

3. Railways:

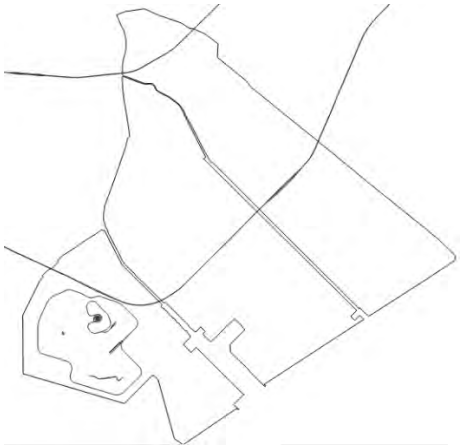

Figure 6-21 Map showing railways line in Urayasu (source Geofabrick).

4. Sewer Pipelines: This shapefile contains the location of each pipe of the sewage network. In particular, Figure 6.22.a represents pipes with two different colours: red lines indicate damaged, blue lines indicate undamaged pipelines. The information relating to damage was obtained from the following map Figure 6-22 .b, contained in the Aftershock Report, prepared by Liquefaction Mitigation Investigation Committee, Chiba Prefecture 2011. Here pink lines are used to indicate damaged sewer pipes, orange dots to indicate uplifted manholes, green and purple points to indicate, respectively, sunk and shear damaged manholes. This document also reports a statistic of damage seen on the sewage pipelines (Figure 6-23) from which it is seen that, although the major part of pipelines has diameter between 200 and 300 mm, the percentage of damaged pipes is slightly dependent on this dimension.

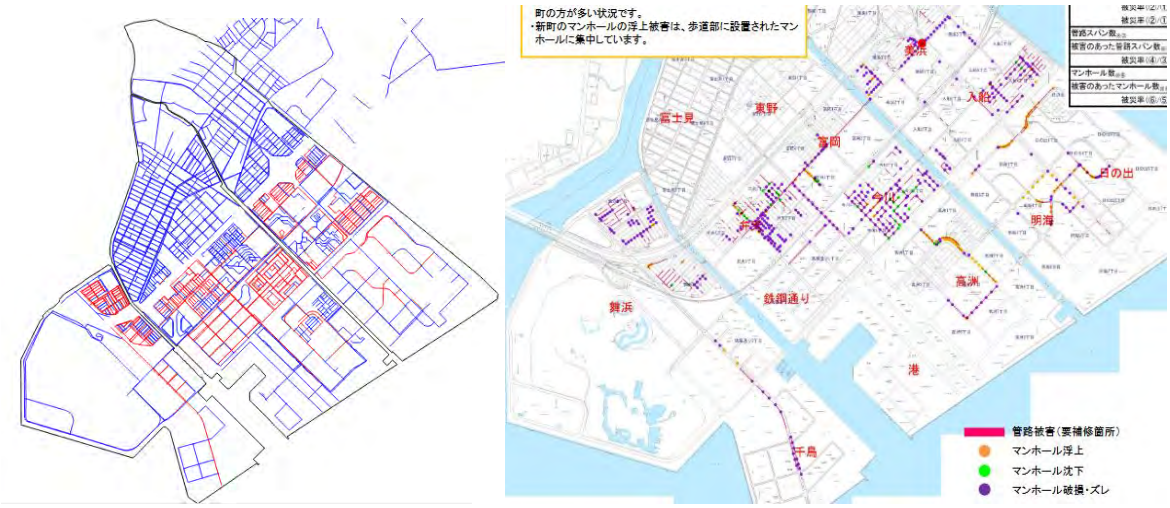

Figure 6-22 Map showing damaged and undamaged sewer pipes (a) and map of damaged sewer pipes and manholes in Urayasu City (b) (Source Liquefaction Mitigation Investigation Committee, Chiba Prefecture 2011).

This project has received funding from the European Union's Horizon 2020 research and innovation programme under grant agreement No. 700748

(a) (b)

Figure 6-23 Percentage of damaged pipes for each class of diameter (a) (purple represents damaged, salmon undamaged pipelines) and length of damaged pipes for each class of diameter (b).

6.3.2.3 Land damage

The purpose of this database is to collect data on the effects of soil liquefaction, in order to validate liquefaction risk assessment methods. Usually, liquefaction appears at the ground level in the form of cracks, fissures or sand boils (Figure 6.24.a). All evidences of liquefaction were surveyed in the days immediately after the earthquakes and photos were taken to certify the extent of liquefaction damage. The total number of available photos is 204, of which 185 taken in places that have suffered liquefaction and 19 taken in areas that did not show evidences. Photos mostly showed damage to roads, parking lots or public areas, because the Japanese laws on privacy does not allow the disclose photos of private buildings. All noticed liquefaction evidences have been reported in a shapefile and indicated with triangles in the map of Urayasu (Figure 6-24 .b). It is immediately evident that most the phenomena occurred in Nakamachi and Shinmachi areas, i.e. in the most recent reclaimed areas, while Motomachi was substantially spared from the phenomenon.

Another typical effect of liquefaction is ground settlements. Tokimatsu et al. (2012.a and b) have provided a map that shows the subsidence over the area (Figure 6-25) produced by the main shock. The data have been obtained by comparing the elevation present in two different aerial surveys measured with the LIDAR technique: the first, carried out in December 2006, based on a digital elevation model 2x2m spacing and the second carried out after the earthquake. The map shows widespread settlements of about 0.2-0.4 m and maximum values as high as 0.8 m in the eastern extreme portion of the peninsula.

This project has received funding from the European Union's Horizon 2020 research and innovation programme under grant agreement No. 700748

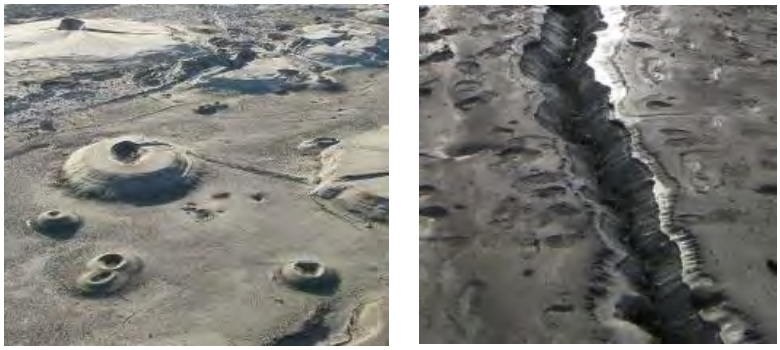

(a)

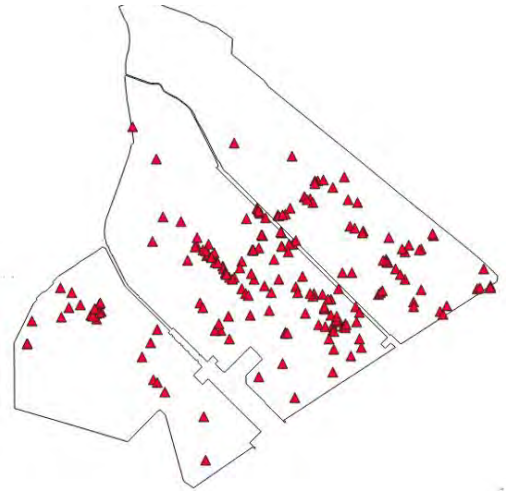

(b)

Figure 6-24 Evidences of liquefaction (sand boils and fracture) in Nakamachi (a) and map reporting the evidences of liquefaction with red triangles (b. Source Geotechnical Extreme Events Reconnaissance).

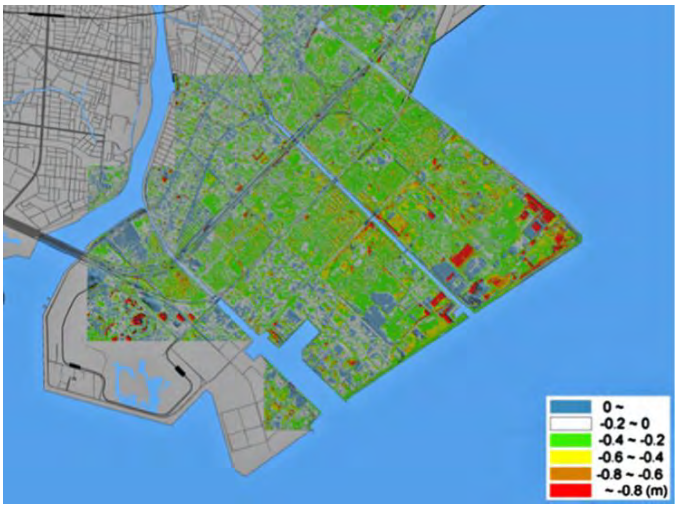

Figure 6-25 Map of Urayasu City showing ground subsidence due to the main shock measured with LIDAR.

For the present analysis, the raster file of this map, not available online, has been obtained with 3x3m resolution from the georeferenced photo in .jpeg format, using the Georeferencer tool in QGIS. After georeferencing, the value of settlements corresponding to each color have been estimated linking colors to the legend in the photo. This operation was performed automatically considering the three color bands (red, green and blue, RGB) converting the file into a single band raster with RGB to PCT tool in QGIS.

To assign to each cell the settlement value, a second conversion was performed using Raster to Vector tool in QGIS, transforming the raster file into a shape file consisting of polygons: each polygon was associated with a color and, for each color, a value of subsidence has been given according to the legenda; thus, a settlement equal to the average value of the range corresponding to its color has been assigned to each 3x3m cell, modifying the attributes table. Finally, the resulting shape file consisting of 1623299 cells, was converted with the Rasterize (Vector to Raster) tool in QGIS, obtaining a new 3x3m spacing raster shown in Figure 6-26.

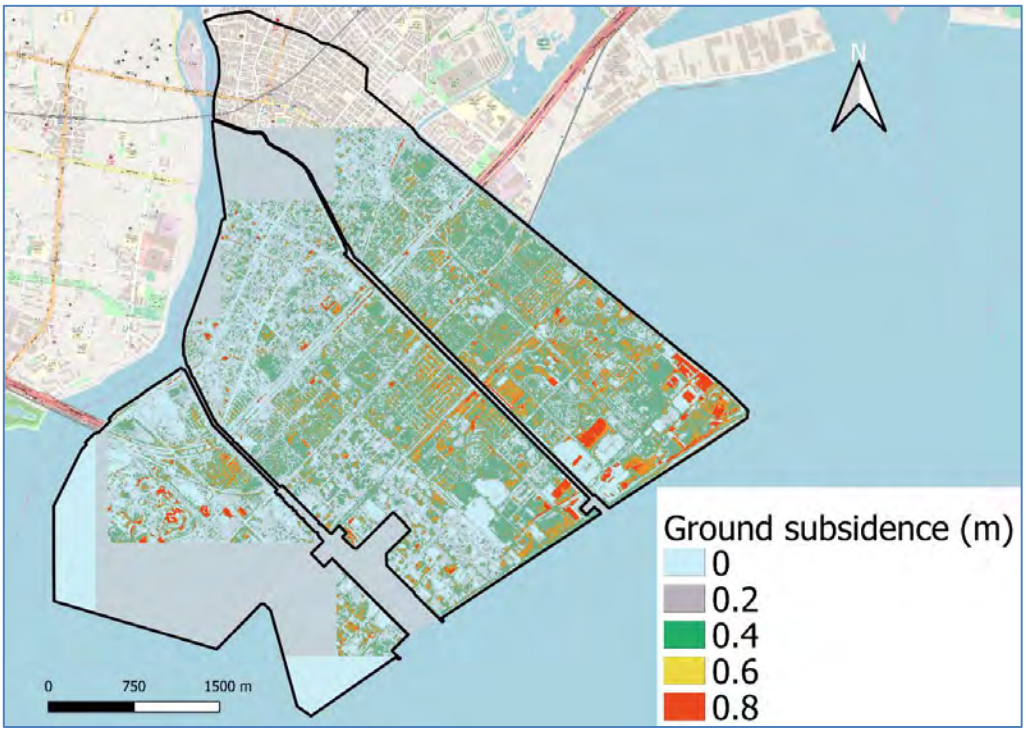

Figure 6-26 The raster created from Figure 6.25.

6.3.3 Liquefaction Susceptibility

The liquefaction susceptibility of Urayasu has been quantified at a macro and microscale level. For the first, the geological map of Kantō Region (Geological Survey of Japan, https://www.gsj.jp) has been accessed focusing on the territory of Urayasu. This map (Figure 6-27) shows the city partly located on a Holocene deposit consisting of mud, partly on reclaimed sand. Youd & Perkins (1978) classify the former as moderately susceptible, the latter as very highly or poorly susceptible depending on the applied compaction (Table 5.2).

This project has received funding from the European Union's Horizon 2020 research and innovation programme under grant agreement No. 700748

Figure 6-27 Kantō Region geological map (Source GSJ): zoom on Urayasu city.

On the microscale level, the analysis was carried out summarizing information contained in 222 boreholes logs, collected by Chiba Prefecture (https://map.pref.chiba.lg.jp): the stratigraphic and the groundwater information enable to define the crust thickness (Figure 6-28a) and the cumulated thickness of liquefiable layer for each borehole (Figure 6-28b). The plots show relatively constant thicknesses of the crust, presumably formed by the hill sand and variable cumulated thickness of the liquefiable layer while proceeding from inland to the shoreline (Chong et al., 2005).

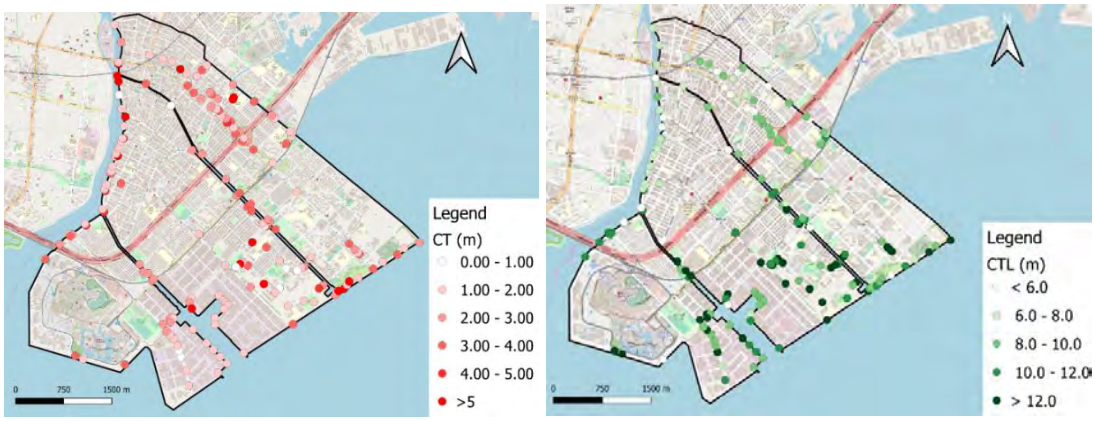

Figure 6-28 Thickness of the crust (a) and of the cumulated liquefiable layers (b) in Urayasu.

6.3.4 Assessment of hazard and vulnerability of sewage pipelines

The uneven distribution on the territory of the subsoil investigation and the liquefaction evidences (Figure 6-29.a), both in terms of land damage and pipelines ruptures, and therefore the lack of overlapped information, does not allow to validate the methods for predicting the hazard and damage based on a direct comparison between prediction performed on the results of SPT tests and observation, as achieved for the

This project has received funding from the European Union's Horizon 2020 research and innovation programme under grant agreement No. 700748

other case studies forming the present deliverable. However, considering that the whole territory is diffusively covered by the survey of liquefaction settlements, in the present study it has been proposed to use this variable as a key factor to relate information.

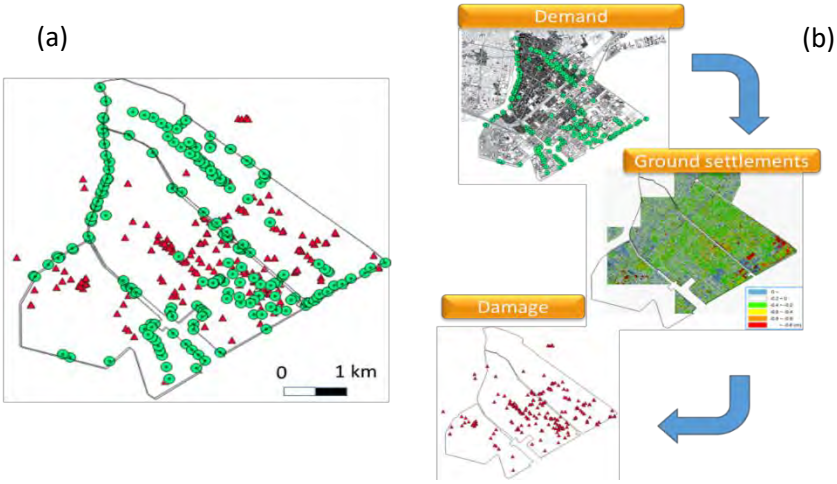

Figure 6-29 Distribution of subsoil investigation and land damage on the territory of Urayasu (a) and outline of the methodology followed for the assessment of hazard and vulnerability (b).

In details, analyses have been attempted to relate hazard indicators and damage separately with the observed settlement then, once these relations are established, an indirect correlation has been established between hazard variables and damage observation (Figure 6-29.b).

6.3.4.1 Hazard indicator vs measured settlement

The analysis of liquefaction triggering is based on the SPT-based procedure of Boulanger & Idriss (2014) on each available subsoil profile of Urayasu city for the (M_w 9.0) March 11th 2011 Tohoku earthquake. Starting from the SPT data, the following indicators have been calculated to predict the effects of earthquake: Liquefaction Potential Index (Iwasaki, 1978, 1981 and 1982) map, Liquefaction severity number (van Ballegooy, 2014), Settlement w (Zhang et al., 2002). The values of these indicators have been computed for each SPT profile then interpolated over the territory using geostatistical tools to obtain maps of liquefaction severity. As shown in Figure 6.30, the value of the indicators is not homogeneously distributed over the territory, even though there is a strong similarity among all plots. In particular, the highest values of indicators are seen for the newest areas of Nakamachi and Shinmachi, while the values for Motomachi are generally lower than the thresholds defined by the authors for liquefaction damage. Exploiting the coexistence in the same position of hazard indicator (Figure 6-30) and settlement computed with LIDAR (Figure 6-26) has led to find the relations plotted in Figure 6-31 between these variables.

Each dot in the figures represent the average values of the considered variable within a specified range. The plots generally show that larger hazard indicators correspond to larger settlements produced by the earthquake.

This project has received funding from the European Union's Horizon 2020 research and innovation programme under grant agreement No. 700748

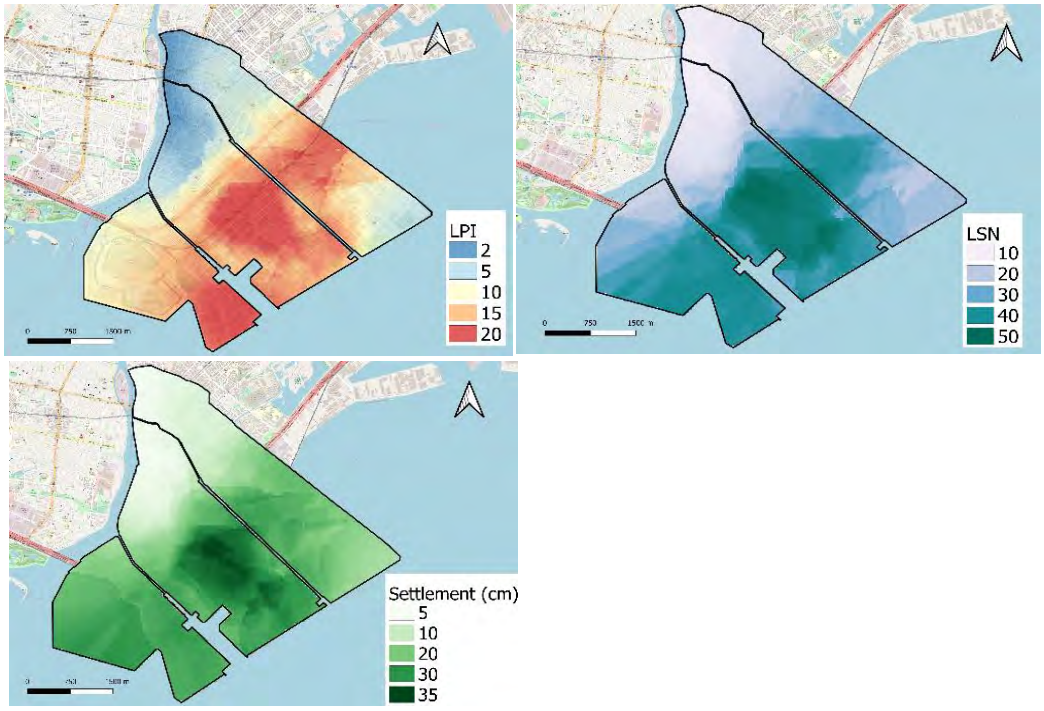

Figure 6-30 Maps of LPI (Iwasaki, 1978), LSN (van Ballegooy, 2014) and w (Zhang et al., 2002) on the territory of Urayasu.

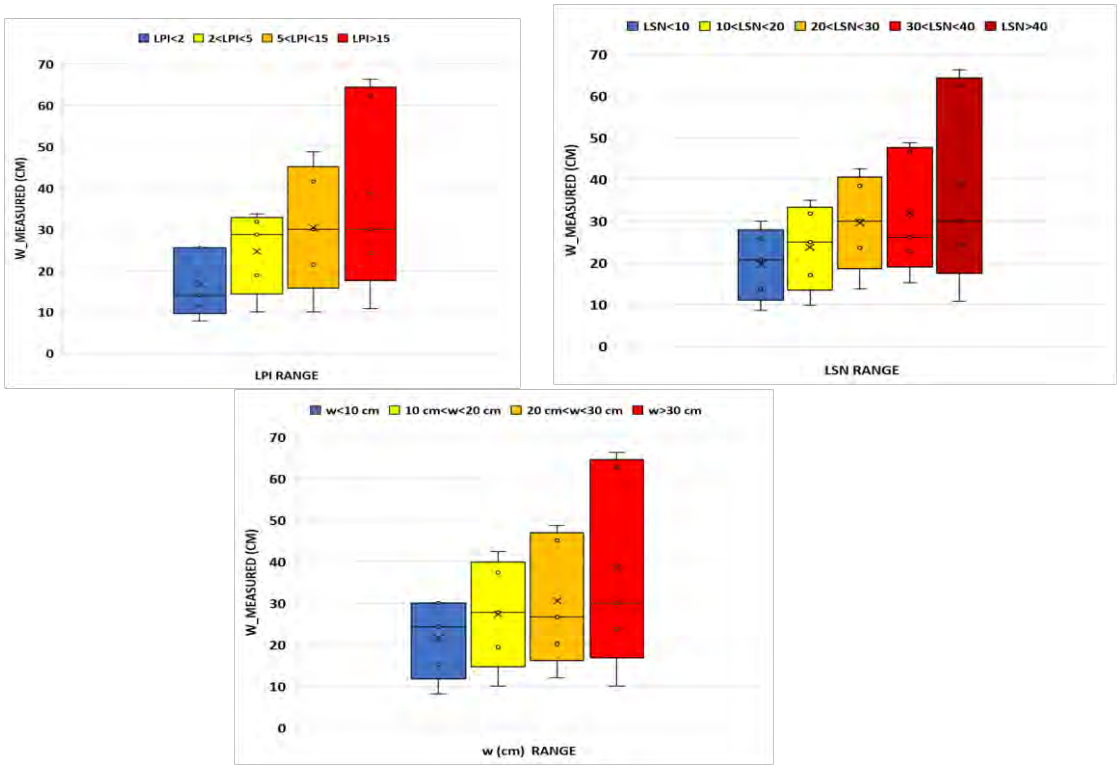

Figure 6-31 Relation between hazard indicators LPI (a), LSN (b) , w(c) and measured settlement.

6.3.4.2 Measured settlement vs land damage

The relation between settlements obtained with the LIDAR technique and land damage has been verified adopting the Receiver Operating Curve method (Kongar et al., 2015; Powers, 2011). To this aim, a mesh with squared cells having side equal to 25m has been ideally overlapped to the map and the measured settlements (Figure 6-26) have been taken in each cell as candidate indicator of damage. The event used for the test is the evidence of liquefaction in the cell, marking it as positive or negative depending on the occurrence or not of sand boils after the earthquake (Figure 6-24).

As shown in Figure 6-32.a, the test gives an Area Under Curve value AUC=0.91 as a proof of a strong correlation between settlement and damage. In particular, the strongest correlation is obtained assigning a threshold of about 10 cm to the measured settlement (Figure 6-32.b. In fact, at this value there is a sudden jump in the two curves of Figure 6-32.

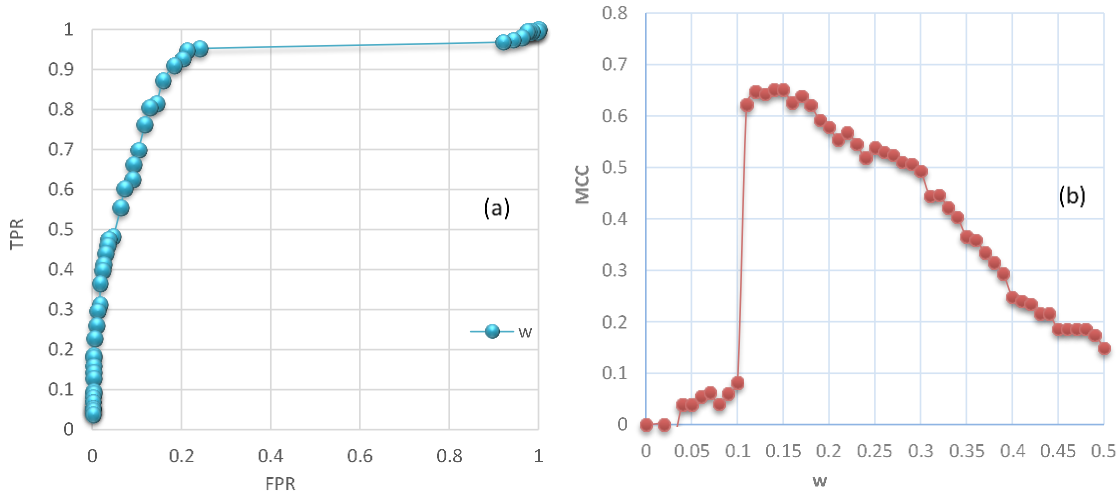

Figure 6-32 Receiver Operating Curve test between ground settlements and damage (a), and definition of the optimal threshold with the Mathews Correlation Coefficient (b).

6.3.4.3 Measured settlement vs damage to sewage pipelines

The vulnerability analysis has been focused on the sewage network, as the position of damage is known with great precision (Figure 6-22). Damages in Shinmachi were almost entirely caused by the lifting of the manholes which is due to a lack of sand compaction during installation (Miyajiama, 2013; Kato et al., 2017): this means that the analysis in this area is meaningless being damage affected by installation and not by subsoil properties. In the area of Motomachi, where limited settlements were recorded, the damage to the pipelines was negligible. Given these considerations, it was then decided to carry out the vulnerability

analysis only considering the Nakamachi area, where a large statically valid sample is available. The map of Figure 6-33.a was then created. An analysis has firstly been attempted subdividing the pipelines into trunks and checking for each length a correlation between damage and settlement derived from LIDAR (Figure 6-33.b).

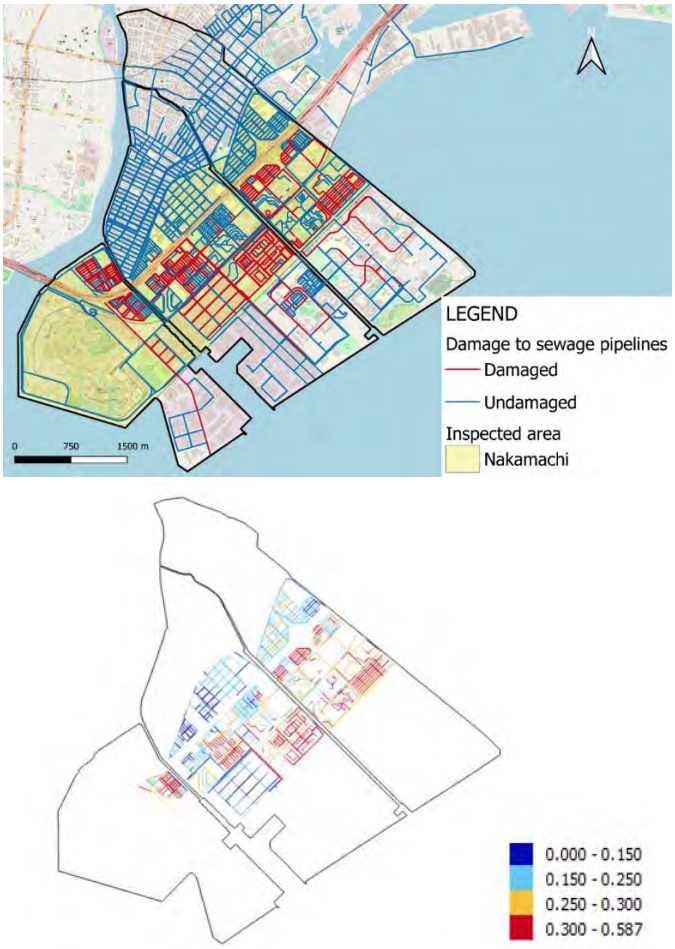

Figure 6-33 Map of damaged sewer pipes (a) and settlements corresponding to the different pipeline trunks (b).

Before checking this correlation, the Bayes theorem was applied to relate the probability of damage on pipelines with the measured settlement as follows:

$$P(damage|w) = \frac{P(w|damage)}{P(w)} P(damage) \quad (2)$$

The obtained curve shows a dual nature of the pipes, because it is possible to identify two distinctive paths in the curve (blue and red). Looking on the map it is seen that the blue curves refers to pipelines built in the western part of Nakamachi. By looking at the available aerial photographs taken at different times, it can be discovered that this area, now occupied by Tokyo Disneyland, was built later (between 1984-1987) and

probably using an installation technique different from the other part built previously in the period 1974-1983.

For the sake of sample homogeneity, the vulnerability analysis was then performed only to the eastern pat of the sewage network. Firstly, the Receiver Operating Curve (Kongar et al., 1986) was applied to attempt a relation between settlements and damage (Figure 6-35.a). The test gives a rather satisfactory result with AUC=0.78 as a proof of the correlation existing between settlements and damage to pipelines. The curve reporting the probability of damage versus settlement shows again the existence of a threshold on the settlements of about 10 cm, below which no damage is recorded on pipelines. With the increase of ground settlements, a progressively large number of pipes reach failure.

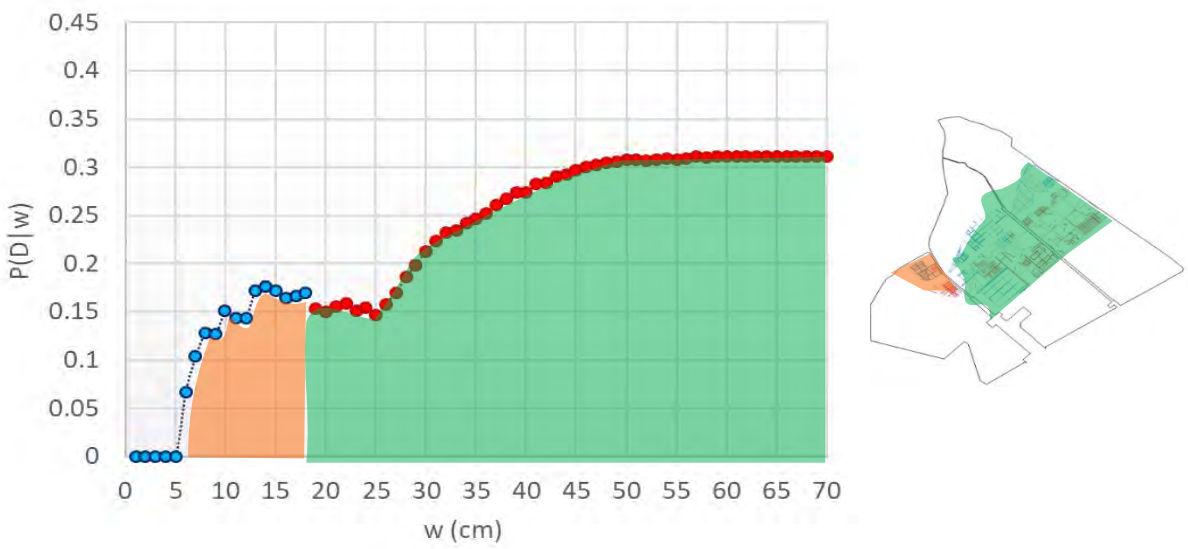

Figure 6-34 Probability of damage curve associated to measured settlement.

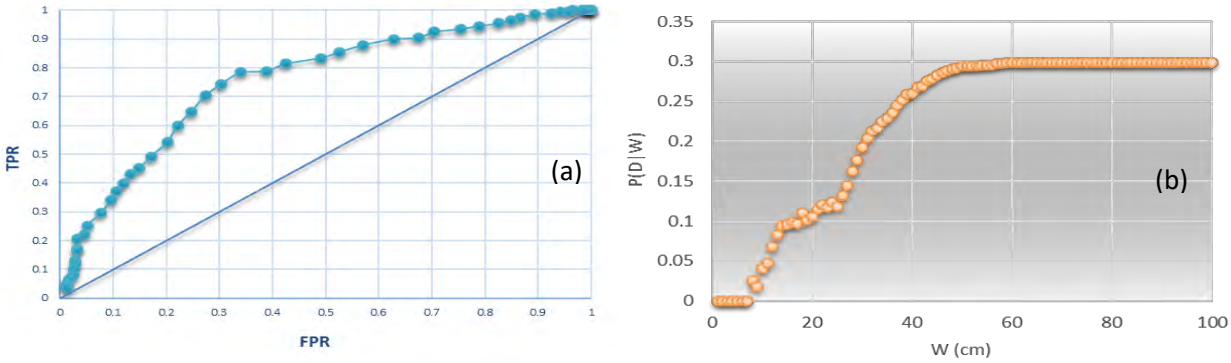

Figure 6-35 Receiver Operating Curve (a) and probability curve (b) relating damage of sewage pipelines measured ground settlement.

6.3.4.4 Fragility model of sewage pipelines

The information contained inFigure 6-35.b, showing the probability of damage on pipelines versus ground settlement, has now been combined with the relation between ground settlements and hazard indicators (Figure 6-31) to provide an analytical tool that predicts the possibility of damage on pipelines based on the seismic and geotechnical characteristics of the site. The result of this calculation is represented by the fragility curves reported in Figure 6-36 that express the probability of damage as functions of the hazard indicators, namely Liquefaction Potential Index (Iwasaki, 1978) map, Liquefaction severity number (van Ballegooy, 2014), Settlement w (Zhang et al., 2002).

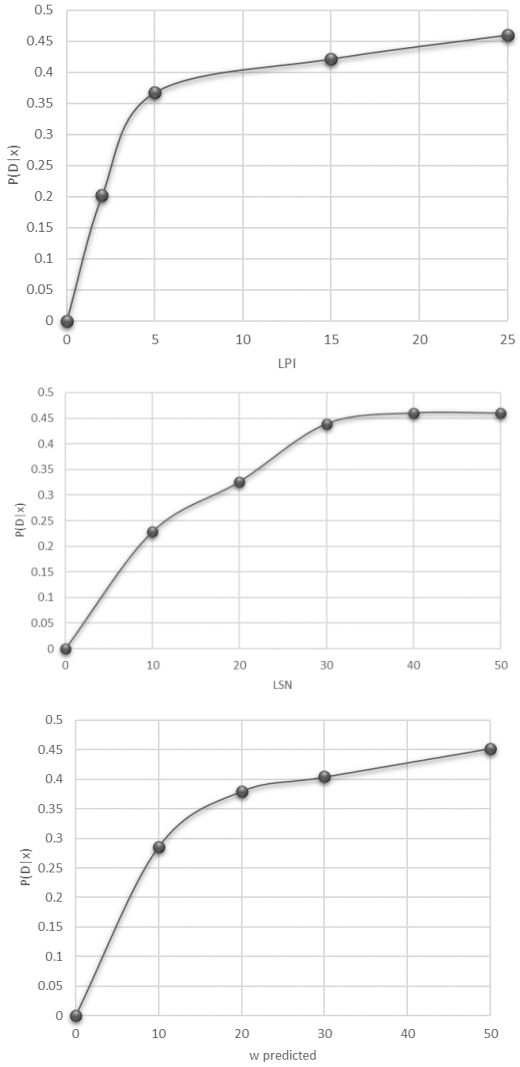

Figure 6-36 Fragility Curve based on LPI (Iwasaki et al., 1978), LSN (van Ballegooy et al., 2014), post-consolidation settlement W (Zhang et al., 2002).

6.4 Bibliography

Bhattacharya S., Hyodo M., Goda K., Tazoh T., Taylor C.A., 2011: "Liquefaction of Soil in The Tokyo Bay Area from the 2011 Tohoku (Japan) Earthquake", Soil Dynamics and Earthquake Engineering 31, 1618-1628.

Boulanger R. W., Idriss I. M., 2014: "CPT and SPT Based Liquefaction Triggering Procedures", Center for Geotechnical Modeling.

Chong O H., Koibuchi Y., Sato S., Isobe M., 2005: "Study on a Change of Bottom Topography and Sediment Characteristics Around Reclaimed Land in Sanbanze", Sediment and Ecohydraulics: INTERCOH, 83-90.

Cox B. R., Boulanger R. W., Tokimatsu K., Clinton M. W., Ashford S., Donahue J., Ishihara K., Kayen K., Katsumata K., Kishida T., Kokusho T., Mason H. B., Moss R., Stewart J. P., Tohyama K, Zekkosl D., 2013: "Liquefaction at Strong Motion Stations and in Urayasu City during the 2011 Tohoku-Oki Earthquake", Earthquake Spectra.

Goto H., Hata Y., Kuwata Y., Yamamoto H., Morikawa H., Kataoka S., 2013: "Earthquake Source and Ground Motion Characteristics in Eastern Japan during the 2011 Off the Pacific Coast of Tohoku Earthquake", Journal of JSCE, Vol. 1, 329-342.

Hayes et al., 2016: "Tectonic Summaries Of Magnitude 7 And Greater Earthquakes From 2000 To 2015", USGS Open-File Report 2016-1192.

Idriss I.M. & Boulanger R.W., 2010: "SPT-Based Liquefaction Triggering Procedures", Center for Geotechnical Modeling, 259.

Idriss I.M. & Boulanger R.W., 2014: "CPT and SPT based liquefaction triggering procedures", Department of Civil and Environmental engineering, University of California at Davis.

Ishikawa K., Yasuda S., 2017: "Study On The Reasonable Liquefaction Prediction In Case Of The Huge Interplate Earthquake Based On The Representative Soil Profile Models", 16th World Conference on Earthquake, 16WCEE 2017, Santiago Chile, January 9th to 13th 2017.

Iwasaki T., Tatsuoka F., Tokida K., Yasuda S., 1978: "A Practical Method for Assessing Soil Liquefaction Potential Based on Case Studies at Various Sites in Japan", [conference] // 2nd International conference on Microzonation. - 1978. - pp. 885-896.

Iwasaki T., Tokida K., Tatsuoka F., 1981: "Soil Liquefaction Potential Evaluation with Use of the Simplified Procedure", International Conferences on Recent Advances in Geotechnical Earthquake Engineering and Soil Dynamics. 12.

Iwasaki, T., Arakawa, T., and Tokida, K. (1982): "Simplified Procedures for Assessing Soil Liquefaction During Earthquakes." Pro-ceedings of the Conference on Soil Dynamics and Earthquake Engineering, Southampton, UK, 925−939.

JGS, 2013: "JIS A 1219:2013, Method for Standard Penetration Test, Japanese Industrial Standard", Japanese Geotechnical Society.

Kamiyama M., 2011: "Strong motion records by Small-Titan during 2011 off the Pacific coast of Tohoku earthquake", http://www.st.hirosakiu.ac.jp/338kataoka/TohokuEQ/KamiyamaSmallTitan01.pdf

Kato S., Kuwata Y., 2017: "Spatial Relationship of Buried-Pipeline Damage And Sand-Boiling Area Due To Liquefaction In Kashima Region", Journal of Japan Association for Earthquake Engineering, Vol.17, No 3.

Kongar I., Rossetto T., Giovinazzi S., 2016: "Evaluating Simplified Methods for Liquefaction Assessment for Loss Estimation", Natural Hazards Earth System Science.

Kunugi T., Aoi S., Suzuki W., Nakamura H., Morikawa N. and Fujiwara H., 2012: "Strong Motions of the 2011 Tohoku-oki earthquake, Research Report on the 2011 Great East Japan Earthquake Disaster" National Disaster Research Report, National Research Institute for Earth Science and Disaster Prevention,No.48, pp.63–72 (in Japanese with English ab-stract and captions).

Miyajima M., 2013: "Performance of Drinking Water Pipelines in Liquefaction Areas in the 2011 Great East Japan Earthquake", Int. J. Lsld. Env. (2013), 1(1), 61-62.

NPAJ, 2019: "Police Countermeasures and Damage Situation Associated With 2011 Tohoku District Off the Pacific Ocean Earthquake", from "deaths" template, National Police Agency of Japan.

Powers, D. M. W., 2011: "Evaluation: from precision, recall and F-measure to ROC, informedness, markedness and correlation", J. of Mach. Lear. Tech, 2(1), 37-63.

Skempton A. W., 1986: "Standard Penetration Test Procedures and The Effects in Sands of Overburden Pressure, Relative Density, Particle Size, Ageing and Overconsolidation"

Suzuki W., Aoi S., Sekiguchi H., Kunugi T., 2011: "Rupture process of the 2011 Tohoku-Oki mega-thrust earthquake (M9.0) inverted from strong-motion data", Geophys. Res. Lett., Vol.38, L00G16.

Technical Committee for Earthquake and Tsunami Measures to Drainage System, 2012: "Summary on the damage to drainage facilities and the earthquake and tsunami measures in East Japan earthquake and disaster". (in Japanese)

Technical Committee on Foundations, 1992: "Canadian Foundations Engineering Manual (1992), Third Edition", Canadian Geotechnical Society.

Technical Committee on Measures Against Liquefaction in Urayasu City, 2012: "Report on measures Against Liquefaction in Urayasu City". (in Japanese)

Tokimatsu K., Katsumata K., 2012.a, "Liquefaction-Induced Damade To Buildings in Urayasu City During The 2011 Tohoku Pacific Eathquake", Proceedings of the International Symposium on Engineering Lessons Learned from the 2011 Great East Japan Earthquake, March 1-4, 2012, Tokyo, Japan.

Tokimatsu K., Tamura S., Suzuki H., Katsumata K., 2012.b, "Building Damage Associated with Geotechnical Problems in the 2011 Tohoku Pacific Earthquake", Soils and Foundations 52, 956-974.

Towhata I., Maruyama S., Kasuda K., Koseki J., Wakamatzu K., Kiku H., Kiyota T.,Yasuda S., Taguchi Y., Aoyama S., Hayashida T., 2014: "Liquefaction In The Kanto Region During The 2011 Off The Pacific Coast Of Tohoku Earthquake", Soils and Foundations 54, 859-873.

van Ballegooy S., Malan P., Lacrosse V., Jacka M.E., Cubrinovski M., Bray J.D., O'Rourke T.D., Crawford S.A., Cowan H., 2014: "Assessment of Liquefaction-Induced Land Damage for Residential Christchurch", Earthquake Spectra, Volume 30, No. 1, pages 31–55, February 2014.

Yasuda S., Harada K., Ishikawa K., Kanemaru Y., 2012: "Characteristics of Liquefaction in Tokyo Bay Area by the 2011 Great East Japan Earthquake", Soils and Foundations 52, 793-810.

Yasuda S., Towhata I., Ishii I., Sato S., Uchimura T., 2013: "Liquefaction-Induced Damage to Structures During The 2011 Great East Japan Earthquake", Journal of JSCE, Vol.1, 181-193.

Youd, T. L., and Perkins, D. M. 1978. "Mapping Liquefaction-induced Ground Failure Potential". J. Geotech. Eng. Div., ASC E, 104, 433–446pp.

Zhang, G., Robertson, P. K., & Brachman, R. W. 2002. Estimating liquefaction induced ground settlements from CPT for level ground. Canadian Geotechnical Journal, 39(5), 1168-1180. doi:10.1139/T02-047

6.5 Webliography

Chiba Information Map:

https://map.pref.chiba.lg.jp/pref-chiba/Agreement?IsPost=False&MapId=6300&RequestPage=%2fpref-chiba%2fPositionSelect%3fmid%3d6300

Geotechnical Extreme Events Reconnaissance:

http://www.geerassociation.org/administrator/components/com_geer_reports/geerfiles/Cover_Tohoku_2011.html

Geofabrick:

https://download.geofabrik.de/osm-data-in-gis-formats-free.pdf

Geological Survey of Japan:

https://www.gsj.jp/Map/EN/geology2-4.html#Tokyo

Geospatial Information Authority of Japan (GSI):

http://www.gsi.go.jp/kankyochiri/gm_japan_e.html

Japanese Seismic Hazard Information Station (J-SHIS):

http://www.j-shis.bosai.go.jp/map/JSHIS2/text/kml_list_en.html

This project has received funding from the European Union's Horizon 2020 research and innovation programme under grant agreement No. 700748

Land Information New Zealand:

https://data.linz.govt.nz/data/tag/new-zealand/global/oceania/new-zealand/canterbury/christchurch-city/?page=2&s=n

National Research Institute for Earth Science and Disaster Resilience (NIED):

http://www.kyoshin.bosai.go.jp/

Sealevel Station Catalog (SSC):

http://www.ioc-sealevelmonitoring.org/ssc/stationdetails.php?id=SSC-mera

Urayasu City website:

http://www.city.urayasu.lg.jp/shisei/johokoukai/shingikai/shichoukoushotsu/1002796/1002934.html

USGS:

https://earthquake.usgs.gov/earthquakes/eventpage/official20110311054624120_30/executive

This project has received funding from the European Union's Horizon 2020 research and innovation programme under grant agreement No. 700748

7 TRANSPORTATION NETWORK – EMILIA ROMAGNA (IT)

7.1 Risk assessment on transportation systems: state of art

The modern societies and customs are based on a quick and multi-level communication: ideas, images, words, services, goods, people move and are shared more rapidly than ever. To both innovative and traditional communication networks it is requested to be reliable, efficient and safe, even if extreme events and disastrous scenarios occur. As far as the conventional transportation networks (as rail or road networks) are concerned, the possible losses due to catastrophic scenarios can be relating to direct and indirect economic aspects. In this Chapter a brief literature review of the main models for the evaluation of the transportation costs increase, caused by disastrous events is presented, a novel methodology is proposed and preliminary results of its application on a case study are reported.

The destructive potential of liquefaction induced by earthquakes is worldwide shown by several events as Christchurch 2010, 2011 and 2016; Tohoku Oki, 2011; Emilia Romagna, 2012; Kumamoto, 2016. Damages affect not only the building asset, but also the facilities connected directly or indirectly to the productive systems, (among which transportation networks are of prominent interest). From early nineties, different methodologies have been developed to estimate the potential losses induced by earthquakes implementing engineering knowledge in geographic information systems (GIS).

Among the most recent National and International projects and researches, from the specific viewpoint of Transportation Networks and Infrastructures, deserving of attention are:

- Project AllTraIn (2013-2015): All-Hazard Guide for Transport Infrastructure was supported by the European Commission, with the aim to provide for both man-made hazards (intentional and exceptional) and natural hazards, qualitative information about the correlation between specific hazard and specific asset (bridges, cuts, embankments and tunnels) and vice versa. The element-analysis is performed, and only "Local" consequences are considered (directly and locally on the asset) (AllTraIn, 2015).
- Project STRIT - Tools and Technologies for Risk Management of Transport Infrastructure (2012-2015) was a research project developed by public and private Italian research centres with the aim to introduce innovative bridge monitoring, Decision Support System (DSS) for maintenance strategies based on Life-Cycle Analysis and new technologies improving seismic resistance of structures. Also in this case the network level analysis and mitigation strategies are disregarded (STRIT project).
- EU project SecMan - Security Risk Management Processes for Road Infrastructures (2011-2013): supported by the European Commission with the aim to provide a practical process for the identification of critical infrastructures, only in terms of man-made (terrorism and other forms of intentionally caused incidents) hazard vulnerability, on European highways (especially bridges and tunnels). It presents a 4-step procedure for the assessment of infrastructures in respect to their criticality for the network, attractiveness for an attack and vulnerability of the object itself. The

assessment procedures act either on network (only in terms of criticality assessment) or element level suggesting efficient measures to mitigate possible attacks. Transportation analysis on post-attack scenarios are disregarded (SecMan Project, 2013).

- Chang' s research (2010) performed with the aimed to develop a systematic approach for risk modeling and disaster management of transportation systems in the context of seismic engineering. The proposed methodologies could be useful for both immediate post-disaster phase (as evaluating the performance of optimal routes for emergency ingress and egress from strategic points) and middle/long term analysis (road network traffic and capacity analysis considering different traffic demand between pre-post event scenarios).
- SYNER-G (2009–2012): is a collaborative integrated research project funded by the European Commission Directorate-General for Research, with the aim to revise and when necessary propose fragility models (useful in the European context) and to develop a systemic and holistic approach to loss estimation at the network level (i.e. socio-economic impacts), considering the dependence on the vulnerability and interactions of all the components system (buildings, lifelines, transportation infrastructures and critical facilities). Both deterministic and probabilistic analyses are available for the seismic risk assessment and the transportation network analysis is performed by means of the user-equilibrium model (SYNER-G, 2009).
- EC-funded project SeRoN - Security of Road Transport Networks project: was funded by the EC Seventh Framework Programme (FP7/2007-2013) with the aim to investigate the impacts of possible terrorist attacks on the transport network, focusing on the resulting regional and supra-regional impacts on transport links and their economic impacts. It provides an holistic procedure to identify critical road infrastructure objects and evaluate cost-effective protection measures: the network strategic elements are ranked according to their network importance which is defined as the benefit which arises from the prevented non-availability of a certain infrastructure element. The proposed methodology is based on a traditional transportation analysis with a fixed travel demand (SeRoN, 2012).
- REDARS™ (Risks from Earthquake Damage to the Roadway System, 2003-2006) which is a methodology, implemented in a software package, for the seismic risk analysis of highway systems, which offers a pre-earthquake or post-earthquake decision-guidance. The transportation network analysis is performed by means of the user-equilibrium assignment model with Variable-Traffic Demand for post-earthquake time obtaining travel time delays, traffic flow disruptions, and reductions in trip demands (S. D. Werner et al. 2006).
- HAZUS® (2004), a tool developed by the Federal Emergency Management Agency (FEMA) and the National Institute of Building Sciences (NIBS) to estimate losses at federal, state, regional and local scale and to plan earthquake risk mitigation, emergency preparedness, response and recovery. The transportation analysis is not provided and the evaluation of direct and indirect losses due to transportation network (in terms of bridges, tunnels and roadways) is addressed by means of a "Damage Ratio" related to replacement costs and other economic sectors losses (HAZUS, 2004).

This project has received funding from the European Union's Horizon 2020 research and innovation programme under grant agreement No. 700748

7.2 Levels for Transportation network Analysis

If a risk-based approach has to be pursued in order to evaluate the socio-economic impact pertaining the post-earthquake scenario, serviceability of critical infrastructures, among which transportation networks are relevant, has to be taken into account. As far as the analysis period is concerned, two main approaches can be usually identified:

- short-term effects, insofar accessibility to small and more isolated communities has to be guaranteed for rescue crews and emergency services in the immediate post-earthquake scenario;
- long term effects, since the serviceability of transportation network can be heavily damaged by an earthquake and therefore repair works aimed at restoring initial conditions have to be undertaken.

A recent review of methodological approaches (SYNER-G, 2009) so far developed for critical infrastructures has identified the followings:

- Level 0 or *Vulnerability Analysis* dealing with the damage level experimented by each road component (bridge, tunnel, embankment, etc) according to a specific seismic scenario;
- Level I or *Connectivity Analysis* where the accessibility to a specific area is evaluated in the post-earthquake scenario, following the loss of service of some connections;
- Level IIa or *Capacity Analysis* dealing with decay of performance level of the whole network itself that in turn will cause a degraded fruition of the infrastructure and a dramatic increase of the user costs.
- Level IIb or *Serviceability Analysis* where all the interdependencies and the effects of a seismic scenario are evaluated to the extent that they can affect all the aspects of the inhabitants' and stakeholders' life and related economic impacts, following an earthquake occurring in a specific area.

Basing on these premises, it is worth to be noticed that transportation managers have to cope with the issue of an optimal planning of seismic mitigation countermeasures with limited budget available.

In this connection, although the Serviceability Analysis seems the most exhaustive in evaluating all the socio-economic aspects impacted by an earthquake scenario in the short and long-term, it requires an in-depth knowledge of all the social and economic framework of an analysis area that is not always available at local level. Therefore, a Capacity Analysis seems the most feasible approach to evaluate, even to a lesser extent, socio-economic impacts related to the mobility that, in turn, represents a significant aspect in overall evaluation of quality of life in the post-earthquake scenario.

7.3 Vulnerability model for transportation systems

The roadway network is composed of different elements and infrastructures which, according to their features (geometry, used materials, age, …), could undergo various levels of damage due to liquefaction events. Within this project, the attention has been focused on the embankments.

For the definition of the damage state limits for highway embankments, the SYNER-G classification (2009) summarised in the Table 7-1 has been adopted:

Table 7-1: Definition of damage state for highway embankments (SYNER-G, 2009).

Damage State	PVG Displacement [m] min	max	mean	Description	Serviceability
minor	0.02	0.08	0.05	Surface slide of embankment at the top of slope; minor cracks on road surface; minor track displacement.	Useful road with speed reduction.
moderate	0.08	0.22	0.15	Deep slide or slump of embankment; medium cracks on road surface and/or settlement; medium track displacement.	Partially open during repair works.
extensive	0.22	0.58	0.40	Extensive slump and slide of embankment; extensive cracks on road surface and/or settlement; extensive tracks displacement.	Closed.

As shown in the table, each damage state corresponds to a road section serviceability limit state, which is used as input data for the road network definition in the post-liquefaction scenario analysis.

7.4 The Exposure concept in the transportation risk analysis

Considering the sequence of sub-systems involved in seismic liquefaction, the risk assessment methodology can be expressed quantifying the probability of occurrence and associated uncertainty on earthquake intensity, ground motion, liquefaction manifestation, structural response, physical damage, and socio-economic losses. The Risk associated to a possible seismic/liquefaction scenario referring to a certain transportation network asset, can be defined as a combination of the Hazard, the Vulnerability and the Exposure.

The concepts related to Liquefaction Hazard and Vulnerability are extensively analyzed in the previous paragraphs and, below, the concept of Exposure relating to transport systems is defined.

The exposure can be defined as the quantification of the socio-economic damages that a catastrophic event can produce to a community. For critical infrastructures, such as transportation networks or lifelines, the evaluation of the exposure can be very difficult because this parameter is intimately related to the estimation of the *Social Costs*.

The definition of the *Social Costs* implies all the social and economic "*Losses*" that a community deals with after a catastrophic event and they can be mainly grouped in:

- direct losses: related to repair/replacement cost of the damaged component of the infrastructure and to casualties and injuries due to a catastrophic event;

- indirect losses: derived from the consequences due to the possible temporary reduction/interruption of service (related also to the resilience/redundancy of the network) that, in case of lifelines and transportation systems, could bring severe repercussion on agriculture, industry and services sectors.

In this study, the indirect losses have been evaluated by means of the Total Delay Cost, TDC, as a consequence of loss of serviceability of the transportation networks, within the *Capacity Analysis*.

7.5 Indirect Looses of Transportation Systems

The consequences of loss of serviceability of the transportation networks could depend on the features of the transportation system such as the network configuration, the redundancies, the traffic demand and capacity, the presence, the quantity and the location of sensitive components (bridges, tunnels, embankments,…).The impacts on the traffic flows and the trips could affect all the economic sectors which daily use the transportation networks for their activities.

For the estimation of the impacts of loss of serviceability of the transportation networks, the evaluation of the Total Delay Cost, TDC, has been adopted. This approach implies that the travel time is one of the most significant item among the different terms contributing to the Generalized Transport Cost, GTC, which can be defined as a measure of the overall cost that is sustained by each transport user in a specific analysis area, computed on a daily basis and for a specific trip purpose, s.

The TDC can be expressed by means of the following equation:

$$\mathrm{TDC} = \mathrm{GTC}_{\mathrm{post}} - \mathrm{GTC}_{\mathrm{pre}} \qquad \text{Equation 7.1}$$

where:

GTC_{post} is the Generalized Transport Cost in the post - catastrophic scenario;
GTC_{pre} is the Generalized Transport Cost in the pre - catastrophic scenario.

The Equation 7.1 provides the costs evaluated on a daily basis, after the catastrophic event and, in order to assess the Overall Social Cost, OSC, related to the mobility in a specific analysis area, the GTC_{post} has to be multiplied by the overall amount of days needed to restore the pre-earthquake event conditions of transportation network.

This project has received funding from the European Union's Horizon 2020 research and innovation programme under grant agreement No. 700748

The TDC analysis requires, at least, the knowledge of the entire Origin-Destination (O/D) trip matrix of the analysis area and, more generally, the development and implementation of a transportation demand forecasting model which is presented below.

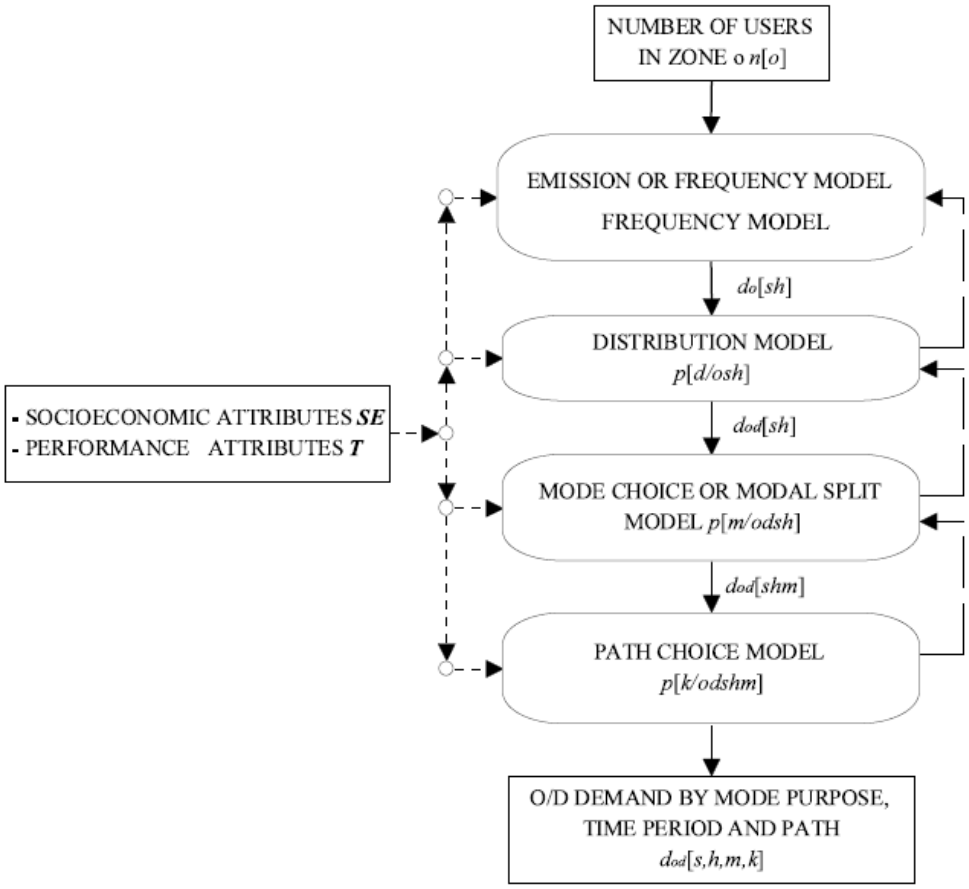

Figure 7-1: Flowchart of a Travel Demand Forecasting Model from (Cascetta, 2009).

7.6 Travel Demand Forecasting Model

The Travel Demand Forecasting Model, TDFM, (Cascetta, 2009) is one of the most known and used prediction model in Transportation Engineering. The TDFM, historically named four-step travel demand model, is a mathematical four-stage model able to reproduce on an hourly basis, all the trips occurring in a specific analysis area, according to its purpose, socio-economic role of the user, time period, origin, destination, transport mode and path. In particular the TDFM is the combination of four separated sub-models: the traffic emission model, the traffic distribution model, the traffic mode-choice model and the path-choice model. In the Figure 7-1 The conceptual representation of a Travel Demand Forecasting Model is reported.

The TDFM can be formally expressed by the following equation:

This project has received funding from the European Union's Horizon 2020 research and innovation programme under grant agreement No. 700748

$$d^{i}_{od}(s,h,m,k) = d^{i}_{o}(sh) \cdot p^{i}(d/osh) \cdot p^{i}(m/oshd) \cdot p^{i}(k/oshdm) \quad \text{Equation 7.2}$$

where:

diod (s, h, m, k) is the average number of trips carried out by class user i, starting from origin traffic zone o, and terminating in the destination traffic zone d, for a specific purpose s, within the time period h, using the transport mode m, and choosing the trip path k;

dio (sh) is the average number of class user i who perform a trip from origin zone o, for purpose s, within the time period h;

pi (d/osh) is the fraction of the aforementioned users who terminate the trip in the destination zone d;

pi (m/oshd) is the fraction of the aforementioned users who choose the transport mode m (known as the);

pi (k/oshdm) is the fraction of the aforementioned users who choose the trip path k.

7.7 Mitigation and Retrofitting Approaches

As far as seismic risk assessment and mitigation interventions decision-making on transportation systems are concerned, the network-level analysis is requested which increases the modelling and assessment difficulty. So far previously studies about mitigation and retrofitting of road networks examined mainly earthquake hazard and, in detail, because bridges are usually considered the most vulnerable components to seismic hazards in a road network mitigating, the focus of the researches were primarily on bridges retrofitting.

For example, the seismic risk reduction decision-guidance process proposed within the REDARS 2 Project, would select retrofit sequence that provides the optimum seismic performance of the system, within tentatively hypothesized mitigation strategies (alternative priorities could be evaluated in terms of the means and standard deviations of the resulting total costs). Furthermore, according to the Chang's method (L. Chang, 2010), it is possible to improve the retrofitting analysis modifying the post- earthquake origin-destination (O/D) matrix respect to the pre-earthquake (static) O/D matrix as an input for traffic flow analysis, in order to take into account the change of traffic pattern after the seismic event and the damage of transportation infrastructures. In particular the trip generation and distribution stages of a traffic analysis are modified to consider the earthquake-induced damage.

7.8 Case Study TERRE DEL RENO

In May 2012, the Emilian Po Valley was struck by an intense seismic activity with two major earthquake sequences occurred respectively on May 20th (Mw = 6.1 - hypocentral depth of 6.3 km) and on May 29th (Mw = 5.8 - hypocentral depth of 10.2 km). Widespread liquefaction was observed in areas located near old abandoned watercourses, especially in the municipalities of Sant'Agostino and Mirabello, located along the old riverbed of the Reno River.

This project has received funding from the European Union's Horizon 2020 research and innovation programme under grant agreement No. 700748

The village of San Carlo, Municipality of Sant'Agostino, is the most emblematic area for the greatest concentration of liquefaction evidence (Fioravante et al., 2013). The subsoil of San Carlo is the product of a relatively recent geologic history, characterized by an intensive depositional sequence of the Reno river and a very shallow water table. Its urban area and road network are mainly built near the paleo-channel and paleo-levees of the Reno River and consequently the subsoil can be categorised in three main units. Starting from the top, fluvial channel deposits few metres deep are located above a stratum of fine-grained materials (swamps) and Pleistocene alluvial plain. Finally, manmade silty sand layers built to protect the area against flooding (paleo-levees) are positioned along the old riverbed.

Karamitros et al. (2013) formula has then been applied to estimate the settlements of the road embankment over the territory of Terre del Reno (for more information see Chapter 1) and the results in terms of the thickness of the liquefiable layer, the thickness of the overlying crust and the embankment height are reported in the Figure 7-2, Figure 7-3 and Figure 7-4, respectively. Finally, the map of settlements computed for the road embankment and related to the specific seismic event of 20 May 2012, is reported in the Figure 7-5.

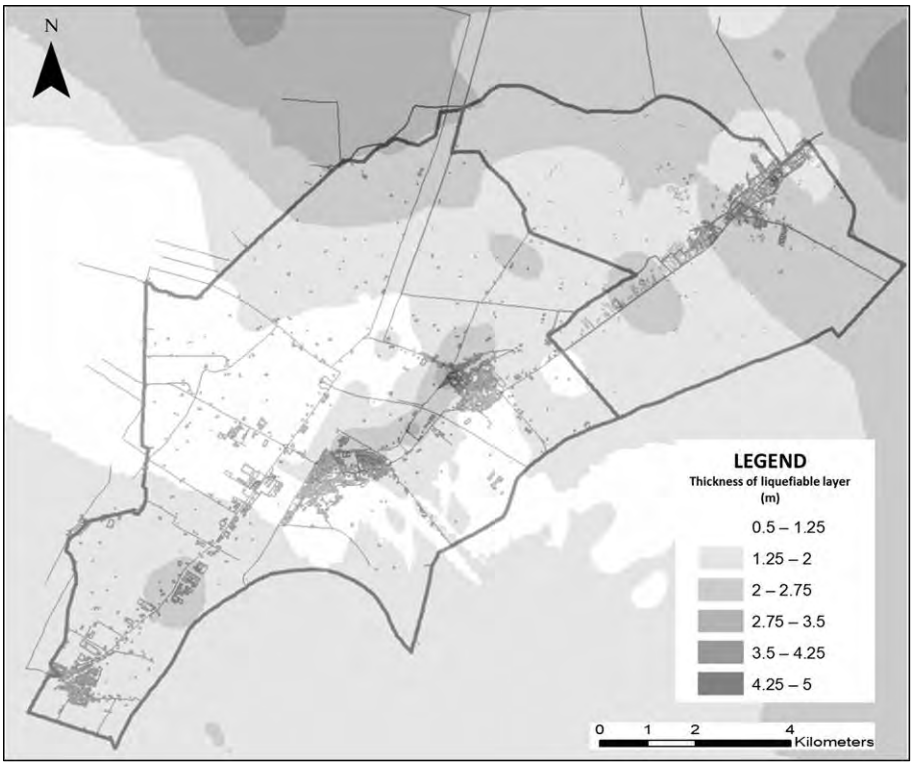

Figure 7-2: Map of the thickness of the liquefiable layer.

This project has received funding from the European Union's Horizon 2020 research and innovation programme under grant agreement No. 700748

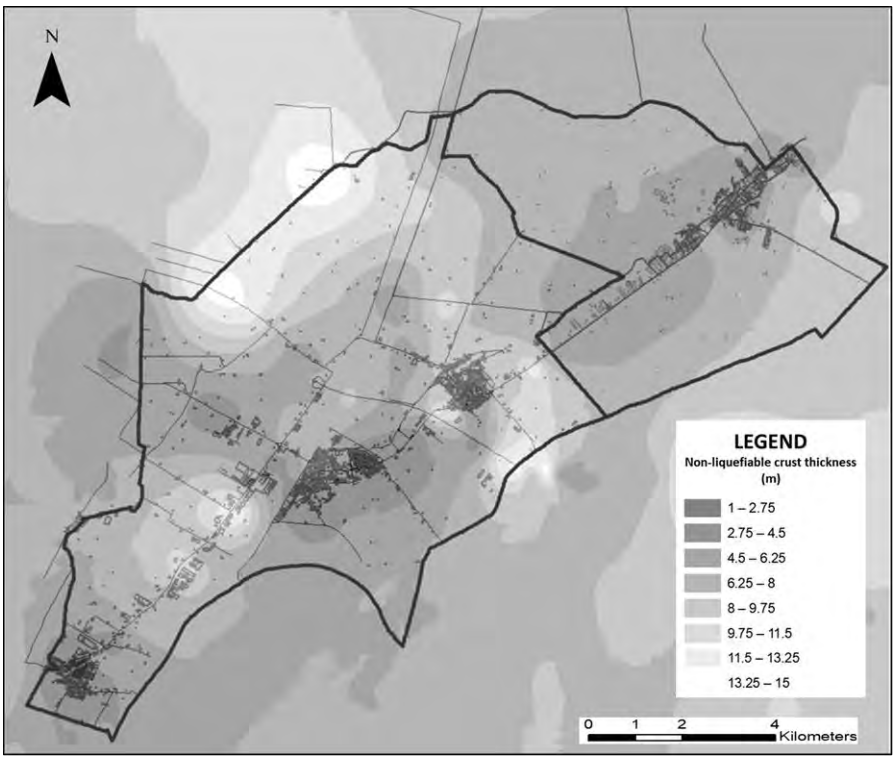

Figure 7-3: Map of the thickness of the overlying crust.

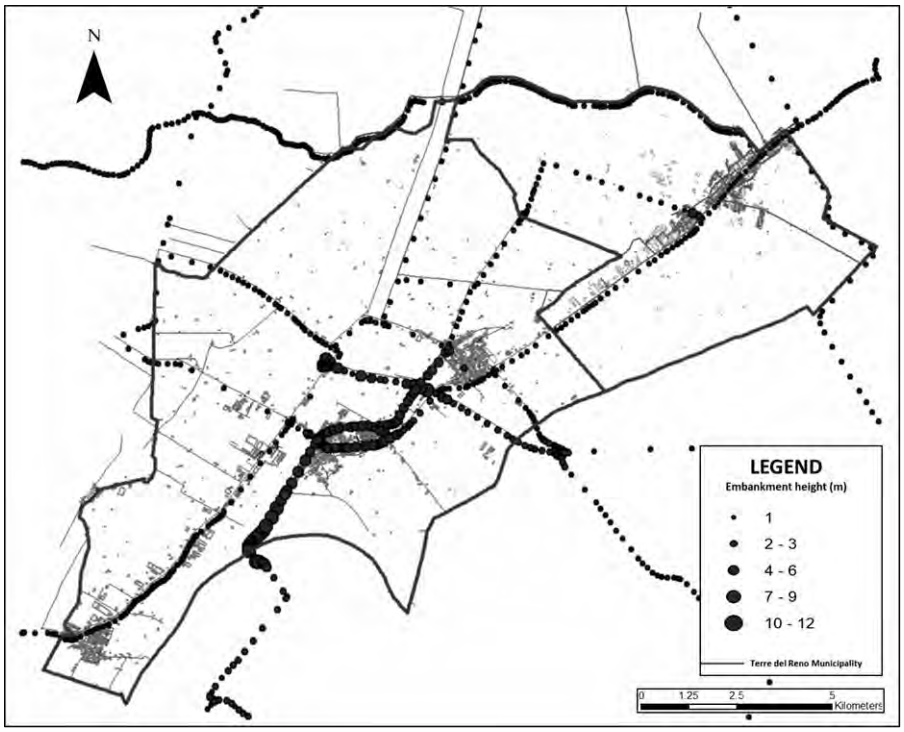

Figure 7-4: Map of the embankment height.

This project has received funding from the European Union's Horizon 2020 research and innovation programme under grant agreement No. 700748

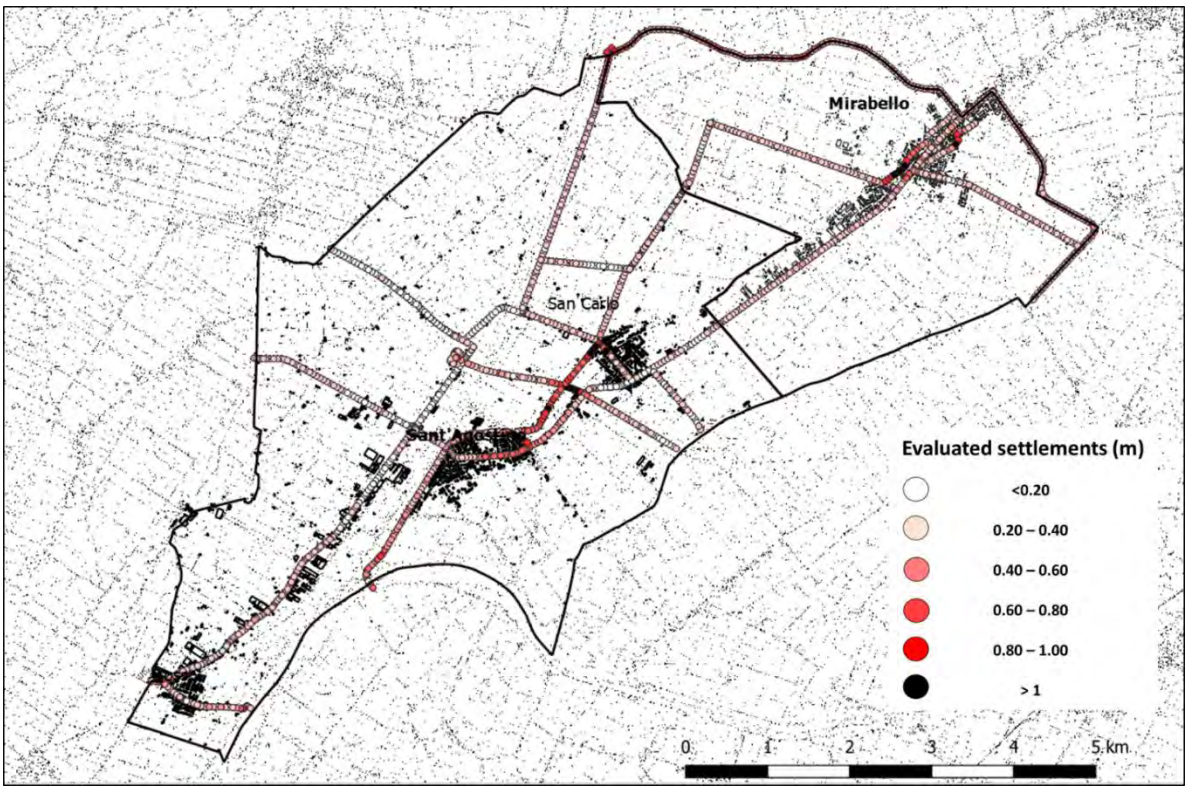

Figure 7-5: Map of evaluated the embankment settlements.

This project has received funding from the European Union's Horizon 2020 research and innovation programme under grant agreement No. 700748

7.8.1 Vulnerability of Embankments

As shown in the Paragraph 7.3, for the definition of the damage state limits for highway embankments, the SYNER-G classification (2009), summarised in the Table 7-1, has been adopted and the results, in terms of Serviceability level have been showed in the Figure 7-6.

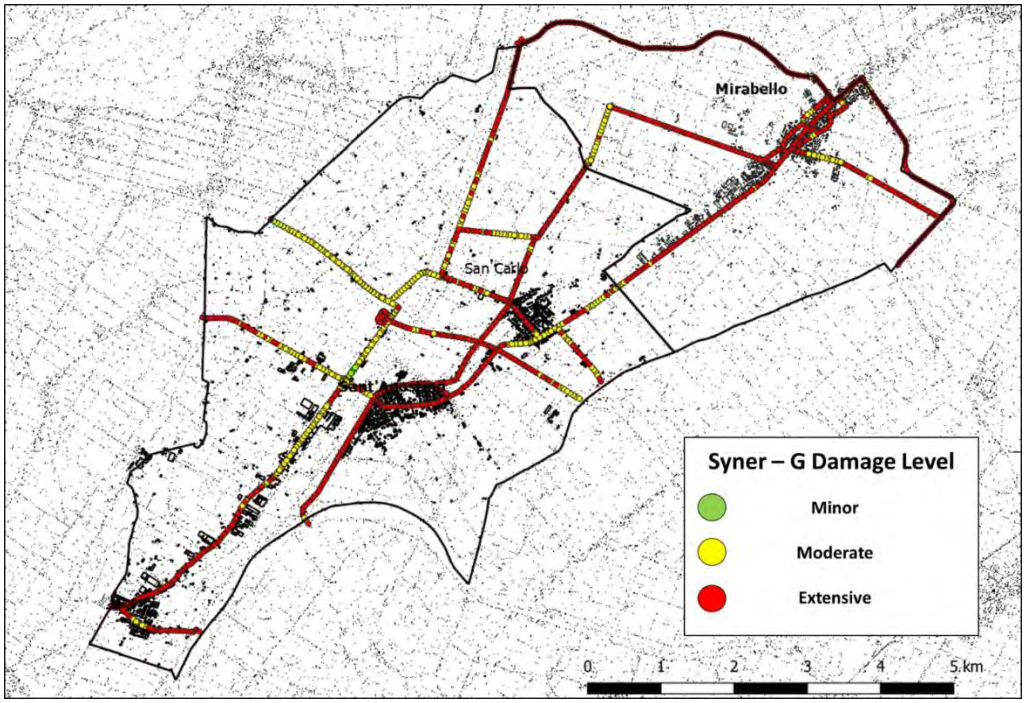

Figure 7-6: Map of the embankment damage levels.

7.8.2 Transportation Network Analysis

Each conurbation and its relative transportation network presents peculiarities which deserve ad hoc preliminary evaluations relating to the identification of relevant spatial dimensions of the transportation network. It consists mainly into the definition of the project area (and study area if needed); the subdivision of the defined area into traffic zones (zoning) and the identification of the basic network (Cascetta, 2009).

Due to the fact that Terre del Reno is characterized by the strong presence of crossing trips, the study and project areas do not coincide. In this case the project area can be identified into San Carlo districts and the dimension of study area (which always includes the first one and encompasses most of the transportation variations' effects) has been defined by the results of the sensitivity analysis: three circular areas with a radius of 20 km, 40 km ad 60 km centred in the project area, have been used as study areas. A TDFM, for each study areas has been developed and the results has been showed in the following Figure 7-7.

This project has received funding from the European Union's Horizon 2020 research and innovation programme under grant agreement No. 700748

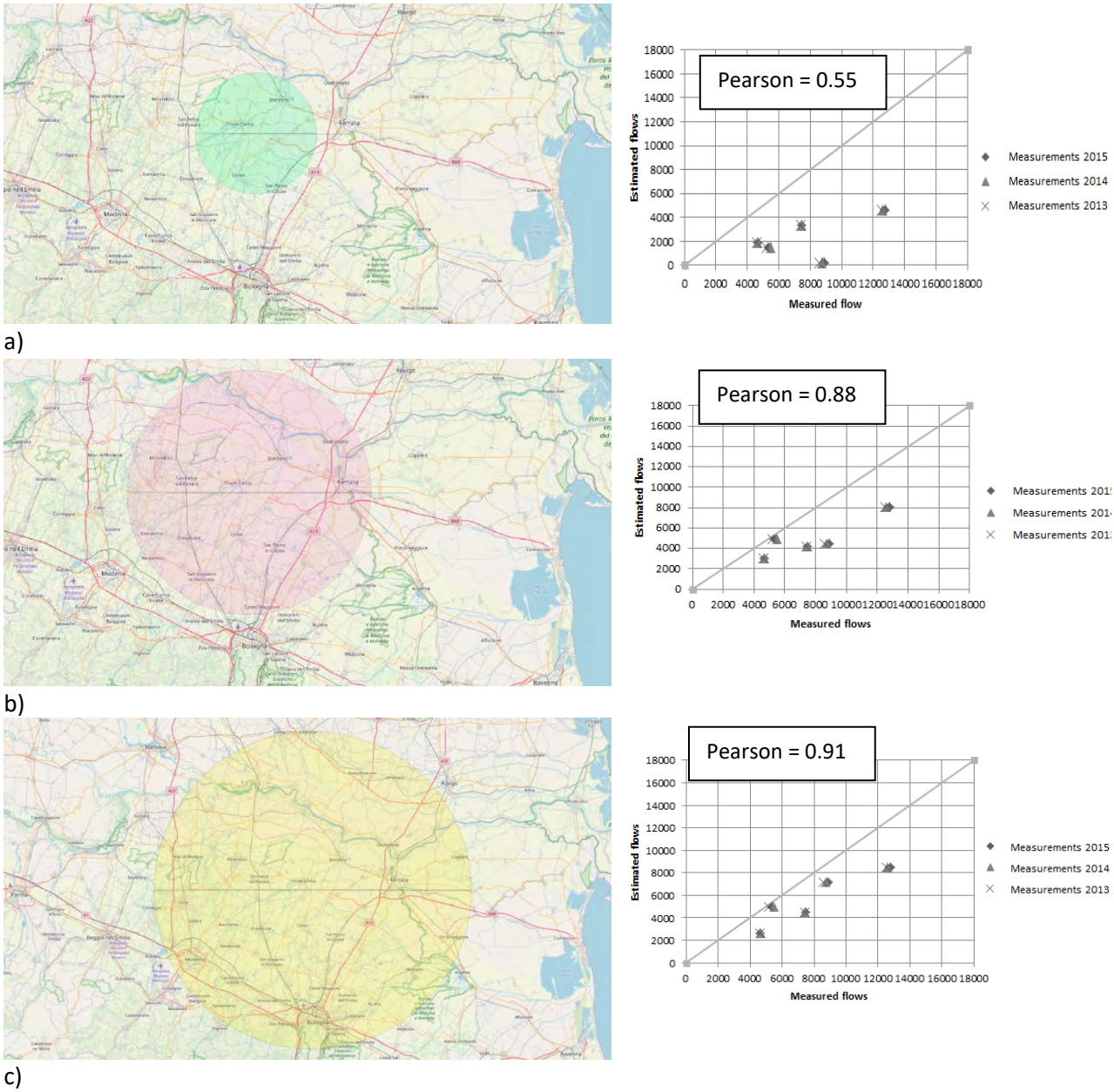

Figure 7-7: Sensitivity analysis with study area's radius dimension of a) 20km; b) 40km and c) 60km.

As shown in the Figure 7-7c, the comparison between estimated and measured flows (into three different years: 2013, 2014 and 2015) suggests a size of the study area of at least 60 km of radius. For this reason, the TDFM has been developed, calibrated and experimentally validated in a buffer area of 60 km of radius around a rural area located in the district of Terre del Reno.

Following of the identification of the study area, 31 centroids and relative traffic zones have been pointed out (Figure 7-8) and the basic network have been highlighted (Figure 7-9).

This project has received funding from the European Union's Horizon 2020 research and innovation programme under grant agreement No. 700748

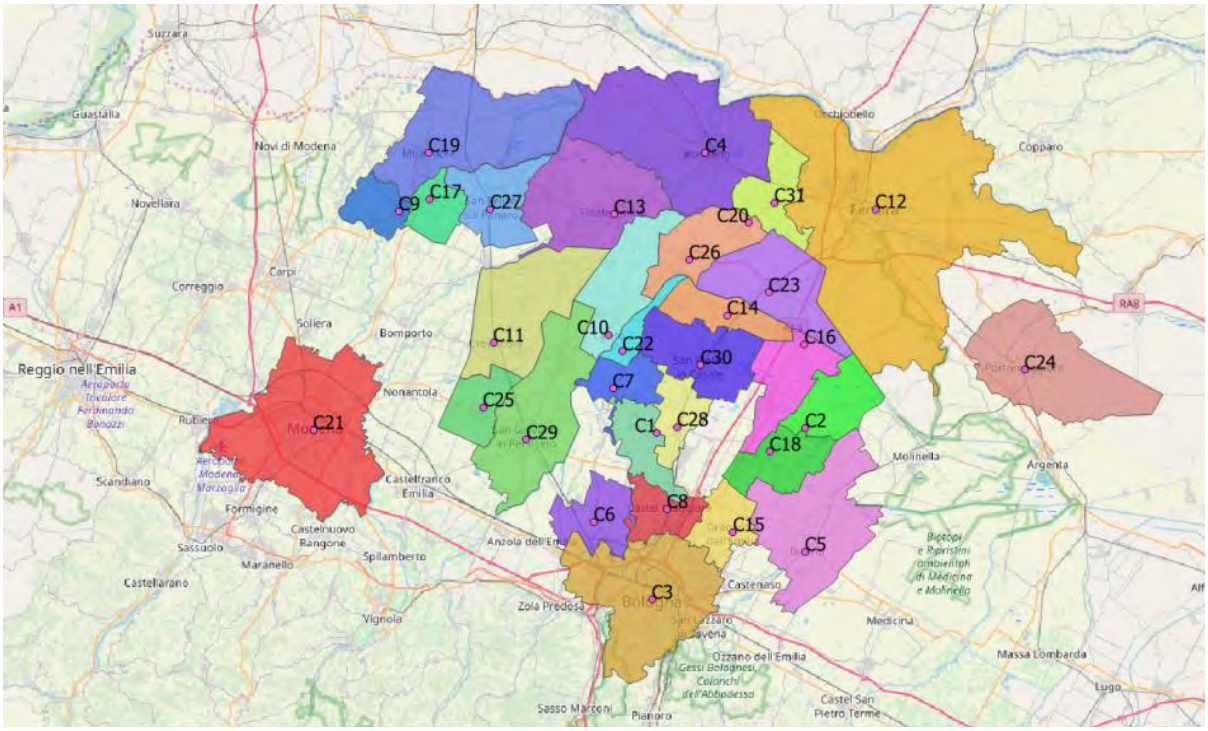

Figure 7-8: Centroids and traffic zones identification.

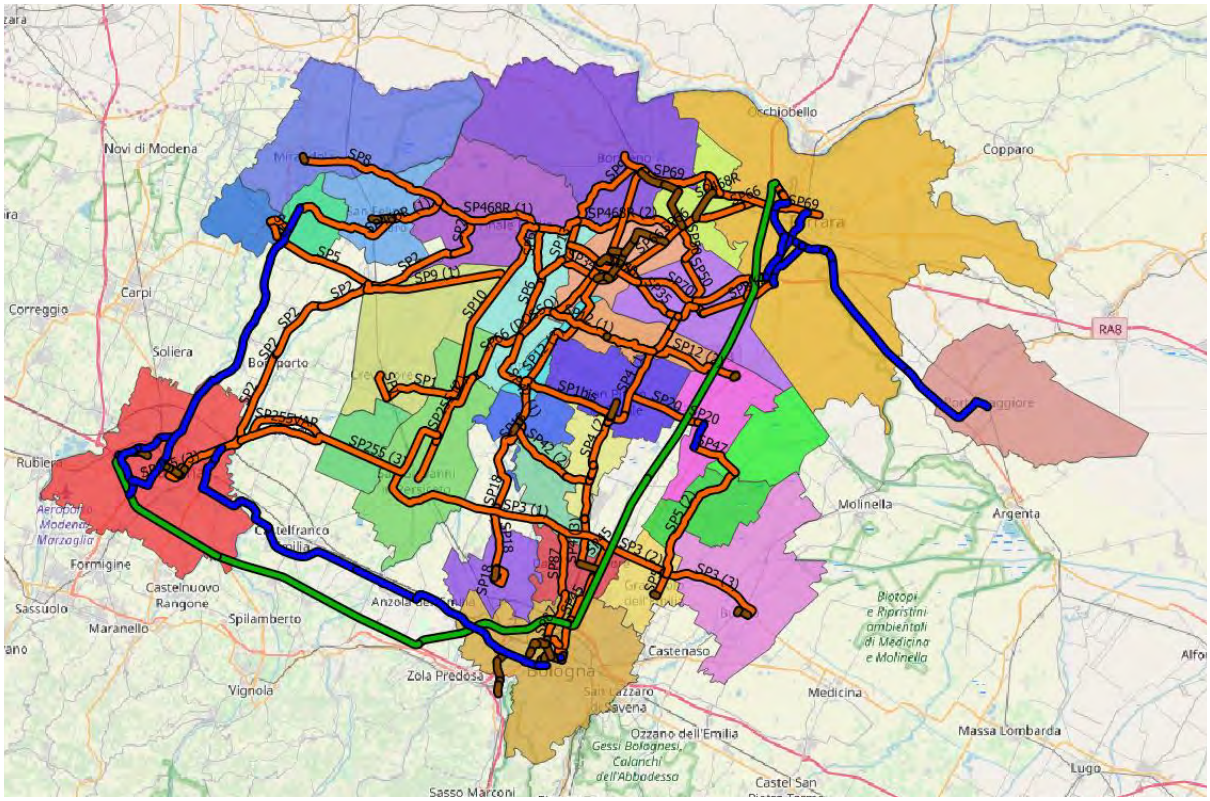

Figure 7-9: Identification of the road basic network.

This project has received funding from the European Union's Horizon 2020 research and innovation programme under grant agreement No. 700748

Due to the variations of the traffic flows occurring within various time frame during the day and different days in a week, several simulations, with different traffic data characterizing the "peak" periods (early morning, lunch and afternoon) and "off-peak" periods have been performed, with the aim to simulate the actual traffic hourly volume on the road network in a typical working day. In this case study, for each scenario (both pre-liquefaction and post-liquefaction), the previous traffic hourly volume values have been assigned according to a "all-or-nothing" conventional rule.

By way of example, the pre and post scenario (related to the specific seismic event of 20 May 2012) within the morning peak period and in the project area, have been reported in the Figure 7-10 and Figure 7-11, respectively. As it can be easily observed from the simulation the disrupt of some road links induced by liquefaction, is responsible for a re-distribution of original traffic flows yielding an increase of travel time and, in turn, of Social Costs.

For each scenario, the travel times on the whole road network, considering a typical working day and the home-based work and home-based school trips, have been evaluated and, according to the travel time cost for heavy and light vehicles, the average transportation generalized cost, have been calculated. By means of the Equation 7.1, the Total Delay Cost for each post-scenario have been evaluated and, in order to assess the Overall Social Cost, the Total Delay Cost should be multiplied by the overall amount of days needed to restore the pre-seismic event conditions of transportation network (no variations in travel demand have been considered during the post-liquefaction event period since, as previously stated, the study area is much more larger than the size of the project area and it has been assumed that the prevailing through traffic travelling in the study area will not be dramatically affected by the seismic event).

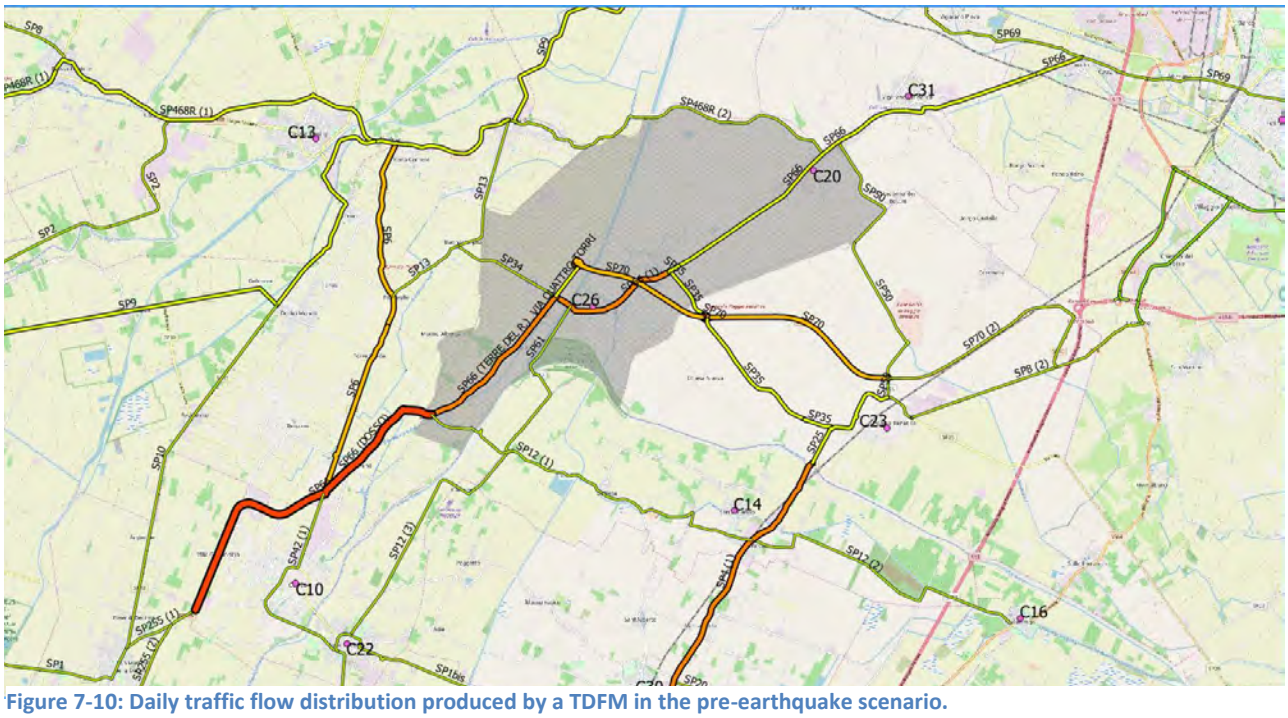

Figure 7-10: Daily traffic flow distribution produced by a TDFM in the pre-earthquake scenario.

This project has received funding from the European Union's Horizon 2020 research and innovation programme under grant agreement No. 700748

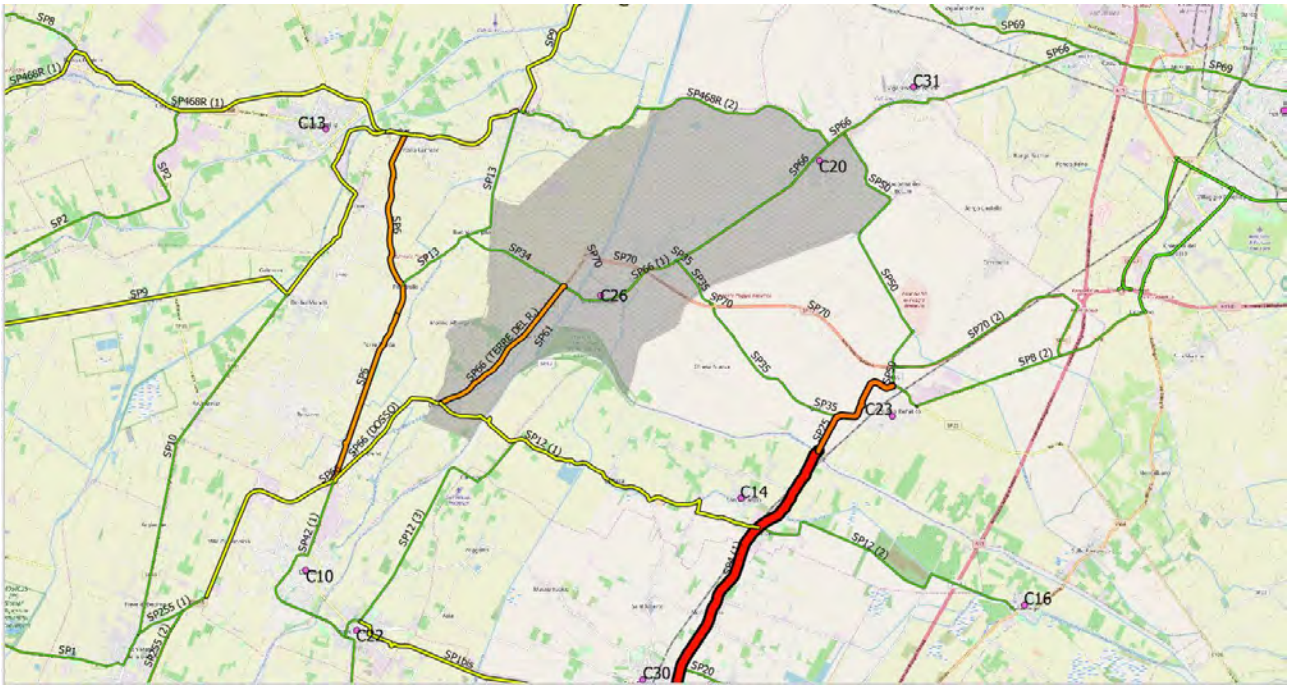

Figure 7-11: Daily traffic flow distribution produced by a TDFM in the post-earthquake scenario.

7.9 Bibliography

AllTraIn ,2015. All-Hazard Guide for Transport Infrastructure. © Copyright 2013 – 2015. The AllTraIn Consorsium. Website: http://www.alltrain-project.eu/

Cascetta, E., 2009. "Transportation Systems Analysis. Models and Applications." Second Edition, Springer Verlag, DOI 10.1007/978-0-387-75857-2, pp. 1-752.

Chang L., 2010. "Transportation system modeling and applications in earthquake engineering". Doctoral Thesis in the Graduate College of the University of Illinois at Urbana-Champaign.

Fioravante, V. et al.,2013. Earthquake geotechnical engineering aspects: the 2012 Emilia Romagna earthquake (Italy). Seventh international Conference on Case Histories in Geotechnical Engineering, April 29 th – May 4th, 2013. Chicago (US).

HAZUS®, 2004. Multi-hazard Loss Estimation Methodology Earthquake Model HAZUS®MH MR4 Technical Manual. National Institute of Building Sciences. (NIBS). Washington, DC 2004. Website: http://www.fema.gov/hazus/.

Karamitros, D.K., Bouckovalas, G. D., Chaloulos Y.K., 2013. Seismic settlements of shallow foundations on liquefiable soil with a clay crust. Soil Dynamics and Earthquake Engineering. 46. 64-76.

SecMan Project "SECURITY MANUAL FOR EUROPEAN ROAD INFRASTRUCTURE" Website: www.secman-project.eu. Copyright: SecMan Consortium, 2013.

SeRoN, 2012. Deliverable D400 "Importance of the structures for the traffic network". © Copyright 2009 – 2012. The SeRoN Consortium.

STRIT project. Website: http://www.stress-scarl.com/it/innovazione/i-progetti-nazionali/strit.html.

SYNER-G ,2009. Systemic Seismic Vulnerability and Risk Analysis for Buildings, Lifeline Networks and Infrastructures Safety Gain. Website: http://www.vce.at/SYNER-G/files/project/proj-overview.html

Werner S.D., Taylor C.E., Cho S., Lavoie J.-P., Huyck C., Eitzel C., Chung H. and Eguchi R. T. ,2006. "REDARS 2 METHODOLOGY AND SOFTWARE FOR SEISMIC RISK ANALYSIS OF HIGHWAY SYSTEMS". Special Report MCEER-06-SP08. Federal Highway Administration.

This project has received funding from the European Union's Horizon 2020 research and innovation programme under grant agreement No. 700748

8 CONCLUSIONS

Within the general scope of the project, aimed at defining an operative strategy to quantify and mitigate the liquefaction risk on critical infrastructures, the Work Package WP7 had the role of validating the defined procedures with the retrospective analysis of past events. This fundamental step of the research served to disclose possible weaknesses of the implemented procedure, show limitations of the adopted models and suggest alternative more effective strategies to characterise and predict the different issue of liquefaction risk assessment. Bearing this goal, six different case studies have been analysed in the present deliverable:

- A single building
- A large city - Christchurch (New Zealand)
- A medium city - Adapazari (Turkey)
- A small town with an industrial district - Terre del Reno (Emilia-Romagna – Italy)
- A pipeline network - Urayasu (Japan)
- A transportation infrastructure – (Emilia Romagna – Italy)

For each case, very big databases have been created on a GIS platform, collecting results of previous studies and information of different nature (seismic hazard, subsoil investigations, characteristics of buildings and survey of damage).
The logic structure proposed for risk assessment implies the layout depicted in Figure 1.2, where a chain of analyses is defined involving the earthquake scenarios, determined by the seismic hazard of the studied area and the local response of subsoil, the susceptibility to liquefaction evaluated independently or in a coupled way with the superstructure, where the interaction between the two elements is relevant, socio-economic implication. Depending on the availability of data, different from case to case, these aspects have been particularised for the above examples. Each step of the analysis has required to schematize the relations between the different elements and to characterize each subject in a way that is appropriate and manageable for the examined scale.
Risk assessment carried out on systems occupying relatively large areas like cities, industrial districts, infrastructural assets implies to quantify on a local basis the different factors forming risk (hazard, vulnerability and exposure) and, for each type of analysis, characterise the mechanisms, define and quantify the representative parameters. In this process, uncertainties are unavoidable and thus the implemented procedure should minimise their effects or, at least, quantify them. As shown by the different examples, assessment has implied to recoil into a unique framework information of different nature, each derived with a specific purpose and accuracy level, and to govern the uncertainty inherently connected with each dataset and with the combination of factors. Particularly convenient from this viewpoint has been the adoption of geostatistical tools for the interpolation of information over the studied area. In geostatistics (Matheron, 1965), the value of a variable in a generic point of the map is computed as a linear interpolation of the values obtained on the investigated positions, but the difference with a straight interpolation with mathematical functions (e.g. polynomial) consists in the fact that estimates are considered as statistical variables and thus a standard deviation is associated to them. Thus, being reliability associated to the estimate (a large standard deviation implies a greater uncertainty and a lower reliability), the quality of the analysis could be improved confining it to the zones where estimates are more robust. The use of geostatistics enabled also to eliminate inconsistencies from the original information, like for instance largely different values of a subsoil variable (thickness of layers, soil relative densities) obtained on boreholes close to each other. This inconsistency, stemming from various

This project has received funding from the European Union's Horizon 2020 research and innovation programme under grant agreement No. 700748

reasons like different standards adopted in the execution of tests, a wrong mapping of the borehole position, errors in the execution of tests etc. has been enlightened with the application of geostatistical tests.

To assess the predictive capability of the models in a quantitative manner, and not just with a subjective evaluation, the method based on the Receiver Operating Curve (ROC) (Kongar et al., 2015) has been adopted. It establishes a binary classification of predictions and observations in a way that, for a specific event and an adopted predictive model, data can be summarized into 2 x 2 contingency tables that identifies true positives (PP), true negatives (NN), false positives (FP), and false negatives (FN) (Figure 1.8). With this method, the correlation between prediction and observation is quantified by the Area Under Curve (AUC) index, equal to 0.5 in case of poor correspondence, approaching 1 for perfect prediction. Once validity of the predictive method is ensured, the method enables also to establish an optimal threshold for the predicting variable, able to distinguish negative and positive events, with the maximum Mathews Correlation Coefficient.

The analysis of the single building has been carried out performing different numerical analyses with the finite difference numerical code FLAC v8 (Itasca Consulting Group, Inc., 2016). This software was chosen considering its flexibility, the possibility of performing two and three-dimensional analyses and of using advanced constitutive models. A well-documented example, located in the municipality of Terre del Reno (Italy), subjected to liquefaction during the May 20th 2012 earthquake, has been taken as reference to calibrate the numerical model with the available subsoil investigations and to validate it with the observed performance of the building (earthquake induced settlements). The model, has been used to see various effects of liquefaction, like the presence of layered subsoil where liquefiable and non-liquefiable strata are alternated. With this regard, the model shows that liquefaction induced in a lower layer tends to filter the seismic signal travelling to the upper levels, prevent the onset of pore pressure, and thus the occurrence of liquefaction. Additionally, the numerical analysis has been particularly focused on the influence of subsoil variability on the settlements induced by liquefaction. In particular, the subsoil variability modelled with a random and a spatially correlated models (using the random field technique, Fenton & Griffiths, 2000) is responsible for the differential settlements of foundations. Two systems have been particularly analysed, an isolated footing and a continuous plate, both showing that, for given correlation length, the absolute and differential settlements are poorly influenced by the random variability of the relative density. The results also show a strong correlation between absolute and differential settlements and this result is even more relevant considering the large variability of both values induced by the earthquake intensity. This correlation is fundamental, being used later in the definition of the fragility function for the buildings.

The back-analysis of the liquefaction occurred in Christchurch and in Terre del Reno has been carried out at the large scale with a similar methodology. In a first step, liquefaction hazard has been assessed using different indicators derived from literature and applying them to predict the effects at the ground level. The analysis does not reveal meaningful differences between the different indicators with a similarly fair performance for all of them. The prediction is more acceptable when the subsoil can be assimilated to a three-layer model, as in the case of Terre del Reno, less effective when multiple liquefiable layers are alternated to non-liquefiable ones, as in Christchurch. In fact, a noticeable improvement in the quality of prediction is obtained in the second case from the application of the indicators only to the subsoil investigation that reveal a profile assimilable to a three layers model. To this aim an equivalence criterion (ESP) defined in the project (Deliverable D3.2) has been adopted to identify those profiles that may be approximated with the three-layer model, an upper crust, a liquefiable layer and a non-liquefiable base layer. In this case values of AUC as high as 0.87 as obtained. The second step of the analysis has been applied to the assessment of building performance. Here the implemented considers the interaction between subsoil and structure and different simplified methodologies have been considered to compute

the foundation settlements (Karamitros et al., 2013, Bray & Macedo, 2017, Bullock et al., 2018). Therefore, the assessment of physical vulnerability adopts the absolute settlement ad Engineering Demand Parameter, transforms it into differential settlement with the previously found correlation and adopt the fragility functions defined by Fotopoulou et al. (2018). The ROC validation procedure reveals a fair performance for the buildings of Terre del Reno and a poor performance for the buildings of Christchurch, possibly due to the more complex subsoil layering in this second case different from the three-layer model assumed in the simplified relations. In fact, the method applied to relatively tall buildings (with more than 3 floors) resting on subsoil profiles assimilable to a three-layer models give much better results. In particular, the prediction is more reliable if absolute settlements are computed with the Bray and Macedo (2018) simplified relation. The third step of the analysis has consisted in the application of risk assessment for the two cases. To this aim, the damage has been transformed into economic losses, considering three components, one due to the repair of structures, the second due to the content and the third due to loss of functionality (business). A cost-benefit analysis has been implemented on annual basis, comparing economic risk and cost of mitigation with ground improvement, the latter computed as product of a cost per unit volume of liquefiable soil times the volume below each building. The analysis clearly shows on maps how the increase of cost for ground improvement reduces the convenience of mitigation. An important issue for the industrial buildings concerns the annual revenue of the factory, that seems to play the most relevant role for decision making.

This full and detailed case study report for the application of the risk/resilience assessment toolbox for the Adapazari EILD cases compares the prediction with the extensive investigation of the buildings affected by the 1999 Adapazari earthquake. A damaged building database was created for Adapazari based on the Sakarya Municipality archives by the Istanbul University-Cerrahpasa team members, consisted of 4550 buildings, 3504 of which were “heavily damaged” and 1406 were “moderately damaged”. 526 of these buildings were identified as possibly affected by liquefaction based on the Sakarya Municipality archives, while for the rest of them no data was available. For 55 buildings, damage due to liquefaction was obvious, and these buildings constructed another database. A detailed study was also carried out to determine the soil profiles in the Adapazari city center. The data was then used in LIQUEFACT Software for hazard analyses and hazard and risk analyses. Spatial distribution of risk analyses were then compared with the field liquefaction data. The results were also compared with the well-known liquefaction indicators, which are Liquefaction Potential Index (LPI) and Liquefaction Severity Number (LSN), which were used both in original and modified forms. For the 526 buildings and hazard and risk analyses, an evaluation was carried out for the LIQUEFACT Software results. Hazard and Risk analyses captured the 78% of the damaged cases for ESP method, which should be accepted as a good estimate. It should be recalled that ESP method was developed within the context of LIQUEFACT Project. For the 526 buildings and hazard analyses, while LSN(ESP) and LPI(Classic) estimations were better in estimating the damage than LSN(Classic). LSN(ESP) was a better indicator in the sense that it estimated damage levels ranging from low to very high for all buildings and there was no estimation for “no damage, none”. The results for hazard analyses for 55 buildings, LSN(ESP) and LPI(Classic) were better indicators in the sense that they estimated damage ranging from low to very high for all buildings and there was no estimation for “no damage, none”. For these 55 buildings, for hazard and risk analyses, LIQUEFACT Software estimated that 15% of the buildings would be not damaged, this is an underestimation. However, for a spatial study, 85% correct estimation of damage should be accepted a very good estimation.

The comparison with the liquefaction assessment indicators is as follows. The results showed that LSN was a better indicator for estimating the liquefaction induced damage levels in Adapazari, in case the values are calculated from the foundation base. Among the LSN approach, the best estimation rates were obtained with LSN-3 and LSN-4 approaches, which took into account the modified I_c and PI values and

seepage induced liquefaction in weak layers overlying the groundwater level. This may be an evidence that, the unsaturated, shallow, weak silty layers (with normalized clean sand equivalent cone tip resistance less than 85) coupled with modified soil behavior index (I_c<2.8 and PI<15) contributed to liquefaction in 1999 Adapazari earthquake. The study carried out in this paper showed that system response approach developed by Cubrinovski et al. (2018) could be applied with great success to Adapazari silty soils. In Adapazari, liquefaction occurred in the first 10 m as described in the system response approach, however with the effect of foundation and shear stresses. The critical layers dominated the liquefaction occurrence and the shallowest critical layer was of critical importance. The saturated silty layers below the foundation levels affected to the liquefaction damage considerably no matter how thin they were. The critical layers in Adapazari were characterized by q_{c1ncs} values between 40 and 85 in all 55 cases. Seepage induced liquefaction was shown to occur in Adapazari cases, in cases where tip resistance, soil behavior index and Plasticity Index criteria were met. While the system response approach defines that a top 2.5 m crust prevents the liquefaction-induced ground damage in Christchurch cases, in Adapazari it was observed that a 3.0 m crust layer below foundation base prevented liquefaction-induced damage.

The analysis of the performance of pipelines in Urayasu has been addressed to find suitable fragility functions to express the rate of damage. Considering the heterogeneous distribution of in situ tests (Standard Penetration Tests) and pipelines over the territory a complex procedure has been implemented to relate the outcomes of the first to damage of the second. The method takes advantage of the ground settlements induced by the earthquake, measured with Lidar and made available on maps. A strong correlation has been firstly found between ground settlements and damage, also confirmed by the ROC curve tests. Simultaneously, other correlations has been found between indicators of the liquefaction performance of subsoil (LPI from Iwasaki et al.,1978; w from Zhang et al., 2002; LSN from van Ballegooy et al., 2014). Finally, the two correlations have been merged to correlate fragility of the pipelines to indicators.

The last analysed case study concerns the effects of liquefaction on the transportation network of Terre del Reno. In this case the project area has been extended out of the district of Terre del Reno performing a sensitivity analysis where three circular areas with a radius of 20 km, 40 km at 60 km centered in the project area have been considered and a TDFM model is developed. The comparison between estimated and measured flows (in three different years: 2013, 2014 and 2015) suggests a study area size of at least 60 km in radius is more suitable for the present study. Thereafter, the TDFM model has been developed, calibrated and experimentally validated in an area of 60 km radius around a rural area located in the Terre del Reno district. Further assumptions underlying of the model consider that the study area of the model embraces, a supra-provincial (but not regional) territorial scale; therefore, since it is a so-called "large area", it was deemed appropriate to assume a discretization of the traffic areas at the municipal scale; the effects of the seismic events that causes liquefaction in the study area are mainly limited to the conurbation of Terre del Reno; the movements that can be monetized are substantially those linked to the home-work / study reason; in this regard, it should be remembered that these types of displacements are marked by the lower rigidity in terms of elasticity of the demand curve with respect to those relating to other reasons and / or recreational activities; travel for home-work / study reasons are considered prevalent in the mobility scenario to be measured; the daily fluctuation of mobility was partitioned considering only two scenarios: a peak one which occurs mainly in two time slots (from 7:00 to 9:00 and from 17:00 to 19:00) and one of soft for the rest of the day; for the reasons outlined above, the Origin / Destination matrix was developed starting from the data on systematic commuters collected through the 2011 ISTAT Census; the creation of any temporary shelter areas was assumed near the main town center at the municipal level and therefore the emission and attraction factors of the traffic areas are considered invariant in the ex-ante scenario and ex-post earthquake; finally, since it is a scenario

This project has received funding from the European Union's Horizon 2020 research and innovation programme under grant agreement No. 700748

simulation in a large area, with displacements also of significant entity (in terms of travel times and trajectories), the mechanisms for choosing the route are considered to be characterized by an average low epistemic level and therefore it seems lawful (also by virtue of the foreseeable installation of the directional vertical signage of a temporary nature) to assume a sub-model of assignment of a predominantly deterministic type. All the above assumption led to calculate the variation of traffic conditions induced by liquefaction on the embankment roads. To this aim, damage is expressed as a function of the absolute settlements, computed with the Karamitros et al. (2013) formula, through a fragility function given by Synergy project.

In conclusion, all the above applications have shown that the holistic risk assessment methodology expressed in Figure 1.2 can be effectively applied to various system, provided a customization is accomplished, specifying each time the mechanical and socio/economic characteristics of the different components of the system. In the present study, simplified methods have been adopted for the different steps, making use of global performance indicators. This approach stems from the limited detail of information usually available at the large scale. More refined schematization and predictive models may replace the simplified ones, provided a higher quality and quantity of information is made available. However, considering that the acquisition of information over urban system is a cumulative process, there is hope that liquefaction risk can be managed with more and more confidence in the future. The proposed methodology traces a strategy for implementing it at different scale.